DEVELOPMENT OF RESONANCE FLUORESCENCE LIDAR FOR STUDIES OF THE AURORA

A

THESIS

Presented to the Faculty

of the University of Alaska Fairbanks

in Partial Fulfillment of the Requirements

for the Degree of

DOCTOR OF PHYLOSOPHY

By

Liguo Su, B.S., M.S.

Fairbanks, Alaska

December 2007

Reproduced with permission of the copyright owner. Further reproduction prohibited without permission.

UMI Number: 3302512

INFORMATION TO USERS

The quality of this reproduction is dependent upon the quality of the copy submitted. Broken or indistinct print, colored or poor quality illustrations and photographs, print bleed-through, substandard margins, and improper alignment can adversely affect reproduction.

In the unlikely event that the author did not send a complete manuscript and there are missing pages, these will be noted. Also, if unauthorized copyright material had to be removed, a note will indicate the deletion.

UMI®

UMI Microform 3302512

Copyright 2008 by ProQuest LLC.

All rights reserved. This microform edition is protected against unauthorized copying under Title 17, United States Code.

ProQuest LLC
789 E. Eisenhower Parkway
PO Box 1346
Ann Arbor, MI 48106-1346

Reproduced with permission of the copyright owner. Further reproduction prohibited without permission.

DEVELOPMENT OF RESONANCE FLUORESCENCE LIDAR

FOR STUDIES OF THE AURORA

By

Liguo Su

RECOMMENDED:

Advisory Committee Chair

Chair, Department of Electrical and Computer Engineering

APPROVED:

Dean, College of Engineering and Mines

Dean of the Graduate School

Nov 8, 2007

Date

Reproduced with permission of the copyright owner. Further reproduction prohibited without permission.

Abstract

In this thesis I present resonance fluorescence lidar studies of the middle and upper atmosphere. I focus on two specific applications; lidar measurements of heat fluxes in the mesosphere, and lidar measurements of auroral nitrogen ions in the thermosphere. In the heat flux study, I determine the limitations in state-of-the-art sodium Doppler wind-temperature lidar measurements. I conduct statistical analysis of current lidar measurements using analytical and Monte Carlo techniques and extend them to consider future measurements. I find that the expected biases for summertime flux measurements in polar regions will be larger than the geophysical values of the fluxes. In the nitrogen resonance lidar study, I conduct a simulation of the measurements under realistic auroral conditions and found that current lidar systems should be able to make statistically significant measurements of the nitrogen profile at a resolution of 6 km and 300 s. I develop a prototype nitrogen resonance lidar system operating at 390 nm. This lidar system is based on an existing dye laser-based iron resonance lidar system that operates at 372 nm. I designed and implemented a tuning control system that allows 1 pm resolution in the laser tuning. I made a set of field measurements and found that the performance of the prototype lidar was less than expected. I conduct an engineering analysis of the measurements and conclude that the lower than expected performance is due to the lasing characteristics of the dye laser.

Reproduced with permission of the copyright owner. Further reproduction prohibited without permission.

Table of Contents

Reproduced with permission of the copyright owner. Further reproduction prohibited without permission.

Page

Reproduced with permission of the copyright owner. Further reproduction prohibited without permission.

Page

Reproduced with permission of the copyright owner. Further reproduction prohibited without permission.

List of Figures

Reproduced with permission of the copyright owner. Further reproduction prohibited without permission.

Page

Reproduced with permission of the copyright owner. Further reproduction prohibited without permission.

Page

Reproduced with permission of the copyright owner. Further reproduction prohibited without permission.

Page

Reproduced with permission of the copyright owner. Further reproduction prohibited without permission.

Page

Reproduced with permission of the copyright owner. Further reproduction prohibited without permission.

List of Tables

Reproduced with permission of the copyright owner. Further reproduction prohibited without permission.

Page

Reproduced with permission of the copyright owner. Further reproduction prohibited without permission.

Acknowledgements

I would like to express my gratitude to Dr. Richard L. Collins for supporting my Ph.D. study at the University of Alaska Fairbanks. I obtained good research training under his supervision in the lidar research laboratory of the Geophysical Institute. I really appreciate his generous help, understanding, and encouragement in my study. I wish to express my sincere thanks to Drs. John D. Craven, Vikas Sonwalkar, William A. Bristow, and Joseph G. Hawkins. As my committee members, they put a lot of effort in directing my study and helped my research work. Their help and guidance have been of great value in my professional life.

My sincere thanks are also due to Drs. Chiao-Yao She and David A. Krueger of Colorado State University. I thank them for their support during my visit to Colorado in 2004 and their effort in preparing our article on lidar measurement of heat flux. I would like to thank Dr. Javier Fochesatto for access to the Raman spectrometer and helping me with optical filter calibration. I would also thank Dr. Kohei Mizutani for providing me with access to the Rayleigh lidar.

I also thank Ms. Brentha Thurairajah and Ms. Agatha Light. They assisted me in my research laboratory work at PFRR as well as in writing my thesis. I wish to extend many thanks to the former students of the Geophysical Institute lidar program who have worked with me, helped me, and given me assistance during the course of my academic studies.

I thank the staff at PFRR for supporting the operation of the lidar research program. I also acknowledge the financial support of the graduate school at the University of Alaska Fairbanks and the CEDAR program at the National Science Foundation.

Last but not the least, I would like to thank my family. They support me always.

Reproduced with permission of the copyright owner. Further reproduction prohibited without permission.

Dedication

To my wife, Lan Yu,

and

my son, William Lee Yu.

Reproduced with permission of the copyright owner. Further reproduction prohibited without permission.

1 Introduction

In this chapter I first present an overview of the structure of the atmosphere. I then discuss the technique of resonance lidar and its application in remote sensing of the atmosphere. Finally I present the scope of this study and an outline of this thesis.

1.1 The Structure of the Atmosphere

The structure of the atmosphere is outlined in Figure 1.1. The temperature profile is from Houghton [1986]. Traditionally the atmosphere is divided into five regions following the thermal variations with altitude. The vertical structure consists of a series of layers. Each layer is called a "sphere" and the boundary between each pair of layers is called a "pause". The lowest layer is called the troposphere and extends from the ground to the tropopause at 8 to 16 km altitude. The altitude of the tropopause varies with latitude and season. In polar regions the tropopause is at an altitude of 8 km with a temperature of about 220 K. About 75 percent of the atmosphere's mass is contained in troposphere. The troposphere is characterized by decreasing temperature with altitude due to convective heating decreasing as height increases. The stratosphere lies immediately above the troposphere. The stratosphere extends up to the stratopause at 45 to 55 km altitude. The stratosphere is characterized by increasing temperature with altitude due to the ultraviolet absorption by ozone in this region. The mesosphere lies immediately above the stratosphere. It extends up to the mesopause at 80 to 90 km altitude. The mesosphere is characterized by decreasing temperature with altitude due to the decrease in ozone. The mesopause is the coldest region in the atmosphere. The thermosphere lies above the mesosphere and extends up to 500 km altitude. The temperature increases rapidly in this region due to an increase of the absorption of ultraviolet and solar particles. The region from the upper mesosphere to the thermosphere is highly ionized by solar radiation and is called the ionosphere. Above 500 km, the exosphere is the region closest to space. Traditionally the atmosphere is divided into lower and upper regions. Meteorology focuses on the study of phenomena in the lower atmosphere (i.e., the troposphere and lower stratosphere) and aeronomy focuses on the study of phenomena in the middle and upper atmosphere (i.e., the stratosphere and above) [Seinfeld and Pandis, 1997].

Reproduced with permission of the copyright owner. Further reproduction prohibited without permission.

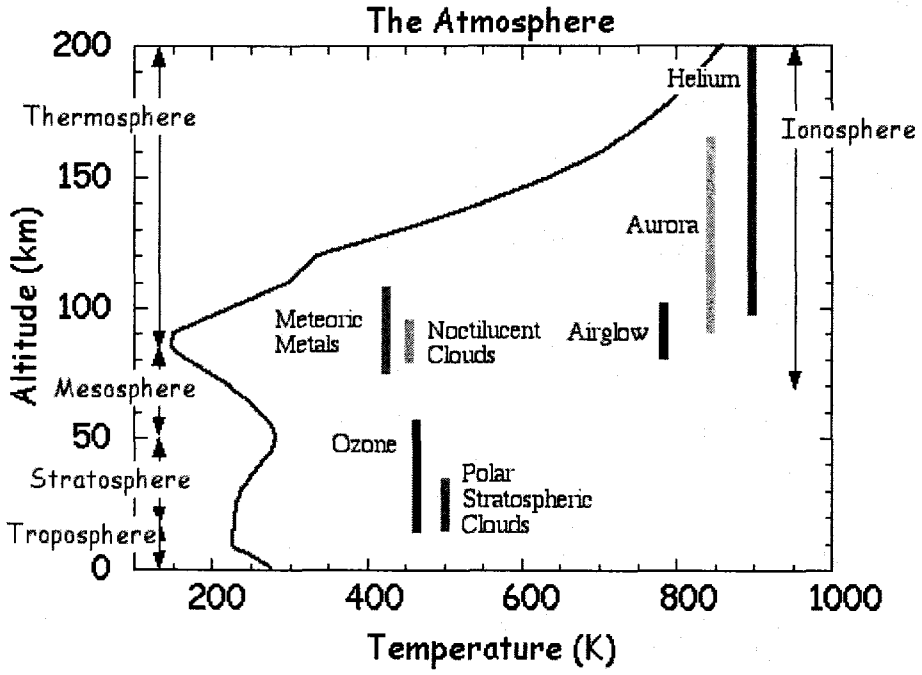

Figure 1.1 The thermal structure of the atmosphere showing the altitude distribution of several atmospheric phenomena.

In Figure 1.1 there are several phenomena in the polar atmosphere region that are of interest to scientists. Above 80 km, there are meteoric metal layers composed of sodium, potassium, calcium, lithium, and iron, that are produced by meteoric ablation; noctilucent clouds, or polar mesospheric clouds, that are formed by water ice; airglow layers (hydroxyl, atomic oxygen, and molecular oxygen), which are formed by weak optical emissions in the upper atmosphere; the ozone layer in the stratosphere; the helium layer in the upper thermosphere; polar stratospheric clouds, which are formed by very cold temperatures in the polar stratosphere; and the aurora borealis (also called the northern lights), which is produced by energized solar wind electrons colliding with atoms and molecules in the Earth's atmosphere. For a general survey of these atmospheric phenomena I recommend that the interested reader should refer to the textbooks by Wayne, [1985], Solomon and Brasseur [2005] and Seinfeld and Pandis [1997].

Reproduced with permission of the copyright owner. Further reproduction prohibited without permission.

1.2 Resonance Lidar

The resonance lidar (light detection and ranging) or laser radar technique, is a spectroscopic remote sensing technique. Lidar is an active optical remote sensing technique, and unlike traditional radar, is species specific. Resonance fluorescence lidar is an application of resonance absorption and subsequent spontaneous emission or fluorescence. The word "resonance" refers to the resonant absorption caused by the interaction between the laser and atmospheric species at a particular frequency or wavelength. The word "fluorescence" refers to the light emitted after the resonant absorption by the excited atoms or molecules.

A typical lidar system configuration is illustrated in Figure 1.2. The fundamental components of the lidar system are a laser that transmits a pulse of light into the sky and a telescope that receives the light that is scattered back by the atmosphere. The frequency of the laser light is determined by the reference and control system. The light received by the telescope is collimated and filtered by optics in the receiver. The collimated and filtered light is converted into electrical signal by the detector (typically a photomultiplier tube, PMT). The electrical signal is captured at high speed by the dedicated data acquisition system. Once the echo from one or several laser pulses has been captured in the data acquisition system, the data is transferred to the computer. The computer synchronizes the transmitter and the receiver and establishes the parameters of the measurement (e.g., temporal and spatial resolution). In middle and upper atmosphere lidar systems, the optical signals from the sky are very weak. The receiver detects signals as a sequence of photons, and counts them as they are detected. The raw lidar signal is measured in photon counts.

Researchers have conducted resonance lidar studies since the 1960s [Bowman et al., 1969]. Resonance fluorescence lidar systems use the strong resonance scatter signals to measure concentration, temperature, and wind in the middle and upper atmosphere (see collection of papers edited by Grant et al. [1997], and review by Chu and Papen [2005]). The year that resonance lidar measurements were first made of a specific mesospheric metal are tabulated in Table 1.1 [Gardner, 1989].

Reproduced with permission of the copyright owner. Further reproduction prohibited without permission.

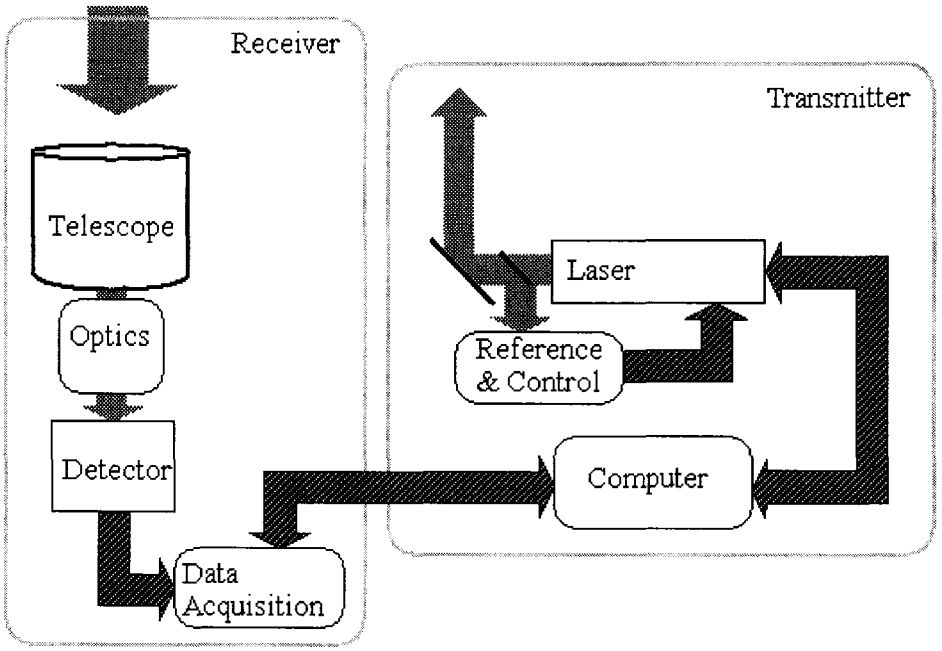

Figure 1.2 A lidar employs a laser transmitter, a telescope receiver, and associated control and acquisition systems.

Table 1.1 First resonance lidar measurements

Species	Wavelength (nm)	Year
Sodium, Na	589.0	1969
Potassium, K	769.9	1973
Lithium, Li	670.8	1980
Calcium, Ca	422.7	1985
Calcium ion, Ca^+	393.4	1989
Iron, Fe	372.0	1989

There are three thermospheric species that have also been studied for use in resonance lidar studies. These are barium, helium, and molecular nitrogen. The barium ion lidar was first proposed by Goree and Neff [1989]. A temperature barium ion lidar was first proposed by Collins and Stenbaek-Nielsen [1995]. The barium ion lidar provides a method of measuring the atmospheric thermal profile between

Reproduced with permission of the copyright owner. Further reproduction prohibited without permission.

altitudes of 200 and 500 km, based on artificial barium clouds released by rockets. The resonance line for the barium ion lidar is at 493.4 nm. No operating barium resonance fluorescence lidar has been reported at this time.

The helium lidar provides a method of measuring the concentration of metastable helium which naturally occurs in the atmosphere [Gerrard et al., 1997]. These measurements support studies of helium escape fluxes, and the impact of solar activity on atmospheric transport at altitudes between 100 and 1500 km. The resonance line for metastable helium lidar is at 1083.0 nm. No operating helium resonance fluorescence lidar has been reported at this time.

The third system is the molecular nitrogen ion resonance lidar [Garner and Dao, 1995; Collins et al., 1997]. This resonance lidar provides a method to measure molecular nitrogen ions that are produced by the aurora in the thermosphere. The optimum resonance line for molecular nitrogen ion resonance lidar is at 390.3 nm, which corresponds to one of the rotational transition wavelengths in the nitrogen first negative band system. No operating nitrogen resonance fluorescence lidar has been reported at this time. The development of the molecular nitrogen ion resonance lidar is the focus of this thesis.

1.3 Resonance Lidar at Poker Flat Research Range

Researchers from the Geophysical Institute (GI) of the University of Alaska Fairbanks (UAF) began resonance lidar observations at Poker Flat Research Range (PFRR, 65° N, 147° W) in 1994. The first resonance lidar system was a sodium resonance lidar that employed a flashlamp-pumped dye laser as a transmitter (Candela Laser Corporation, Bedford, MA). This system allowed measurements of the mesospheric sodium layer but was incapable of atmospheric temperature or wind measurements [Collins et al., 1996; Collins and Smith, 2004]. A Rayleigh lidar system was installed in November 1997 by researchers from the GI and the National Institute of Information and Communications Technology (NICT) [Mizutani et al., 2000]. This system was based on a Nd:YAG flashlamp-pumped laser (Continuum Laser Corporation, Santa Clara, CA) allowed measurements of atmospheric density, temperature and noctilucent clouds [Cutler et al., 2001; Collins et al., 2003]. In 1999, an excimer-pumped dye laser system (Lambda Physik, Gottingen, Germany) was installed to

Reproduced with permission of the copyright owner. Further reproduction prohibited without permission.

complement the Candela laser system and allow simultaneous measurements the mesospheric sodium and iron layers [Gelinas et al., 2005; Lynch et al., 2005]. My goal is to use the excimer-pumped laser as a transmitter for molecular nitrogen ion lidar that will measure aurorally produced species.

1.4 Scope of this Study

This study has the following major elements;

1. Development of an engineering model of sodium Doppler wind-temperature resonance lidar system and the analysis of measurements of wind-temperature fluxes in the upper mesosphere;
2. Development of an engineering model of molecular nitrogen ion resonance lidar system and the analysis of measurements of aurorally produced nitrogen ions in the thermosphere;
3. Development of an integrated spectroscopic system for monitoring and controlling the molecular nitrogen ion resonance lidar system;
4. Execution of field tests of a prototype molecular nitrogen ion resonance lidar system.

A peer-reviewed journal article based on my analysis of lidar wind-temperature measurements has been accepted for publication in the Journal of Atmospheric and Oceanic Technology [Su et al., 2007].

This thesis consists of seven chapters. In Chapter 2, I present the principles of the metal resonance lidar technique based on atomic resonance spectroscopy. I present the detailed spectroscopy of sodium and iron atoms, a description of the lidar system configuration, the lidar equation, and the performance of the lidar system based on a series of measurements at PFRR. I conduct a statistical analysis of the lidar signals, identify the fundamental noise signal, and determine the significance and validity of lidar measurements for a given noise level.

In Chapter 3 I extend my analysis of resonance lidar systems in Chapter 2 to the advanced wind-temperature sodium Doppler lidar. I present a Monte-Carlo simulation to study biases in sodium wind-temperature Doppler lidar measurements of heat fluxes. I present a detailed review of the sodium wind-temperature Doppler lidar technique and the performance of the lidar system based on a series of measurements at Fort

Reproduced with permission of the copyright owner. Further reproduction prohibited without permission.

Collins, CO. I determine the bias and statistical features and compare them to the published results of geophysical heat flux. By simulating the measurements as a function of day and night, season, and receiver telescope size, I estimated the limitations of real lidar measurements.

In Chapter 4 I focus on the principles of molecular nitrogen ion resonance lidar. I present the detailed spectroscopy of molecular nitrogen ions, a description of the lidar system configuration, the lidar equation, and the performance of the lidar system using a simulation based on observations of the aurora at PFRR. I conduct a statistical analysis of the lidar signals, and determine the significance and validity of lidar measurements for typical auroral conditions.

In Chapter 5 I present the development of an integrated bench-top wavelength tuning system based on a Fabry-Perot Interferometer (FPI). I present the operating principles of a Fabry-Perot interferometer. I then present the system configuration and explain how the system controls the wavelength of the dye laser. The hardware integrates hollow cathode lamp signal detection, laser wavelength tuning, laser signal detection, interferometer pressure scanning, and data acquisition. I present both the optical and electronic design and the software design. Finally, I present and analyze a series of laboratory spectroscopic experiments that characterize this system.

In Chapter 6 I present field tests of the prototype molecular nitrogen ion resonance lidar. I conducted a series of tests to confirm the operation of the lidar system at both visible and ultraviolet wavelengths. Finally, I analyze the lidar performance based on these experimental results.

In Chapter 7 I present my conclusions and suggestions for further work. In the Appendix following Chapter 7 I present the schematic diagrams of electronic design in previous chapters as well as the flowchart of the software package designed for the FPI tuning system.

Reproduced with permission of the copyright owner. Further reproduction prohibited without permission.

2 Signal and Noise in Resonance Lidar Signals

In the last chapter I introduced lidar systems and their basic measurements. In this chapter I use the lidar equation to analyze the lidar measurement more closely. I discuss the fundamental uncertainties in the measurement. I discuss the properties of resonance and Rayleigh scattering and how they influence the lidar technique. I show how the lidar equation can be validated with real field measurements. Finally I use a statistical analysis to determine the confidence level associated with a given lidar measurement.

2.1 The Lidar Equation

For a resonance lidar system employing a photon counting detection system, I can express the expected total photon count, $N_{TOT}(z)$, from the altitude range $(z-\Delta z/2, z+\Delta z/2)$ in a time interval Δt as the sum of three terms,

$$N_{TOT}(z) = N_S(z) + N_B + N_D \tag{2.1}$$

where $N_S(z)$ represents the signal detected from the scatters at altitude z, N_B represents the signal due to background skylight conditions, and N_D represents the detector noise. I can express these terms as,

$$N_S(z) = \left[\eta T^2\right] \cdot \left[\frac{E_L R_L \Delta t}{h\nu_L}\right] \cdot \left[C_{eff}(\nu_L, T, V)\rho(z)\Delta z\right] \cdot \left[\frac{A_R}{4\pi z^2}\right] \tag{2.2}$$

$$N_B = \eta\left(H_N R_L \Delta t \pi \left(\frac{\Delta\theta_R}{2}\right)^2 A_R \Delta\lambda\right)\left(\frac{1}{hc\nu_R}\right) \tag{2.3}$$

$$N_D = \left(C_N R_L \Delta t\right)\left(\frac{2\Delta z}{c}\right) \tag{2.4}$$

where η is the receiver efficiency, T is the atmospheric transmission at the transmitted laser frequency, ν_L, E_L is the laser energy per pulse (J), R_L is the repetition rate of the laser (pulse per second, pps), $\rho(z)$ is the concentration of scatters at altitude z (m^{-3}), C_{eff} is the effective scattering cross section at frequency

Reproduced with permission of the copyright owner. Further reproduction prohibited without permission.

ν_L (m^{-2}), temperature T, and velocity V (m^2), h is Planck's constant ($6.63x10^{-34}$ J s), c is the speed of light ($3.0x10^8$ m/s), A_R is the area of the telescope (m^2), H_N is the background sky radiance (W/m^2-μm-sr), $\Delta\theta_R$ is the field-of-view of the receiver (rad), ν_L is the receiver's center frequency, $\Delta\lambda$ is the bandwidth of the detector (μm), and C_N is the dark count rate for the detector (s^{-1}). This form of the lidar equation is consistent with other forms (e.g., Measures, [1992]; Chu and Papen, [2005]). In an Equation 2.2, I assume that the atmosphere is optically thin (i.e., the energy in the laser pulse is not significantly diminished as it propagates through the atmosphere) and that the resonance scattering is isotropic. The term C_{eff} is dependant on the scattering mechanism and the characteristics of the laser radiation (i.e., center wavelength and linewidth of the laser). I will discuss C_{eff} further later in this chapter.

For a Rayleigh lidar system, I can express the signal as,

$$N_S(z) = \left[\eta T^2\right] \cdot \left[\frac{E_L R_L \Delta t}{h\nu_L}\right] \cdot \left[\sigma_\pi^R(\nu_L)\rho(z)\Delta z\right] \cdot \left[\frac{A_R}{z^2}\right] \tag{2.5}$$

where ρ(z) is the density of air molecules at altitude z (m^{-3}), and σ_π^R is the Rayleigh backscatter cross section (m^2/sr). Rayleigh scatter is not isotropic but strongest in the forward and backward direction. The fact that Rayleigh scatter is directional while resonance scatter is isotropic results in the difference of a factor of 4π in Equations 2.2 and 2.5. The Rayleigh backscatter cross section is usually expressed as a function of wavelength (e.g., Measures, [1992]).

$$\sigma_\pi^R(\lambda) = 5.45 \cdot \left[\frac{550}{\lambda}\right]^4 \cdot 10^{-32} m^2 sr^{-1} \tag{2.6}$$

The terms in the expected signal photon count (Equations 2.2 and 2.5) are grouped into four bracketed terms. The term in the first (leftmost) bracket is less than unity and represents the product of the transmission of the atmosphere and the optical efficiency of the receiver. The term in the second bracket represents the total number of photons that have been transmitted by the laser into the atmosphere. The term in the third bracket represents the probability of scattering by the target species. The

Reproduced with permission of the copyright owner. Further reproduction prohibited without permission.

fourth bracketed term represents the probability of a scattered photon being intercepted by the telescope. From Equations 2.2 and 2.5 the expected lidar signal can be increased in a variety of ways: by making measurements from the top of a high mountain or an airplane (increase T); by making measurements with a larger area telescope (increase A_R); and by reducing the resolution of the measurement (increase Δz and/or Δt). For a given laser system it may not be possible to change E_L and R_L. For example, in flashlamp-pumped solid state lasers, increasing the pump voltage increases the flashlamp emission and E_L but also results in an increase in the heat of the laser rod. The increase in heat can lead to variations in the refractive index of the rod that causes lensing effects (i.e., thermal lensing), focusing of the laser beam and hence damage to the laser rods and eventual failure of the laser.

I plot a typical measurement of a sodium resonance fluorescence lidar in Figure 2.1. I obtained this profile obtained on the night of 7 April 2007 between 2341 and 0147 LST (= UT - 9h). This integrated profile is the total photon count produced by the

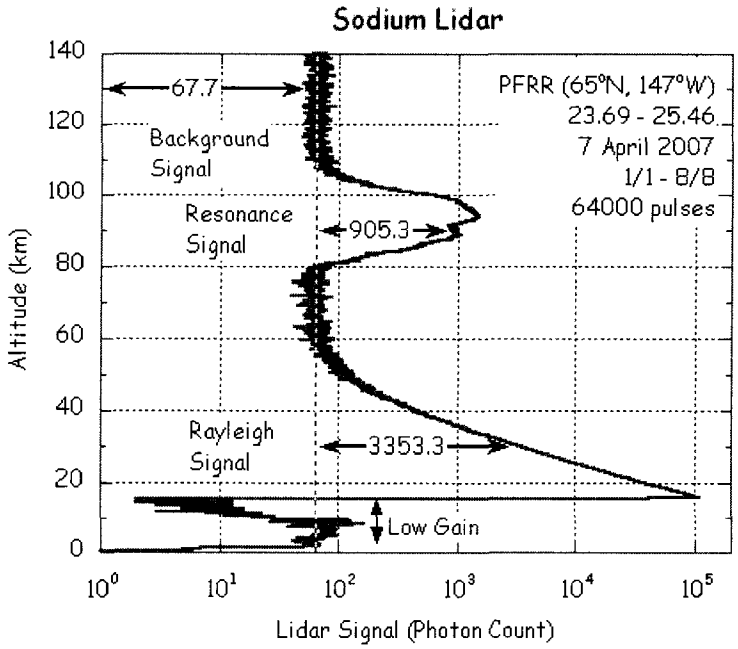

Figure 2.1 Raw sodium lidar signal profile measured on the night of 7-8 April 2007 at PFRR.

Reproduced with permission of the copyright owner. Further reproduction prohibited without permission.

echoes from 64,000 laser pulses over 107 minutes with an altitude resolution of 75 m. The dye laser is operated at the sodium D_2 line (589.2 nm). Below 60 km, the signal is primarily produced by Rayleigh scattering (i.e., elastic scattering from atoms and molecules introduced by a varying dipole moment). The Rayleigh scatter signals decreases with altitude as the density of the atmosphere decreases with altitude. The signal is low below 18 km, where the electronic blanking unit suppressed the large signal received from the denser lower atmosphere close to the receiver. The low gain prevents the detector from being overloaded. The gain of the detector is lowered by controlling the voltage for a very short time period after the laser is fired. Despite this low gain, strong echoes produced by Mie scattering (i.e., elastic scattering from small particles and aerosols of large size when compared to the incident wavelength) from clouds near 10 km are visible. The sodium resonance fluorescence echo is visible between 80 km and 110 km.

Several signal values are indicated in Figure 2.1. The value of the background and detector dark signal (67.7 photon counts) is estimated by taking the average of the signal from 120 to 125 km. The value of the sodium resonance fluorescence signal is 905.3 photon counts at 90 km. The value of the Rayleigh signal is 3353.3 photon counts at 30 km. These signal values are non-integer because the value of the background and detector dark signal is an average. The total signal at 90 km and 30 km have integer values of 973 (= 67.7 + 905.3) and 3421 (= 67.7 + 3353.3) photon counts respectively.

If I subtract the estimated background noise signal ($\tilde{N}_B$), I can estimate the concentration of sodium atoms, p(z), at an altitude z in the metal layer from the ratio of the resonance lidar signal at an altitude z and the Rayleigh lidar signal at an altitude z_R,

$$\rho(z) = \frac{N(z) - \tilde{N}_B}{N_R(z_R) - \tilde{N}_B} \cdot \frac{\sigma_\pi^R(\nu_L)}{C_{eff}(\nu_L)} \cdot \frac{4\pi z^2}{z_R^2} \cdot \rho(z_R) \qquad (2.7)$$

Equation 2.7 shows the power of the resonance lidar technique. By taking the ratio of the signals in the middle and upper atmosphere the terms for atmospheric transmission, system efficiency and the laser energy are cancelled out and I do not have to determine them, and the lidar system is effectively self-calibrating. The

Reproduced with permission of the copyright owner. Further reproduction prohibited without permission.

density at the Rayleigh altitude, $\rho(z_R)$, is calculated from the temperature and pressure profile measured by radiosonde launched at Fairbanks International Airport 50 km from PFRR. These meteorological soundings are archived by the University of Wyoming and available online at <http://weather.uwyo.edu/upperair>. The value of the atmospheric density, $p(z_R)$, is considered a constant because the atmospheric density varies by less than a few percent while the metal concentration, $\rho(z)$, can vary by factors of 1-10. I plot the sodium concentration profile retrieved from the raw signal in Figure 2.1 in Figure 2.2. The concentration profile is determined from the signal in the 70-120 km region, where the signal is due to resonance scatter from the sodium atoms in the mesospheric sodium layer. The sodium layer is clearly detected with the main layer between 80 and 110 km. The peak of the sodium layer at 94.04 km has a concentration of 2376 cm^{-3}.

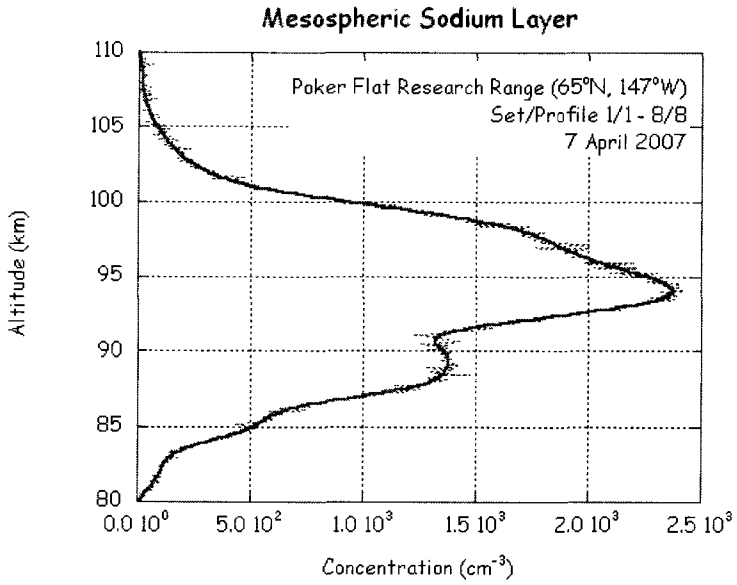

Figure 2.2 Sodium lidar concentration profile measured on 7-8 April 2007 at PFRR. (The profile determined from the raw lidar signal profile in Figure 2.1. The profile is plotted as a thin dashed line. The profile, smoothed with a 2 km running average is overplotted as a thick line.

Reproduced with permission of the copyright owner. Further reproduction prohibited without permission.

I can use the lidar equation to determine the value of C_{eff}. The value of C_{eff} can be estimated from the resonance and Rayleigh lidar signals as follows,

$$C_{eff}(\nu_L) = \frac{N(z) - \tilde{N}_B}{N_R(z_R) - \tilde{N}_B} \cdot \sigma_\pi^R(\nu_L) \cdot \frac{4\pi z^2}{z_R^2} \cdot \frac{\rho(z_R)}{\rho(z)} \tag{2.8}$$

If a series of lidar measurements are made in quick succession so that $\rho(z)$ and $\rho(z_R)$, remain constant the ratio of the resonance to Rayleigh signal at each frequency is proportional to the effective scattering cross section C_{eff}. A curve fitting procedure can be used to determine the value of C_{eff} and the linewidth of the laser. Thus, I can calibrate the resonance lidar system. I discuss this further in the next section.

Finally, I can also use the lidar equation to check the lidar system performance. The efficiency factor (ηT^2) can be estimated from the resonance and Rayleigh lidar signals as follows,

$$\left[\eta T^2\right] = \frac{N(z) - \tilde{N}_B}{\left[\frac{E_L R_L \Delta t}{h\nu_L}\right] \cdot \left[\rho(z) C_{eff}(\nu) \Delta z\right] \cdot \left[\frac{A}{4\pi z^2}\right]} \tag{2.9}$$

$$\left[\eta T^2\right] = \frac{N(z_R) - \tilde{N}_B}{\left[\frac{E_L R_L \Delta t}{h\nu_L}\right] \cdot \left[\rho(z_R) \sigma_\pi^R(\nu) \Delta z\right] \cdot \left[\frac{A}{z_R^2}\right]} \tag{2.10}$$

In Equation 2.9, the value of C_{eff} must be known. I determine the efficiency of the lidar system in the next section.

2.2 The Effective Scattering Cross Section, C_{eff}

2.2.1 Sodium Scattering and Effective Scattering Cross Section

Sodium is one of the alkali metal elements with atomic number 11. There is only a single valance electron of sodium, so the atomic spectrum is easily derived. The energy diagram of sodium is plotted in Figure 2.3. This diagram shows the energy states with increasing precision from the simple singlet spectral model to the full hyperfine spectral model. The atomic orbital configuration $KL3s^1$ corresponds to the sodium ground state. The ground state term energy is ^2P. The atomic orbital

Reproduced with permission of the copyright owner. Further reproduction prohibited without permission.

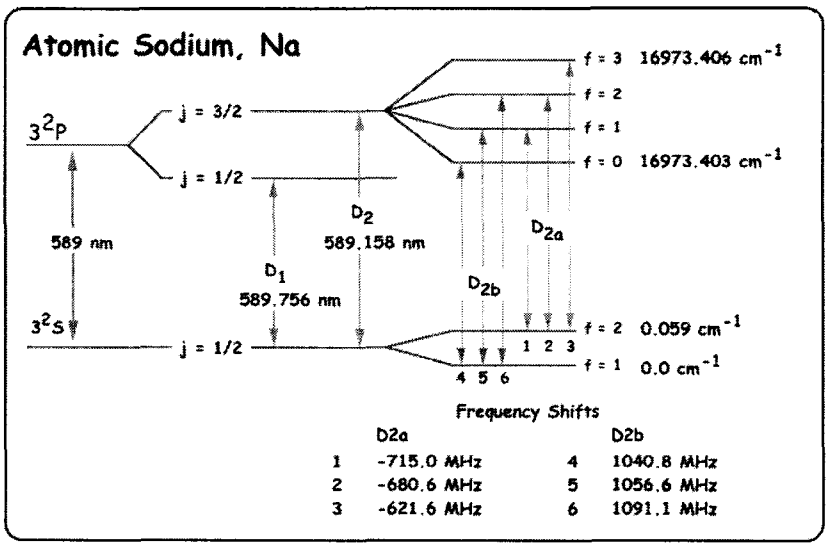

Figure 2.3 Sodium energy level diagram.

configuration $KL3p^1$ corresponds to the first excited state of sodium. The first excited state term energy is ^2S. The upper state is split into two fine states by the spin-orbital coupling effect. The D_1 line denotes the transitions between $^2P_{1/2}$ and $^2S_{1/2}$; The D_2 line denotes the transitions between $^2P_{3/2}$ and $^2S_{1/2}$. The D_1 line oscillator strength equals 0.320 with center wavelength at 589.7558 nm. The D_2 line oscillator strength equals 0.641 with center wavelength at 589.1583 nm. The states are further split into hyperfine states due to the nuclear spin of sodium (I = 3/2). In the D_2 line the $^2P_{3/2}$ state is split into four hyperfine states and the $^2P_{1/2}$ is split into two hyperfine states. The frequencies of the six hyperfine transitions are given relative to the D_2 center frequency ($\nu_0 = c/\lambda_0$) in Figure 2.3. The six hyperfine transitions in the D_2 line are grouped into the D_{2a} and D_{2b} lines, yielding the well-known D_2 doublet. The separation between D_{2a} and D_{2b} is 1771.6 MHz.

The absorption cross section of the sodium atom is given by,

Reproduced with permission of the copyright owner. Further reproduction prohibited without permission.

$$\sigma_{abs}(\nu) = \frac{1}{\sqrt{2\pi}\cdot\sigma_D}\frac{e^2 f}{4\varepsilon_0 m_e c}\sum_{n=1}^{6} S_n \exp\left(-\frac{(\nu_n - \nu(1-\frac{V_R}{c}))^2}{2\sigma_D^{\,2}}\right) \tag{2.11}$$

where e denotes electron charge ($1.60\text{x}10^{-19}$ C), f denotes the oscillator strength, ε_0 denotes the permittivity of free space ($8.85\text{x}10^{-12}$ F/m), m_e denotes the mass of single electron ($9.11\text{x}10^{-31}$ kg), c denotes the speed of light ($3.00\text{x}10^{8}$ m/s), ν_n and S_n are the center frequencies and the line strengths of the six hyperfine transitions, respectively, ν is the laser frequency, and V_R is the radial velocity of the atom moving away from the laser source. The standard deviation or Doppler width of the line shape, σ_D, that due to the Brownian motion of the sodium atoms in the atmosphere, is determined from Equation 2.12,

$$\sigma_D^{\,2} = \frac{kT}{m\lambda_0^{\,2}} \tag{2.12}$$

where k is the Boltzmann constant ($1.38\text{x}10^{-23}$ J/K), and T is the temperature. The line strength S_i is determined by the Einstein coefficient, A_{ul}, for the D_2 transition and the Einstein coefficients, A_n (n = 1, .. 6), for the six hyperfine transitions.

$$S_i = \frac{A_i}{A_{ul}} \quad , \quad A_{ul} = \sum_{n=1}^{6} A_n \tag{2.13}$$

The oscillator strength f is written as,

$$f = \frac{A_{ul}\varepsilon_0 m_e c \lambda_0^{\,2} g_u}{2\pi e^2 g_l} \tag{2.14}$$

where g_u is the combined degeneracy of the 4 upper hyperfine states and g_l is the combined degeneracy of the 2 lower states. Using the doublet D_{2a} and D_{2b} line groups, Equation 2.11 can be approximated as,

$$\sigma_{abs}(\nu) = \frac{\sigma_0}{\sqrt{2\pi}\cdot\sigma_D}\left[S_a \exp\left(-\frac{(\nu-\nu_a)^2}{2\sigma_D^{\,2}}\right) + S_b \exp\left(-\frac{(\nu-\nu_b)^2}{2\sigma_D^{\,2}}\right)\right] \tag{2.15}$$

line strength S_a and S_b are,

Reproduced with permission of the copyright owner. Further reproduction prohibited without permission.

$$S_a = \frac{A_1 + A_2 + A_3}{A_{ul}} \quad , \quad S_b = \frac{A_4 + A_5 + A_6}{A_{ul}} \tag{2.16}$$

and,

$$\sigma_0 = \frac{e^2 f}{4\varepsilon_0 m_e c} = \frac{A_{ul}\lambda_0^{\,2} g_u}{8\pi g_l} \tag{2.17}$$

The doublet approximation is good enough to represent the resonant absorption cross section. It yields differences of less than 0.5% in the estimated scattering cross sections. I ignore branching ratio between the hyperfine transitions because the lidar receiver bandwidth is wide enough to detect light from the whole D_2 band.

Effective scattering cross section, C_{eff}, is the convolution of absorption cross section σ_{abs} and laser line shape function g_L.

$$C_{eff}(\nu_L) = g_L(\nu_L,\nu) * \sigma_{abs}(\nu)\cdot\Phi = \int_0^\infty g_L(\nu_L,\nu)\,\sigma_{abs}(\nu)\,d\nu \tag{2.18}$$

where Φ denotes the branching ratio that has a value of 100% for this transition. For a laser with center frequency of ν_L and linewidth σ_L the laser line shape, $g_L(\nu)$, is a Gaussian function of the form,

$$g_L(\nu) = \frac{1}{\sqrt{2\pi}\cdot\sigma_L}\left[\exp\left(-\frac{(\nu-\nu_L)^2}{2\sigma_L^{\,2}}\right)\right] \tag{2.19}$$

and the effective scattering cross section C_{eff} is,

$$C_{eff}(\nu_L) = \frac{\sigma_0}{\sqrt{2\pi}\cdot\sigma_{eff}}\left[S_a\exp\left(-\frac{(\nu_L-\nu_a)^2}{2\sigma_{eff}^{\,2}}\right) + S_b\exp\left(-\frac{(\nu_L-\nu_b)^2}{2\sigma_{eff}^{\,2}}\right)\right] \tag{2.20}$$

where the effective width is given by,

$$\sigma_{eff} = \sqrt{\sigma_L^2 + \sigma_D^2} \tag{2.21}$$

The linewidth of laser and absorption lines is often expressed as the full-width at half maximum (FWHM), $\Delta\nu$. For a Gaussian lineshape the FWHM is related to the rms width, σ, as follows,

Reproduced with permission of the copyright owner. Further reproduction prohibited without permission.

$$\Delta\nu = 2\sqrt{2\ln 2}\,\sigma \tag{2.22}$$

I plot the resonant absorption cross section for the sodium D_2 line as a function of frequency in Figure 2.4. The two peaks correspond to the D_{2a} (-700 MHz) and D_{2b} (~1 GHz) line groups.

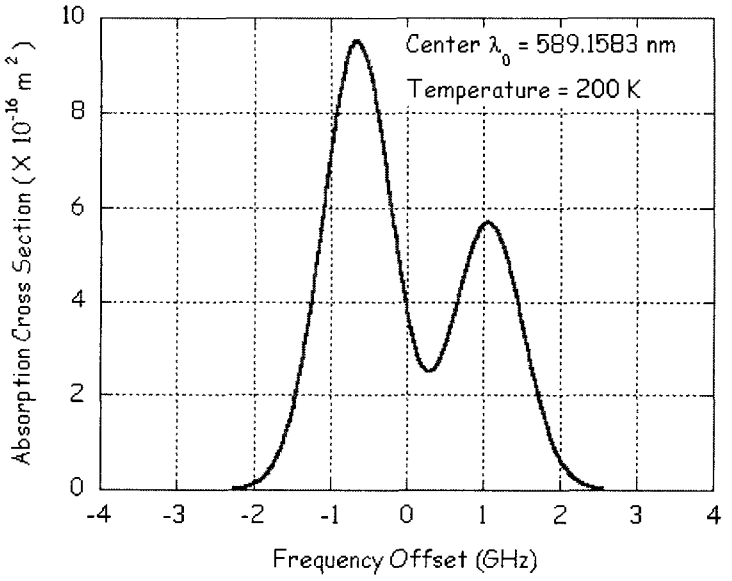

Figure 2.4 Sodium absorption cross section as a function of frequency. The sodium is taken at a temperature of 200 K and at rest.

I plot the sodium effective scattering cross section as a function of laser frequency in Figure 2.5. The solid line corresponds to the laser linewidth of 120 MHz, and the dashed line corresponds to the laser linewidth of 5 GHz. The effective cross section decreases with increasing laser linewidth and with increasing offset between the laser and the resonance frequency. The lidar signal is proportional to the effective scattering cross section and is larger for narrow linewidth lasers than for broadband lasers.

Reproduced with permission of the copyright owner. Further reproduction prohibited without permission.

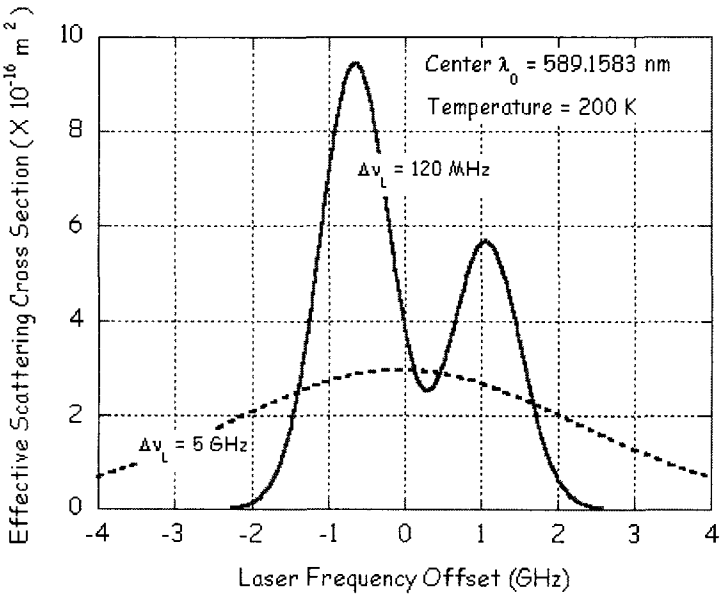

Figure 2.5 Sodium effective scattering cross section. The solid line shows the cross section as a function of frequency for a laser of linewidth 120 MHz. The solid line shows the cross section as a function of frequency for a laser of linewidth 5 GHz. The sodium is taken at a temperature of 200 K and at rest.

For a given laser, I can measure C_{eff} using the resonance fluorescence signal from the sodium layer. By tuning the frequency of the laser transmitter and recording the corresponding resonance fluorescence signal, the value of C_{eff} can be determined [Hou, 2002]. I conducted such an experiment on the night of 7 April 2007. I made consecutive measurements of the sodium layer at laser wavelengths from 589.034 pm to 589.041 nm. The relative tuning resolution of the dye laser is 0.14 pm at 589 nm. The measurements were conducted at 1pm resolution. The raw lidar signal measured at 589.035 and 589.037 nm is shown in Figure 2.6. The signal profiles represent the integrated signal for 2000 laser pulses. Clearly the signal is stronger at 589.037 nm. The complete measurement data and best fit are plotted in Figure 2.7. The two profiles in Figure 2.6 correspond to the second and sixth data points in Figure 2.7. The value of the laser linewidth is 3.9 GHz (or 4.5 pm) (FWHM) and the maximum value of

Reproduced with permission of the copyright owner. Further reproduction prohibited without permission.

the effective cross section is 3.5 $x10^{-16}$ m^2. These value and variation of the C_{eff} measurements agrees with the theoretical calculations in Figure 2.5,

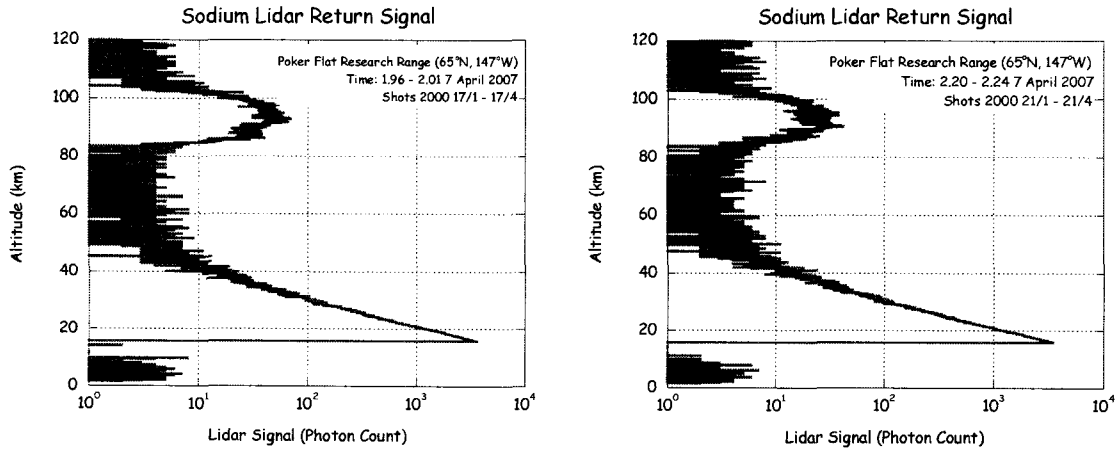

Figure 2.6 Raw sodium lidar signal plotted as a function of altitude. (left) Measurement with laser wavelength at 589.035 nm; (right) Measurement with laser wavelength at 589.037 nm.

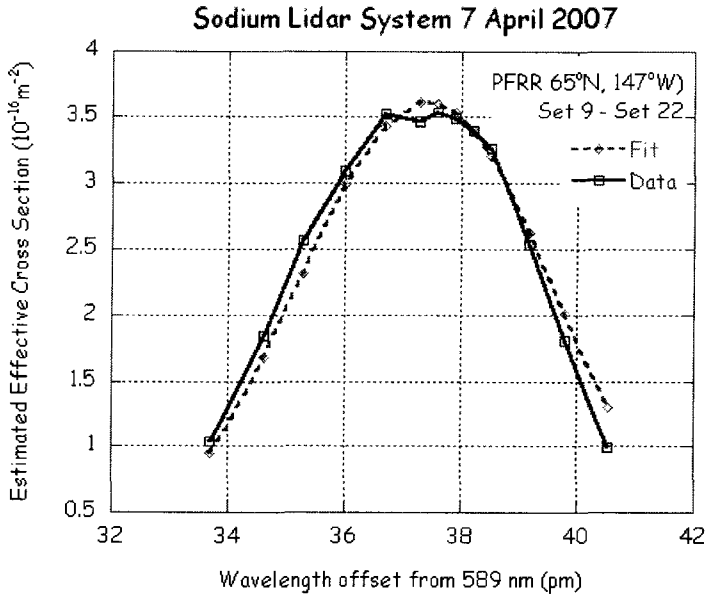

Figure 2.7 Measurement of sodium lidar C_{eff} as function of laser wavelength.

Reproduced with permission of the copyright owner. Further reproduction prohibited without permission.

Clearly the laser wavelength does not directly correspond to the value of the sodium resonance wavelength at vacuum. Thus the laser wavelength is not absolutely accurate, but is relatively accurate. The tuning measurements show that despite this lack of accuracy, I can use the lidar signal to tune the laser to the resonance transition. However, I also have a wavelength reference that is used to tune the sodium resonance lidar. This reference is a hollow cathode lamp (HCL). The principle and development of hardware for HCL are well-established and has been used extensively in lidar experiments at PFRR [Peshave, 2004]. The HCL is a sodium vapor discharge lamp with a hollow metal cathode and an anode. The current through the lamp is maximized when the cathode is illumined with laser light corresponding to the sodium resonance frequency. I conducted a HCL experiment on 25 January 2007. The variation of HCL current (recorded as a voltage across a load resistor) with laser wavelength is plotted in Figure 2.8. Each measurement represents the integration of 20 laser pulses. The laser wavelength corresponding to the D_2 wavelength is clearly detected. The hollow cathode lamp provides a reference for determine the D_2 wavelength. However, the width of the response depends on the physics of the discharge process which is nonlinear, and so I cannot use the HCL to determine C_{eff}.

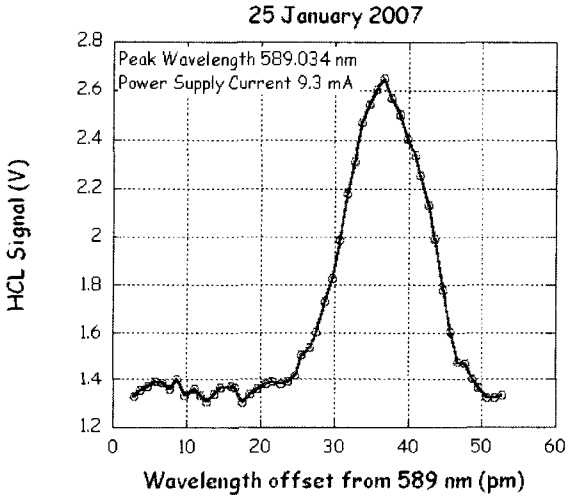

Figure 2.8 Variation of load voltage in a sodium hollow cathode lamp circuit as a function of laser wavelength.

Reproduced with permission of the copyright owner. Further reproduction prohibited without permission.

2.2.2 Iron Scattering and Effective Scattering Cross Section

The spectroscopy of iron atoms is more complicated than that of sodium atoms. Iron is one of the group 8 metal elements with atomic number 26. Compared to the sodium atom, iron has more valance electrons, which results in a huge number of combinations of quantum numbers [Hollas, 2005]. Usually, the spectrum of atomic iron is reported through experiments rather than quantum mechanical calculations. I plot a partial energy diagram of iron in Figure 2.9. Iron has many strong lines in the ultraviolet that cannot be used in resonance lidar because they are strongly absorbed in the ozone layer. The transition at 372 nm is useful because of it is reasonably strong and the fact that the wavelength is not absorbed by the ozone layer. The atomic orbital configuration $KL3s^2 3p^6 3d^6 4s^2$ corresponds to the iron ground state, a^5D. The atomic orbital configuration $KL3s^2 3p^6 3d^6 4s4p$ corresponds to the iron excited state, z^5F_0. Iron dues not have any hyperfine spectroscopy because iron has no nuclear spin. The ground state has five manifolds. The upper state z^5F_0, has five manifolds, also. There are two major transitions at 372 nm and 374 nm, respectively. The transition between J=4 in the ground state and J=5 in the excited state at 372 nm is the major transition employed by most iron resonance fluorescence lidars. The fluorescence wavelength is the same as the transmitting wavelength and the branching ratio is 100% for this transition. The other transition between J=4 in the ground state and J=4 in the excited state at 374 nm can be combined with the 372 nm transition to carry out Boltzmann temperature measurements [Gelbwachs, 1994]. For the transition at 374 nm, there are two fluorescence transitions: the wavelength of the first transition is the same as the transmitting wavelength, and the second transition is at 368 nm. The branching ratio is 91% for the fluorescence signal at 374 nm and 9% for the fluorescence signal at 368 nm. [Chu and Papen, 2005].

The effective cross section, C_{eff}, of iron has a simpler expression than that of sodium because the iron line is a singlet rather than a doublet. For the transition at 372 nm the iron lidar resonant absorption cross section can be expressed as,

$$\sigma_{abs}(\nu) = \frac{\sigma_0}{\sqrt{2\pi}\cdot\sigma_D}\left[\exp\left(-\frac{(\nu-\nu_0)^2}{2\sigma_D{}^2}\right)\right] \tag{2.23}$$

Reproduced with permission of the copyright owner. Further reproduction prohibited without permission.

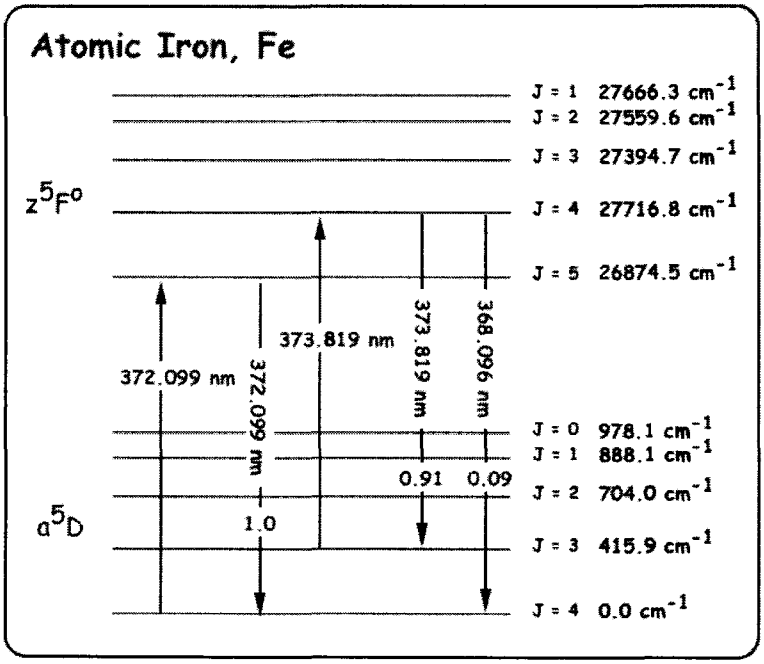

Figure 2.9 Partial energy level of iron.

and iron lidar scattering cross section C_{eff} for a given frequency ν can be expressed as,

$$C_{eff}(\nu_L) = \frac{\sigma_0}{\sqrt{2\pi}\cdot\sigma_{eff}} \exp\left(-\frac{(\nu_L - \nu_0)^2}{2\sigma_{eff}^{\ 2}}\right) \tag{2.24}$$

For a temperature of 200 K, I can plot the resonant absorption cross section profile corresponding to the wavelength offset of the center wavelength of iron transition at 372.0 nm in Figure 2.10. The peak corresponds to wavelength at 372.0993 nm.

I plot the effective scattering cross section for iron in Figure 2.11. The solid line corresponds to the laser linewidth of 120 MHz, and the dashed line corresponds to the laser linewidth of 5 GHz. Again, a broader laser linewidth yields a lower effective scattering cross section. Because the effective scattering cross section is proportional to the lidar signal photon counts, for resonance fluorescence lidar application a narrow line laser produces a higher lidar signal.

Reproduced with permission of the copyright owner. Further reproduction prohibited without permission.

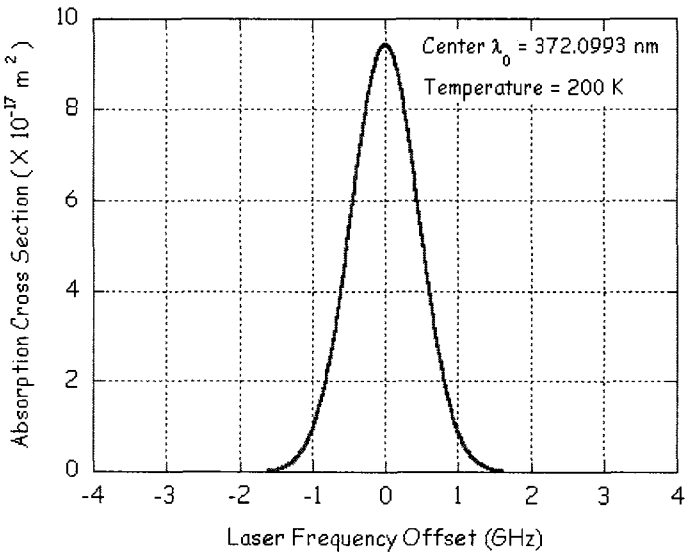

Figure 2.10 Iron absorption cross section as a function of frequency. The iron is taken at a temperature of 200 K and at rest.

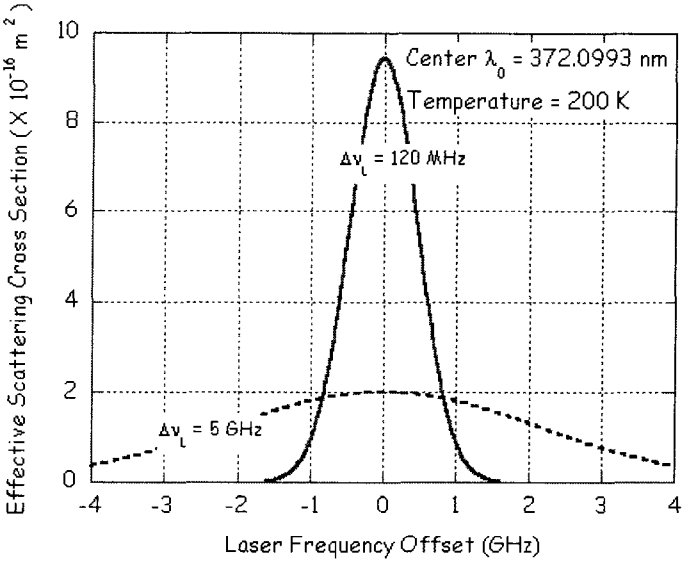

Figure 2.11 Iron effective scattering cross section. The solid line shows the cross section as a function of frequency for a laser of linewidth 120 MHz. The solid line shows the cross section as a function of frequency for a laser of linewidth 5 GHz. The iron is taken at a temperature of 200 K and at rest.

Reproduced with permission of the copyright owner. Further reproduction prohibited without permission.

I can measure C_{eff} using the resonance fluorescence signal from the iron layer in exactly the same way that I measured C_{eff} from the sodium layer. I conducted such an experiment on the night of 17 April 2007. I made consecutive measurements of the iron layer at laser wavelengths from 372.008 pm to 372.010 nm. The relative tuning resolution of the dye laser is 0.089 pm at 372 nm. The measurements were conducted at 1pm resolution. The raw lidar signal measured at 372.0091 and 372.0086 nm is shown in Figure 2.12. The signal profiles represent the integrated signal for 6000 laser pulses. Clearly the echo is stronger at 372.0091 nm. The complete measurement data and best fit are plotted in Figure 2.13. The two profiles in Figure 2.12 correspond to the second and sixth data points in Figure 2.13. The value of the laser linewidth is 2.4 GHz (or 1.1 pm) (FWHM) and the maximum value of the effective cross section is 4 $x10^{-17}$ m^2. The measured value of and variation in C_{eff} agree with the theoretical calculations in Figure 2.11.

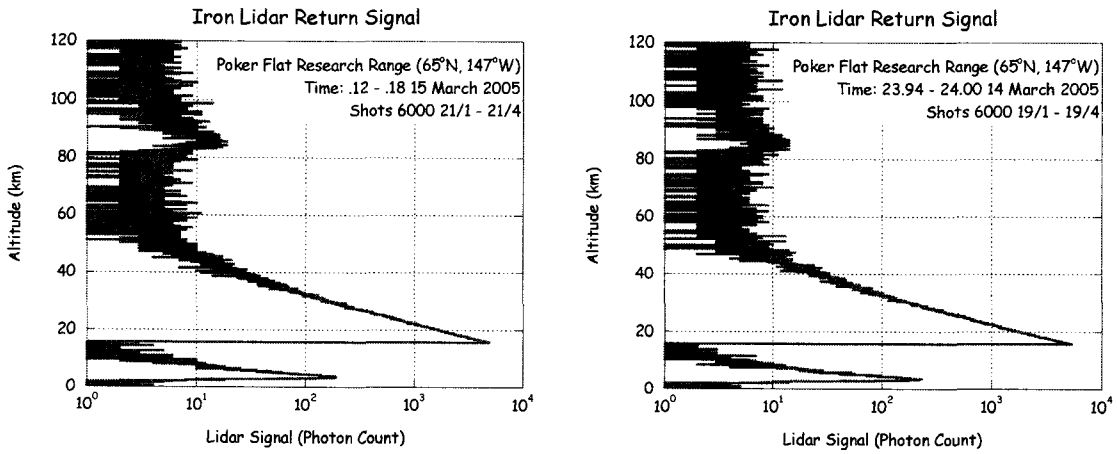

Figure 2.12 Raw iron lidar signal profile. (left) Laser wavelength at 372.0091 nm; (right) Laser wavelength at 372.0086 nm.

Reproduced with permission of the copyright owner. Further reproduction prohibited without permission.

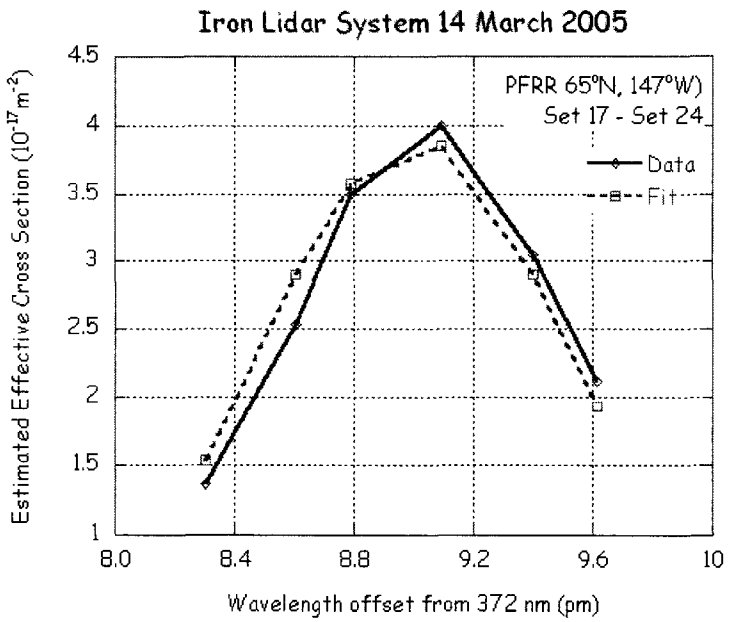

Figure 2.13 Measurement of iron lidar C_{eff} as a function of laser wavelength.

2.3 The Efficiency of Lidar Systems

Having calculated C_{eff} for the sodium and iron resonance lidar systems, I can now determine the efficiency of the lidar systems using Equations 2.9 and 2.10. I have shown the sodium lidar signal profile and corresponding concentration profile in Figures 2.1 and 2.2, I use the resonance signal at the peak of the sodium layer, the Rayleigh signal at 22.5 and 32.5 km, and the background signal between 120 and 125 km with the calculated effective scattering cross section to determine the value of (ηT^2). The values used and the results are tabulated in Table 2.1. The calculated value of the efficiency (~1%) is reasonable for typical values of atmospheric transmission and system efficiency.

Reproduced with permission of the copyright owner. Further reproduction prohibited without permission.

Table 2.1 Sodium lidar system performance

Date	7 April 2007
Lidar System	Sodium
Transmitter Wavelength (nm)	589
Data Sets Numbers	1-8
Number of Laser Pulses	64000
Telescope Diameter (cm)	60
Energy per Laser Pulse (mJ)	5
Total Photons Transmitted	4.75×10^{21}
Laser Linewidth (pm)	4.5
Effective Cross Section (10^{-16} m^2)	3.5
Peak Sodium Density (cm^{-3})	2421
Peak Altitude (km)	94.04
Averaged Peak Sodium Density 93-95 km (cm^{-3})	2376
Column Abundance(cm^{-2})	2.59×10^9
Integrated Signal 20 - 25 km (Photon Counts)	1445955
Integrated Signal 30 - 35 km (Photon Counts)	139534
Integrated Signal 120 - 125 km (Photon Counts)	4534
Integrated Signal 93 - 95 km (Photon Counts)	38551
ηT^2 (%) 20 - 25 km	1.03
ηT^2 (%) 30 - 35 km	0.94
ηT^2 (%) 93 - 95 km	0.91

I show a typical signal profile of a iron resonance fluorescence lidar signal in Figure 2.14. This profile was obtained on the night of 17 April 2007 between 2307 and 2414 LST (= UT - 9h). This integrated profile is the total photon count produced by the echo from 32,000 laser pulses over 67 minutes with an altitude resolution of 75 m. The dye laser is operated at the iron line (372.0 nm). Below 60 km, the signal is primarily produced by Rayleigh scattering. The Rayleigh scatter signals decreases with altitude as the density of the atmosphere decreases with altitude. The signal is low below 18 km, where the electronic blanking unit suppressed the large signal received from the denser lower atmosphere close to the receiver. The low gain prevents the detector from being overloaded. The gain of the detector is lowered by controlling the voltage for a very short time period after the laser is fired. Despite this low gain, strong

Reproduced with permission of the copyright owner. Further reproduction prohibited without permission.

echoes produced by Mie scattering from clouds near 10 km are visible. The iron resonance fluorescence echo is visible between 80 km and 100 km.

Several signal values are indicated in Figure 2.14. The value of the background and detector dark signal (25.7 photon counts) is estimated by taking the average of the signal from 120 to 125 km. The value of the sodium resonance fluorescence signal is 51.3 photon counts at 90 km. The value of the Rayleigh signal is 1480.3 photon counts at 30 km. These signal values are non-integer because the value of the background and detector dark signal is an average. The total signal at 90 km and 30 km have integer values of 77 (= 25.7 + 51.3) and 1506 (= 25.7 + 1480.3) photon counts respectively.

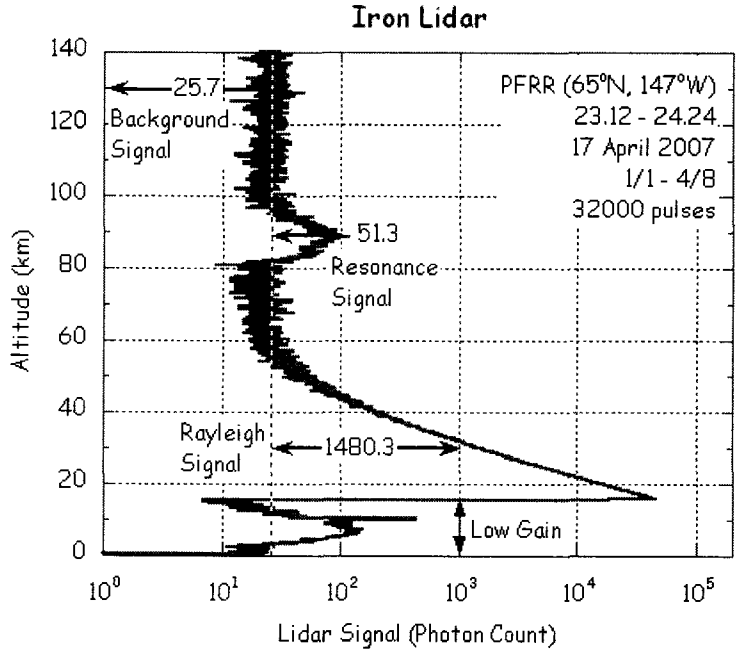

Figure 2.14 Raw iron resonance lidar signal profile at 372 nm measured on 17 April 2007.

I plot the iron concentration profile retrieved from the raw signal in Figure 2.14 in Figure 2.15. The concentration profile is determined from the signal in the 70-120 km region, where the signal is due to resonance scatter from the iron atoms in the mesospheric iron layer. The iron layer is clearly detected with the main layer between

Reproduced with permission of the copyright owner. Further reproduction prohibited without permission.

80 and 100 km. The peak of the iron layer at 88.75 km has a concentration of 10,210 cm^{-3}.

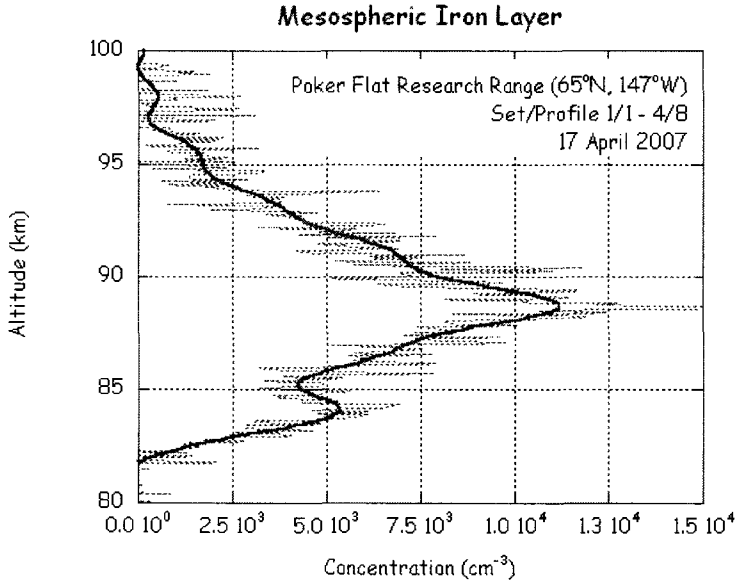

Figure 2.15 Iron lidar concentration profiles measured on 17-18 April 2007 at PFRR. The profile determined from the raw lidar signal profile in Figure 2.14. The profile is plotted as a thin dashed line. The profile, smoothed with a 2 km running average is plotted thick.

Consider the integrated resonance fluorescence lidar signal profiles in Figure 2.13. I again combine the lidar signals at different altitudes with the measured effective scattering cross section to determine the efficiency of the lidar system. The results are listed in Table 2.2. The calculated value of the efficiency (~0.2%) is 5 times less than the sodium resonance fluorescence lidar system due to a decrease in the system performance and atmospheric transmission at UV wavelengths relative to visible wavelengths.

Reproduced with permission of the copyright owner. Further reproduction prohibited without permission.

Table 2.2 Iron lidar system performance

Date	17 April 2007
Lidar System	Iron
Transmitter Wavelength (nm)	372
Data Set	1-4
Number of Laser Pulses	32000
Telescope Diameter (cm)	60
Energy per Laser Pulse (mJ)	5
Total Photons Transmitted	1.20×10^{21}
Laser Linewidth (pm)	1.1
Effective Cross Section (10^{-17} m^2)	4.0
Peak Iron Density (cm^{-3})	15797
Peak Altitude (km)	88.75
Averaged Peak Iron Density 87 - 89 km (cm^{-3})	10210
Column Abundance(cm^{-2})	6.88×10^9
Integrated Signal 20 - 25 km (Photon Counts)	620500
Integrated Signal 30 - 35 km (Photon Counts)	62421
Integrated Signal 120 - 125 km (Photon Counts)	1719
Integrated Signal 87 - 89 km (Photon Counts)	2160
ηT^2 (%) 20 - 25 km	0.22
ηT^2 (%) 20 - 25 km	0.22
ηT^2 (%) 93 - 95 km	0.21

2.4 Resonance Lidar Signal Statistics

In a fluorescence scattering experiment, while the average number of photons scattered per unit time is known, the precise arrival time of each photon is unknown. Thus in any given time period Δt, I have a Bernoulli process as to the probability of a photon being present or absent. For a single interval I have a single trial with the probability p of "photon present in the interval" or q (= 1-p) of "no photon present in the interval". The probability of k photons being detected in n trials is given by,

$$P_n(k) = \binom{n}{k} p^k q^{n-k} \tag{2.25}$$

As n tends to ∞ and p tends to 0, so that their product ($np = \lambda$) remains constant, the

Reproduced with permission of the copyright owner. Further reproduction prohibited without permission.

probability becomes,

$$P_n(k) = \frac{\lambda^k}{k!} e^{-\lambda} \tag{2.26}$$

This is the Poisson distribution function which has a mean value λ and a variance λ [Papoulis and Pillai, 2002]. Thus for a photon counting experiment the signal are Poisson random variables where the variance in the total photon count, N_{TOT}, is the expected value N_{TOT}.

This process also is found inside the photomultiplier tube detector The number of electrons generated by the photons has a Poisson distribution [Engstrom, 1980; Measures, 1992; Oliver, 1965]. The distribution equation can be written as,

$$P(n_e, < n_e >) = \frac{< n_e >^{n_e}}{n_e!} \exp(- < n_e >) \tag{2.27}$$

where $<n_e>$ denotes the expected number of electrons generated by photons in a series of measurements. Additionally, the secondary emission process is also a Poisson distribution, and the rms shot-noise current at the output of a photomultiplier equals [RCA, 1974],

$$\left(i_n^2\right)^{1/2} = M_k \left[(2eIB) \left(1 + \frac{1}{\delta_1} + \frac{1}{\delta_1 \delta_2} + \ldots + \frac{1}{\delta_1 \delta_2 \delta_3 \ldots \delta_k} \right) \right]^{1/2} \tag{2.28}$$

where $M_k = \delta_1 \cdot \delta_2 \ldots \delta_k$, which equals the total gain of the photomultiplier, e denotes the charge of the electron, I denotes the total average photocathode current, B denotes the bandwidth, and $\delta_1, \delta_2 \ldots \delta_k$ denotes the secondary emission gain factors for each dynode stage. Note that in the above discussion I assume all dynodes are identical. Assuming the dynode secondary emission gain factors are comparable, the noise is dominated by the first stage of secondary emission. I can simplify Equation 2.28 as,

$$\left(i_n^2\right)^{1/2} = M_k \left[(2eIB) \left(\frac{1}{1 - 1/\delta_1} \right) \right]^{1/2} \tag{2.29}$$

Reproduced with permission of the copyright owner. Further reproduction prohibited without permission.

By combining the these effects, the statistics follow a Poisson distribution, the relative uncertainty in the lidar total signal N_{TOT} is given by,

$$\frac{\Delta N_{TOT}}{N_{TOT}} = \frac{\sqrt{N_{TOT}}}{N_{TOT}} = \frac{1}{\sqrt{N_{TOT}}} \tag{2.30}$$

Moreover, as $n \to \infty$, and $npq \to \infty$, according to the DeMoivre-Laplace theorem, the probability $P_n(k)$ in Equation 2.26 can be approximated by a normal distribution,

$$P_n(k) \simeq \frac{1}{\sqrt{2\pi npq}} e^{-(k-np)^2/2npq} \tag{2.31}$$

or as $p \to 0$, and $q \to 1$, Equation 2.31 can be rewritten as,

$$P_n(k) \simeq \frac{1}{\sqrt{2\pi\lambda}} e^{-(k-\lambda)^2/2\lambda} \tag{2.32}$$

Therefore I can model a given lidar signal with expected value of N_{TOT} as a Normal random variable of mean N_{TOT} and variance N_{TOT}. For a perfect measurement with no background or detector signal (i.e., $N_B + N_D = 0$) and a signal of 20 counts (i.e., $N_S = N_{TOT} = 20$), I expect the signal photon count is expected to have an associated photon count uncertainty of 4.5 counts and a relative uncertainty of 22%. The same signal with a background and detector signal of 63 counts (i.e., $N_B + N_D = 63$, $N_S = 20$, $N_{TOT} = 83$) would have an associated photon count uncertainty of 9.1 counts yielding a relative uncertainty of 46%. In top panel of Figure 2.16, two Normal approximations to Poisson distributions with large mean values are plotted with signal relative errors of 22% and 46%, respectively. 100,000 trials of random variables are involved in each approximation. Both plots show consistency between Normal distribution and Poisson distribution. In lower panel, curves of relative difference in percentage are plotted. Within same width, larger mean approximation yields less difference between Normal distribution and Poisson distribution. The large difference on both sides in each plot is due to the very small number of trials that fall in the wings of the histogram.

Reproduced with permission of the copyright owner. Further reproduction prohibited without permission.

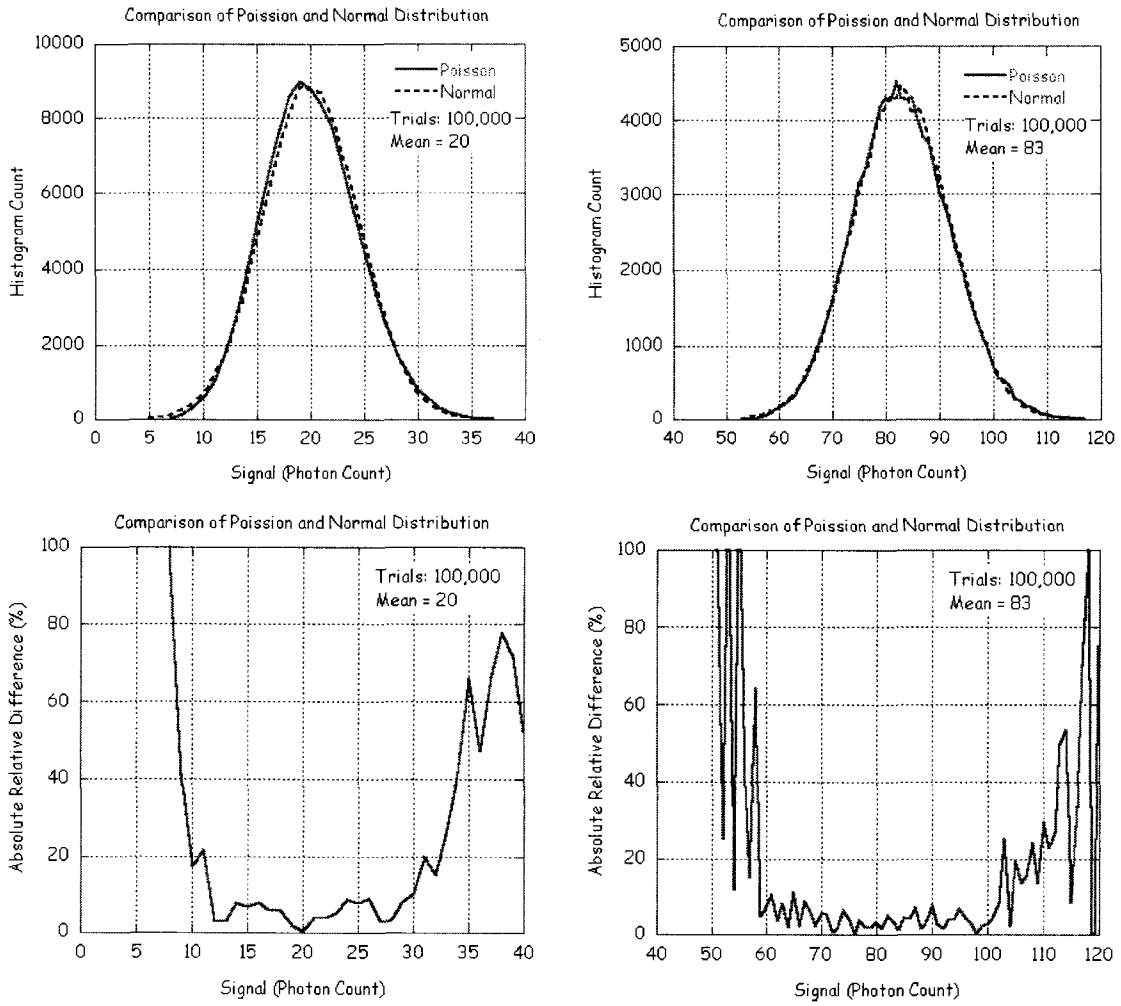

Figure 2.16 Comparison of normal and Poisson distributions for the same values mean and variance. (upper left) Histogram from 100,000 trials with mean 20 and variance of 20. (upper right) Histogram from 100,000 trials with mean 20 and variance of 83. (lower left) Relative difference in Normal and Gaussian histograms for mean of 20. (lower right) Relative difference in Normal and Gaussian histograms for mean of 83.

2.5 Confidence Levels in Lidar Signals.

Given a raw lidar signal with a certain relative error I now wish to estimate my confidence in the lidar measurement. I model the lidar signal as the sum of an

Reproduced with permission of the copyright owner. Further reproduction prohibited without permission.

expected value (i.e., the deterministic signal) and an additive random value that has zero mean and variance equal to the expected value (i.e., the statistical noise). The confidence level is determined by the following question; "what is the probability that a given signal value represents an expected value of the deterministic signal rather than an fluctuation in the additive noise ?". Alternatively, I can consider the question "if I have some signal of value a, what is the probability that the zero mean additive noise with variance a remains less than that value ?" If the noise is a random variable, X, with probability density function, $f_X(x)$ then the confidence level in a given signal level a, is given by the probability,

$$P(X < a) = \int_{-\infty}^{a} f_X(x)dx \tag{2.33}$$

For a lidar signal with a large expected value, the Poisson random variables behave like a normal random variables. The signal level is the value of the signal photon count, N_S, and the variance of the zero mean noise has the value, N_{TOT}. My confidence level, y, in the signal, N_S, is given by,

$$P(X < N_S) = \frac{1}{\sqrt{2\pi N_{TOT}}} \int_{-\infty}^{N_S} \exp(-\frac{x^2}{2N_{TOT}})dx \tag{2.34}$$

This probability can be expressed under the change of variable $y = x/(N_{TOT})^{1/2}$ as,

$$P(X < N_S) = \frac{1}{\sqrt{2\pi}} \int_{-\infty}^{N_S/\sqrt{N_{TOT}}} \exp(-\frac{y^2}{2})dy \tag{2.35}$$

This integral is the cumulative distribution function of the normal (or Gaussian) random variable with zero mean and unit variance, $G(N_S/\sqrt{N_{TOT}})$. However, the argument of the cumulative distribution function is the inverse of the relative error or the Signal to Noise Ratio (SNR) of the lidar signal. Thus, the confidence level or significance of a given lidar measurement is the cumulative distribution function of the SNR, G(SNR). I can now interrelate a given SNR with a confidence level, a scattering signal, N_S, and a background signal, N_B. If assume that N_D can be ignored, I can express the square of the SNR as,

Reproduced with permission of the copyright owner. Further reproduction prohibited without permission.

$$SNR^2 = \frac{N_S^2}{N_{TOT}} = \frac{N_S^2}{N_S + N_B} \tag{2.36}$$

For a given value of SNR and N_B I can determine N_S by,

$$N_S = \frac{SNR^2 \pm \sqrt{SNR^4 + 4SNR^2 N_B}}{2} \tag{2.37}$$

and, for a given SNR and N_S I can determine,

$$N_B = \frac{N_S^2 - SNR^2 N_S}{SNR^2} \tag{2.38}$$

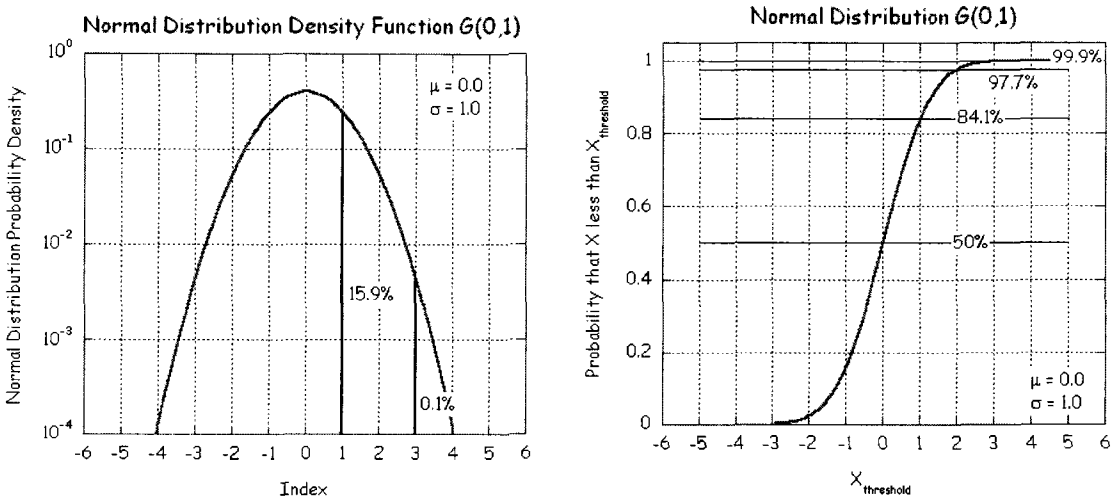

Figure 2.17 Probability density function and cumulative probability of the normal distribution N(0,1).

Consider the sodium or iron lidar raw signal; the mean is a nonzero value and equals N_S. The Normal distribution becomes,

$$F_x(x) = G\left(\frac{x - N_S}{\Delta N_S}\right) = G\left(\frac{x - N_S}{\sqrt{N_S + N_B}}\right) \tag{2.39}$$

Reproduced with permission of the copyright owner. Further reproduction prohibited without permission.

The Signal to Noise Ratio (SNR) of the lidar signal is defined follows,

$$SNR = \frac{N_S}{\Delta N_S} \tag{2.40}$$

The probability of noise signal photon counts greater than lidar signal photon counts equals,

$$P(\Delta N_S > N_S) \sim P(y > SNR) \tag{2.41}$$

where y is a G(0,1) process. Thus, the confidence level is G(SNR); solve this quadratic equation. If N_S is given by,

$$N_S = \frac{SNR^2 \pm \sqrt{SNR^4 + 4SNR^2 N_B}}{2} \tag{2.42}$$

and, furthermore, if N_B is given by,

$$N_B = \frac{N_S^2 - SNR^2 N_S}{SNR^2} \tag{2.43}$$

To illustrate the variation of confidence level with signal I consider the confidence level of the following values; 50%, 62.7%, 75%, 90%, 95%, 99%, 99.5%, and 99.9%. These levels determine the SNR, and I then determine corresponding values of N_S for a given N_B or corresponding values of N_B for a given N_S. I choose the following standard values of N_B; 0, 1, 10, 100, 1000. I choose values of N_B and N_S from GI-UAF lidar measurements of the sodium and iron layers. I choose the following values of N_B; 67.7, 25.7. I choose the following corresponding values of N_S; 1498, 117. I choose values of N_B and N_S from CSU lidar measurements of the sodium layer. I choose the following values of N_B; 0.5, 1.3, 40, 63. I choose the following corresponding values of N_S 1150, 150, 130 20. I plot the variation of scattering signal and background signal with confidence level in Figure 2.18 and 2.1F signal levels I also determine the variations a factor of 10 greater than and less than these measured signal values.

From the plot of the standard signals in Figure 2.18 I see that the required scattering signal increases with required confidence level and background signal level.

Reproduced with permission of the copyright owner. Further reproduction prohibited without permission.

For a confidence level of 95% I require scattering signals of 3.8, 4.7, 8.4, 21.6 and 63.9 for background signal levels of 0, 1, 10, 100, and 1000 respectively. I see that for a 95% confidence level while the background signal level increases by a factor of 1000 the required scattering signal need only increase by a factor of 14. From Figures 2.18 and 2.19 I see that the confidence levels for the GI-UAF lidar are greater than 99% for the measured values of N_S and N_B. Increases in the value of N_B by a factor of 10 still yield confidence levels greater than 99%. Deceases in the value of N_S by a factor of 10 again still yield these high confidence levels. I see that the confidence levels for the CSU lidar are greater than 95% for the most challenging measured values of N_S (20) and N_B (63). The other CSU measurements are having associated 99.9% confidence levels.

To calculate lidar N_B, N_S is fixed. The profile is plotted in Figure 2.19. Confidence levels are still less than or equal to 99.5% in Figure 2.19. The upper panel corresponds to the UAF lidar cases; the lower panel corresponds to the CSU lidar cases. From Figure 2.19, it can be seen that if N_B decreases, the corresponding confidence level increases. If N_S increases, given the same N_B value, the confidence level will increase too. The rate of the confidence level decreasing will speed up as N_B becomes smaller.

Reproduced with permission of the copyright owner. Further reproduction prohibited without permission.

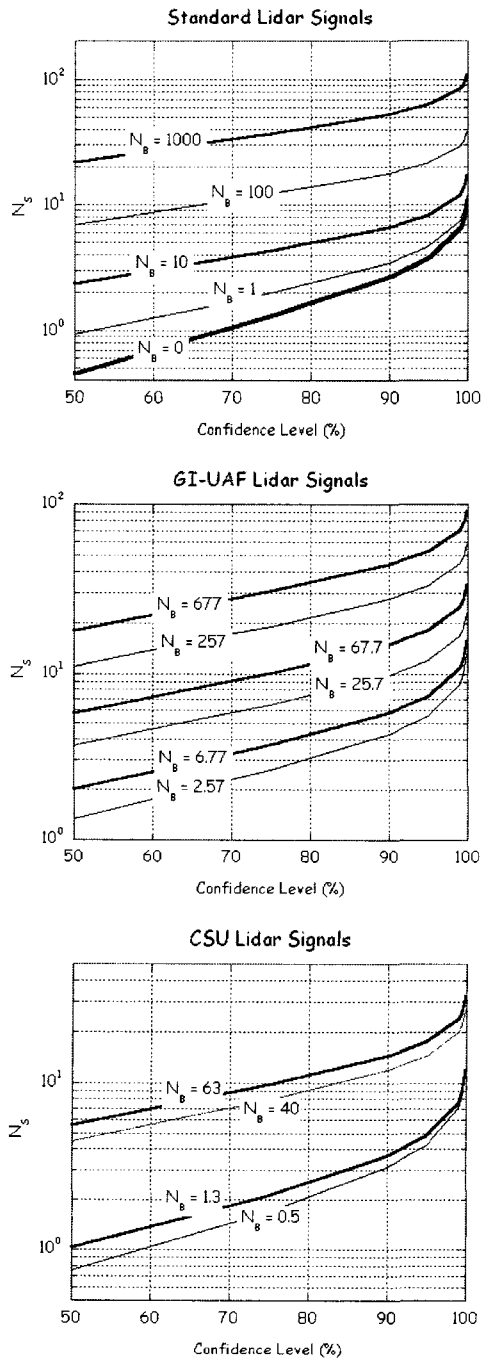

Figure 2.18 Lidar signal as a function of confidence level for different values of background signal level. (upper) Standard background signal values. (middle) GI-UAF lidar system values. (lower) CSU lidar system values.

Reproduced with permission of the copyright owner. Further reproduction prohibited without permission.

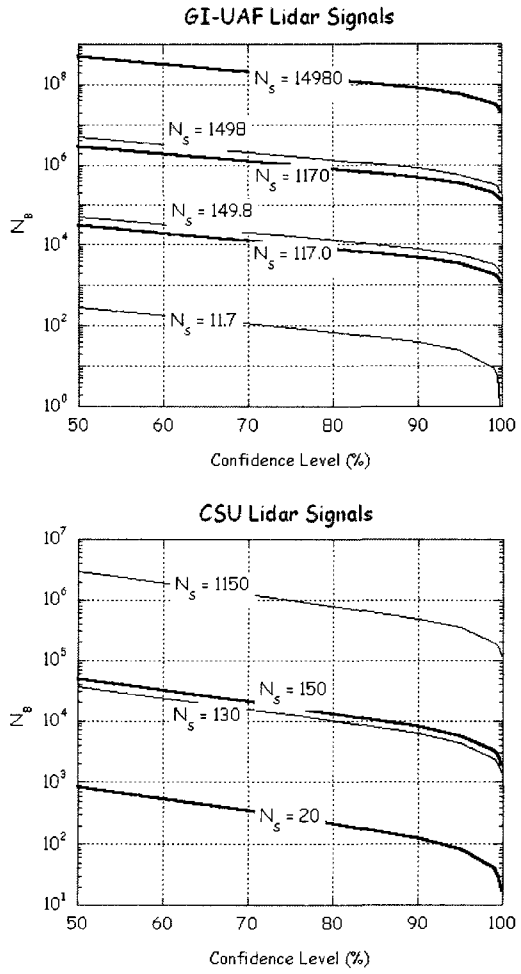

Figure 2.19 Lidar background signal as a function of confidence level for different values of scattering signal level. (upper) GI-UAF lidar system values. (lower) CSU lidar system values.

Reproduced with permission of the copyright owner. Further reproduction prohibited without permission.

3 Resonance Lidar Measurements of Heat Fluxes in the Mesosphere

In this chapter I present a statistical study of the errors in sodium Doppler lidar measurements of wind and temperature in the mesosphere that arise from the statistics of the photon counting process that is inherent in the technique. I use data from the Colorado State University (CSU) sodium Doppler wind-temperature lidar, acquired from a midlatitude site, to define the statistics of the lidar measurements in different seasons under both daytime and nighttime conditions. Finally, I discuss the results in terms of current lidar measurements and proposed measurements at high-latitude sites.

3.1 Middle Atmosphere Heat Fluxes

Investigation of the mesosphere has been prompted by the fact that the region is maintained far from radiative equilibrium by dynamic and chemical heating effects [Andrews et al., 1987]. Inertial gravity (or buoyancy) waves, with periods of several minutes to several hours and vertical wavelengths on order of km, have been recognized as a major contribution to the general circulation of the middle atmosphere since the 1970s [Houghton, 1978]. These waves are primarily generated in the troposphere and propagate upward in the atmosphere. As they propagate through the middle atmosphere, gravity waves interact with other waves, tides and mean winds. In these interactions, the gravity waves loose their energy and contribute to both the general circulation and the turbulent mixing and diffusion of constituents. Efforts to quantify the forcing of the circulation by gravity waves have generally employed three approaches: direct observations of the small-scale motions associated with these waves, atmospheric model studies that employ parameterizations of the wave forcing and are constrained by observations, and balance studies where the forcing that cannot be explained in terms of large-scale planetary waves is attributed gravity waves (see discussion in recent collections of papers in the monographs edited by Johnson and Killeen [1995], and Siskind et al. [2000], and the review article by Fritts and Alexander [2003]).

Reproduced with permission of the copyright owner. Further reproduction prohibited without permission.

The small-scale wave perturbations (i.e., three wind components (zonal: u', meridional: v', and vertical: w'), temperature (T') and/or density (ρ')) typically represent relative perturbations of a couple of percent. Accurate measurement of these quantities has driven the development of lidar, radar and airglow instruments that are capable of high-precision and high-resolution measurements of wind, temperature, and constituent concentrations. The accurate determination of the associated wave-generated Reynolds stresses or momentum and heat fluxes (i.e. $\overline{u'w'}$, $\overline{v'w'}$, $\overline{w'T'}$), and the resultant forcing of the mean flow due to the vertical gradients in these fluxes places even greater demands on the accuracy and precision of the measurements. Measurements of the momentum flux have attracted most attention because the formulation of the gravity wave forcing arises in the momentum equations of the general circulation and radar systems capable of measuring winds have been operated since the 1980s [Vincent and Reid, 1982; Wang and Fritts, 1990]. However, determination of the fluxes is complicated by the large natural variability in the atmosphere [Kudeki and Franke, 1998; Gardner and Yang, 1998]. Furthermore, Thorsen et al. [2000] studied the use of single instruments that make multiple line-of-sight velocity measurements to determine the momentum flux (i.e. $\overline{u'w'}$, $\overline{v'w'}$). Thorsen and co-workers found that the viewing geometry can bias the momentum flux estimate and should be carefully chosen based on the geophysical variability in the horizontal and vertical winds.

In principle, the measurement of thermal fluxes does not suffer from these problems of measurement geometry, as a single beam zenith-pointing lidar system is capable of common-volume temperature and vertical wind measurements along a single line-of-sight. The average thermal flux associated with non-breaking gravity waves that propagate freely, conserve their energy, and grow with altitude is identically zero. The net thermal flux associated with breaking gravity waves can be viewed as having two components: the heat flux associated with the turbulence generated by the waves, and the wave flux convergence associated with the breaking waves that no longer grow freely with altitude. The flux associated with breaking gravity waves is expected to be negative and these wave motions are expected to cool the mesosphere while the turbulence that is generated results in heating [Schoeberl et

Reproduced with permission of the copyright owner. Further reproduction prohibited without permission.

al., 1983]. Studies have shown the cooling by the wave heat flux divergence is greater than the heating by the turbulence [Huang and Smith, 1991; Becker, 2004]. Walterscheid [1981] has shown that wave breaking due to Doppler shifting of waves by tides also yields a negative vertical heat flux. In comparison, aircraft measurements of eddy heat fluxes in the boundary layer, associated with atmospheric turbulence, show mostly small positive and negative values that average to near zero with occasional positive spikes associated with convective plumes [Stull, 1989].

Gardner and colleagues have made sodium Doppler wind-temperature lidar observations with large aperture (> 3 m) telescopes that have yielded high-resolution (2.5 min, 480 m) vertical wind and temperature measurements and estimates of the heat flux in the mesopause region (~ 85-100 km). Gardner and Yang [1998] reported a vertical heat flux associated with dissipating gravity waves of -2.29±0.4 (Km/s) from 65 h of measurements employing the large-aperture telescope (3.5 m) at the Starfire Optical Range (SOR), New Mexico (35°N, 107°W). Gardner et al. [2002] have subsequently reported a vertical heat flux associated with dissipating gravity waves of -1.55±0.2 (Km/s) from over 200 h of measurements at SOR. Liu and Gardner [2005] reported a vertical heat flux associated with dissipating gravity waves of -1.40±0.5 (Km/s) from over 100 h of measurements employing the large-aperture telescope (3.7 m) at the Advanced Electro-Optic System (AEOS) Haleakala, Hawaii (21°N, 156°W). The value of these heat fluxes measured at SOR and AEOS correspond to wave induced cooling rates of -30 to -50 K/day. Gardner and Yang [1998] presented an extensive analysis of the errors and uncertainties in the flux measurements, but did not consider the cross-correlation between the errors, and concluded that the biases in the measured heat flux of 8×10^{-5} Km/s. Given the extensive presentation, analysis, and discussion of the experimental technique by Gardner and Yang, I compare the results of this study with the SOR measurements of Gardner and Yang [1998].

In this study I extend the analysis of Gardner and Yang to consider the how the biases in the heat flux measurements vary with telescope aperture, geographic location, and season. The statistical quality of the lidar measurement improves with increase in signal. The power-aperture product, effective backscatter Cross section of the sodium atoms, and sodium concentration all combine to determine the magnitude of the lidar signal and the sensitivity and accuracy of the lidar system (see review by

Reproduced with permission of the copyright owner. Further reproduction prohibited without permission.

Chu and Papen, [2005]) The sodium concentration (and thus the amplitude of the lidar signal) varies with season, having a winter maximum and summer minimum, and a more extreme variation at the poles than the equator (e.g., Gardner et al., [1988]; Plane, [1991]; Gardner et al., [2005]). I use measurements from the Colorado State University (CSU) sodium Doppler wind-temperature lidar at Fort Collins, Colorado (41N, 105°W) [Arnold and She, 2003], to prescribe the sodium concentrations and system performance under daytime and nighttime conditions in both summertime and wintertime. I conduct a forward random variable analysis from the lidar signals as well as Monte Carlo simulation to determine the expected biases in the flux measurements. I use these simulations to determine the range of geophysical conditions and telescope apertures that can be used to make reliable vertical heat flux measurements.

3.2 The Sodium Doppler Wind-Temperature Lidar Measurement Technique

3.2.1 Laser Spectroscopy of Sodium Wind-temperature Lidar

Sodium resonance wind-temperature lidar systems employ the same spectroscopy technique as traditional sodium resonance fluorescence lidar discussed in Chapter 2. Sodium resonance wind-temperature lidar systems use the sodium D_2 fluorescence from the mesospheric sodium layer to measure wind and temperature profiles in the mesopause region (~ 80 - 100 km). The width of the sodium spectrum varies with temperature and the relative position of the spectrum shifts with wind. In Figure 3.1 the sodium absorption cross section by Doppler shift and broadening is plotted. The wind and temperature can be determined from the relative strength of the laser echo at different frequencies. The first measurements of temperature were reported in the late 1970s [Gibson et al., 1979] with subsequent measurements reported in the mid 1980s [Fricke and von Zahn, 1985]. Both these early systems employed pulsed-dye lasers with tunable Fabry-Perot Interferometers to transmit tunable narrowband laser light. Modern wind-temperature systems were developed using Doppler-free spectroscopy and pulsed dye lasers seeded with continuous-wave ring-dye lasers in the 1990s [She et al., 1990; Bills et al., 1991; She and Yu, 1995].

Reproduced with permission of the copyright owner. Further reproduction prohibited without permission.

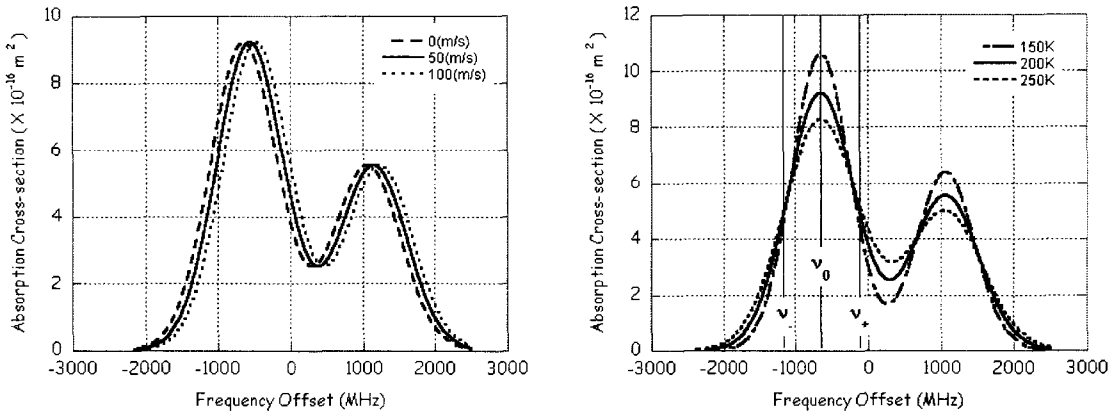

Figure 3.1 Absorption cross section of sodium with Doppler effect. (left) Absorption cross section with Doppler shift due to wind at 0, 50, 100 m/s; (right) Absorption cross section with Doppler broadening due to temperature at 150, 200, 250 K. ν_-, ν_0, ν_+ correspond to three frequencies utilized by Doppler wind-temperature lidar.

Table 3.1 Parameters of the sodium D_1 and D_2 transition lines

Transition Lines	Central Wavelength (nm)	Transition Probability (10^8 s^{-1})	Radiative Lifetime (nsec)	Oscillator Strength f
$D_1(^2P_{1/2}\rightarrow{}^2S_{1/2})$	589.7558	0.614	16.29	0.320
$D_2(^2P_{3/2}\rightarrow{}^2S_{1/2})$	589.1583	0.616	16.23	0.641
Group	$^2S_{1/2}$	$^2P_{3/2}$	Offset (GHz)	Relative Line Strength
		F=2	1.0911	5/32
D_{2a}	F=1	F=1	1.0566	5/32
		F=0	1.0408	2/32
		F=3	-0.6216	14/32
D_{2b}	F=2	F=2	-0.6806	5/32
		F=1	-0.7150	1/32
Doppler-Free Saturation-Absorption Features of the Sodium D_2 Line				
f_a(MHZ)	f_c(MHZ)	f_b(MHZ)	f_+(MHZ)	f_-(MHZ)
-651.4	187.8	1067.8	-21.4	-1281.4

Reproduced with permission of the copyright owner. Further reproduction prohibited without permission.

Several researchers have presented detailed reviews of the spectroscopy of sodium in the mesosphere [Fricke and von Zahn, 1985; Bills et al., 1991; She et al., 1992; She and Yu, 1995; Chu and Papen, 2005]. Some studies have modeled the sodium spectrum using the doublet fine structure (e.g., Bills et al., [1991]) while others have used the complete hyperfine structure (e.g., Fricke and von Zahn, [1985]). Here I calculated the spectroscopic parameters based on discussions in Chapter 2. I model the Doppler-broadened sodium line as the superposition of six hyperfine lines. I adopt the values for the spectroscopic parameters presented in Table 3.1 (taken from Table 5.1 of Chu and Papen, [2005]).

3.2.2 Lidar Measurement of Temperature and Wind

Both the lidar equation and signal statistic distribution remain the same for wind-temperature lidar system. As discussed in Chapter 2, I can model a given lidar signal with expected value of N_{TOT} as a Normal random variable of mean N_{TOT} and standard deviation $(N_{TOT})^{1/2}$.

If the sodium concentration and laser power remain constant for measurements at two frequencies, ν_{L1} and ν_{L2}, then from Equation 2.2,

$$\frac{N_S(\nu_{L2},T,v,z)}{N_S(\nu_{L1},T,v,z)} = \frac{\sigma_{eff}(\nu_{L2},T,V)}{\sigma_{eff}(\nu_{L1},T,V)} \tag{3.1}$$

(where T is the temperature, and V is the wind velocity) the ratio of the signal equals the ratio of the effective scattering cross sections. Early wind-temperature lidars made these measurements using Doppler-free spectroscopy to lock the laser line near the D_{2a} and D_{2b} peak frequencies, ν_{D2a} and ν_{D2b}, as well as near the cross-over frequency ν_{D2c}, midway between the peak frequencies [Bills et al., 1991]. In these systems, the operators first tuned the laser to one frequency where the lidar signal was integrated over multiple laser pulses and then tuned the laser to another frequency where the lidar signal was again integrated over multiple laser pulses. The ratios of the signals were then used to determine the temperature and/or wind. Due to the integration of the lidar signal at different frequencies these measurements included inaccuracies due to variations in the sodium concentration, wind, and

Reproduced with permission of the copyright owner. Further reproduction prohibited without permission.

temperature on a time scale of minutes.

Acousto-optic modulation techniques have subsequently been developed that yield robust three-frequency lidar measurements [White 1999; Sherman, 2002]. The laser is locked to the deepest Lamb-dip in the Doppler-free spectrum at a frequency, ν_0, close to the frequency of the D_{2a} peak, ν_{D2a} ($\nu_0 = \nu_{D2a}$ - 10.4 MHz) [She and Yu, 1995]. The acousto-optic modulation then generates two shifted frequencies, ν_+ ($=\nu_0 + \Delta\nu_{AO}$, $\Delta\nu_{AO}$ = 630 MHz)), and ν_- ($= \nu_0 - \Delta\nu_{AO}$). The laser frequency changes sequentially on a pulse-to-pulse basis (every 0.02 s) and thus avoids the inaccuracies due to variations in the sodium concentration that were inherent in early wind-temperature lidar systems. The characteristics of the CSU lidar system are presented in Table 3.2.

Table 3.2 Characteristics of CSU sodium Doppler wind-temperature lidar

Laser Pulse Energy	20 mJ
Laser Repetition Rate[1]	50 pps
Laser Linewidth	120 MHz
Laser Pulse Length	5 ns
Laser Beam Divergence	0.9 mrad
ν_0[2]	-651.4 MHz
ν_+	-21.4 MHz
ν_-	-1281.4 MHz
Telescope Diameter	35 cm

1: Laser cycles through three frequencies (ν_0, ν_+ and ν_-) and so repetition rate at each frequency is 50/3 pps.

2: Frequencies are relative to sodium D_2 wavelength of 589.1583 nm.

Based on three-frequency measurements, I can define ratios that are sensitive to temperature and wind velocity,

Reproduced with permission of the copyright owner. Further reproduction prohibited without permission.

$$R_T = \frac{\sigma_{eff}(\nu_+,T,V)+\sigma_{eff}(\nu_-,T,V)}{2\sigma_{eff}(\nu_0,T,V)}$$
$$R_V = \frac{\sigma_{eff}(\nu_+,T,V)-\sigma_{eff}(\nu_-,T,V)}{\sigma_{eff}(\nu_0,T,V)} \qquad (3.2)$$

Contours of R_T and R_V for constant T and V are plotted in Figure 3.2. From Figure 3.2, I see that R_T is most sensitive to changes in temperature and R_V is most sensitive to changes in radial velocity. However, the contours show that the ratios, R_T and R_V, are also both dependent upon temperature and velocity. If R_T were independent of velocity, and R_V independent of temperature, then the contours would be straight horizontal and vertical lines. From Equation 3.1 the received lidar signal is proportional to the product of the effective scattering cross section and the sodium concentration. For a three-frequency sodium Doppler wind-temperature that is rapidly tuned on a pulse-to-pulse basis, the sodium concentration cancels out and I can express the ratios directly in terms of the lidar signals,

$$R_T = \frac{N_S(\nu_+)+N_S(\nu_-)}{2N_S(\nu_0)}$$
$$R_V = \frac{N_S(\nu_+)-N_S(\nu_-)}{N_S(\nu_0)} \qquad (3.3)$$

where $N(\nu_+)$, $N(\nu_-)$, and $N(\nu_0)$ are the lidar signals measured at frequencies of ν_+, ν_-, and ν_0 respectively. I can relate the expected signal photon counts at ν_+ and ν_- to the signal photon count at ν_0 as,

$$N_S(\nu_+) = N_S(\nu_0)\frac{\sigma_{eff}(\nu_+,T,V)}{\sigma_{eff}(\nu_0,T,V)}$$
$$N_S(\nu_-) = N_S(\nu_0)\frac{\sigma_{eff}(\nu_-,T,V)}{\sigma_{eff}(\nu_0,T,V)} \qquad (3.4)$$

Using the characteristics of the CSU sodium Doppler lidar in Table 3.2, and assuming the volume in the sodium layer is assumed to have a temperature, T_0 (= 200 K), and a line-of-sight wind, V_0 (= 0 m/s), I find that effective scattering cross sections, $\sigma_{eff}(\nu_+)$, $\sigma_{eff}(\nu_0)$, and $\sigma_{eff}(\nu_-)$, have values of 4.06, 9.22, and 3.50 ($\times 10^{-16}$ m^2) respectively.

Reproduced with permission of the copyright owner. Further reproduction prohibited without permission.

The ratio of $\sigma_{eff}(\nu_+)/\sigma_{eff}(\nu_0)$ equals to 0.440, and the ratio of $\sigma_{eff}(\nu_-)/\sigma_{eff}(\nu_0)$ equals to 0.380. The value of R_T (i.e., R_{T0}) is 0.410 and the value of R_V is (i.e., R_{V0}) is 0.0604.

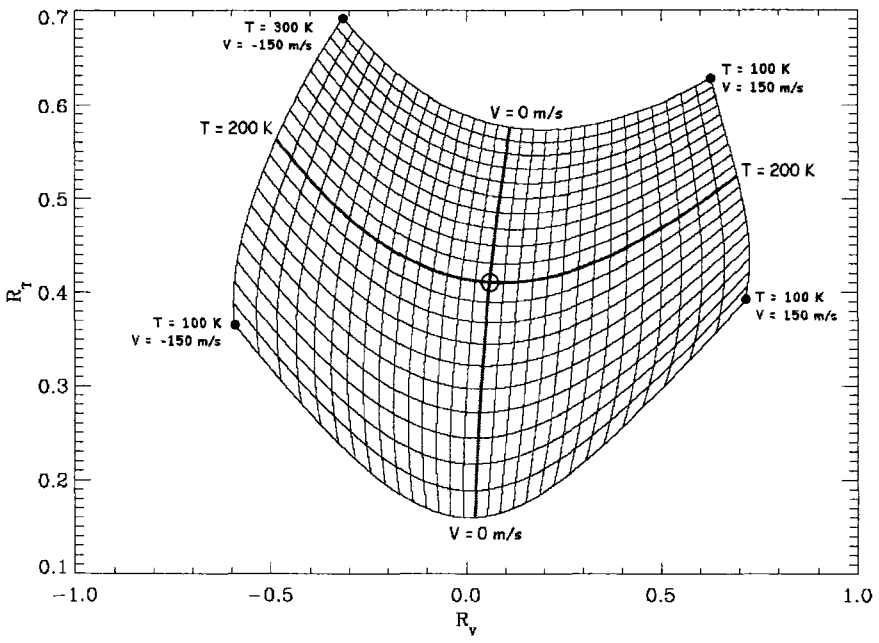

Figure 3.2 Contours of R_T and R_V plotted as functions of temperature, T, and velocity, V. Temperature varies between 100 and 300 K at a resolution of 0.1 K. Velocity varies between -150 m/s and + 150 m/s at a resolution of 0.1 m/s. The contours of RT and RV are plotted at 10 K and 10 m/s. The circle denotes the point (0.0604, 0.410) that corresponds to the ambient environmental conditions (200K, 0 m/s).

3.2.3 Inversion Method

Retrieving temperature, T, and wind, V, is essentially interpolation from a table of unequally spaced pairs of temperature ratio and velocity ratio (R_T, R_V). I calculate (R_T, R_V) pairs from Equation 3.7 over a range of temperatures and winds (i.e., 100,

Reproduced with permission of the copyright owner. Further reproduction prohibited without permission.

100.1, ... 300K, and -150, -149.9, ... +150 m/s). I cover the resultant (R_T, R_V) surface with n_{TV} (= $n_T \times n_V$) = 150×100 = 150000) rectangles with centers at (R_{Tij}, R_{Vij}) and introduce the following bilinear forms for T and V within each rectangle,

$$\begin{aligned} T &= \alpha_{0ij} + \alpha_{1ij}(R_T - R_{Tij}) + \alpha_{2ij}(R_V - R_{Vij}) \\ &\quad + \frac{1}{2}\alpha_{3ij}(R_T - R_{Tij})^2 + \frac{1}{2}\alpha_{4ij}(R_V - R_{Vij})^2 \\ &\quad + \alpha_{5ij}(R_T - R_{Tij})(R_V - R_{Vij}) \\ V &= \beta_{0ij} + \beta_{1ij}(R_T - R_{Tij}) + \beta_{2ij}(R_V - R_{Vij}) \\ &\quad + \frac{1}{2}\beta_{3ij}(R_T - R_{Tij})^2 + \frac{1}{2}\beta_{4ij}(R_V - R_{Vij})^2 \\ &\quad + \beta_{5ij}(R_T - R_{Tij})(R_V - R_{Vij}) \end{aligned} \tag{3.5}$$

I find the α's and β's from a least-squares fit to the generating values of (T,V) from the calculated values of (R_T, R_V). Thus the inversion is reduced to evaluating two bilinear forms.

The accuracy of the inversion depends on the bilinear form and the size of the (R_T, R_V) rectangles. The mean rms error between the original (T,V) and the retrieved (T,V) from Equation 3.5 is 0.003 K and 0.002 m/s. The rectangles span approximately 3 K and 2 m/s, so that when the amplitudes of the temperature and wind fluctuations are less than these values, the coefficients of a single (R_T, R_V) rectangle can be used to determine the fluctuations from analytic expressions. The lidar experiments in this study include cases with larger rms errors. Thus, I expect some disagreement between the results of single-rectangle analytical calculations and simulations that include variations over several rectangles.

3.3 Scope of Study

I determine the flux bias that would be measured by the lidar in the absence of a heat flux. I assume that the sodium layer is at constant temperature (200 K) and at rest (0 m/s).

I first consider experiments where there is no background skylight or detector noise (i.e., $N_D + N_B = 0$) and where $N_S(\nu_0)$ (= $N_{TOT}(\nu_0)$) has an associated error of

Reproduced with permission of the copyright owner. Further reproduction prohibited without permission.

0.1%, 0.5%, 1% and 5% (i.e., $N_S(v_0)$ = 1×10^6, 4×10^4, 1×10^4, and 4×10^2 respectively). These experiments represent the situation where the uncertainty in the measurements is determined by the statistics of the lidar signal. I term these cases the standard error experiments. I then consider experiments based on actual photon count data from the CSU sodium Doppler wind-temperature lidar system. I tabulate these signal levels in Table 3.3. I consider measurements under four scenarios: midday in summer, nighttime in summer, midday in winter, and nighttime in winter. In summary, the sodium concentrations are three times smaller in summer than winter and the lidar signals are eight times smaller in daytime than nighttime due to transmission losses associated with the additional narrowband optics required to reject sunlight. The CSU lidar system employed a 0.35-m diameter telescope. I scale the CSU lidar measurements to consider lidar systems employing a 1-m, 1.8-m or 3.5-m diameter telescope at a resolution of 2.5 min (150 s) and 480 m. These telescope diameters are representative of the receiver telescopes of contemporary single-telescope lidar systems. The diameter of the lidar telescope at ALOMAR, Andoya, Norway (69°N, 16°E) is 1.8 m and that of the SOR telescope is 3.5 m. The resolution of the simulated lidar measurements is chosen to match the measurements of Gardner and Yang [1998]. I term these cases the specific lidar system experiments.

Reproduced with permission of the copyright owner. Further reproduction prohibited without permission.

Table 3.3 CSU sodium Doppler wind-temperature lidar signal levels[1]

Date	Time	Signal N_S (Photon Count)	Background and Detector Dark Signal $N_B + N_D$ (Photon Count)	Sodium Concentration (atoms/m^3)	Relative Error (%)	Confidence (%)
24 June 2002	1200 LT[2]	20	63	1.9×10^9	45.6	98.6
24 June 2002	0400 LT	150	0.5	2.8×10^9	8.2	~100
6 Nov. 2002	1200 LT	130	40	6.0×10^9	10.0	~100
6 Nov. 2002	0300 LT	1150	1.3	9.0×10^9	3.0	~100

1: Measurement resolution : Δt = 120 s, Δz = 150 m.
2: LT = UT - 7 h

3.4 Method of Estimation of Flux Bias

3.4.1 Analytical Approach

I can determine the expected values of the temperature, E(T), and wind, E(V) directly from Equation 3.5. From Equation 3.5 I can express the fluctuations in the measured temperature, T' (= T - T_0), as the difference of two equations,

$$\begin{aligned} T = T - T_0 = {} & \alpha_{1ij}((R_T - R_{Tij}) - (R_{T0} - R_{Tij})) + \alpha_{2ij}((R_V - R_{Vij}) - (R_{V0} - R_{Vij})) \\ & + \frac{1}{2}\alpha_{3ij}\alpha_{1ij}((R_T - R_{Tij})^2 - (R_{T0} - R_{Tij})^2) + \frac{1}{2}\alpha_{4ij}((R_V - R_{Vij})^2 - (R_{V0} - R_{Vij})^2) \\ & + \alpha_{5ij}\ ((R_T - R_{Tij})(R_V - R_{Vij}) - (R_{T0} - R_{Tij})(R_{V0} - R_{Vij})) \end{aligned} \quad (3.6)$$

where R_{T0} and R_{V0} are the values of R_T and R_V at T_0 and V_0, and the other terms have the same meaning as in Equation 3.5. I linearize Equation 3.6 to obtain the following expression for the temperature fluctuation,

$$T' = \alpha_{1ij}(R_T - R_{T0}) + \alpha_{2ij}(R_V - R_{V0}) \quad (3.7)$$

Similarly I can express the fluctuations in the measured radial wind speed, v'(= V - V_0),

$$V' = \beta_{1ij}(R_T - R_{T0}) + \beta_{2ij}(R_V - R_{V0}) \quad (3.8)$$

Reproduced with permission of the copyright owner. Further reproduction prohibited without permission.

I can determine the flux, f', defined as f' = T' × v', from Equations 3.7 and 3.8 as,

$$f' = T'V' = \gamma_1 (R_T - R_{T0})^2 + \gamma_2 (R_V - R_{V0})^2 + \gamma_3 (R_T - R_{T0})(R_V - R_{V0}) \tag{3.9}$$

where

$$\begin{aligned} \gamma_1 &= \alpha_{1ij}\beta_{1ij} \\ \gamma_2 &= \alpha_{2ij}\beta_{2ij} \\ \gamma_3 &= (\alpha_{1ij}\beta_{2ij} + \alpha_{2ij}\beta_{1ij}) \end{aligned} \tag{3.10}$$

I can express the expected value of the flux, E(f'), as,

$$\begin{aligned} E(f') = {} & \gamma_1 E(R_T^2) + \gamma_2 E(R_V^2) + \gamma_3 E(R_T R_V) \\ & - [2\gamma_1 R_{T0} + \gamma_3 R_{V0}] E(R_T) - [2\gamma_2 R_{V0} + \gamma_3 R_{T0}] E(R_V) \\ & + \gamma_1 R_{T0}^2 + \gamma_2 R_{V0}^2 + \gamma_3 R_{T0} R_{V0} \end{aligned} \tag{3.11}$$

This expected flux is the bias in the flux measurement due to the statistical fluctuations in the lidar signal. I can think of the bias as an instrumental or apparent flux. From Equation 3.11 I see that there are two contributions to the flux bias. There is the bias due to the cross-correlation between R_T and R_V based on the fact that they are calculated from a common triple of lidar signals ($N(v_0)$, $N(v_+)$, $N(v_-)$). This cross-correlation is the source of the bias. The second contribution to the bias is due to the sensitivity of R_T to V and R_V to T (i.e., the magnitude of α_{2ij} and β_{1ij}). This sensitivity magnifies the bias. If R_T was independent of V and R_V was independent of T the contours in Figure 3.2 would have no curvature and be vertical and horizontal. This independence would yield zero values of γ_1 and γ_2 and a value of $\gamma_3 = \alpha_{2ij}\beta_{2ij}$, and thus reduce the magnitude of the flux bias (Equation 3.11).

In principle, I can determine the expected value as well as all higher statistics of the flux bias if I know the probability density functions of R_T, R_V, $R_T R_V$, R_T^2, and R_V^2. Standard techniques yield a normal distribution for the sums and differences of Normal random variables, a Chi-square distribution for squares of zero mean Normal random variables, and a Cauchy distribution for ratios of zero mean Normal random variables. However, the ratios of non-zero mean random variables do not in general have analytic probability density functions [Marsaglia, 1965]. Thus I cannot determine

Reproduced with permission of the copyright owner. Further reproduction prohibited without permission.

analytic forms for the probability density functions of R_T, R_V, R_TR_V, R_T^2, R_V^2 and I limit our attention to solving for the expected values of R_T, R_V, $R_T \times R_V$, R_T^2, R_V^2. Since the lidar signals are independent random variables, I can express these expected values as,

$$
\begin{aligned}
E(R_T) &= \frac{1}{2} E\left(N_{TOT}(\nu_+) + N_{TOT}(\nu_-) - 2(N_D + N_B)\right) \times E\left(\frac{1}{N_{TOT}(\nu_0) - (N_D + N_B)}\right) \\
E(R_V) &= E\left(N_{TOT}(\nu_+) - N_{TOT}(\nu_-)\right) \times E\left(\frac{1}{N_{TOT}(\nu_0) - (N_D + N_B)}\right) \\
E(R_T R_V) &= \frac{1}{2} E\left(N_{TOT}(\nu_+)^2 - N_{TOT}(\nu_-)^2 - 2(N_D + N_B)(N(\nu_+) - N(\nu_-))\right) \\
&\quad \times E\left(\frac{1}{\left(N_{TOT}(\nu_0) - (N_D + N_B)\right)^2}\right) \\
E(R_T^2) &= \frac{1}{4} E\left(\left(N_{TOT}(\nu_+) + N_{TOT}(\nu_-) - 2(N_D + N_B)\right)^2\right) \times E\left(\frac{1}{\left(N_{TOT}(\nu_0) - (N_D + N_B)\right)^2}\right) \\
E(R_V^2) &= E\left(\left(N_{TOT}(\nu_+) - N_{TOT}(\nu_-)\right)^2\right) \times E\left(\frac{1}{\left(N_{TOT}(\nu_0) - (N_D + N_B)\right)^2}\right)
\end{aligned}
\tag{3.12}
$$

Using Equation 3.12 I calculate the expected values by integrating the product of the function and the probability density function over the domain of the random variable (e.g., Papoulis and Pillai, [2002]) using the Romberg method as implemented in a standard computational package [Press et al., 1992; Research Systems, 1999].

3.4.2 Monte Carlo Simulation

I use a standard computational package to generate a sequence of the random variable, X, (i.e., X_1, X_2, X, ... X_n) having a normal distribution with a zero mean and unit standard deviation [Research Systems, 1999]. I then generate three lidar signals using standard linear transformation of the random variable X following Equation 3.4,

Reproduced with permission of the copyright owner. Further reproduction prohibited without permission.

$$N_S(\nu_0)_j = X_i \cdot \left(N_S(\nu_0) + N_D + N_B\right)^{1/2} + N_S(\nu_0)$$

$$N_S(\nu_+) = X_{i+1} \cdot \left(N_S(\nu_0)\frac{\sigma_{eff}(\nu_+)}{\sigma_{eff}(\nu_0)} + N_D + N_B \right)^{1/2} + N_S(\nu_0)\frac{\sigma_{eff}(\nu_+)}{\sigma_{eff}(\nu_0)}$$

$$N_S(\nu_-) = X_{i+2} \cdot \left(N_S(\nu_0)\frac{\sigma_{eff}(\nu_-)}{\sigma_{eff}(\nu_0)} + N_D + N_B \right)^{1/2} + N_S(\nu_0)\frac{\sigma_{eff}(\nu_-)}{\sigma_{eff}(\nu_0)} \qquad (3.13)$$

For j = 1, n, and i = 1, 3n-2. I point out that while the expected signal count varies with frequency, the expected background and detector count does not. As discussed in Section 3.2 the effect of the background skylight and detector noise (N_B + N_D) is to increase the standard deviation of the signal (N_S). Finally, I generate R_T and R_V following Equation 3.3, and I use the inversion method of Equation 3.5 to determine the temperature and wind estimates (T,V). Thus I determine n sample pairs of temperature and wind estimates (T_j,V_j) from n samples of the triplet ($N(\nu_0)_j$, $N(\nu_+)_j$, $N(\nu_-)_j$).

I calculate the mean wind and temperature (i.e., T_0, V_0) and fluctuating components of the wind and temperature (i.e., T', v') for the n values. I then calculate the flux estimates are then calculated as the product of the wind and temperature fluctuations (i.e., f' = T' × v') and the flux bias as the mean flux. I determine the accuracies of the mean temperature, wind, and flux estimates by repeating each experiment n_E times and calculating the sample standard deviation of the n_E estimates of the mean. I can calculate the number of samples required for the sample histogram of a normal random variable of zero mean and unit variance to converge to the probability density function within a given accuracy. The ratio of the standard deviation to the mean of the histogram scales as the square root of the number of samples. For values between 3.00 and 3.05 (i.e., between 3.00 and 3.05 standard deviations above the mean) the ratio of the standard deviation to the mean of the histogram is 23 for 10 samples and has a value of 7.0×10^{-2} for 10^6 samples. Thus, I require one million samples to guarantee that a sample histogram has converged within 7% to the probability density function at 3.00-3.05 standard deviations from the mean. In this study I present the histograms for R_T, R_V, T, v' and

Reproduced with permission of the copyright owner. Further reproduction prohibited without permission.

f' for 16 experiments of 10^5 and 10^6 samples each.

3.5 Results

3.5.1 Statistics of RT and RV in Standard Error Experiments

I conduct 16 experiments of 10^6 samples to determine the statistics of R_T and R_V. The mean and standard deviations are tabulated in Table 3.4.

Table 3.4 Statistics of R_T and R_V[1]

Relative Uncertainty in Photon Count		0.1 %	0.5 %	1.0 %	5.0 %
R_T	Mean	4.10×10^{-1}	4.10×10^{-1}	4.10×10^{-1}	4.11×10^{-1}
	Standard Deviation	6.11×10^{-4}	3.06×10^{-3}	6.11×10^{-3}	3.08×10^{-2}
R_V	Mean	6.04×10^{-2}	6.04×10^{-2}	6.04×10^{-2}	6.06×10^{-2}
	Standard Deviation	9.08×10^{-4}	4.54×10^{-3}	9.08×10^{-3}	4.56×10^{-2}

1. Average of sample mean and standard deviation for 16 experiments of 1×10^6 samples.

As expected the standard deviations in R_T and R_V scale with the uncertainties in the photon counts, progressively increasing by the same factor as the uncertainties in the photon counts as the uncertainties increase from 0.1 % to 5%. I determine the average histogram for the 16 experiments and fit Normal curves to the histograms of R_T and R_V. The histograms of R_T and R_V and Normal fits for the 1% standard error case are plotted in Figure 3.3. The histograms are slightly asymmetric with differences of 6% or less between the standard deviation for values less than the mean and the standard deviation for values greater than the mean. The fits to the histograms of the populations have a linear correlation coefficient, r, greater than 0.99. Under the assumption of a Student's t-distribution, I estimate that the significance of these correlations is greater than 99% [Press et al., 1992; Pearson and Johnson, 1968].

Reproduced with permission of the copyright owner. Further reproduction prohibited without permission.

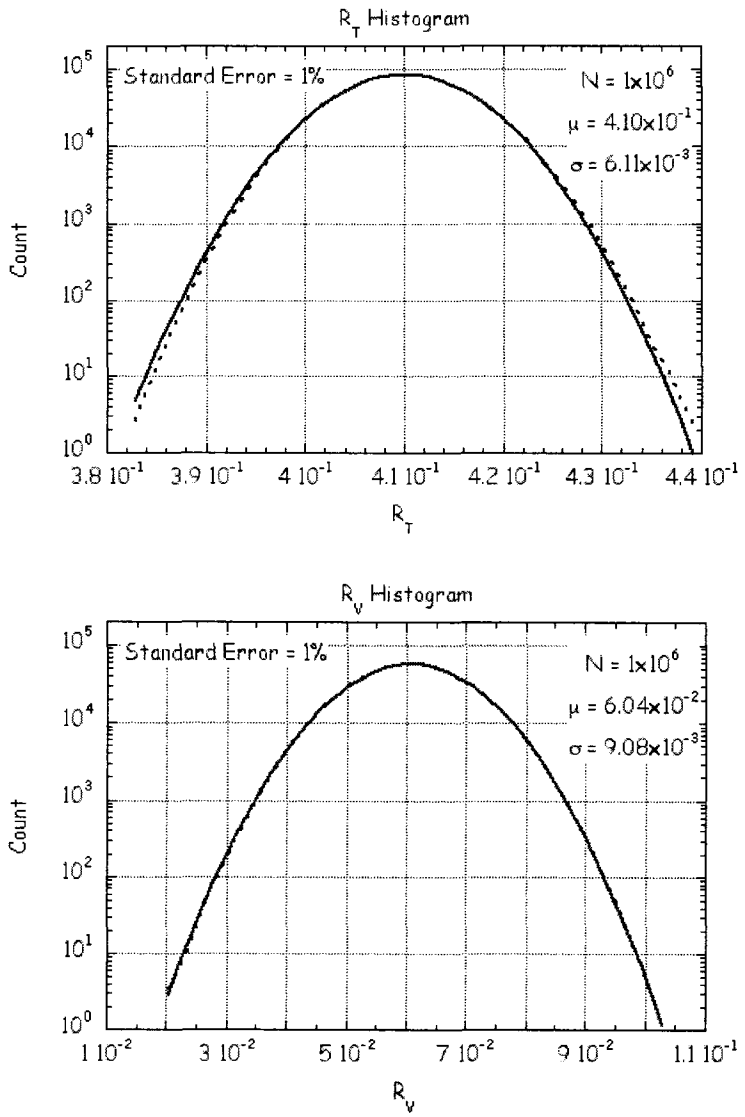

Figure 3.3 Histogram of temperature ratio, R_T, (upper) and velocity ratio, R_V, (lower) measured by the lidar system for photon count errors of 1% (dashed). The histograms are each the average of 16 histograms each of which contain 1×10^6 samples. Normal fits to each histogram are plotted for comparison (solid).

Reproduced with permission of the copyright owner. Further reproduction prohibited without permission.

3.5.2 Statistics of Temperature, Wind and Flux Measurements in Standard Error Experiments

I conduct 16 experiments of 10^6 samples to determine the statistics of temperature, T, wind, V, and flux, f'. The mean and standard deviations are tabulated in Table 3.5 (see next page). As expected the bias in the wind and flux estimates increases with the uncertainty in the lidar signals. The estimates of the flux biases for both the analytic and Monte Carlo approaches show the same behavior; the flux bias increases with the square of the relative uncertainty in the lidar signal. The cross-correlation coefficient of the temperature and velocity fluctuations is determined from the ratio of the mean flux bias to the product of the standard deviations of the temperature and velocity estimates. The net negative flux reflects the fact that the error fluctuations in temperature and velocity are correlated with a cross-correlation coefficient of 3%.

The histograms for T and V and their Normal fits for the 1% standard error case are plotted in Figure 3.4. The distributions are slightly asymmetric with differences of 13% or less in the standard deviation for values less than and greater than the mean. The fits to the histograms of the populations have a linear correlation coefficient, r, greater than 0.99 and I conclude that the significance of the observed correlation is greater than 99%.

Reproduced with permission of the copyright owner. Further reproduction prohibited without permission.

Table 3.5 Statistics of temperature, wind, and heat flux

Relative Uncertainty in Photon Count		0.1 %[1]	0.5 %[2]	1.0 %[1]	5.0 %[2]
Analytic					
Temperature	Mean (K)	200.0	200.0	200.0	200.5
Wind	Mean (m/s)	-3.55×10^{-5}	-1.48×10^{-3}	-6.01×10^{-3}	-1.53×10^{-1}
Flux	Mean (K m/s)	-1.95×10^{-3}	-4.87×10^{-2}	-1.95×10^{-1}	-4.99
Monte Carlo					
Temperature	Mean (K)	200.0	200.0	200.0	200.6
	Standard Deviation (K)	0.3	1.5	3.0	15.2
	Standard Deviation of Mean (K)	2.8×10^{-4}	3.7×10^{-3}	2.8×10^{-3}	3.8×10^{-2}
Wind	Mean (m/s)	1.85×10^{-5}	-5.07×10^{-4}	-5.34×10^{-3}	-1.43×10^{-1}
	Standard Deviation (m/s)	0.25	1.23	2.47	12.4
	Standard Deviation of Mean (m/s)	2.29×10^{-4}	2.93×10^{-3}	2.28×10^{-3}	3.02×10^{-2}
Flux	Mean (K m/s)	-1.90×10^{-3}	-4.52×10^{-2}	-1.92×10^{-1}	-4.98
	Standard Deviation (K m/s)	7.36×10^{-2}	1.84	7.38	193
	Standard Deviation of Mean (K m/s)	7.21×10^{-5}	4.11×10^{-3}	7.12×10^{-3}	4.31×10^{-1}
Correlation (%)		2.5	2.5	2.6	2.6

1. Average of sample mean and standard deviation for 16 experiments of 1×10^6 samples.
2. Average of sample mean and standard deviation for 16 experiments of 1×10^5 samples.

Reproduced with permission of the copyright owner. Further reproduction prohibited without permission.

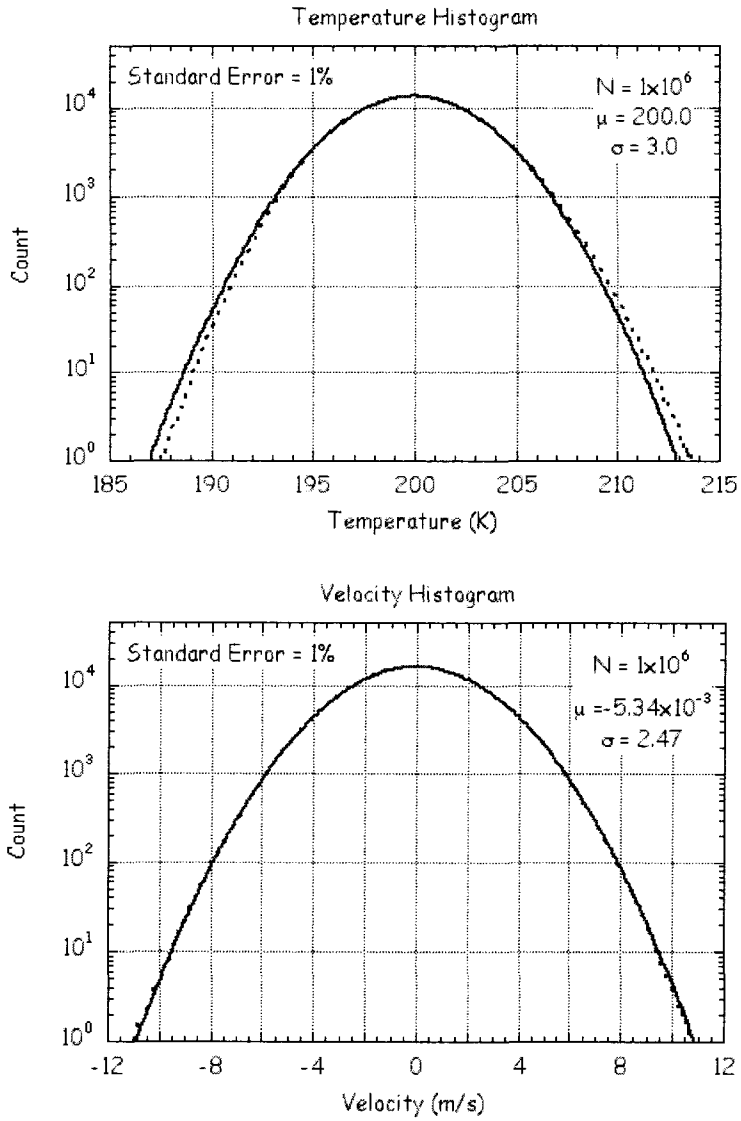

Figure 3.4 Histogram of temperature (upper) and velocity (lower) measured by the lidar system for photon count errors of 1% (dashed). The histograms are each the average of 16 histograms each of which contain 1×106 samples. Normal fits to each histogram are plotted for comparison (solid).

The flux, f', does not behave as a Normal random variable. The flux histogram in the 1% case has an asymmetric exponential distribution (~exp(-λ|x|)) with a constant,

Reproduced with permission of the copyright owner. Further reproduction prohibited without permission.

λ, of 0.157 for positive flux values and 0.148 for the negative flux values (Figure 3.5). The difference in the constants (0.009) is greater than the uncertainty in these fitted values (0.001). I observe this asymmetry, where the constant for positive flux has larger magnitude than the constant for the negative flux is observed in all cases, where the difference in the constants is greater than three times the uncertainty in the fit. I find that the fits to the positive and negative portions of the flux histogram have a linear correlation coefficient, r, greater than 0.99 and the significance of this correlation is again greater than 99%. The asymmetry of the flux histogram reflects the negative bias in the flux estimates. I linearize the expressions for T', V', R_T and R_V and obtain a bilinear form for f' in the random variables with contributions proportional to X_i^2, X_iX_{i+1}, X_iX_{i+2}, etc. I take appropriate linear combinations, Y_a, Y_b, Y_c, of the X_i, X_{i+1}, and X_{i+2}, and obtain a diagonal form, $f' = E_aY_a^2 + E_bY_b^2 + E_cY_c^2$.

The Y's are again normal random variables with zero average and unit standard deviations. For photon count error of 1%, I find $E_a = -3.775$, $E_b = 0$, $E_c = 3.586$. This allows us to obtain the distribution of f' values from integration of $\iint dY_a dY_c (2\pi)^{-1}\exp(-Y_a^2 - Y_c^2)$ over appropriate limits. Fitting these distributions for $f' < 0$ I find that $\lambda = 0.146$ and for $f' > 0$ that $\lambda = 0.154$ in close agreement (less than 2% difference) with the values determined from the Monte Carlo approach.

3.5.3 Statistics of Temperature, Wind and Flux Measurements for Specific Lidar System Experiments

I need to scale the CSU lidar measurements to measurements made with lidar systems having 1-m, 1.8-m and 3.5-m telescopes at a resolution of 2.5 min (150 s) and 480 m. Accordingly, I multiply the photon counts in Table 3.3 by factors of 32.6, 106, and 400 respectively. I tabulate the photon count uncertainties for each case in Table 3.6.

Reproduced with permission of the copyright owner. Further reproduction prohibited without permission.

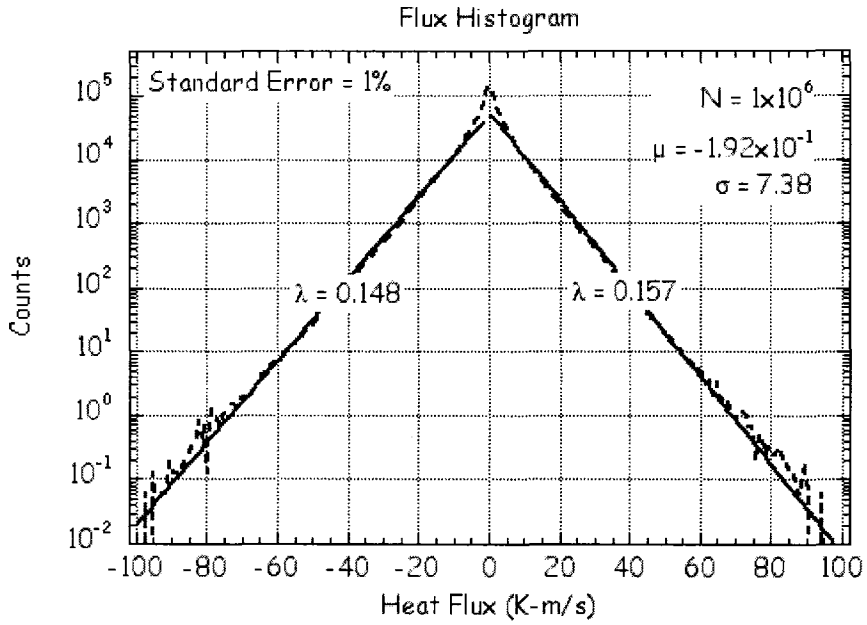

Figure 3.5 Histogram of fluxes measured by the lidar system for photon count errors of 1% (dashed). The histogram is the average of 16 histograms each of which contain 1x106 samples. Exponential fits to the positive and negative side of the histogram are plotted for comparison (solid). The flux histogram has an asymmetric exponential distribution (~exp(-λ|x|)) with a constant of 0.157 for positive flux values and 0.148 for the negative flux values. The histogram is calculated over 201 1 Km/s intervals distributed between -100 Km/s and +100 Km/s.

Table 3.6 Doppler wind-temperature lidar signal measurement errors[1]

	Relative Photon Count Error (%)			Confidence (%)		
Telescope Diameter	1 m	1.8 m	3.5 m	~100	~100	~100
Summer Midday	8.0	4.4	2.3	~100	~100	~100
Summer Night	1.4	0.8	0.4	~100	~100	~100
Winter Midday	1.8	1.0	0.5	~100	~100	~100
Winter Night	0.5	0.3	0.2	~100	~100	~100

1: Measurement resolution . Δt = 150 s, Δz = 480 m.

Reproduced with permission of the copyright owner. Further reproduction prohibited without permission.

I conduct simulations under the four sets of different geophysical conditions for 1-m (Table 3.7), 1.8-m (Table 3.8) and 3.5-m (Table 3.9) telescopes. In all the simulations the uncertainties in the mean values are the value of the standard deviation divided by $(10^5)^{1/2}$ as expected.

Reproduced with permission of the copyright owner. Further reproduction prohibited without permission.

Table 3.7 Statistics of temperature, wind, and heat flux for CSU lidar and 1 m telescope[1]

		Summer Midday	Summer Night	Winter Midday	Winter Night
Analytic					
Temperature	Mean (K)	200.9	200.0	200.1	200.0
Wind	Mean (m/s)	-6.49×10^{-1}	-1.24×10^{-2}	-2.23×10^{-2}	-1.59×10^{-3}
Flux	Mean (Km/s)	-60.3	-4.07×10^{-1}	-1.30	-5.23×10^{-2}
Monte Carlo					
Temperature	Mean (K)	200.3	200.0	200.1	200.0
	Standard Deviation (K)	30.0	4.3	5.7	1.5
	Standard Deviation of Mean (K)	1.0×10^{-1}	1.0×10^{-2}	1.5×10^{-2}	3.8×10^{-3}
Wind	Mean (m/s)	-5.96×10^{-1}	-9.54×10^{-3}	-1.83×10^{-2}	-5.79×10^{-4}
	Standard Deviation (m/s)	29.0	3.55	5.04	1.28
	Standard Deviation of Mean (m/s)	7.09×10^{-2}	8.46×10^{-3}	1.20×10^{-2}	3.03×10^{-3}
Flux	Mean (Km/s)	-60.6	-3.84×10^{-1}	-1.25	-4.87×10^{-2}
	Standard Deviation (Km/s)	926	15.2	28.9	1.97
	Standard Deviation of Mean (Km/s)	1.70	3.37×10^{-2}	6.34×10^{-2}	4.40×10^{-3}
Correlation(%)		7.0	2.5	4.4	2.5

1. Average of sample mean and standard deviation for 16 experiments of 1×10^5 samples.

Reproduced with permission of the copyright owner. Further reproduction prohibited without permission.

Table 3.8 Statistics of temperature, wind, and heat flux for CSU lidar and 1.8 m telescope[1]

		Summer Midday	Summer Night	Winter Midday	Winter Night
Analytic					
Temperature	Mean (K)	200.3	200	200	200
Wind	Mean (m/s)	-1.96×10^{-1}	-3.79×10^{-3}	-6.84×10^{-3}	-4.71×10^{-4}
Flux	Mean (K m/s)	-18.2	-1.25×10^{-1}	-3.99×10^{-1}	-1.61×10^{-2}
Monte Carlo					
Temperature	Mean (K)	200.3	200.0	200.0	200.0
	Standard Deviation (K)	16.9	2.4	3.2	0.9
	Standard Deviation of Mean (K)	4.5×10^{-2}	5.8×10^{-3}	8.0×10^{-3}	2.1×10^{-3}
Wind	Mean (m/s)	-1.82×10^{-1}	-2.23×10^{-3}	-4.63×10^{-3}	7.64×10^{-5}
	Standard Deviation (m/s)	16.0	1.97	2.79	7.08×10^{-1}
	Standard Deviation of Mean (m/s)	3.85×10^{-2}	4.68×10^{-3}	6.63×10^{-3}	1.68×10^{-3}
Flux	Mean (K m/s)	-18.0	-1.18×10^{-1}	-3.84×10^{-1}	-1.47×10^{-2}
	Standard Deviation (Km/s)	275	4.67	8.85	6.04×10^{-1}
	Standard Deviation of Mean (K m/s)	5.97×10^{-1}	1.04×10^{-2}	1.96×10^{-2}	1.36×10^{-3}
Correlation(%)		6.7	2.5	4.3	2.3

1. Average of sample mean and standard deviation for 16 experiments of 1×10^5 samples.

Reproduced with permission of the copyright owner. Further reproduction prohibited without permission.

Table 3.9 Statistics of temperature, wind, and heat flux for CSU lidar and 3.5 m telescope[1]

		Summer Midday	Summer Night	Winter Midday	Winter Night
Analytic					
Temperature	Mean (K)	200.1	200.0	200.0	200.0
Wind	Mean (m/s)	-5.15×10^{-2}	-9.87×10^{-4}	-1.79×10^{-3}	-1.07×10^{-4}
Flux	Mean (Km/s)	-4.79	-3.31×10^{-2}	-1.06×10^{-1}	-4.26×10^{-3}
Monte Carlo					
Temperature	Mean (K)	200.1	200.0	200.0	200.0
	Standard Deviation(K)	8.6	1.2	1.6	0.4
	Standard Deviation of Mean (K)	2.3×10^{-2}	3.0×10^{-3}	4.1×10^{-3}	1.1×10^{-3}
Wind	Mean (m/s)	-4.49×10^{-2}	-1.93×10^{-4}	-6.70×10^{-4}	1.64×10^{-4}
	Standard Deviation (m/s)	8.20	1.01	1.44	3.65×10^{-1}
	Standard Deviation of Mean (m/s)	1.95×10^{-2}	2.40×10^{-3}	3.41×10^{-3}	8.65×10^{-4}
Flux	Mean (Km/s)	-4.68	-3.06×10^{-2}	-1.01×10^{-1}	-3.96×10^{-3}
	Standard Deviation (Km/s)	71.0	1.24	2.34	1.61×10^{-1}
	Standard Deviation of Mean (Km/s)	1.54×10^{-1}	2.76×10^{-3}	5.21×10^{-3}	3.60×10^{-4}
Correlation(%)		6.6	2.5	4.4	2.7

1. Average of sample mean and standard deviation for 16 experiments of 1×10^5 samples.

Reproduced with permission of the copyright owner. Further reproduction prohibited without permission.

In summary, for a 1-m telescope based sodium Doppler wind-temperature lidar system the bias in the vertical heat flux measurements varies from -60.6 Km/s at midday in summer to -4.87×10^{-2} Km/s at night in winter. For a 1.8-m telescope based sodium Doppler wind-temperature lidar system the bias in the vertical heat flux measurements varies from -18.0 Km/s at midday in summer to -1.47×10^{-2} Km/s at night in winter. For a 3.5-m telescope based sodium Doppler wind-temperature lidar system the bias in the vertical heat flux measurements varies from -4.68 Km/s at midday in summer to -3.96×10^{-3} Km/s at night in winter. The source of the flux bias is due to the fact that the temperature and wind error fluctuations are correlated with a correlation coefficient of 2-7%. The estimates of the flux bias from both the analytic and Monte Carlo approaches in Tables 6-8 show the same variation with geophysical conditions. Again, I find that the analytic estimates and the Monte Carlo estimates differ by amounts less than or equal to the uncertainty in the Monte Carlo estimates.

The performance of the lidar systems as a function of telescope diameter is summarized in Figure 3.6 where I plot the magnitude of the flux bias against telescope diameter for each of the four geophysical scenarios. I plot three horizontal lines for comparison: the magnitude vertical heat flux (2.29 Km/s) measured at SOR by Gardner and Yang [1998], 10% of the Gardner and Yang SOR measurement (0.229 Km/s), and the flux bias for 1% standard case (0.192 Km/s). Clearly the summer midday measurements provide the greatest challenge where the measurement biases are greater than the actual flux for lidar systems employing 1-m and 1.8-m telescopes. At midday in summer the 3.5-m telescope yields a bias that is 70% of the actual flux measured by Gardner and Yang. However, under all other conditions (i.e., summer night, winter midday, and winter night) the flux bias is less than 10% of the value measured by Gardner and Yang. The 1.8-m telescope-based system yields biases that are less than 10% of the actual flux at night in all seasons. The 1-m telescope-based system yields biases that are less than 10% of the actual flux only at night in winter. The cross-correlation coefficients of 2-7% are less than the values of 12% reported by Gardner and Yang.

Reproduced with permission of the copyright owner. Further reproduction prohibited without permission.

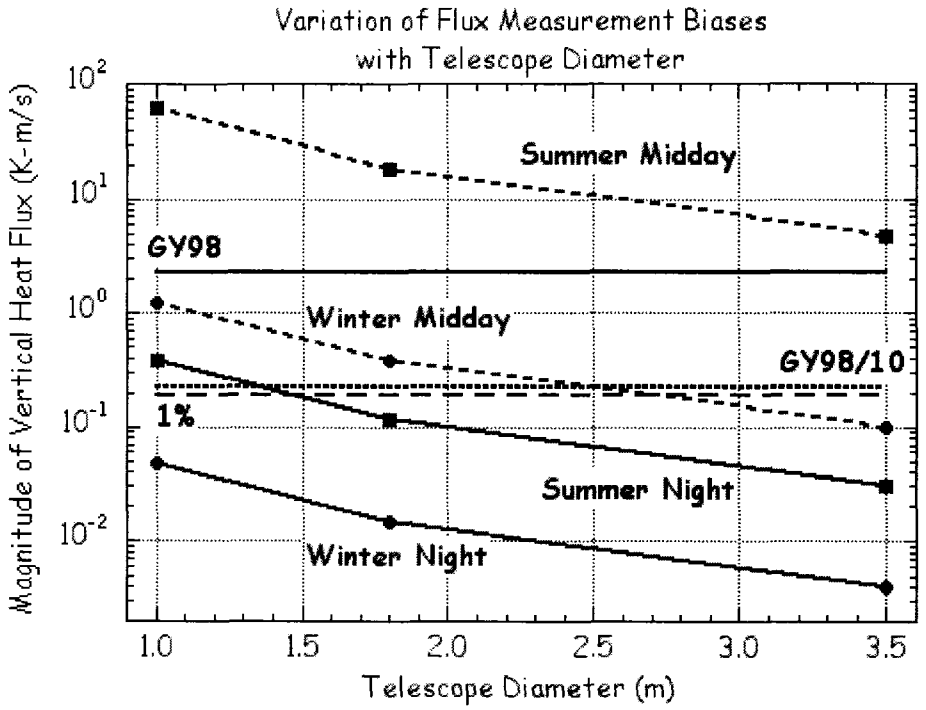

Figure 3.6 Magnitude of bias in vertical heat flux measured by sodium Doppler wind-temperature lidar systems as a function of telescope diameter under different geophysical conditions; summer midday (dash square), winter midday (dash circle), summer night (solid, square), and winter night (solid circle). The vertical heat flux measured by Gardner and Yang (1998) (GY98) (horizontal solid line at 2.29 Km/s), the value of 10% of the vertical heat flux measured by Gardner and Yang (GY98/10) (horizontal short dash line at 0.229 Km/s), and the flux bias for 1% measurements (Table 3.5) (horizontal long dash line at 0.192 Km/s) are plotted for comparison.

3.5.4 Comparison with Method of Gardner and Yang

As discussed earlier, Gardner and Yang [1998] employed the sodium Doppler wind-temperature lidar technique to make vertical heat flux measurements at SOR. They defined R_T and R_V as,

Reproduced with permission of the copyright owner. Further reproduction prohibited without permission.

$$R_T = \frac{N_S(\nu_+) + N_S(\nu_-)}{\left(1 + N_S(\nu_0)\right)}$$
$$R_V = \frac{N_S(\nu_-)}{\left(1 + N_S(\nu_+)\right)} \qquad (3.14)$$

I have simulated the lidar experiment using these definitions. The values of R_T and R_V are different (mean values of 0.820 and 0.863 respectively) than the values I have calculated using the definition given in Equation 3.3 (Table 3.4). In our simulations I compare the statistics of the temperature, wind and flux measurements using Gardner and Yang's method (Equation 3.14) and the method of She and coworkers used in this study (Equation 3.3). The differences in the temperature estimates are less than 1% of the mean and 1% of the standard deviation. The differences in the mean values of the wind estimates are less than 3% of the standard deviation. Finally, I find that the mean value of the flux is negative and differs from our definition by less than 6% of the mean and 1% of the standard deviation.

Gardner and Yang [1998] estimate a value of 8×10^{-5} Km/s for the magnitude of the bias associated with a lidar signal level of 3.0×10^{4} counts for measurements at a resolution of 480 m and 150 s. The current study indicates that sodium Doppler wind-temperature lidar measurements of the vertical heat flux have an instrumental flux bias -4×10^{-3} Km/s for a system employing a transmitter equivalent to the CSU lidar system and a 3.5-m telescope at the same resolution at nighttime in winter. This bias is associated with a measurement resolution and a lidar signal level of 4.6×10^{5} counts and a background and dark count signal of 520 counts. The Gardner and Yang estimate does not include the effect of correlation of R_T with V and R_V with T (see their Equations A17 through A23), and hence is a lower bound on the flux bias. Our study shows that for the measurement conditions at SOR the actual bias in the heat flux is greater than that reported by Gardner and Yang, but is still be much smaller than the actual vertical heat flux.

3.6 Discussion

While the flux bias decreases with increasing signal level, the lidar signal is not

Reproduced with permission of the copyright owner. Further reproduction prohibited without permission.

infinitely scalable. From Equations 3.2 and 3.3 the accuracy of the lidar measurements is improved by increasing the laser pulse energy (increasing N_S) or reducing the laser beam divergence (decreasing N_B). However, saturation effects in the mesospheric metal layer limit the amplitude of the lidar signal [Megie et al., 1978]. As the energy flux of the laser pulse is increased (by increasing the pulse energy or decreasing the beam divergence) a higher fraction of the sodium atoms are excited by the leading edge of the pulse and due to the nonzero lifetime of the excited state (~16 ns) are unable to interact with the photons in the trailing edge of the pulse. Under these conditions, the sodium layer is saturated and the actual lidar signal is less than expected. Following Megie et al., I use the system parameters in Table 3.2 and calculate that the lidar signals are over 99.5% of the unsaturated values. Decreasing the laser beam divergence to 0.2 (0.1) mrad decreases the background skylight by a factor of 20 (81) and yields signals that are over 90.7% (69.3%) of the unsaturated values.

Current lidar receiver signals are also limited by the (nonzero) width of the electronic pulses generated in the photomultiplier tubes of the lidar receiver. Typical pulse widths of 5 ns correspond to maximum count rates of 200 MHz [Engstrom, 1980]. The data in Table 3.3 indicates count rates in winter of 5.75×10^5 Hz and count rates in summer of 4.15×10^4 Hz. These count rates scale to 57.5 MHz and 4.15 MHz for a single 3.5-m telescope receiver. The summertime measurements could be further improved by use of larger telescopes. The results presented in Tables 3.6-3.8 suggest that the bias in the flux measurement decreases proportionally to the lidar signal level (or equivalently the telescope area). Increasing the signal level by a factor of 10 would yield an acceptable count rate and reduce the flux bias in daytime summer measurements to -0.16 Km/s or 7% of the actual flux measured by Gardner and Yang. Use of receivers with multiple telescopes and multiple detectors would also alleviate the problem at the cost of extra experimental resources and effort in optical alignment and calibration.

Our study highlights the impact of the geophysical conditions on flux measurements. The column abundance of the sodium layer has a strong seasonal variation with maximum in winter and minimum in summer. This seasonal variation is

Reproduced with permission of the copyright owner. Further reproduction prohibited without permission.

more pronounced at high latitudes than low latitudes, thus I expect that summertime measurements in the polar regions to be the most challenging. These measurements are based on resonance signals that are approximately five times lower than those expected at mid-latitudes and are made under daylight conditions [Gardner et al., 2005]. I scale the summer midday measurements from Table 3.3 and find that the expected relative photon count errors in 150 s, 480 m measurements would be 36%, 20% and 10% for the 1-m, 1.8-m and 3.5-m telescope-based lidar systems respectively.

The biases that I have computed in this study are associated with the CSU sodium Doppler wind-temperature lidar. The CSU lidar uses a dye laser with a three-frequency technique that incorporates acousto-optic modulation to rapidly switch between laser frequencies. Gardner [2004] has reviewed three-frequency lidar techniques for application in a variety of metals (e.g., sodium, iron, potassium, and calcium). Iron lidar systems have attracted increasing attention as they can employ solid-state alexandrite lasers, rather than dye lasers, to measure the temperature of the mesospheric iron layer [Chu et al., 2002]. Gardner [2004] presents different R_T and R_V metrics for such three-frequency techniques that yield different flux biases. The flux bias will change with the acousto-optic frequency shift since the relative curvature of the (R_T,R_V) surface (Figure 3.2) will be altered. Furthermore, the flux bias will vary with the seasonal variation in environmental conditions as curvature of the (R_T,R_V) surface varies with temperature. In principle I can choose the acousto-optic frequency shift to minimize the flux bias under different environmental conditions. Lautenbach and Höffner [2004] have presented temperature measurements from an iron resonance lidar that employed a frequency scanning, rather than a three-frequency approach. I expect that such a system could be developed to make optimized measurements of the heat fluxes with minimum biases.

3.7 Summary

In this study I have analyzed sodium Doppler wind-temperature lidar measurements of the vertical heat flux. I used experimental data from current sodium Doppler wind-temperature systems to determine the statistical parameters of the photon counting process associated with lidar measurements in winter and summer, day and night with

Reproduced with permission of the copyright owner. Further reproduction prohibited without permission.

a range of telescopes (1-m, 1.8-m, and 3.5-m diameter). I considered the flux bias that would be estimated from wind-temperature measurements of a sodium layer at rest that has a constant temperature. The variability in the measurements is due to the Poisson statistics of the photon counting process inherent in the measurement technique.

I find a cross-correlation coefficient of 3-7% between the lidar wind and temperature estimates. I find that the biases vary from -3.96 $x10^{-3}$ Km/s for wintertime measurements at night with a 3.5-m telescope to -60.6 Km/s for summertime measurements at midday with a 1-m telescope. I find that during winter at night all three systems (1-m, 1.8-m, and 3.5-m) yield biases in their heat flux measurements that are less than 10% of the reported value of the heat flux. During summer at night the 1.8-m and 3.5-m systems yield biases in their heat flux measurements that are less than 10% of the reported vertical heat flux of 2.3 Km/s. During winter at midday the 3.5-m system yields biases in their heat flux measurements that are less than 10% of the geophysical value. During summer at midday all of the systems yield biases that are greater than the geophysical value of the heat flux.

I have limited our analysis to that of the sodium Doppler wind-temperature lidar system that is currently operated at CSU. Lidar systems employing other mesospheric metals (e.g., iron), different laser technologies (e.g., alexandrite), and different temperature and wind metrics are under development in the middle atmosphere lidar community. However, these other lidar systems also employ photon-counting techniques with the same general class of bilinear inversion methods. I have presented an analysis that provides a general framework for determining the flux biases associated with these systems.

Reproduced with permission of the copyright owner. Further reproduction prohibited without permission.

4 Design and Simulation of a N_2^+ Resonance Lidar System

In Chapter 2 I discussed resonance lidar in terms of atomic resonance in sodium and iron. In this chapter I present the principles of the molecular nitrogen ion (N_2^+) resonance lidar for studying the aurorally modified thermosphere. I first review molecular spectroscopy. I then conduct an engineering simulation and analysis of an auroral lidar system.

4.1 Spectroscopy of N_2^+

4.1.1 Molecular Orbital Theory of Diatomic Molecules

In the molecular orbital theory of atomic chemical bonding, an electron occupies an orbital that spreads out throughout the molecule. The square of the amplitude of the orbital is proportional to the electron probability density function. It is a common practice to construct molecular orbitals as linear combinations of atomic orbitals. The underlying assumption is that the atoms in the molecule maintain most of their integrity as atoms (e.g., Atkins [1991], Brown [1998], Hollas, [2005]). Thus an electron in the neighborhood of a particular nucleus experiences the same interactions as if the nucleus was that of a free atom. The molecular orbitals are the wavefunctions calculated when the electron energy includes the kinetic energy and the potential energy due to attraction between each electron and the nuclei (i.e., one-electron terms) but not the potential energy due to repulsion between each electron and all other electrons (i.e., two-electron terms).

When two atomic orbitals are combined, one molecular orbital is formed from the sum of the orbitals and the other molecular orbital is formed from their difference. The sum of two atomic orbitals yields constructive interference in the internuclear region. The difference of the two atomic orbitals yields destructive interference in the internuclear region and the amplitude of the wavefunction may become zero, forming a node that separates regions of opposite sign in the wavefunction. Thus in the sum case electrons can reside in the internuclear region, the energy of the molecule is less than the two independent atoms, and the molecular orbital is termed a bonding orbital. However, in the difference case electrons cannot reside in the internuclear

Reproduced with permission of the copyright owner. Further reproduction prohibited without permission.

region, the energy of the molecule is more than two independent atoms, and the molecular orbital is termed as an anti-bonding orbital. For instance, in molecular Hydrogen (H_2) the two electrons reside in the bonding orbital, while the antibonding orbital remains empty. The molecular orbital diagram is shown in Figure 4.1. Thus the H_2 molecule has a lower energy than the separated atoms.

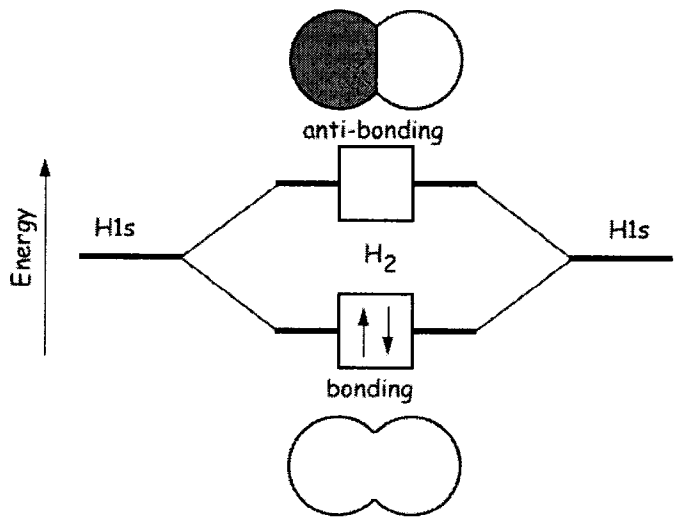

Figure 4.1 Hydrogen (H_2) molecular orbital diagram.

Furthermore, molecular orbitals either have cylindrical symmetry around the internuclear axis (sigma (σ) orbital) or do not have cylindrical symmetry around the internuclear axis (pi (π) orbital). The orbitals are shown in Figure 4.2. Diatomic molecules have a point of inversion (or symmetry) midway between the two nuclei. In a bonding σ-orbital the amplitude of the orbital has the same sign and magnitude under inversion, and the orbital is termed even (gerade in German) and denoted g. In an anti-bonding σ-orbital the amplitude of the orbital has the opposite sign and same magnitude under inversion, and the orbital is termed odd (ungerade in German) and denoted u. In a bonding π-orbital the amplitude of the orbital has the opposite sign

Reproduced with permission of the copyright owner. Further reproduction prohibited without permission.

under inversion, and the orbital is labeled u. In an anti-bonding π-orbital the amplitude of the orbital has the same sign under inversion, and the orbital is labeled g. Thus bonding σ orbitals are g and anti-bonding σ orbitals are u while bonding π orbitals are u and π anti-bonding orbitals are g.

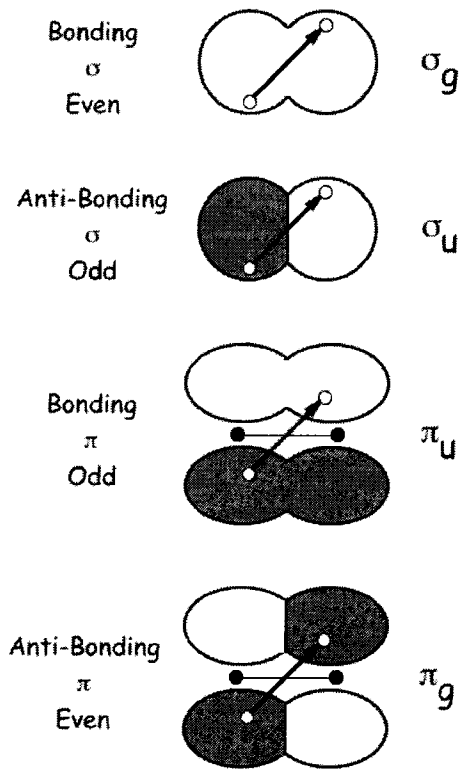

Figure 4.2 Combination of molecular orbitals.

In Period 2 homonuclear molecules the two 2s and the three 2p orbitals of the atoms can build eight molecular orbitals. Four of these orbitals are σ-orbitals built from the two 2s and the two $2p_Z$ orbitals (where z is the internuclear direction). Four of these orbitals are σ-orbitals built from the two $2p_X$ and two $2p_Y$ orbitals (where x and y are the directions perpendicular to the internuclear direction). The molecular

Reproduced with permission of the copyright owner. Further reproduction prohibited without permission.

orbital diagrams for N_2 (having 10 valance electrons) and O_2 (having 12 electrons) are shown in Figure 4.3. The difference in the orbitals is due to the difference in the energy separation between the 2s and 2p atomic orbitals. Mixing of orbitals of similar symmetry (i.e., σ_g 2s and σ_g 2p) can occur and the σ_g 2s orbital is lowered in energy while the σ_g 2p is raised in energy. These energy shifts increase as the 2s-2p separation decreases. The 2s-2p energy separation increases as I cross the periodic table from Li to Ne. For the molecules Li_2 through N_2 these effects are significant. For the molecules O_2 and F_2 these effects are not significant.

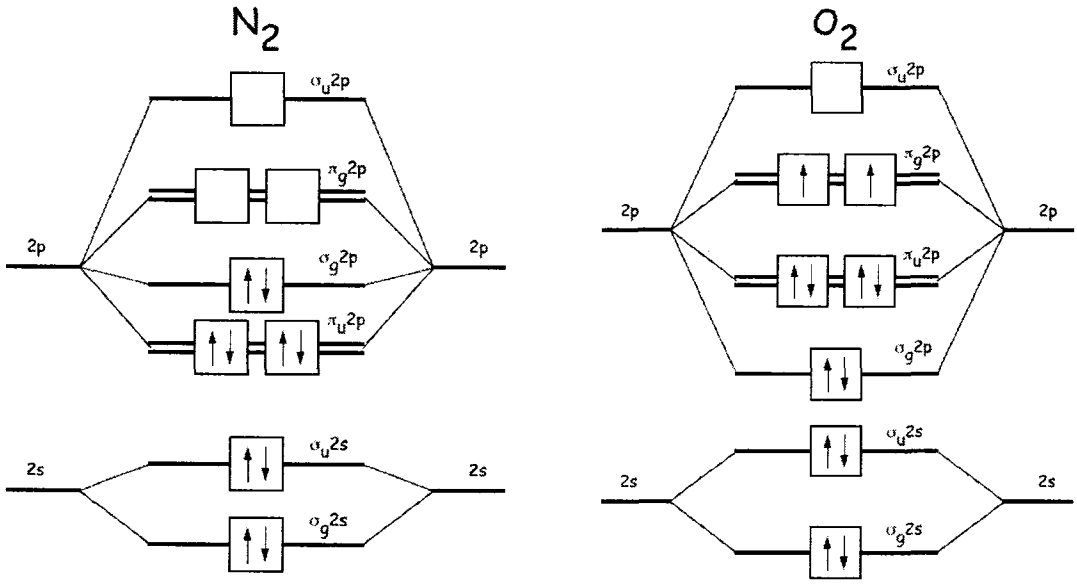

Figure 4.3 Molecular orbital diagrams for N_2 and O_2.

I can write out the ground state configuration of the 14-electron nitrogen molecule as [Lofthus and Krupenie, 1977],

$$(\sigma_g 1s)^2(\sigma_u 1s)^2(\sigma_g 2s)^2(\sigma_u 2s)^2(\pi_u 2p)^4(\sigma_g 2p)^2 \qquad (4.1)$$

I can write the electronic structure of the valance states of ion nitrogen molecule as,

Reproduced with permission of the copyright owner. Further reproduction prohibited without permission.

$$(\sigma_g 1s)^2(\sigma_u 1s)^2(\sigma_g 2s)^2(\sigma_u 2s)^a(\pi_u 2p)^b(\sigma_g 2p)^c(\pi_g 2p)^d(\sigma_u 2p)^e \quad (4.2)$$

where the values of a, b, c, d, and e are integers. Usually the $2\sigma_u$ is expected to be filled (i.e., a = 2). However, in the case of the N_2^+ ion the ionization can result in removal of one electron from this (non-valence) orbital. I tabulate the possible configurations in Table 4.1 [Lofthus and Krupenie, 1977]. For example, in the ground state of N_2^+, $X^2\Sigma_g^+$, the value of a is 2, the value of b is 4, and the value of c is 1, and the value of d and e are zero. The electronic structure of the $X^2\Sigma_g^+$ is written as,

$$(\sigma_g 1s)^2(\sigma_u 1s)^2(\sigma_g 2s)^2(\sigma_u 2s)^2(\pi_u 2p)^4(\sigma_g 2p)^1 \quad (4.3)$$

The $B^2\Sigma_u^+$ and $C^2\Sigma_u^+$ states have two structures, one with $(\sigma_u\ 2s)^2$ and one with $(\sigma_u\ 2s)^1$. In one configuration of the $B^2\Sigma_u^+$ state of N_2^+, the value of a is 1, the value of b is 4, the value of c is 2, and the value of d and e is zero. The electronic structure of this $B^2\Sigma_u^+$ state is written as,

$$(\sigma_g 1s)^2(\sigma_u 1s)^2(\sigma_g 2s)^2(\sigma_u 2s)^1(\pi_u 2p)^4(\sigma_g 2p)^2 \quad (4.4)$$

In the second configuration of the $B^2\Sigma_u^+$ state of N_2^+, the value of a is 2, the value of b is 3, the value of c is 1, and the value of d is 1, and the value of e is zero. The electronic structure of this $B^2\Sigma_u^+$ state is written as,

$$(\sigma_g 1s)^2(\sigma_u 1s)^2(\sigma_g 2s)^2(\sigma_u 2s)^2(\pi_u 2p)^3(\sigma_g 2p)^1(\pi_g 2p)^1 \quad (4.5)$$

The symbols "+" and "-" indicate symmetry due to reflection in the plane containing the internuclear axis. If the amplitude of the orbital does not change on reflection, the orbital is symmetric (or has even symmetry) and is labeled "+". If the amplitude of the orbital changes on reflection, the orbital is antisymmetric (or has odd symmetry) and is labeled "-". This symbolism is applied to all states. But unlike Σ states, other states are doubly degenerate and the "+/-" symbol is not often labeled [Hollas, 2005]. I use the transition between $X^2\Sigma_g^+$ and $B^2\Sigma_u^+$ in the resonance fluorescence lidar.

Reproduced with permission of the copyright owner. Further reproduction prohibited without permission.

Table 4.1 Partial electron configuration of N_2^+

Molecule	State	$\sigma_u 2s$	$\pi_u 2p$	$\sigma_g 2p$	$\pi_g 2p$	$\sigma_u 2p$
N_2	$X^1\Sigma g^+$	2	4	2	0	0
	$A^3\Sigma_u^+$	2	3	2	1	0
	$W^3\Delta_u$	2	3	2	1	0
	$B^3\Pi g$	2	4	1	1	0
	$C^3\Pi_u$	1	4	2	1	0
N_2^+	$X^2\Sigma g^+$	2	4	1	0	0
	$A^2\Pi_u$	2	3	2	0	0
	$B^2\Sigma_u^+$	1	4	2	0	0
		2	3	1	1	0
	$C^2\Sigma_u^+$	2	3	1	1	0
		1	4	2	0	0

For linear diatomic molecules, I have the following quantum numbers [Atkins, 1991]:

i. The orbital angular momentum projection quantum number, Λ. It represents the component of angular momentum L along the internuclear axis, which is $\Lambda h/2\pi$, here h is the Plank constant. Λ can be designated as Σ, Π, Δ, Φ, Γ when Λ equals 0, 1, 2, 3.... Except for the Σ state, all states are doubly degenerated;

ii. The spin projection quantum number, Σ. It represents the component of spin angular momentum S along the nuclear axis, which is $\Sigma h/2\pi$. Σ ranges from -S, -S+1,..., +S;

iii. The total angular momentum projection quantum number, Ω. $\Omega = \Lambda + \Sigma$;

iv. The vibrational quantum number, v. It represents a specific vibrational state energy level. v ranges from 0, 1, 2...;

v. The rotational quantum number, J. It represents a specific rotational state energy level. J ranges from 0, 1, 2....

For example, given the electronic ground state configuration $X^2\Sigma_g^+$, Λ is 0, Σ ranges from -1/2, 0, 1/2, g denotes the inversion symmetry and "+" denotes the

Reproduced with permission of the copyright owner. Further reproduction prohibited without permission.

symmetry in the plane reflection.

For vibrational transitions, electronic transitions are mostly dipole type interactions like a bar magnet. The selection rules are given as,

$$\Delta\Lambda = 0, \pm 1 \quad \Delta S = 0 \quad \Delta\Sigma = 0 \quad \Delta\Omega = 0, \pm 1$$
$$+ \not\leftrightarrow - \quad + \leftrightarrow + \quad + \leftrightarrow +$$
$$g \leftrightarrow u \quad g \leftrightarrow g \quad u \not\leftrightarrow u \tag{4.6}$$

Moreover, the selection rule for rotational transition is,

$$\Delta J = 0, \pm 1$$
$$+ \leftrightarrow - \tag{4.7}$$

Transitions corresponding to ΔJ = -1, 0 and +1 belong to the P, Q and R branches, respectively. For the $\Sigma^{\pm} \leftrightarrow \Sigma^{\pm}$ transition in diatomic molecules, the Q branch is forbidden. The line strength factor is given by the Honl-London factors. The quantum number Λ has a projection along the z axis which contributes to the z vector of total angular momentum J, thus the formulae of Honl-London factors contains Λ. If ΔΛ = 0, the Q branch is stronger at lower Js than the upper Js; If ΔΛ = ±1, the Q branch will increase linearly with Js [Brown, 1998]. Considering the Σ-Σ transition only which is the transition N_2^+ lidar concerned, ΔΛ equals 0, both ground state Λ" and upper state Λ' are zero too, the Honl-London formulae are given as [Herzberg, 1950],

$$HLF_{ij}^{R} = \frac{(i+1+\Lambda'')(i+1-\Lambda'')}{i+1} = \frac{(j+\Lambda')(j-\Lambda')}{j}$$
$$HLF_{ij}^{Q} = \frac{(2i+1)\Lambda''^2}{i(i+1)} = \frac{(2j+1)\Lambda'^2}{j(j+1)}$$
$$HLF_{ij}^{P} = \frac{(i+\Lambda'')(i-\Lambda'')}{i+1} = \frac{(j+1+\Lambda')(j+1-\Lambda')}{j+1} \tag{4.8}$$

4.1.2 Optimized Spectrum for N_2^+ Resonance Fluorescence Lidar

The molecular N_2^+ spectrum contains a wide spectrum ranging from the ultraviolet to the infrared (127 nm to 1770 nm) [Lofthus and Krupenie, 1977]. The term energy of both neutral and ionized nitrogen molecules is plotted in Figure 4.4. The B-X transition,

Reproduced with permission of the copyright owner. Further reproduction prohibited without permission.

also called the first negative band, is the transition N_2^+ resonance lidar will focus on. In this band the strongest vibrational transition is the (0-0) transition. The band head of the 0-0 transition is around 391.4 nm.

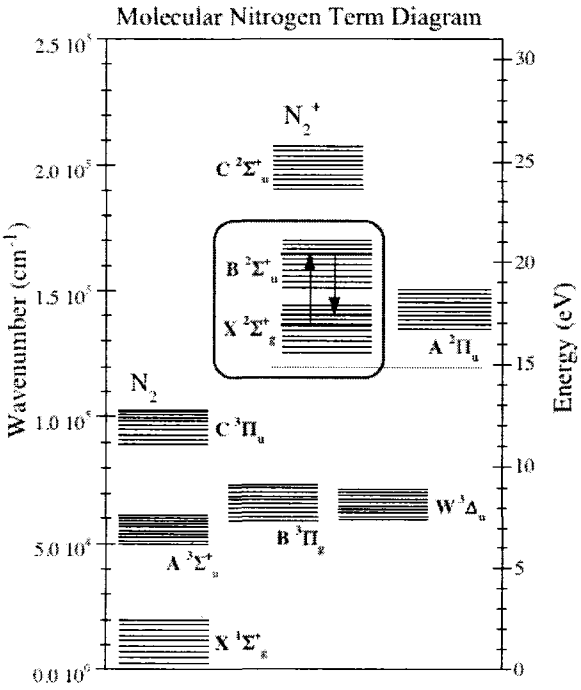

Figure 4.4 Molecular nitrogen (neutral, ion) spectrum.

Collins et al [1997] discussed the optimized N_2^+ resonance lidar performance and did spectroscopic analysis on the lidar photon counting spectrum. Considering the vibrational transition as well as the rotational transition spectroscopy, Collins et al calculated the lidar signal based on the aurora resonance fluorescence lidar equation. Based on the fluorescence cross section and vibrational data, Collins et al determined the optimum transitions as follows: Band system spectroscopic data was used to determine the vibrational transitions that yield the largest emission cross sections between the given electronic states. The rotational states in each electronic-

Reproduced with permission of the copyright owner. Further reproduction prohibited without permission.

vibrational state are populated according to a Boltzmann distribution. For a given temperature, the rotational quantum number that corresponds to the most populated state is determined. Having chosen the initial rotational quantum number J_1, all transitions follow selection rules where the change in rotational quantum number must be less than or equal to one. The optimum rotational lidar transitions are determined by maximizing the product of the population of the lowest state and the Honl-London ratios. The precise frequencies of the transitions are then determined from spectroscopic reference data. The atmospheric transmission is from the MODTRAN model under subarctic conditions. Finally, the optimized laser operation wavelength is determined to be at 390.303 nm for a thermospheric environmental temperature of 500 K. This wavelength will vary according to different temperatures.

I show the rotational transitions of N_2^+ with the associated Honl-London factors in Figure 4.5. As discussed earlier, the Q branch is a forbidden line (i.e., Honl-London factor has a value of zero). The R-branch transition at 390.303 nm has a lower Honl-London factor than the P-branch transition at 391.537 nm. Collins et al. [1997] chose the P-transition as the optimum signal. However, I use the R-branch transition in the lidar system simulations as this allows me measure both the elastic Rayleigh signal and resonance signal with a single-channel receiver at the same wavelength. A dual-channel receiver lowers the system efficiency due to losses in the additional optical components (e.g., beamsplitters, narrowband bandpass filters). For lidar measurements the Rayleigh signal is such an important indicator of the system efficiency and performance that I choose to use the a single wavelength for both the transmitting and receiving wavelengths. Simulations in this chapter will extend Collins et al's analysis and ensure that this simulation better agrees with real measurement practice.

Reproduced with permission of the copyright owner. Further reproduction prohibited without permission.

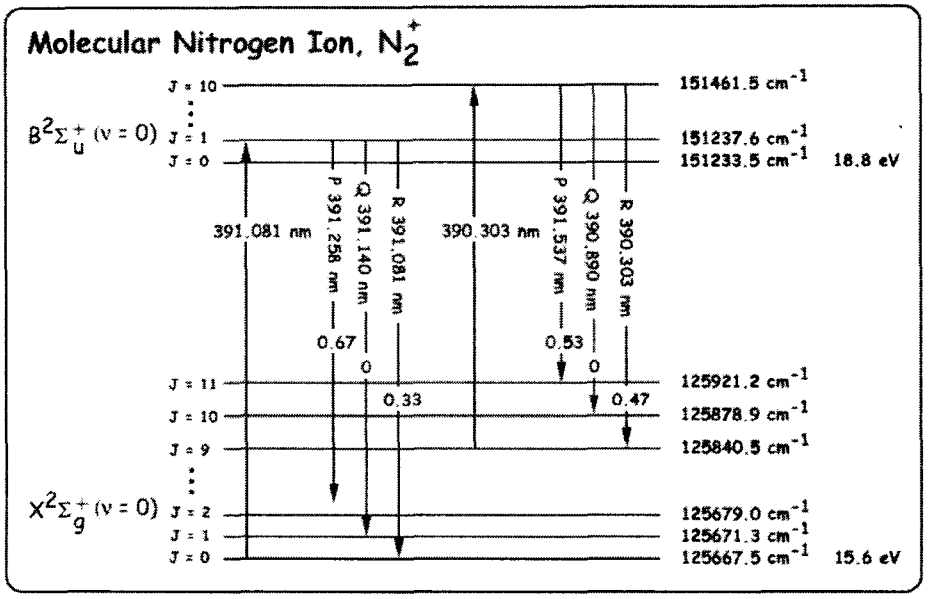

Figure 4.5 Rotational transitions of N_2^+ lidar.

4.2 Photometric Measurements of the Aurora

Photometers, like the Meridian Scanning Photometer (MSP), make integrated line-of-sight measurements of the aurora. At PFRR, the MSP makes measurements of the aurora at four wavelengths (i.e., 557.7 nm, 427.8 nm, 620.0 nm and 486.1 nm) while scanning the sky from the northern horizon to the southern horizon along the magnetic meridian [Morse and Romick, 1982]. The MSP scans from horizon to horizon every 16 seconds and has an instantaneous field-of-view of 1°. The observed surface brightness is corrected for atmospheric extinction, assuming an emission altitude of 100 km. Due to the relatively low light levels, the MSP measures photon flux density in Rayleighs rather than conventional SI units. The unit of Rayleigh can be expressed as:

$$1\,\text{Rayleigh} = \text{an emission rate of } 10^6 \text{ photons/cm}^2 \text{ (column) sec} \qquad (4.9)$$

For auroral lidar studies, given the geophysical variability of the aurora, the performance of a given lidar system is highly dependent on the choice of a typical aurora. A more active aurora produces higher concentrations of excited species at lower altitudes and yields higher-quality lidar measurements, while less active nights

Reproduced with permission of the copyright owner. Further reproduction prohibited without permission.

yield lower-quality lidar measurements [Collins et al., 1997]. I reviewed two years of MSP observations and picked MSP data carefully to derive auroral lidar background signal. The selected night, 6-7 February 1994 (UT day 38), is representative of moderate auroral activity with varying particle characteristics. Figure 4.6 shows the photon flux density measured at these four channels on the night of 6-7 February 1994. The 427.8 nm signal has a maximum value of 54,320 Rayleighs, a minimum value of 103 Rayleighs, and an average value of 1,752 Rayleighs. The 557.7 nm signal has a maximum value of 153,890 Rayleighs, a minimum value of 405 Rayleighs, and an average value of 7,547 Rayleighs. The 486.1 nm signal has a maximum value of 128 Rayleighs, a minimum value of 1 Rayleighs, and an average value of 13 Rayleighs. The 630.0 nm signal has a maximum value of 3,438 Rayleighs, a minimum value of 196 Rayleighs, and an average value of 699 Rayleighs. The maximum value of the 427.8 nm, 557.7 nm, and 486.1 nm signals occurs at 0050 LST, while the maximum value of the 630.0 nm signals occurs at 1840 LST.

Reproduced with permission of the copyright owner. Further reproduction prohibited without permission.

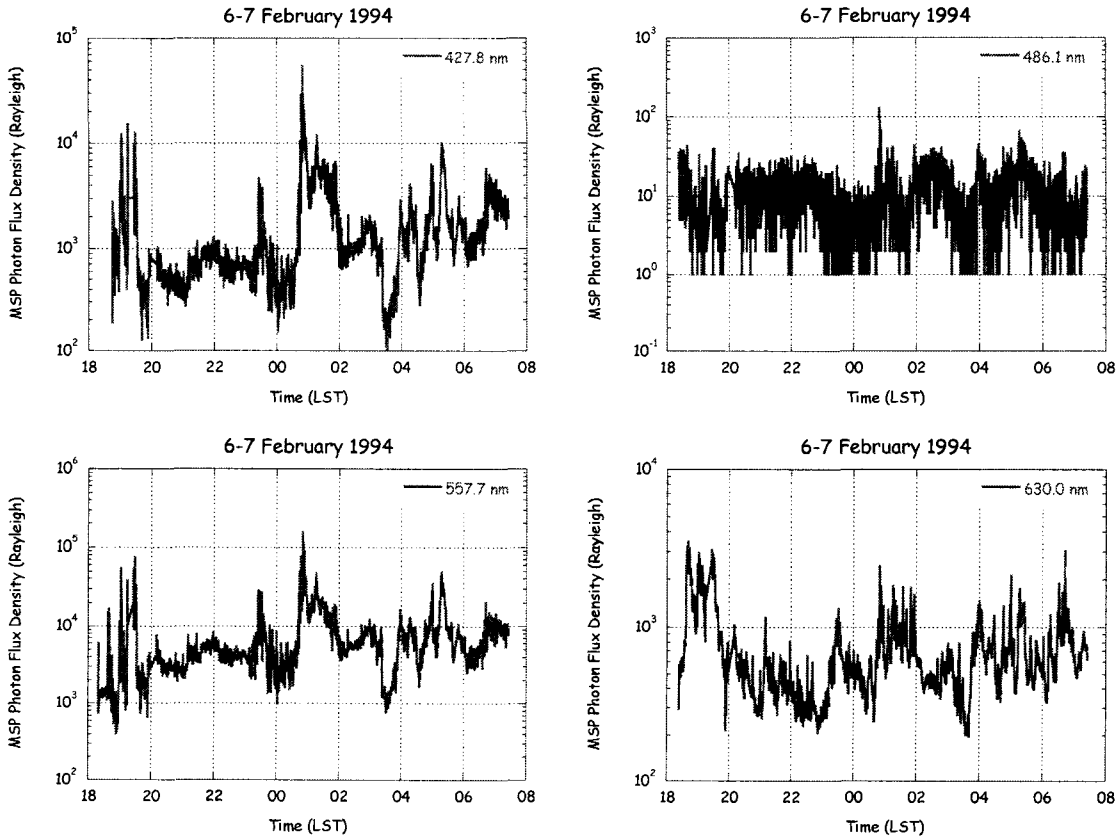

Figure 4.6 MSP measurements of photon flux density from auroral emissions at 427.8 nm (upper left), 486.1 nm (upper right), 557.7 nm (lower left), and 630.0 nm (lower right) on the night of February 6-7, 1994 at PFRR.

4.3 Chemistry Model and Results

4.3.1 Auroral Chemistry Model

The auroral precipitation and resultant modification of the thermosphere are simulated using a model that includes transport of energetic and thermal particles, ionic and neutral chemical reactions, and heating, cooling and thermal conduction [Lummerzheim, 1987; Lummerzheim et al., 1989]. The three main elements of the model consist of an electron transport code, a chemistry and diffusion code, and an energy balance code. The electron transport code solves a linear, one-dimensional Boltzmann equation, which describes the scattering, energy loss, and secondary

Reproduced with permission of the copyright owner. Further reproduction prohibited without permission.

electron production of precipitating energetic electrons. The precipitating electrons are given as a function of energy and pitch angle at an altitude high enough that scattering by neutrals can be neglected above it. For the present calculations, I set this upper boundary at 500 km. Additional sources for electrons result from photoionization in the sunlit part of the thermosphere, and from secondary electrons from proton precipitation. As these electrons penetrate the thermosphere, they ionize the ambient neutrals, heat the ambient plasma, dissociate neutral molecules, and leave ions and neutrals in excited states. The model includes 41 electron impact cross sections for collisions with N_2, O_2, and O. In addition to these reactions, the chemistry necessary to determine the $O(^1D) \rightarrow O(^3P)$ (630.0 nm) emission rate and the processes that control the concentrations of N_2 ($A^3\Sigma^+_u$) are added. Many of the excited states decay spontaneously, giving rise to observable auroral emissions, while others lose their energy through a chain of chemical reactions. To determine the auroral emissions that eventually result from the incident electrons, a time-dependent chemistry model is coupled with the electron transport calculation [Lummerzheim and Lilensten, 1994].

Inputs to the ionospheric auroral model are the neutral concentrations as a function of altitude, the energy spectrum of the precipitating particles, the incident solar EUV flux, and the downward heat flux into the thermosphere. The simulation employs MSP optical observations from PFRR, to determine the auroral conditions. The calculations also require the MSISE-90 neutral concentrations and temperature (see Figure 4.7) for the appropriate day and activity level and the solar EUV flux scaled to the solar $F_{10.7}$ flux for the day. Total energy flux and the characteristic energy of the spectrum are determined from auroral observations. The auroral model with a number of isotropic Maxwellian incident energy spectra, ranging in characteristic energy from 100 eV to 10 keV, determines the brightness of the $O(^1D) \rightarrow O(^3P)$ doublet at 630.0 nm and the $N_2^+ B^2\Sigma_u^+ \rightarrow X^2\Sigma_g^+$ brightness at 427.8 nm. The ratio of these two intensities is a measure for the characteristic energy and the total brightness of the N_2^+ first negative emission is a measure for the total incident energy flux. The model brightness and the model ratio of the observed emission features determine the

Reproduced with permission of the copyright owner. Further reproduction prohibited without permission.

energy flux and characteristic energy of the electron precipitation for this night. Successive MSP observations were averaged together and smoothed with a 5-minute running average before being used in the model. These measured electron characteristics then drive the model. The output from the model includes excitation rates of all excited neutral and ion states for which cross sections are known, electron and ion temperatures, and plasma concentration and composition.

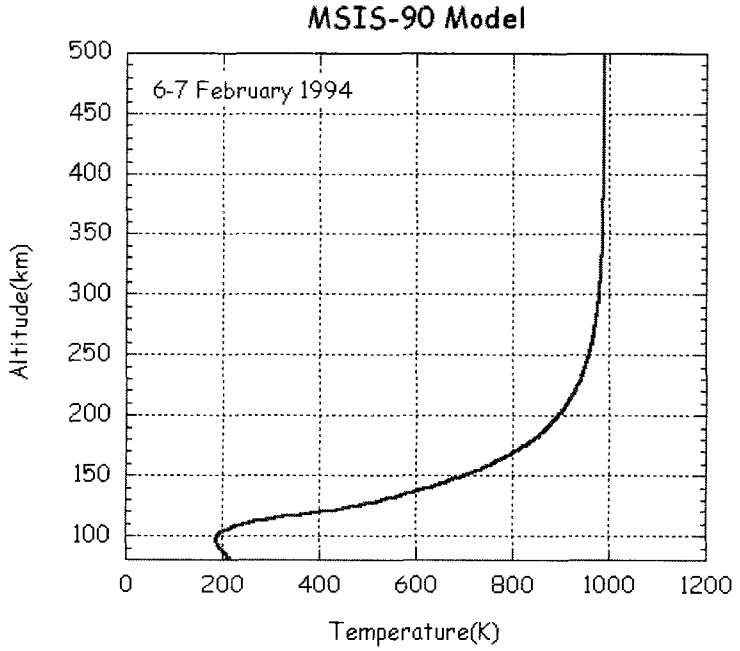

Figure 4.7 Temperature profile from MSISE-90 atmospheric model used in ion-chemistry model. (MSISE-90: http://modelweb.gsfc.nasa.gov/models/msis.html).

The model calculation of N_2^+ density and the ion excitation (or ionization) rate for the observations of the 6-7 February 1994 are plotted in Figures 4.8 and 4.9. The layer of N_2^+ ions is clearly seen with a peak between 100 and 300 km. The maximum peak density is 8.17×10^3 (cm^{-3}) at an altitude of 166 km at 1907 LST. The maximum ionization rate is 3.62×10^5 (cm^{-3}/s) at an altitude of 100 km at 0057 LST. I plot the

Reproduced with permission of the copyright owner. Further reproduction prohibited without permission.

average N_2^+ density profile in Figure 4.10. The population of the lowest vibration level is taken as 0.3 of the total population of N_2^+ ions [Morrill and Benesch, 1996]. This model output has a resolution of 2 km and 300 s.

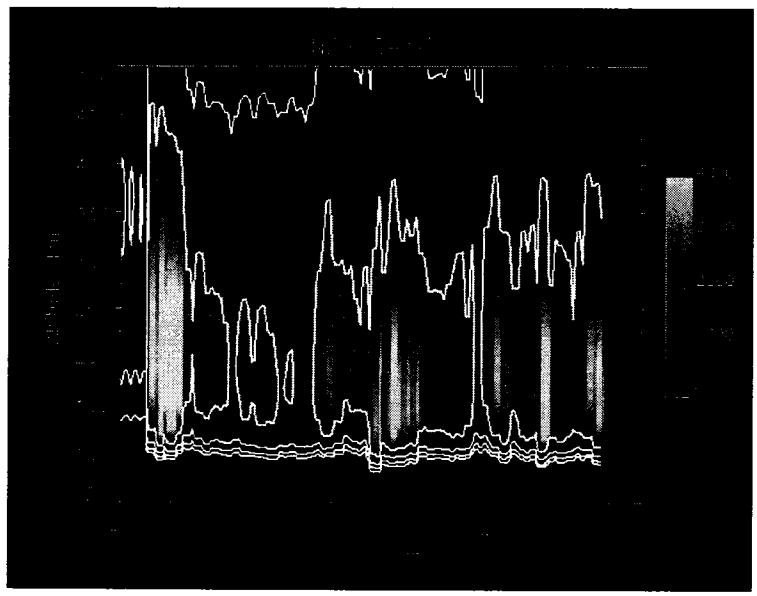

Figure 4.8 False color plot of N_2^+ density as a function of local time and altitude. The density is plotted in (ions/cm^{-3}). The contour levels are 1, 10, 100 and 1000.

Reproduced with permission of the copyright owner. Further reproduction prohibited without permission.

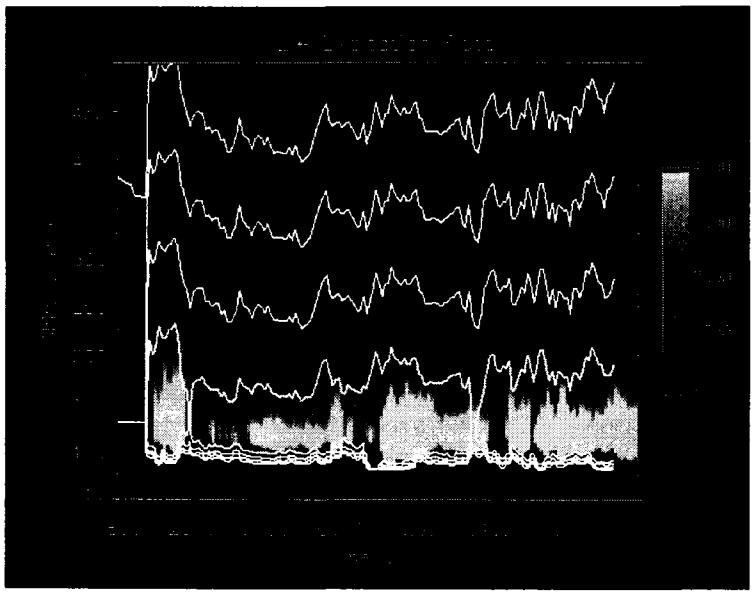

Figure 4.9 False color plot of N_2^+ ionization rate as a function of local time and altitude. The ionization rate is plotted in ((ions/cm-3)/s). The contour levels are 1, 10, 100 and 1000.

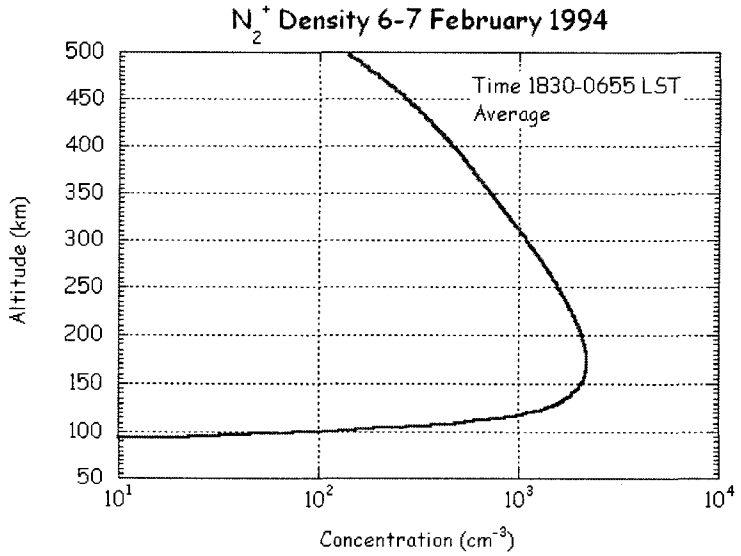

Figure 4.10 Average N_2^+ density profile plotted as a function of altitude.

Reproduced with permission of the copyright owner. Further reproduction prohibited without permission.

4.3.2 Determination of X-B(0-0) Emission from MSP Measurements of X-B(0-1) Emission

To determine the background light signal detected by the lidar system I must first determine the brightness of the aurora at 391.4 nm. The MSP is calibrated with a white light reference and measures the absolute brightness of an optical emission in the band of a bandpass filter. The photon flux density measured by the MSP is a fraction of the flux density from the whole X-B(0-1) band at 427.8 nm. The MSP signal in Rayleighs can be written as,

$$R_a(t) = K_a(t)\int_0^\infty S_a(\nu,t) f_a(\nu) d\nu \tag{4.10}$$

where $K_a(t)$ is the brightness of the emission band, $S_a(\nu,t)$ is the spectrum of the emission, $f_a(\nu)$ is the transmission function of the filter, the subscript a denotes the specific band. I regridded the 427.8 nm MSP signal in time to correspond to the times of the N_2^+ profiles in the ion chemistry model. I plot this regridded signal in Figure 4.11.

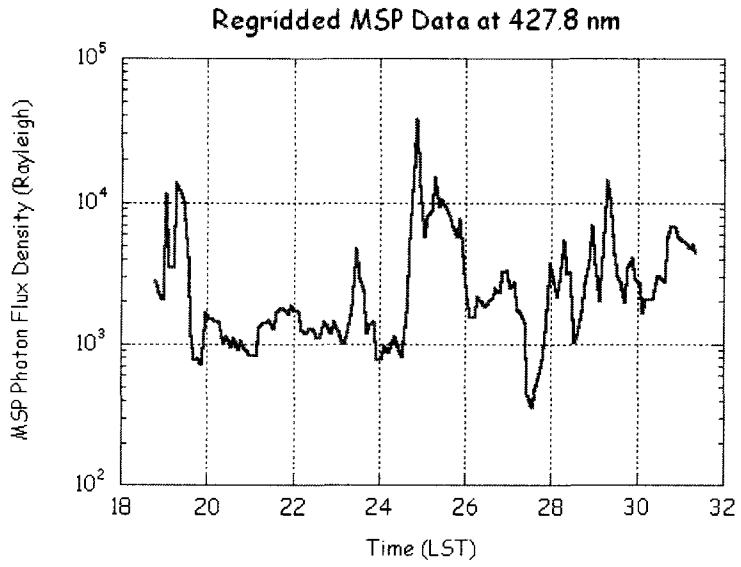

Figure 4.11 Regridded MSP signal at 427.8 nm plotted as a function of time.

Reproduced with permission of the copyright owner. Further reproduction prohibited without permission.

The filter only transmits a fraction of emission from the whole band. This fraction, the band transmission of the filter ($T_f(t)$), is given as,

$$T_f(t) = \frac{\int_0^{\infty} S_a(t,\nu) f_a(\nu) d\upsilon}{\int_0^{\infty} S_a(t,\nu) d\upsilon} \tag{4.11}$$

The spectrum at the ground represents integration of the spectra of the emission at each altitude over the altitude of the emission, as illustrated in Figure 4.12.

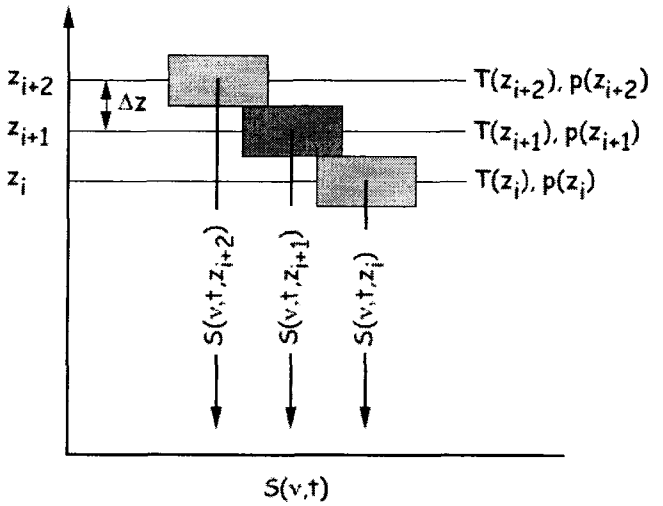

Figure 4.12 Contribution of spectra of emissions at each altitude S(v, t, z) to the total spectrum observed at the ground, S(v, t), with altitudes and time. The temperature and emission probability vary with altitude.

Thus the ground spectrum can be expressed as,

$$S_a(t,\nu) = T_a \int_{z_1}^{z_2} S_a(t,z,\nu) p(t,z) dz \tag{4.12}$$

Reproduced with permission of the copyright owner. Further reproduction prohibited without permission.

where T_a (= 0.75 at 427.8 nm) is the transmission of emission through the atmosphere, S_a is the spectrum of light at altitude z, p is the relative probability of emission from altitude z at time t, and the emission layer extends in altitude from z_1 to z_2. The probability p is defined in terms of the ionization rate, e(t, z), of the auroral electrons,

$$p(t,z) \triangleq \frac{e(t,z)}{\int_{z_1}^{z_2} e(t,z)dz} \tag{4.13}$$

transition (denoted a). I plot the ionization profile (left panel) and the derived probability profile (right panel) at 0050 LST, corresponding to the maximum photon flux density at 0050 LST in Figure 4.13.

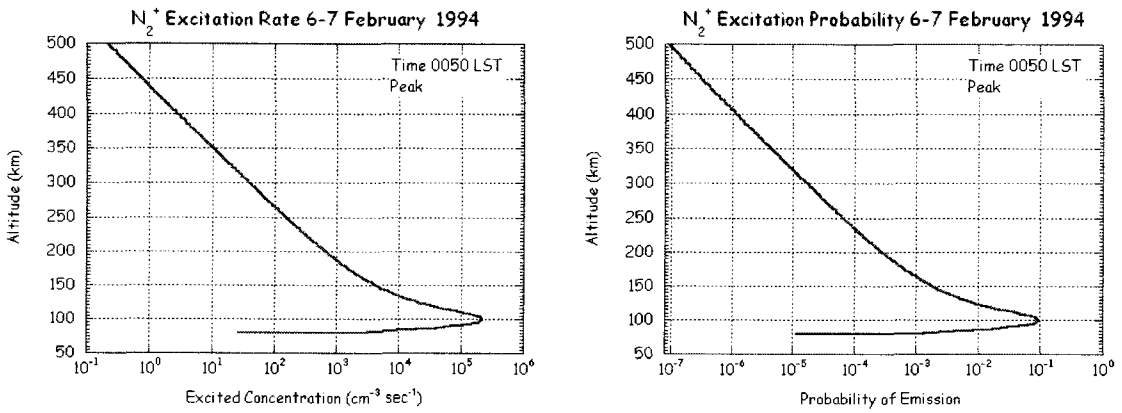

Figure 4.13 N_2^+ ionization rate (left) and emission probability (right) profiles as a function of altitude from ion chemistry model at 0050 LST.

The vibrational-rotational line spectrum at each altitude can be written as,

$$S_a(t,z,\nu) = \sum_{i=1}^{\infty} \alpha_{ai}(z)\delta(\nu - \nu_{ai}) \tag{4.14}$$

where ν_{ai} is the line frequency, and $\alpha_{ai}(z)$ is given by,

Reproduced with permission of the copyright owner. Further reproduction prohibited without permission.

$$\alpha_{ai}(z) = H_i \times \frac{hc}{kT(z)} B_a (2J_i + 1) e^{-\frac{hc}{kT(z)} B_a J_i (J_i + 1))} \quad (4.15)$$

the product of the Honl-London factor for the specific vibrational-rotational line, Hi, and the relative population of the upper state of the transition, where J_i is the rotational quantum number of the upper level, B_a is the rotational constant for the vibrational level a, and T(z) is the temperature at altitude z. The temperature T(z) is taken from MSISE-90 and is constant in time. The difference in the spectra at different temperatures is clearly observed in Figure 4.14, where I plot the spectra as a function of wavelength at 80 km at a temperature of 217.9 K (left panel) and at 498 km at a temperature of 990.2 K (right panel). Clearly the spectrum varies with temperature due to the temperature variation in altitude. Thus the spectrum also varies in time due to the variation in the altitude of the emission as altitude of the ionization varies with the auroral activity.

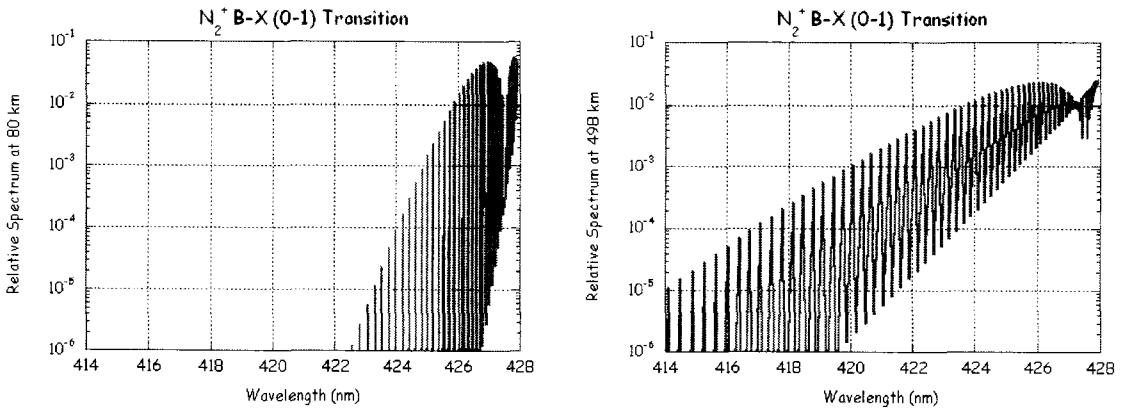

Figure 4.14 Relative spectrum, S_{ai}, for N_2^+ 0-1 transition at 217.9 K (left) and 990.2 K (right).

In Figure 4.15 I plot the time variation of the band transmission of the MSP bandpass filter that had Gaussian lineshape with a center wavelength of 427.8 nm and

Reproduced with permission of the copyright owner. Further reproduction prohibited without permission.

a FWHM bandwidth of 0.7 nm.

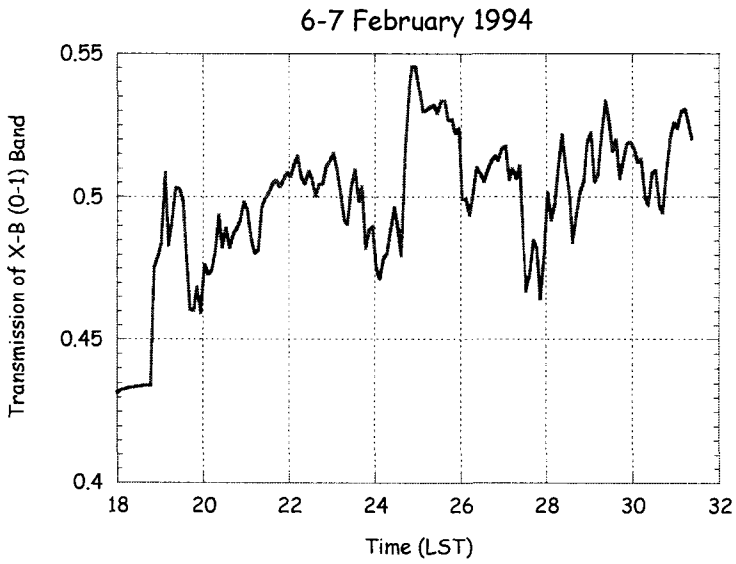

Figure 4.15 Transmission of X-B (0-1)band at 427.8 nm by MSP bandpass filter.

Thus, using the characteristics of the MSP bandpass filter, the transmission of the atmosphere, the temperature profile, and the ionization rates, I can determine the value of K_a, the true brightness of the whole emission (0-1) band at 427.8 nm, from the MSP measurement. Finally I can calculate the value of K_b, the true brightness of the whole emission (0-0) band at 391.4 nm,

$$K_b = K_a \frac{A_b}{A_a} \tag{4.16}$$

where A_a is the Einstein A coefficient for the (0-1) transition (3.71x106 s-1) and A_b is the Einstein A coefficient for the (0-0) transition (1.14x107 s-1).

Given K_b I can now use the methodology above to determine the spectrum of the emission in the (0-0) vibrational-rotational band at 391.4 nm. I use the transmission of

Reproduced with permission of the copyright owner. Further reproduction prohibited without permission.

the atmosphere at 391.4 nm (= 0.67) and the spectroscopic constants for the (0-0) transition. I plot the photon flux density at the ground for the whole (0-0) transition at 391.4 nm in Figure 4.16. I will use this photon flux density to determine the background signal in the lidar measurements in the next section.

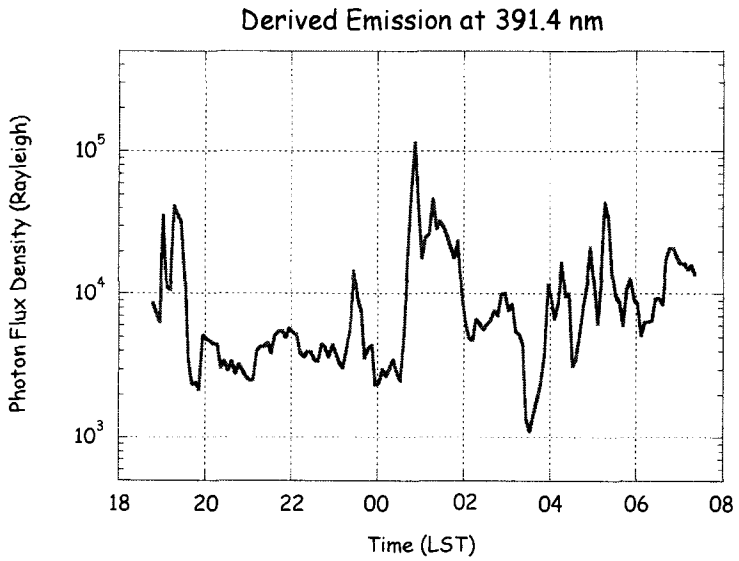

Figure 4.16 Derived emission for entire (0-0) transition at 391.4 nm.

4.4 Lidar Simulation

I can now determine the expected lidar signal for measurements made on a night where the auroral conditions are the same as those of the night of 6-7 February 1994 at PFRR. I use the N_2^+ data from the ion chemistry model and the MSISE-90 temperature profile to determine the resonance scatter signal. I use the MSISE-90 atmospheric density to determine the Rayleigh scatter. I use the emission derived from the MSP measurements to determine the background signal. I assume the dark signal in the detector is negligible. I present the characteristics of the N_2^+ X-B lidar in Table 4.2. I choose the operating wavelength of the lidar to match the J = 9 → J = 10 transition as the J = 9 state is the most populated rotational state at 500 K.

Reproduced with permission of the copyright owner. Further reproduction prohibited without permission.

The output of the ion-chemistry model was provided at a resolution of 2 km and 300 s. The MSP data is provided at a resolution of 15 s. The MSISE-90 data is provided at a resolution of 2 km. In the simulation I use interpolation and integration to first determine the lidar signals at a resolution of 100 s and 1 km. I then integrate the signals in altitude and/or time to multiples of that fundamental 100 s and 1 km resolution.

Table 4.2 N_2^+ X-B lidar system parameters

Parameter	Symbol	Value
System Efficiency	η	0.05
One-way Atmospheric Transmittance	T	0.67
Laser Energy Per Pulse	E_L	50 mJ
Laser Pulse Repetition Rate	R_L	20 pps
Laser Wavelength	λ	390.303 nm
Laser Linewidth	$\Delta\lambda$	1.0 pm
Lower Rotational State	J_l	9
Upper Rotational State	J_u	10
Honl-London Factor	H	0.48
Telescope Diameter	$(A_R/\pi)^{1/2}$	1.04 m
Field-of-View	$\Delta\theta_R$	0.5 mrad
Filter Bandwidth	BW	0.3 nm
Measurement Temporal Resolution	Δt	300 s
Measurement Altitude Resolution	Δz	6000 m

4.4.1 Lidar Equation for Molecular Species

The expected N_2^+ resonance lidar signal can be determined by the resonance lidar equation as,

Reproduced with permission of the copyright owner. Further reproduction prohibited without permission.

$$N_S(z) = \left[\eta T^2\right] \cdot \left[\frac{E_L R_L \Delta t}{hc/\lambda_L}\right] \cdot \left[\rho_{N^{2+}}(z)(C_{eff}(v,T)\gamma)\Delta z\right] \cdot \left[\frac{A_R}{4\pi z^2}\right] \quad (4.17)$$

This equation is identical to the lidar equation presented in Chapter 2 (Equation 2.2), except that I have highlighted the density of N_2^+ (ρ_{N2^+} (z)) and have included the branching ratio γ. The factor γ is the product of the vibrational branching ratio (= 0.71) and the rotational branching ratio (= 0.48) and has a value of 0.34. The vibrational branching ratio is determined from the Einstein A coefficients of the transitions from the upper vibrational level to the first 10 lower vibrational levels in the X-B band [Gilmore et al., 1992]. The effective scattering cross section includes the degeneracies of the rotational states (i.e., $g_u = (2J_u+1)$, and $g_l = (2J_l+1)$). The effective cross-section varies with temperature due to the temperature variation of the Doppler width of the absorption cross-section (Equation 2.23). From the temperature profile in Figure 4.7 the temperature varies from 187.7 K to 990.2 K. The value of the effective absorption cross section is plotted in Figure 4.17. The absorption cross section varies from 1.88 $x10^{-17}$ m^2 to 2.95 $x10^{-17}$ m^2. At 200 K, 500 K and 1000 K, the effective absorption cross section equals 2.92 $x10^{-17}$ m^2, 2.36 $x10^{-17}$ m^2, and 1.87 $x10^{-17}$ m^2, respectively. I use Equations 2.5 and 2.6 to calculate the Rayleigh signal.

4.4.2 Calculation of Background Signal

I calculate the background signal from the derived emission at 391.4 nm (Figure 4.16). I first determine the photon flux density transmitted through the bandpass filter of the lidar receiver. The filter has a Gaussian lineshape with a center wavelength of 390.303 nm and a FWHM bandwidth of 0.3 nm. I plot the (0-0) X-B band transmission for this filter in Figure 4.18. I plot the filtered photon flux density, $R_b(t)$, in Figure 4.19. I then use the lidar system parameters to convert the photon flux density in Rayleighs to the expected background lidar signal in photon counts as follows,

$$N_B(t) = R_b(t) \cdot L(t) \quad (4.18)$$

$$L(t) = 10^6 \eta \frac{1}{4\pi}\left(\pi\left(\frac{\Delta\theta_R}{2}\right)^2\right)\left(R_L \Delta t \frac{2\Delta z}{c}\right) A_R \quad (4.19)$$

Reproduced with permission of the copyright owner. Further reproduction prohibited without permission.

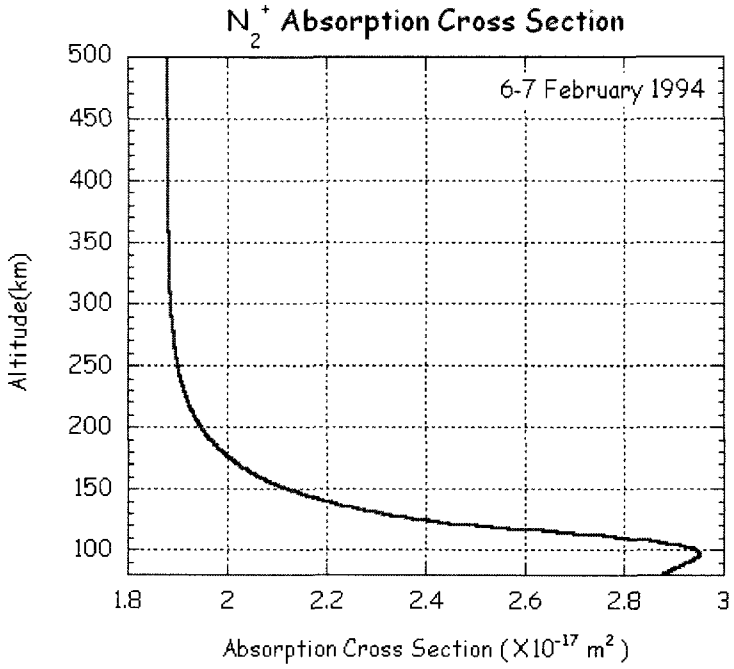

Figure 4.17 N_2^+ absorption cross section.

I plot the calculated background signal as a function of time in Figure 4.20. The background signal varies between 144 photon counts and 11,498 photon counts with an average value of 1329 photon counts.

Reproduced with permission of the copyright owner. Further reproduction prohibited without permission.

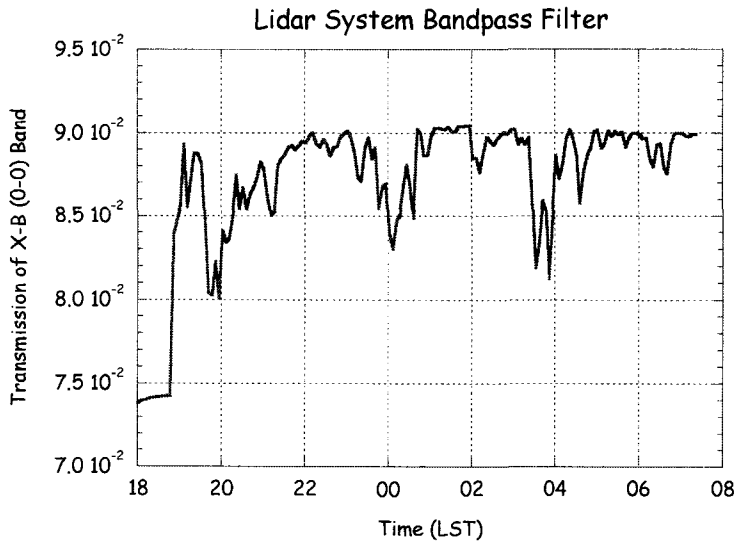

Figure 4.18. Transmission of (0-0) band emission through lidar receiver bandpass filter as a function of time.

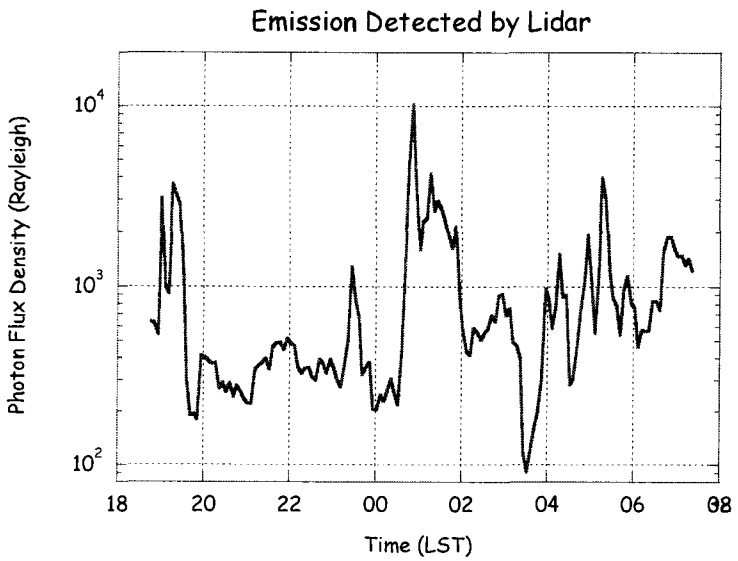

Figure 4.19. Photon flux density of (0-0) band emission at lidar detector as a function of time.

Reproduced with permission of the copyright owner. Further reproduction prohibited without permission.

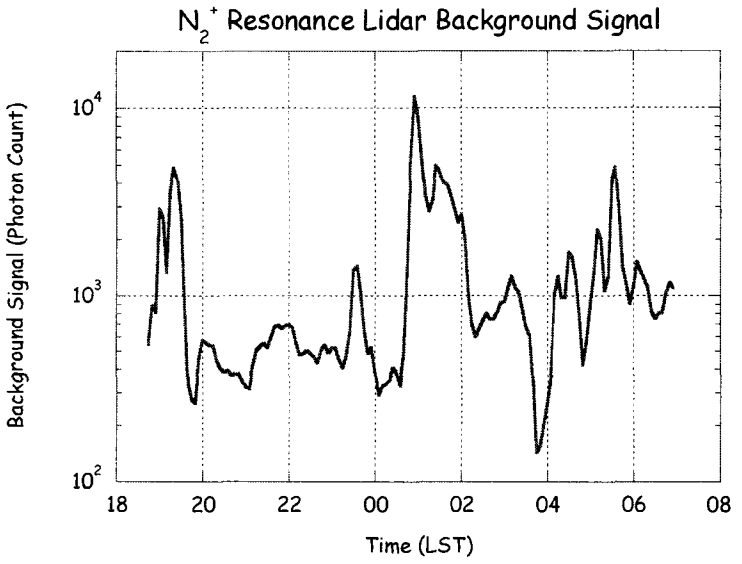

Figure 4.20. Lidar background signal as a function of time.

4.5 Results of Simulation

I plot the total lidar signal (i.e. the sum of the Resonance, Rayleigh and background signals, N_{TOT}) in Figure 4.21 as a function of altitude and time. The variation in the signal is dominated by the variation in the background signal (that appears as vertical stripes in the false color plot) and the Rayleigh signal that dominates the total signal at altitudes below 80 km (that appears as the horizontal band at the bottom of the false color plot). I plot the integrated lidar signal integrated over the whole observation period of 12 h and 10 min and SNR in Figure 4.22. The peak signal from the N_2^+ layer has a value of 207,023 photon counts with a background signal of 195,395 and an associated SNR of 26. The associated confidence level is 100%. The SNR of the integrated signal is greater than 10 from 108 to 186 km. The integrated lidar signal is 95% significant (SNR > 1.64) up to 306 km, is 99% significant (SNR > 2.34) up to 282 km, and is 99.9% significant (SNR > 3.10) up to 264 km.

Reproduced with permission of the copyright owner. Further reproduction prohibited without permission.

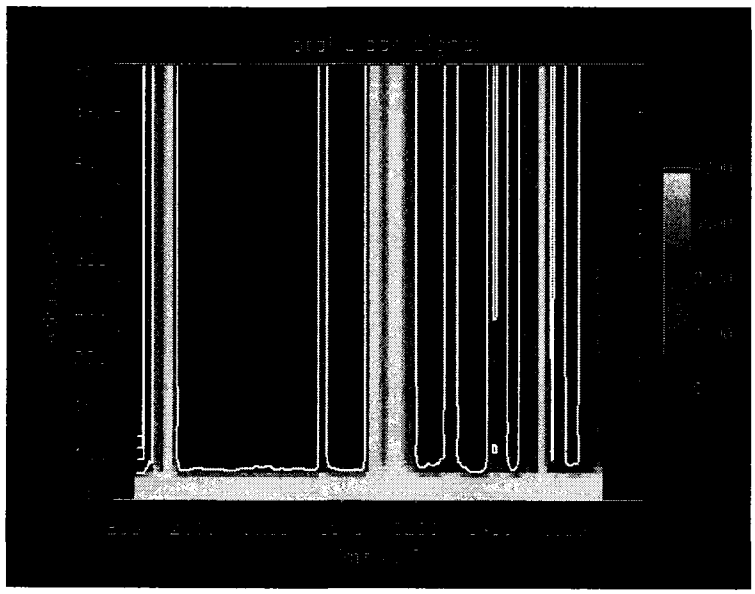

Figure 4.21 False color plot of N_2^+ total lidar signal (N_{TOT}) as a function of time and altitude. The signals are plotted in units of photon counts. The contour levels are 1, 10, 100, and 1000.

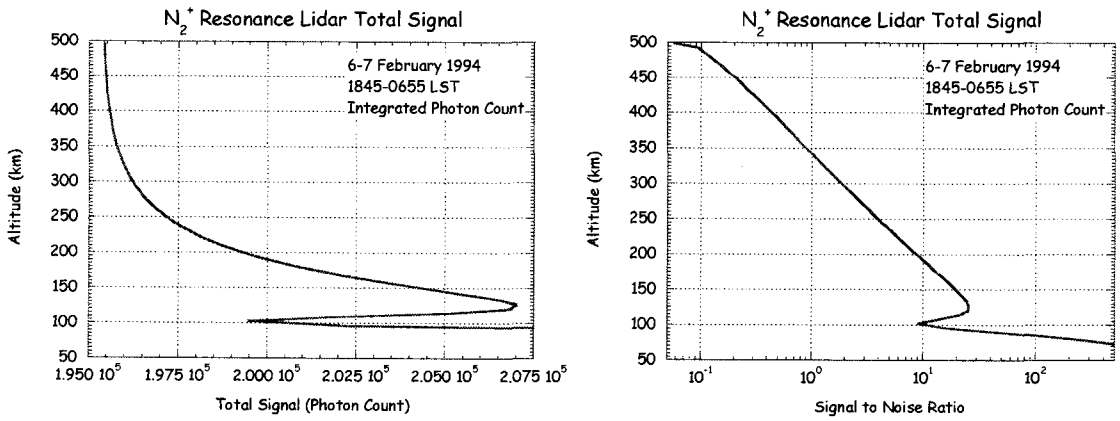

Figure 4.22 N_2^+ total lidar signal integrated over the observation period (left) and corresponding SNR (right) plotted as a function of altitude.

Reproduced with permission of the copyright owner. Further reproduction prohibited without permission.

I plot the sum of the resonance and Rayleigh component (i.e., N_S) of the lidar signal in Figure 4.23. The variation of the resonance scatter signal is much clearer in this figure than in the plot of the total lidar signal. The signal is dominated by Rayleigh scattering below 100 km and by resonance scattering above 100 km. The variation of the resonance scatter signal in Figure 4.23 follows the variation of the N_2^+ density (Figure 4.9). The maximum resonance signal levels detected at ~ 1900, 0100, 0500 and 0700 LST correspond to maximum N_2^+ densities. On average, resonance signals of greater than 100 photon counts are detected below 175 km, resonance signals of greater than 10 photon counts are detected below 250 km, and resonance signals of greater than 10 photon counts are detected below 425 km The N_2^+ resonance signal from has a maximum value of 355 photon counts at an altitude of 114 km at 0055 LST. I plot the associated SNR in Figure 4.24. The SNR associated with the Rayleigh scatter signals below 100 km are larger than 1 and rapidly increase with decreasing altitude. The SNR associated with the resonance scatter signals above 100 km are less than 5.4.

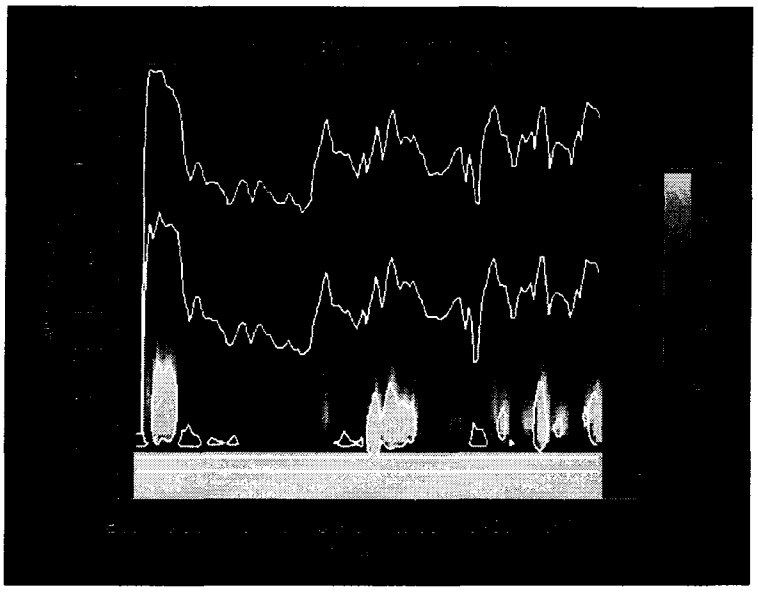

Figure 4.23 False color plot of sum of resonance and Rayleigh lidar signal (N_S) as a function of time and altitude. The signals are plotted in units of photon counts. The contour levels are 1, 10 and 100.

Reproduced with permission of the copyright owner. Further reproduction prohibited without permission.

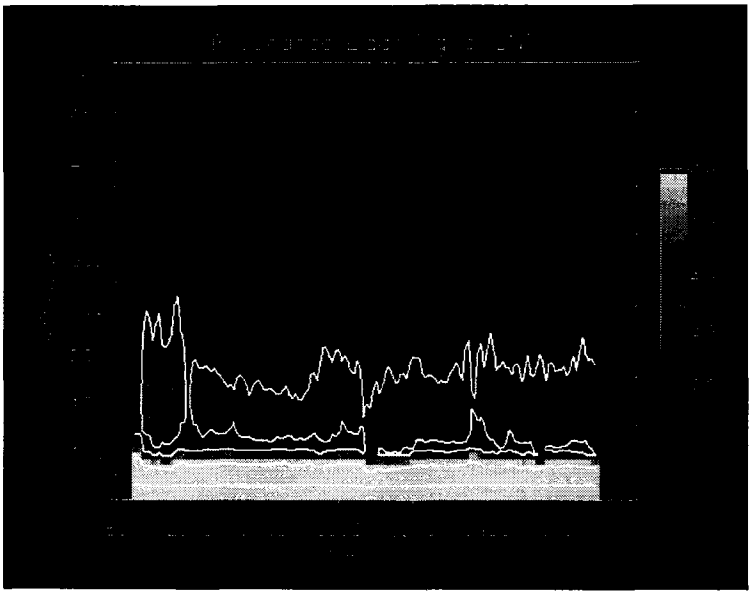

Figure 4.24 False color plot of N_2^+ total lidar signal as a function of time and altitude. The signals are plotted in units of photon counts. The contour levels are 1, 10 and 100.

To examine the variation of SNR during the observation, I determine the maximum SNR above 100 km for each lidar signal profile. The maximum SNR of 5.4 occurs at an altitude of 126 km at 1905 LST while the minimum SNR of 0.87 at an altitude of 162 km at 1955 LST. The fact that the maximum and minimum SNR are found within 1 h of each other during a 12 h observation highlights the inherent variability in these lidar measurements of the aurorally modified thermosphere. The SNR associated with the maximum resonance lidar signal measured at 114 km at 0055 LST is 3.7. I tabulate the lidar signals, SNR, and confidence levels in Table 4.3 and I plot the lidar signal profiles and corresponding SNRs in Figure 4.25.

Reproduced with permission of the copyright owner. Further reproduction prohibited without permission.

Table 4.3 N_2^+ X-B resonance lidar performance

LST (hour)	1905	1955	0055
Altitude(km)	126	162	114
N_{TOT} (Photon Count)	2884	470	9250
N_S (Photon Count)	292	19	355
N_B (Photon Count)	2593	451	8895
SNR	5.4	0.87	3.7
Confidence Level (%)	100.0	80.8	100.0

Resolution of lidar measurement is 6 km and 300 s
Probabilities taken from tables in Abramowitz and Stegun [1972]

Clearly the lidar is capable of making statistically significant measurements of the auroral N_2^+ at a resolution of 6 km and 300 s. The resolution of the measurements can be reduced to yield measurements with higher confidence. The aurora varies dramatically in time, the altitude resolution of the measurement could be reduced while the temporal resolution is increased to allow the measurements to capture the temporal variations. In reality the lidar observations would be conducted at high resolution (e.g., 100 s, 1 km) and then integrated to a lower resolution during their analysis.

In this chapter I have assumed that the lidar is perfectly tuned to the resonance wavelength of the N_2^+ absorption line. I will discuss the control of the laser tuning in the next chapter.

Reproduced with permission of the copyright owner. Further reproduction prohibited without permission.

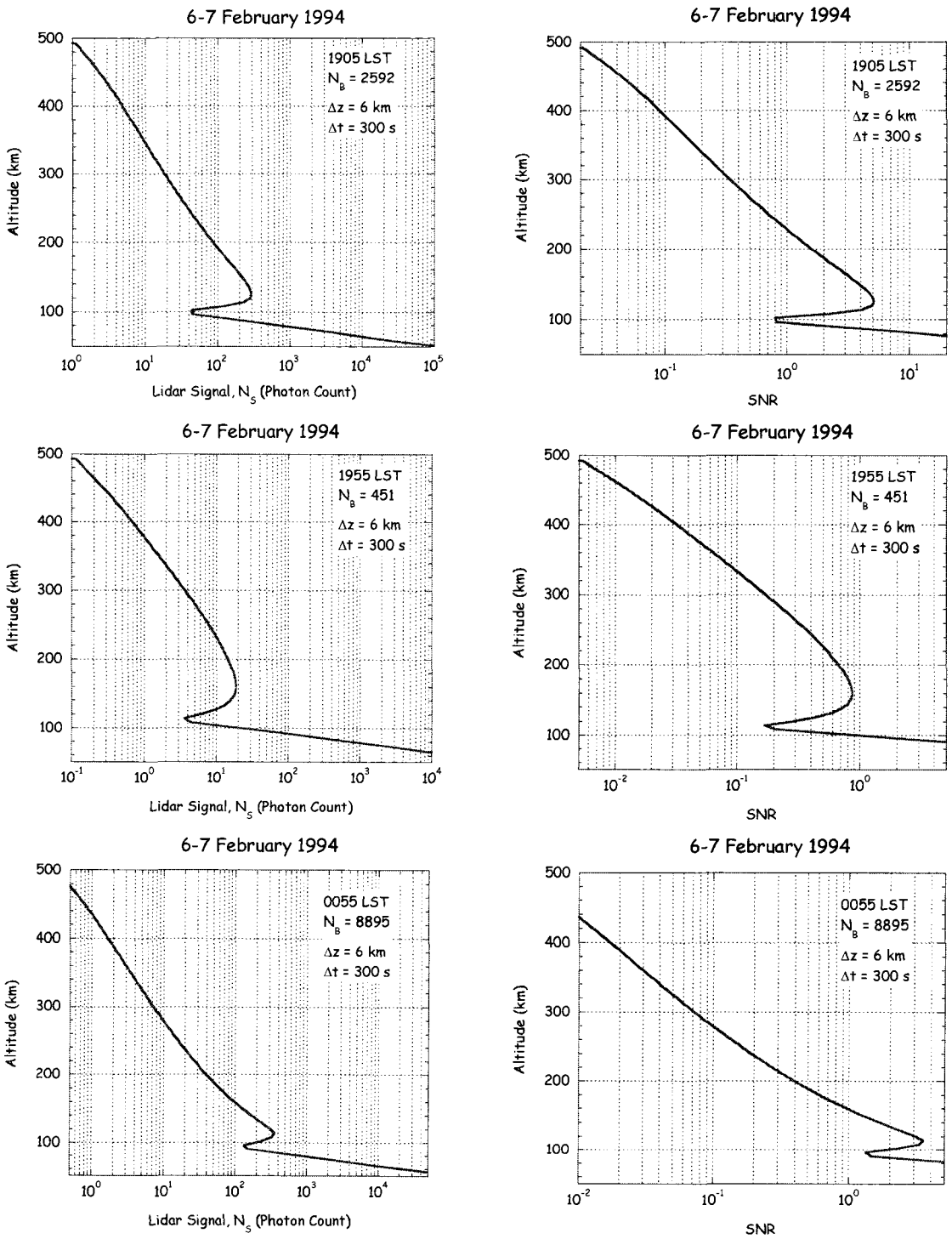

Figure 4.25. Lidar signal (left) and associated SNR (right) plotted as a function of altitude at 1905 LST (upper), 1955 LST (middle), and 0055 LST (lower).

Reproduced with permission of the copyright owner. Further reproduction prohibited without permission.

5 Design and Implementation of Tuning Control System for a N_2^+ Resonance Lidar System

In Chapter 2, I discussed the spectral sensitivity of the lidar signal in the lidar equation (Equations 2.11 and 2.15). When I tune the laser so that the laser frequency equals the resonance frequency (i.e., on-resonance) the effective cross section and the expected signal have their maximum values. When I tune the laser so that the difference between the laser frequency and resonance frequency is non-zero (i.e., off-resonance), the effective cross section decreases and the expected signal decreases. The relative uncertainty in the lidar signal increases as the magnitude of the signal decreases. Furthermore, if the laser frequency is not tuned to the resonance frequency, the determination of the species concentration is an underestimate of the true value. Thus the laser tuning determines the accuracy and precision of the resonance lidar measurements. In this chapter I discuss dye laser wavelength tuning and the design of a system to monitor and control the frequency of the laser. I begin by reviewing lidar performance data that shows the magnitude of the variability in the laser tuning. I then review the use of atomic and molecular references. Finally I present the principles, design and implementation of a tuning system based on a Fabry-Perot Interferometer (FPI).

5.1 Variation of Laser Tuning

For resonance lidar systems the frequency of the transmitted laser light needs to be tuned to the resonance frequency of the target atom or molecule. The Scanmate® dye laser employs a Littrow grating mount as the major tuning part. The operating wavelength of the laser is varied by adjusting the pitch angle of the grating. The input wavelength is input by the laser operator to the laser control computer, which then uses a stepping motor to set the pitch of the diffraction grating. The relative resolution is 0.14 pm at 589 nm and 0.089 pm at 372 nm and 390 nm [Hou, 2002; Peshave, 2004]. However, a given laser wavelength does not always correspond to a given frequency. As the temperature and pressure inside the laser room varies the refractive index varies, and hence the frequency varies for a given wavelength.

Reproduced with permission of the copyright owner. Further reproduction prohibited without permission.

Consequently, when the laser computer tunes the dye laser to the same wavelength value, the corresponding frequency varies with ambient temperature and pressure. Peshave [2004] showed that frequency variations of 10 pm could occur due to changes in temperature of 10 °C or changes of pressure of 60 hPa. Thus for each lidar observation the laser must be tuned over several pm to find the operating laser wavelength that precisely corresponds to the resonance frequency of the target species.

In Figure 5.1 I plot the operating laser wavelength used in 43 nights of iron resonance lidar measurements from 15 December 2000 to 12 December 2003. For each observation the operator recorded the operating wavelength that corresponded to the resonance frequency (i.e., the wavelength where the echo from the iron layer was a maximum). The operating laser wavelengths range from 371.992 nm to 372.024 nm, with an average value of 372.010 nm and a sample standard deviation of 8 pm. The vacuum wavelength of the (a^5D J=4 → z^5F_0 J=5) transition has a value of 372.099 nm (λ_{VAC}) corresponding to 371.994 nm (λ_{STP}) at standard temperature (15 °C) and pressure (101,325 Pa). The horizontal dashed line is plotted at the value of the STP wavelength. The average operating wavelength has a positive bias of 16 pm relative to the STP wavelength.

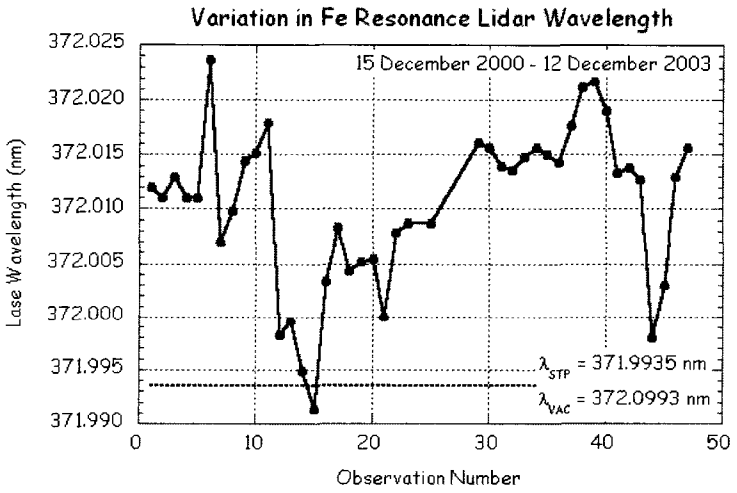

Figure 5.1 Variation of resonance lidar wavelength over time.

Reproduced with permission of the copyright owner. Further reproduction prohibited without permission.

During sodium lidar measurement I use a sodium hollow cathode lamp as an absolute wavelength reference. As I discussed in Chapter 2, sodium has a simple spectrum (2 major lines D_1 and D_2) and strong spectral line intensity. The sodium spectral lines information is listed in Table 5.1 [NIST, 2007]. The discharge current through the sodium hollow cathode lamp is a maximum when the lamp is irradiated with light at the resonance frequency. At the resonance frequency the sodium atoms in the lamp are excited and more easily ionized, thus increasing the discharge current through the lamp (see discussion by Peshave, [2004]). I use a commercial hollow cathode lamp as a bench-top spectral reference for sodium lidar measurements at PFRR.

Table 5.1 Sodium sensitive lines

Element	Air Wavelength (nm)	Relative Intensity
Na I	588.995	80000
Na I	589.952	40000

Iron lidar systems operating at 372 nm require more sophisticated references as the spectroscopy of iron is complicated than that of sodium due to the more complicated nature of the iron atom (see discussion by Hou, [2002]). Researchers have reported over 700 allowed transitions with associated spectral lines in the iron atom [Fuhr et al., 1988] compared to 86 in the sodium atom [Wiese et al., 1969]. The strongest iron spectral lines are in the UV at 248 nm (a^5D J=4 → x^5F_0 J=5) with Frank-Condon factors that are over 10 times larger than those at 372 nm. I have tested two commercial iron hollow cathode lamps (Photron Pty, Ltd, Australia) as tuning references for iron lidar measurements but were not successful in obtaining a useful current response in the lamps.

During sodium and iron lidar observations, the operator can tune the laser to the resonance frequency by making sequential measurements at different wavelengths.

Reproduced with permission of the copyright owner. Further reproduction prohibited without permission.

While the laser does not have absolute tuning accuracy, the relative tuning is accurate and reproducible. This allows us to scan the resonance lines in a given observation period. The wavelength that yields the maximum echo from the mesospheric layer corresponds to the resonance frequency. This method is successful because the sodium and iron column abundances remain relatively constant over the time taken to tune the laser. I use this tuning method for iron lidar measurements at PFRR. However, this method is not well-suited for observations of auroral molecular nitrogen, where the column abundance varies significantly over the time taken to tune the laser, and thus a maximum in the echo may represent an increase in the amount of molecular nitrogen overhead rather than a maximum in the effective scattering cross section. For this reason I wish to develop a bench-top spectral reference for tuning the laser.

5.2 Spectral References at 390 nm

Absorption lines in molecular iodine and tellurium are commonly used spectroscopic reference in the visible and infra-red at wavelengths longer than 400 nm. Extensive atlases of these molecular spectra have been published (e.g., Gerstenkorn, 1978; Cariou and Luc, 1980). Researchers have cataloged atomic spectral lines in the neighborhood of the lidar transmitting wavelength at 390.303 nm. Sensitive lines from 387.418 nm to 393.367 nm are listed in Table 5.2 [Phelps, 1982]. The elements are listed in standard form, where I denotes the unionized atom, and II denotes the singly ionized atom. These line intensities are obtained from arc, spark, or discharge emission experiments. The R in the intensity column means wide-reversal and the W means very wide band. In this wavelength region most of the emission lines have weak intensities (compare the values to the 80,000 value for sodium). The low intensity lines are difficult to detect in discharges due to the noise induced by the electro-optical circuitry or attenuation induced by quenching mechanisms (e.g., collisions) in buffer gas. All lines are atomic spectral lines.

The element with the closest wavelength to the air wavelength of 390.192 nm (390.303 nm in vacuum) is molybdenum. The intensity of this molybdenum line is large compared to other lines in this spectral region. The spectrum of molybdenum is plotted in Figure 5.2, and the corresponding atomic spectrum and listed spectral lines in Table 5.3 [NIST, 2007]. The line at 390.296 nm is the second strongest line in the

Reproduced with permission of the copyright owner. Further reproduction prohibited without permission.

atomic spectrum of molybdenum. The relative intensity of the line at 390.296 nm is over an order of magnitude larger than the neighboring lines.

Table 5.2 Spectral lines in 390 nm region

Wavelength (nm)	Element	Arc	Intensity Spark Discharge
393.367	Ca II	600 R	600 R
391.181	Sc I	150	30
390.748	Sc I	125	25
390.632	Er	25	12
390.553	Si I	20	15 W
390.296	Mo I	1000 R	500 R
389.179	Ba II	18	25
389.102	Ho	200	40
388.865	He I	-	[1000]
387.418	Tb	200	200

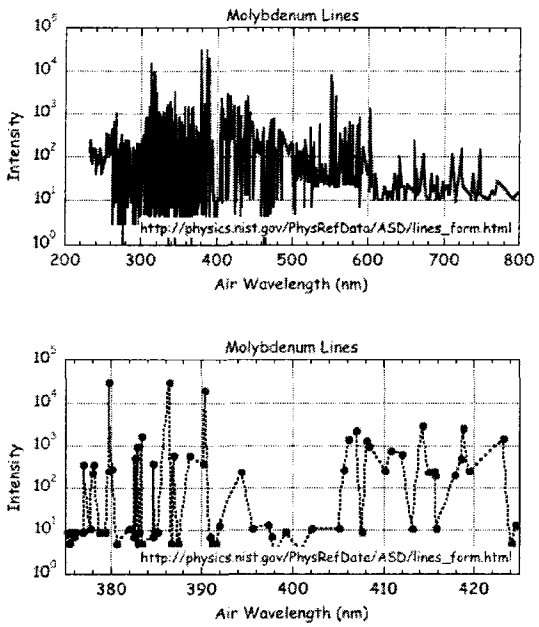

Figure 5.2 Spectral lines of molybdenum as a function of air wavelength.

Reproduced with permission of the copyright owner. Further reproduction prohibited without permission.

Table 5.3 Molybdenum (Mo I) spectral lines

Observed Wavelength Air (nm)	Relative Intensity
379.825	290000
386.411	290000
386.908	580
388.682	580
390.177	380
390.296	19000
394.304	230

There are several other elements with spectral lines close to 390.303 nm. Thorium is one of them. I list the thorium atomic spectral lines in Table 5.4 [NIST, 2007]. The closest line to 390.192 nm is 390.166 nm. The intensity of this line is relatively low (50). The thorium ion (Th II) also has a line with a comparable intensity (170) at 390.519 nm. The low intensity of the thorium lines makes the design of an operating detection system quite difficult.

Table 5.4 Thorium spectral lines

Element	Air Wavelength (nm)	Relative Intensity
Th I	389.542	340
Th I	390.166	50
Th I	390.310	110
Th I	390.875	50
Th I	391.191	85
Th I	391.642	50
Th I	391.902	110
Th II	390.519	170

Reproduced with permission of the copyright owner. Further reproduction prohibited without permission.

Uranium has several spectral lines in the neighborhood of 390.303 nm. Uranium has many lines in the UV region. I list the uranium spectral lines in Table 5.5 [NIST, 2007]. The closest line to 390.303 nm is 390.255 nm and the relative intensity is 410. However, this line is found in ionized uranium (Ur II). Neutral uranium (Ur I) has a line at 390.645 nm with relative intensity of 380. Unfortunately, both lines are of similar intensity to adjacent lines.

Table 5.5 Uranium spectral lines

Element	Air Wavelength (nm)	Relative Intensity
U II	389.677	490
U II	389.978	620
U II	390.255	410
U II	390.430	460
U I	390.645	380
U II	391.167	330
U II	391.588	380

Ionized tellurium (Te II) also has spectral lines in the 390.303 nm region. I list these spectral lines of tellurium in Table 5.6 [NIST, 2007]. There are only two lines between 389.5 nm to 391.5 nm. The closest line to 390.192 nm is 390.567 nm and the relative intensity is 20. However, it is a line from the ionized tellurium atomic spectrum with fairly low intensity.

Table 5.6 Tellurium sensitive lines

Element	Air Wavelength (nm)	Relative Intensity
Te II	390.567	20
Te II	391.854	20

Reproduced with permission of the copyright owner. Further reproduction prohibited without permission.

I tested two commercial molybdenum hollow cathode lamps (Photron Pty, Ltd, Australia) at PFRR. I operated these lamps with a variety of bias currents. However, due to the low voltage signal induced, no significant response was found at 390.296 nm. The failure to obtain a useful response could have been due to the quenching mechanism or a too low an ionization rate within the plasma. Rather than attempt to build a custom hollow cathode lamp based on a particular species, I decided to use an interferometer as a spectral reference. In principle this approach would allow us more flexibility to conduct lidar studies at a variety of wavelengths rather than one fixed wavelength.

5.3 The Fabry-Perot Interferometer

The basic theory of the interferometer was first presented by the English astronomer George Airy [Born and Wolf, 1993]. The first Fabry-Perot Interferometer (FPI) was implemented by Charles Fabry and Alfred Perot in the late 19th century [Hernandez, 1988]. I show a typical configuration of an FPI on the left in Figure 5.3. I show the fringe pattern for a He-Ne laser at 632 nm on the right in Figure 5.3. The fringe pattern (i.e., the pattern of concentric circles) corresponds to the Airy pattern for transmission through the FPI. The FPI that I use consists of two planes with parallel, highly reflecting surfaces. The plates are constructed as a slight wedge to prevent interference reflected from the non-parallel surface

The transfer equation for an FPI can be determined by considering the wave reflection and transmission function [Hecht and Zajac, 1973]. Given an incident wave $E_0 e^{i\omega t}$ traveling into one of the planes with amplitude E_0, let t^+ be the transmission coefficient of a positive incident beam, t^- is the transmission coefficient of negative going incident beam; r^+ is the reflection coefficient of a positive incident beam, r^- is the reflection coefficient of negative incident beam, and R and T be the surface intensity reflection and transmission coefficients, for a single surface [Vaughan, 1989],

$$r^+ = -r^-; T = t^+ t^-; R = t^{+2} = t^{-2}; R + T = 1 \tag{5.1}$$

If the refractive index of air inside of Fabry-Perot interferometer cavity is μ; the spacing of plates is d; the incident angle is θ, and the wavelength of the incident

Reproduced with permission of the copyright owner. Further reproduction prohibited without permission.

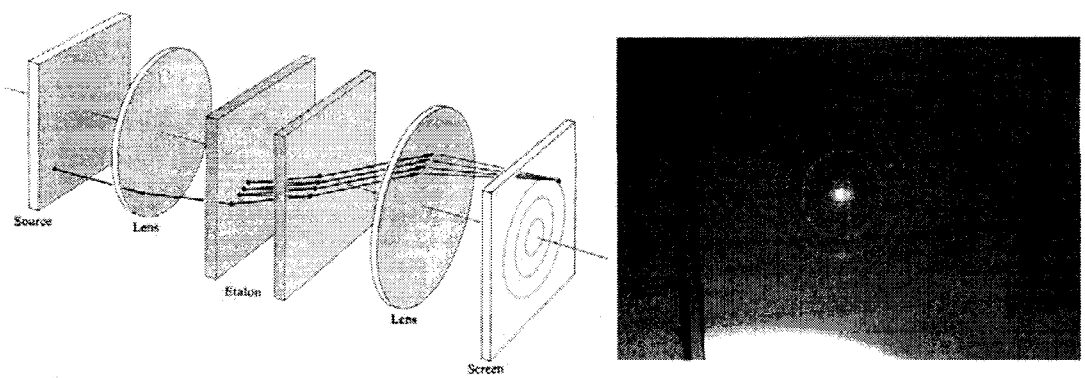

Figure 5.3 Left: Schematic diagram of FPI [Hecht and Zajac, 1974]. Right: Photograph of fringe pattern for Helium-Neon (He-Ne) laser. The pressure in the FPI chamber is 43 psi.

beam is λ_0, then the optical path difference between two adjacent rays equals,

$$\Lambda = 2\mu d\cos\theta \tag{5.2}$$

and the phase lag φ of successive reflection due to the round trip in the cavity is,

$$\varphi = 2\pi\cdot(2\mu d\cos\theta)/\lambda_0 \tag{5.3}$$

Except for the first reflection, both sets of beams have the same transmission factor $r_1^- r_2^+ e^{i\varphi}$. The reflected scalar wave and the transmitted scalar wave are,

$$E_r = E_0 e^{i\omega t}\left[r^+ + \frac{r^- t^+ t^- e^{-i\varphi}}{1-r^{-2}e^{-i\varphi}}\right] \tag{5.4}$$

$$E_t = E_0 e^{i\omega t}\left[\frac{t^+ t^-}{1-r^{+2}e^{-i\varphi}}\right] \tag{5.5}$$

The irradiance function is given as $I = EE^*/2$, the reflected irradiance and the transmitted irradiance are,

$$I_r = I_i\cdot\frac{\left(2r^+/(1-r^{+2})\right)^2\sin^2(\varphi/2)}{1+\left(2r^+/(1-r^{+2})\right)^2\sin^2(\varphi/2)} \tag{5.6}$$

Reproduced with permission of the copyright owner. Further reproduction prohibited without permission.

$$I_t = I_i \cdot \frac{1}{1+\left(2r^{+}/(1-r^{+2})\right)^2 \sin^2(\varphi/2)} \tag{5.7}$$

Consequently, the maximum and minimum values of irradiance of the reflected and transmitted beams are,

$$I_{r\min} = 0; I_{r\max} = I_i \cdot \frac{4r^{+2}}{(1+r^{+2})^2} \tag{5.8}$$

$$I_{t\min} = I_i \cdot \frac{(1-r^{+2})^2}{(1+r^{+2})^2}; I_{r\max} = I_i \tag{5.9}$$

To simplify Equation 5.8 and 5.9, define the coefficient of finesse, F, as,

$$F = \frac{4r^{+2}}{(1+r^{+2})^2} \tag{5.10}$$

Thus I can derive an expression for the ratio of the transmitted intensity and the reflected intensity to the incident intensity as,

$$\frac{I_r}{I_i} = \frac{F\sin^2(\varphi/2)}{1+F\sin^2(\varphi/2)} \tag{5.11}$$

$$\frac{I_t}{I_i} = \frac{1}{1+F\sin^2(\varphi/2)} = A(\varphi/2) \tag{5.12}$$

The function A is called the Airy function. When $\varphi/2 = m\pi$, the value of the Airy function is 1 and all incident light is transmitted. The m value is the order number of a particular fringe. The transmission is a maximum at each integer value of m. The coating on the plane surface can introduce an additional phase shift, Φ, the phase lag is,

$$\varphi = 2\pi \cdot (2\mu d\cos\theta)/\lambda_0 + 2\phi \tag{5.13}$$

For cases where $d >> \lambda_0$, the phase lag may be ignored. If the medium of interferometer absorbs a fraction A of incident flux density, the relation between R, T, and A is,

$$R+T+A=1 \tag{5.14}$$

Reproduced with permission of the copyright owner. Further reproduction prohibited without permission.

Under these conditions the transmission function equals,

$$\frac{I_t}{I_i} = \left(1 - \frac{A}{1-R}\right)^2 \cdot A(\varphi/2) \tag{5.15}$$

and the peak value, when $\varphi/2 = m\pi$, becomes,

$$\frac{(I_t)_{\max}}{I_i} = \left(1 - \frac{A}{1-R}\right)^2 \tag{5.16}$$

which is less than the value of 1 associated with the lossless FPI. I can control the transmission by varying parameters in the phase lag. For instance I can adjust the spacing of the parallel plates, d, using a piezoelectric transducer (PZT). By changing the plate spacing, while leaving the refractive index fixed, the wavelength corresponding to a given fringe-order changes and so I can use the FPI as a wavelength selective transmission device (i.e., a tunable filter). I can also adjust the air refractive index, μ. The refractive index is a function of pressure and temperature; by placing an FPI in a sealed chamber with windows, I can change the refractive index inside interferometer pressure chamber, while leaving the plate spacing fixed, and the wavelength corresponding to a given fringe-order changes. Thus, I can again use the FPI as a tunable filter. The chamber has gas inlets and outlets with valves, and a temperature sensor. Thus the operator can control the pressure by injecting or releasing air into and out of the vessel. The FPI has a nominal spacing, d (0.5 mm) and a reflectance R (0.9). The transmission function is a function of five independent variables: plate spacing, d, angle of incidence, θ, wavelength, λ_0, temperature, T, and pressure p. The spectral variation is also determined in terms of frequency. For default values of 0.5 mm, 0°, 589.153 nm, 21.2 psi, and 22 °C I can determine the characteristics of the FPI transmission as a function of each of the variables alone. I tabulate these results in Table 5.7, where I present the peak, the full-width at half maximum (FWHM), the full-width at 0.9 of maximum (FW0.9M), and the free spectral range (FSR) (i.e., distance between adjacent peaks or fringes) as a function of the variables; wavelength of incident light, frequency of incident light, angle of incidence, temperature of air between plates, pressure of air between plates, and distance between plates (i.e., plate spacing).

Reproduced with permission of the copyright owner. Further reproduction prohibited without permission.

Table 5.7 FPI transmission characteristics

	Peak	FWHM	FW0.9M	FSR
Wavelength	589.15 nm	11.64 pm	4.09 pm	347 pm
Frequency	509 THz	10 GHz	4 GHz	300 GHz
Angle	0.0 °	0.55 °	0.34 °	1.95 °
Temperature	22.0 °C	15.2 °C	5.0 °C	N/A
Pressure	21.2 psi	1.07 psi	0.348 psi	31.95 psi
Plate Spacing	0.5 mm	1.76 μm	0.586 μm	2.939 μm

In this study I study the performance of the FPI as I vary two of the six parameters; the wavelength of the incident light and the pressure of the gas inside the FPI chamber. I connect the FPI chamber to a high-pressure cylinder of air. I use two valves (one inlet and one outlet valves) to control the pressure in the chamber. Both valves are DC voltage controlled. The inlet valve model is MA0248A-00010RV with resolution of 10 standard cubic centimeters per minute (sccm). The outlet valve model is MA0248A-01000RV with resolution of 1000 sccm. I can alternately open and close the control inlet and outlet valves to adjust the pressure in the chamber from 14 psi (ambient atmospheric pressure) to 80 psi (maximum safe pressure for supply lines from air cylinder). A pressure sensor and a temperature sensor monitor the air condition inside the interferometer. The interfacing circuits were designed by the staff of the electronic shop at the Geophysical Institute, University of Alaska Fairbanks.

5.4 Interferometer-based Tuning System

The system configuration is illustrated in Figure 5.4. The system has six major components;

1. The Scanmate® dye laser system
2. The fixed plate Fabry-Perot interferometer, pressure chamber, and control unit
3. The laser pulse detection board
4. The Closed-Loop Tuning Controller
5. The laser PC
6. The User (or Master) or PC with NI-DAQ ® PCI 6251 (National Instruments, Austin, Texas, USA)

Reproduced with permission of the copyright owner. Further reproduction prohibited without permission.

The Scanmate® laser generates laser pulse in the UV and visible with a pulse duration of ~10 nm. A beam-splitter intercepts 5% of the laser beam energy and sends it via a multi-mode optical fiber to the FPI system and the closed-loop tuning controller (CLTC). The CLTC was designed by Peshave [Peshave, 2004] to support sodium lidar measurements using a hollow cathode lamp. The CLTC detects the current pulse induced by the laser in the hollow cathode lamp, and records the peak of the pulse. The CLTC is capable of controlling the laser as an autonomous micro-controller based system. In this controller I have incorporated the CLTC circuitry to allow detection of the change in amplitude of the hollow cathode lamp current in response to changes in the laser and comparison of the spectral response of the hollow cathode lamp with that of the FPI. The temperature of FPI chamber is monitored (typically ~20 °C) while the pressure is both monitored and controlled by sending air into and releasing air from the chamber. The chamber is connected to a gas cylinder that provides air through a regulator at pressures up to 100 psi. The minimum pressure in the chamber is the ambient atmospheric pressure (~14 psi). I collimate the light from the optical fiber with a x4 beam expander before transmitting it through the FPI. I use a focusing lens to focus the light from the FPI on the active area of the photodiode. For reasons of operational safety, space, and environmental control, I house the laser and laser PC together, in a separate laboratory from the FPI controller. I house the user PC in the lidar control room with the lidar data acquisition systems. I use an RS232 3-wire serial communication cable to connect the laser PC and user PC; I use a flat cable to connect between the laser pulse detection board and the user PC; I use a BNC cable to connect the CLTC electronics to the user computer, and I use a multimode fiber to deliver light from the dye laser to the Fabry-Perot interferometer. In the following sections I discuss the various components and sub-components of the system. Figure 5.5 shows photos of this wavelength tuning system during operating.

Reproduced with permission of the copyright owner. Further reproduction prohibited without permission.

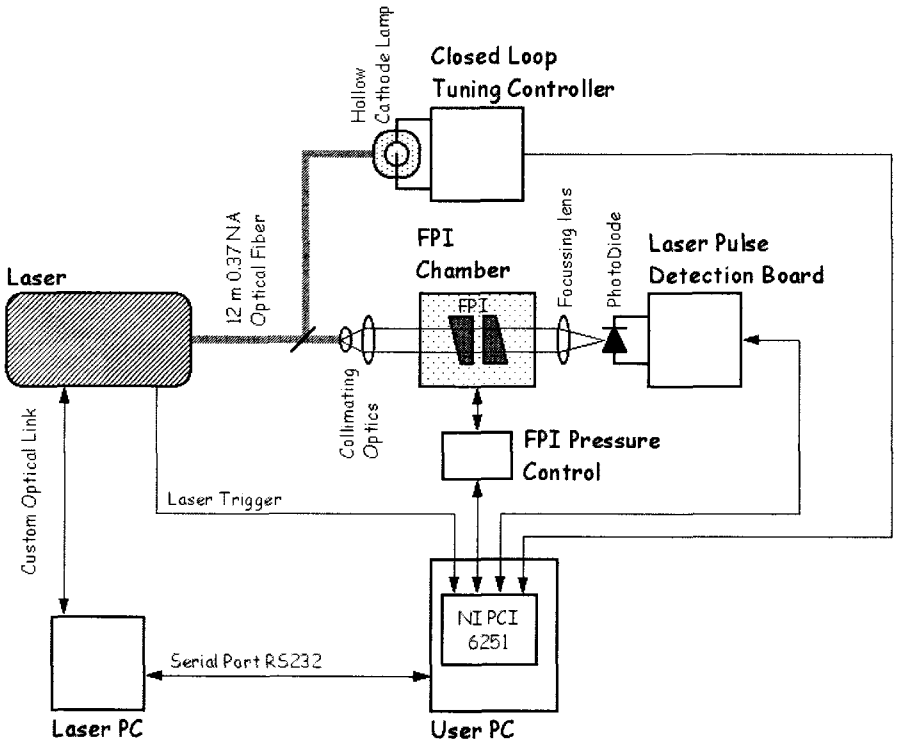

Figure 5.4 FPI wavelength tuning system.

Reproduced with permission of the copyright owner. Further reproduction prohibited without permission.

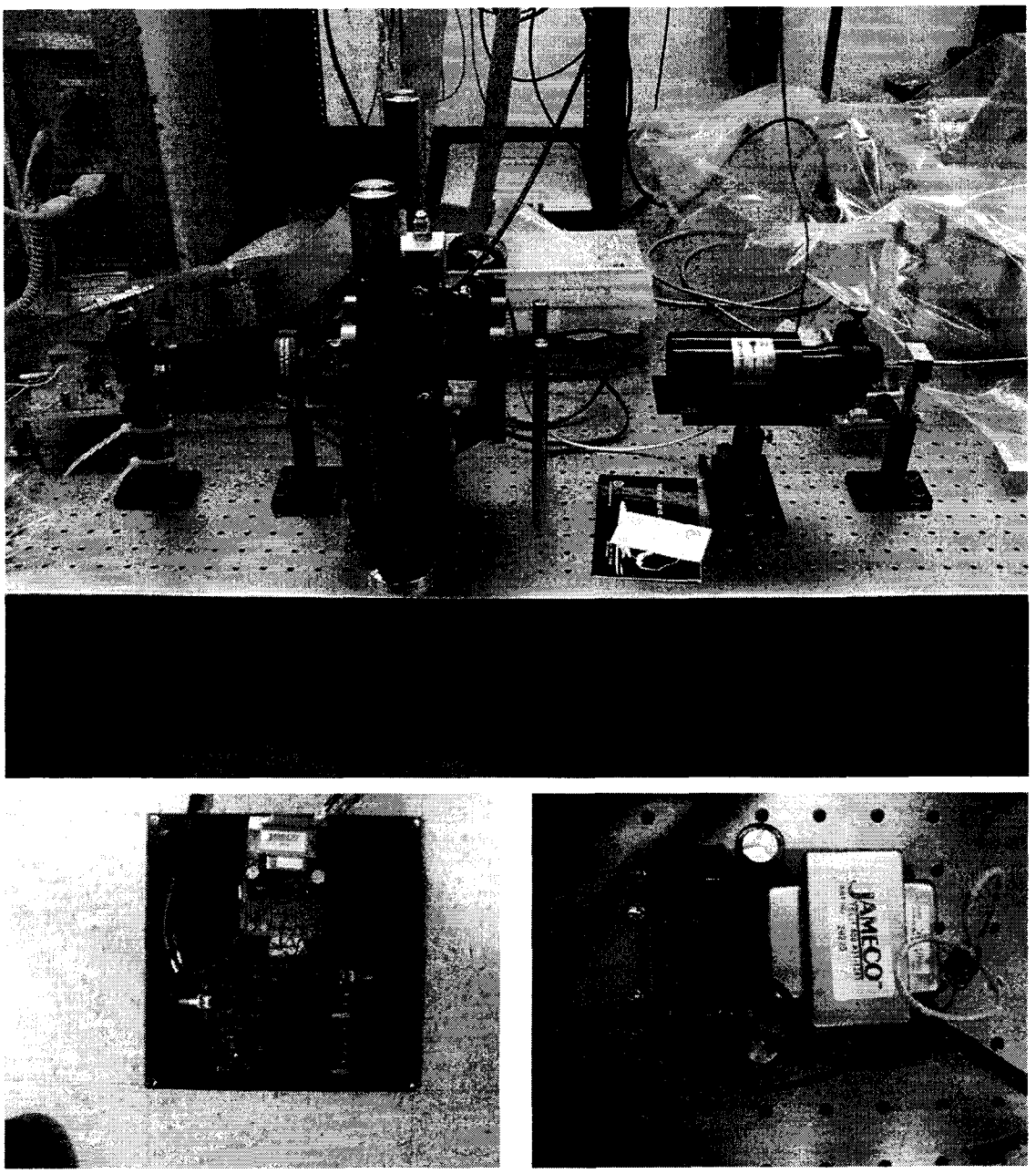

Figure 5.5 FPI wavelength tuning system in operation (upper) FPI channel and circuit board; (lower left) HCL channel; (lower right) peak detector power supply.

Reproduced with permission of the copyright owner. Further reproduction prohibited without permission.

5.4.1 Software

I developed the user software package in Visual BASIC 6.0 ®. I chose Visual BASIC because (like Borland C++), the programming package includes rapid application development (RAD) that greatly shortens the development period. I display the software flowchart in Figure 5.6. The software performs a variety of functions;

a. I can monitor or tune the dye laser over a range of wavelengths (i.e., wavelength scan) and record the wavelength information;
b. I can record the signal from the photodiode detector;
c. I can record the signal from the hollow cathode lamp;
d. I can monitor or change the pressure in the FPI chamber over a range of pressures (i.e., pressure scan) and record the pressure and temperature.

With these functions, I can conduct the following experiments;

a. I can tune the laser while recording the hollow cathode lamp optogalvanic signal as a function of laser wavelength;
b. I can tune the laser while maintaining the FPI at fixed pressure and record the signal transmitted through the FPI as a function of laser wavelength;
c. I can scan the FPI in pressure while maintaining the dye laser at a fixed wavelength and record the signal transmitted through the FPI as a function of pressure.

I can choose the experimental parameters by entering them in the software configuration dialog. I can acquire and record all the experimental parameters and measurements can be acquired and displayed in real time. Some of the information is analyzed and plotted by this software to provide real-time feedback to the operator.

Reproduced with permission of the copyright owner. Further reproduction prohibited without permission.

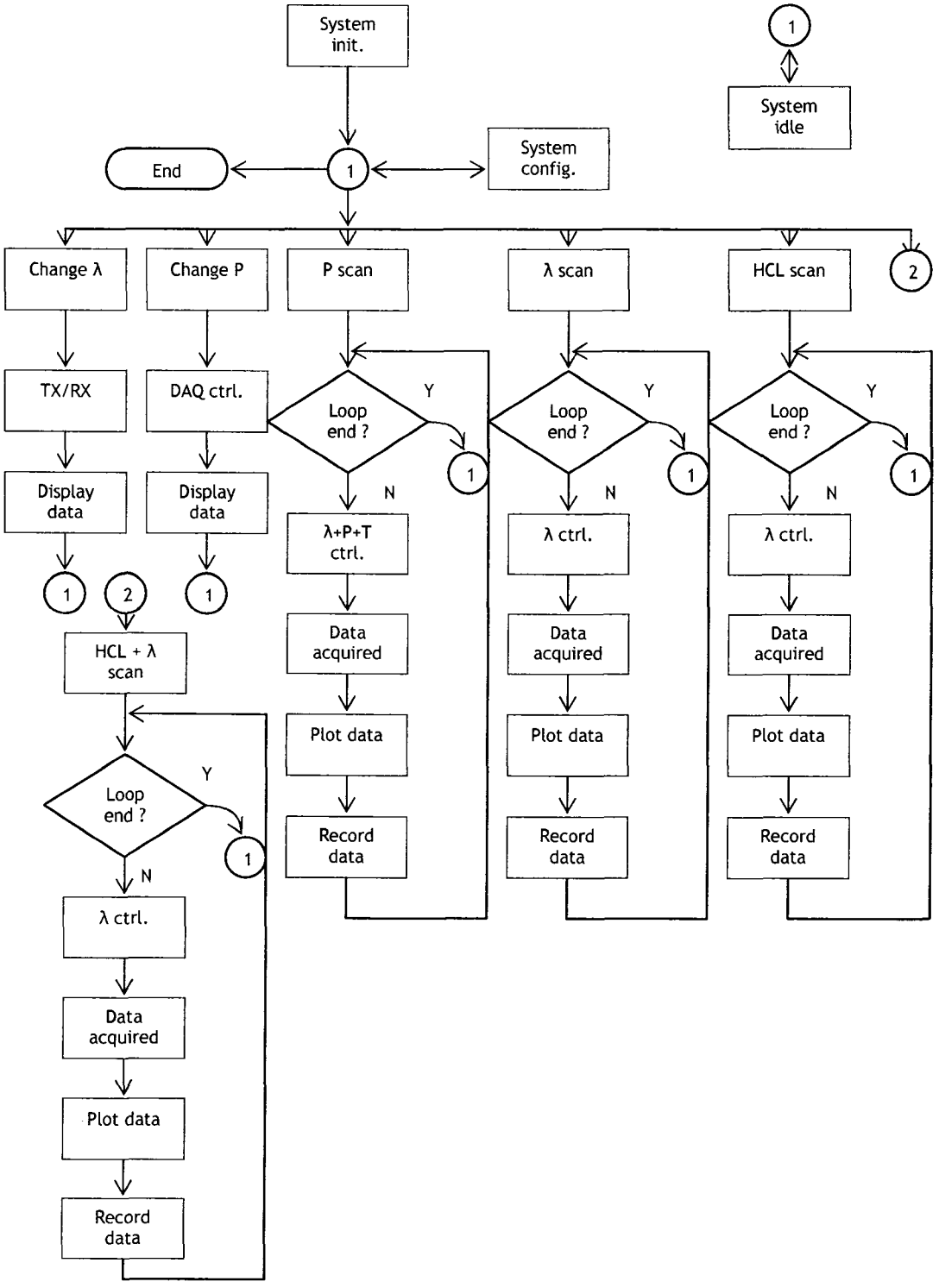

Figure 5.6 FPI tuning system software flow diagram.

Reproduced with permission of the copyright owner. Further reproduction prohibited without permission.

5.4.2 Laser Control

The laser computer and user computer communicate through RS232 serial ports. I can tune the operating wavelength of the laser by changing the pitch angle of the diffraction grating in the laser. A stepping motor sets the pitch angle of the grating. The laser PC communicates with the laser via a custom software package and a dedicated optical communication link. I can run the custom laser software package in remote mode, and send commands from user computer to the laser computer, to drive the stepping motor to the desired setting, and thus tune the laser. The remote wavelength control supports two working modes: macro mode and basic mode [Lambda Physik, 1997; Hou, 2002]. In the macro mode I can tune the wavelength of the laser at 1 pm resolution and in the basic mode I can step the motor by one step. In basic mode, the wavelength, λ, can is determined by,

$$\lambda(nm) = (s \times 7.184353 \times 10^{-4} + 2265.883)/m \tag{5.17}$$

where s denotes the integer motor step number and m denotes the grating order number. I can determine the wavelength resolution for a given grating order as the wavelength change, Δλ associated with a change in step, Δs,

$$\Delta\lambda = \Delta s \cdot \frac{7.184353 \times 10^{-4}}{m} \tag{5.18}$$

At UV wavelengths the grating order is 8, and thus for a change in step of 1, I have a corresponding wavelength change of 0.090 pm. At visible wavelengths the grating order is 7 and thus for a change in step of 1, I have a corresponding wavelength change of 0.103 pm.

5.4.3 Fiber Optic Cable

I use a fiber optic cable to transmit the laser pulse from the dye laser to the FPI. I need to use a fiber that can transmit light at both visible and UV wavelengths, and so the fiber must be able to work over a wide spectrum. While the laser spot is small, I need a fiber with a large diameter to reduce the coupling loss. Based on these requirements, I choose a Thorlabs 0.37NA polymer clad multimode fiber. The core of fiber is pure silica. The numerical aperture of the fiber is 0.37. The fiber has a Tefzel

Reproduced with permission of the copyright owner. Further reproduction prohibited without permission.

coating and is designed to operate over a wide temperature range from -40 °C to +150 °C. The fiber has a wide working spectral range and is designed to operate over the 300-1200 nm range. The diameter of the round window of interferometer is 1.5 inches, and to let the laser light sent into the Fabry-Perot interferometer be uniformly distributed, a beam expander is used between the end of fiber and the interferometer.

5.4.4 Data Acquisition Card

The data acquisition card is the essential part of the wavelength tuning system. I use a data acquisition card instead of microcontroller, as I can more conveniently integrate the card into the Visual BASIC environment of the user PC. If I used a microcontroller I would have to develop and implement RS232 or RS485 serial protocols to communicate with the user PC. This process could be lengthy. The data acquisition card is also designed to integrate different kinds of instruments and signals. There are many commercial products available, but I identified several key features before selecting the card. The first feature is the sampling rate of the signals. While I have no strict requirements for sampling, I set a ~1 MHz sampling rate as good enough. The second feature is the number of signal channels. I require four analog input channels, two analog output channels, one digital input channel, and analog and digital ground channels. I tabulate these channels and their uses in Table 5.8. The resolution of the analog channel will determine the accuracy of the digitized signal. A high resolution card can offer superior performance on precision detection. The compatibility with computer is another issue. In earlier years, the Windows 98® platform was opened to the developer. Low level I/O ports could be accessed directly from the program. In recent years, the Windows platform enclosed most of the low level I/O ports. A user must use professional development tools like Windows Driver Module (WDM) to access those ports. The data acquisition card can be controlled by a driver file called by other development languages (e.g., LabVIEW ®).

Reproduced with permission of the copyright owner. Further reproduction prohibited without permission.

Table 5.8 DAQ channels

Channel Type	Description	Instrument
Analog Input	Pressure sensing	Interferometer
Analog Input	Temperature sensing	Interferometer
Analog Input	DC sensing	Photodiode
Analog Input	DC sensing	Hollow cathode lamp
Digital Input	Triggering	Excimer laser
Analog Output	Pressure control	Inlet valve
Analog Output	Pressure control	Outlet valve
Analog Ground	Grounding	Analog signal
Digital Ground	Grounding	Digital signal

I choose a NI DAQ PCI 6251 card from National Instruments as the data acquisition card. This NI PCI 6251 card is designed for multifunction, high speed data acquisition applications. It has two 16 bit analog outputs with sampling rate of 1.25 M/s, ranging from -10 V to +10 V; 24 digital I/O channels; analog and digital triggering input channels. The driver is provided by the National Instruments. User can call the DAQmx® dynamic link library to operate each channel. This card can be programmed through LabVIEW®, Visual BASIC, or VISUAL C++. It offers a good measurement accuracy, resolution as well as sensitivity for the wavelength tuning design. I list a summary of the specifications of the NI DAQ PCI 6251 card in Table 5.9.

Reproduced with permission of the copyright owner. Further reproduction prohibited without permission.

Table 5.9 Characteristics of NI PCI-6251 data acquisition card

Bus Type	PCI
OS Support	Windows, Linux, Real-Time, Mac OS, RTX
Triggering	Analog, Digital
Number of DMA Channels	2
I/O Connector	68-pin VHDCI female
On-Board Memory	4095 samples
Input Bias Current	±100 pA
Number of Counter/Timers	2
Current Drive per Channel	24 mA
Analog Input	
Sample Rate	1.25 MS/s
Resolution	16 bits
Analog Output	
Number of Channels	2
Update Rate	2.86 MS/s
Range	-10 V to 10 V
Digital I/O	
Number of Channels	24 DIO
Logic Levels	TTL
Resolution	16 bits
Input impedance	
Device On	>10 GΩ and 100 pF
Device Off	820 Ω

5.4.5 Photodiode Detector

The duration of the dye laser pulse is 27 ns to 28 ns. I require a fast detector to record such a short duration pulse. To choose a good semiconductor detector, I need to consider the response speed, the operational spectral range, detector active area as well as the detection efficiency. The range of spectral sensitivity of different material is listed in Table 5.10 [Hauptmann, 1993]. Data in this table gives the general range of sensitivity of different detectors. The commercial silicon detector spectral

Reproduced with permission of the copyright owner. Further reproduction prohibited without permission.

sensitivity ranges from 0.2 to 1.1 μm. The commercial InGaAs detector spectral sensitivity ranges from 0.8 to 2.6 μm.

Table 5.10 Range of spectral sensitivity

Material	Range of Sensitivity at T=20 °C
Si	0.4-1.1
Ge	0.5-1.8
GaAs	0.7-0.9
InGaAs	0.8-1.8
InAs	1.0-5.5
InSb	1.0-5.5 (T = 77K)
PbS	1.0-3.5
PbSe	1.0-6.0

As the dye laser output ranges from 200 to 1100 nm, I conclude that the silicon photodiode is the best choice within this range. Silicon photodiodes are rugged, compact, lightweight semiconductor light sensors that have low noise, excellent photoelectric conversion linearity, and respond over a wide spectral range [Hamamatsu, 2007]. The photodiode senses the incident light by generating current through a P-N junction. A P-N junction consists of a P-layer which is active sensing layer and N-layer which is substrate layer. The region between P-layer and N-layer is a depletion region. The spectral response is determined by the doping concentration or thickness of those layers. When a photon is absorbed by the photodiode, an electron in P-layer will be stimulated. If the photon energy is greater than the band gap energy, the electron will escape from the valence band to the conducting band and leave a hole in the valence band. Holes from the N-layer will diffuse into the depletion layer between the P and N layer. The electron-hole flow is accelerated in the depletion layer. If the photodiode is part of a complete circuit, the electro-hole pairs generate a current which is proportional to the incident light. This is the basic principle of

Reproduced with permission of the copyright owner. Further reproduction prohibited without permission.

photodiode detection.

Silicon photodiodes are widely used for precision photometry, optical communication or high spectral photometry, low light detection, or image sensing. I choose a DET10A Silicon photodiode made by Thorlabs [Thorlabs, 2007]. A photo of this photodiode is shown to the left in Figure 5.7. The DET10A photodiode is a fast response photodiode with rise time of 1 ns. This photodiode is enclosed in a ruggedized anodized aluminum housing with BNC output coupler. A simple 12 V DC biasing circuitry guarantees the signal is ready for use. It has a wide spectral response range from 200 to 1100 nm. The peak response is 0.45 A/W at 730 nm. The response between 500 to 600 nm is greater than 0.3 A/W. In the UV region the photoelectric conversion gain is about 0.10 A/W. Compared with other high gain silicon photodiode, DET10A has a large active area. The diameter of active area is 1 mm. I tabulate the characteristics of the DET10A in Table 5.11. The spectral response curve as a function of wavelength is plotted to the right in Figure 5.7 [Thorlabs, 2007]. From Figure 5.7, I see that the photodiode response is optimum at 700 nm with a response of 0.4 A/W, and a response of 10% of that maximum in the near UV.

Table 5.11 Characteristics of DET10A photodiode [Thorlabs, 2007]

Spectral Response	200-1100nm
Active Diameter	1.02mm
Active Area	$0.81mm^2$
Rise Time (RL=50Ω)	<1ns (20V bias)
Fall Time (RL=50Ω)	<1ns (20V bias)
NEP@900nm(@20V bias)	5.0×10^{-14} W/√Hz
Dark Current	2.5nA max (20V)
Junction Capacitance (typ)	10pF @ 0V bias 2pF @ -10V bias
Package	T05, 0.36" can
Damage Threshold CW	$100\ mW/cm^2$
Damage 10ns Pulse	$500mJ/cm^2$
Maximum Bias Voltage	25V

Reproduced with permission of the copyright owner. Further reproduction prohibited without permission.

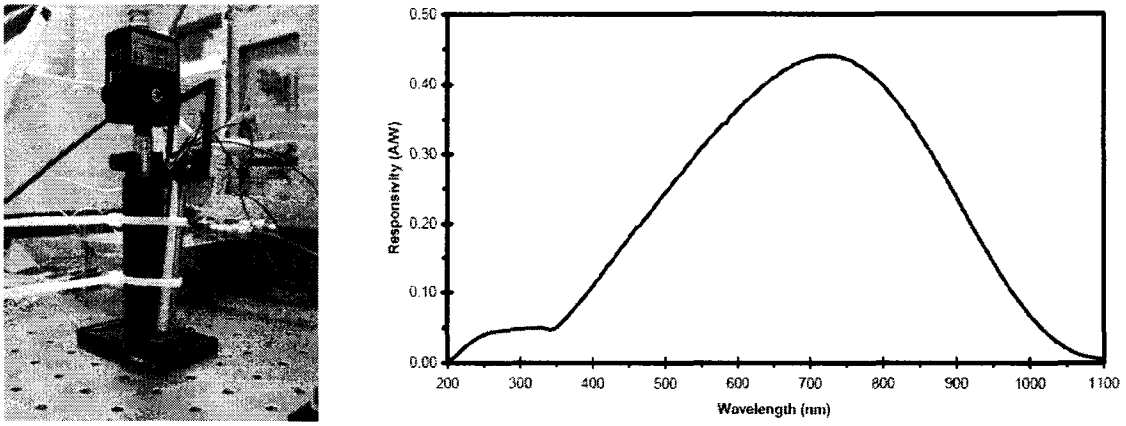

Figure 5.7 (left) photograph of DET10A photodiode module. (right) spectral sensitivity as a function of wavelength of DET10A photodiode [Thorlabs, 2007].

I compared the spectral response of the DET10A photodiode with two power meters (a Molectron J25LP-1 080 power meter and a ScienTech 365 power meter) on 25 April 2006. I show the normalized signal curves in Figure 5.8. The dye laser was operated in the visible region from 560 nm to 600 nm. The dye used was rhodamine 6G dissolved in methanol. From Figure 5.7 it is clearly seen that the energy measured by the different detectors are consistent and give the expected result for energy produced by the laser with the rhodamine 6G dye.

I operated the photodiode in reverse bias mode. The reverse bias current is proportional to the generation of carriers by the incident light, and thus proportional to the intensity of the incident light. I plot the reversed biasing circuitry in Figure 5.9. Inside the housing package, a 12 V battery acts as the biasing voltage source. A RC circuitry acts as a filter to remove noise. An ON/OFF switch controls the biasing. The BNC output signal is the direct photocurrent out of the DET10A anode. The induced photocurrent is a function of the incident irradiance (W/m^2) and wavelength. The external resistance load R converts the photocurrent into voltage.

Reproduced with permission of the copyright owner. Further reproduction prohibited without permission.

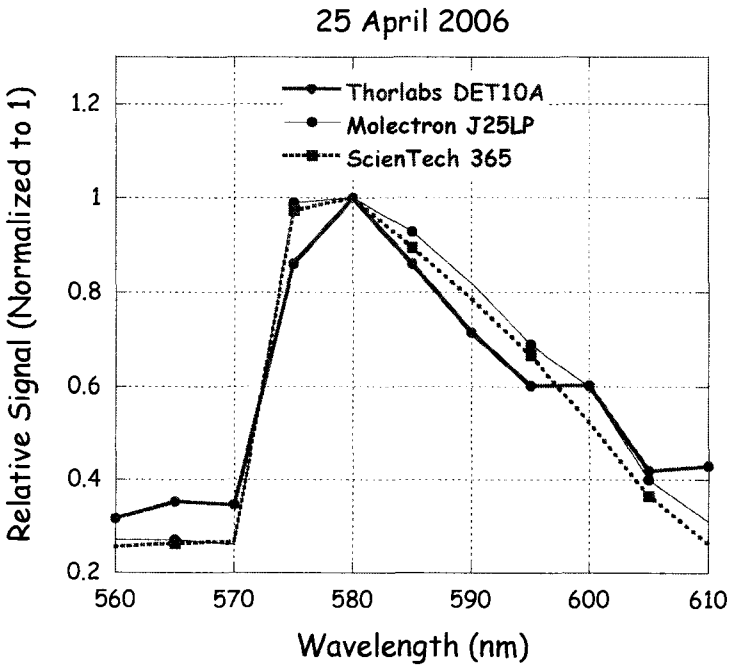

Figure 5.8 Laser energy as a function of wavelength measured by three different detectors.

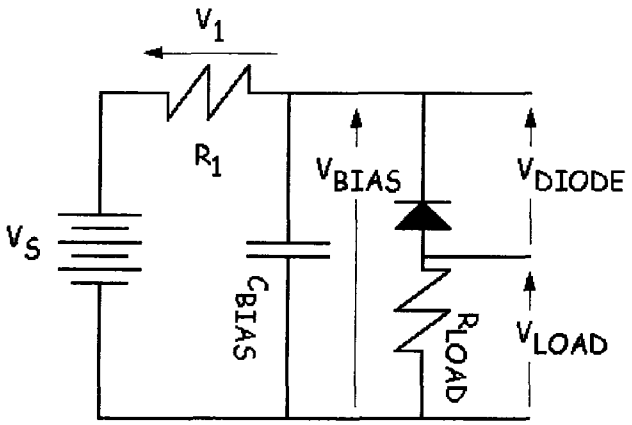

Figure 5.9 DET10A biasing circuits.

Reproduced with permission of the copyright owner. Further reproduction prohibited without permission.

On 23 January 2007, I applied a Scanmate® dye laser pulse via the fiber directly to the photodiode detector. I operated the dye laser operated at 589 nm. I used a 50 Ω external resistor in the photodiode circuit. I used a neutral density (N_D) filter to protect the photodiode from damage caused by high intensity radiation. I recorded the electrical pulse with a 200 MHz high-speed oscilloscope (LeCroy, Chestnut Ridge, NY, USA). I plot a single pulse in the upper panel of Figure 5.10. The small ringing signal is caused by the unmatched impedance of interconnects in the circuit. I conducted multiple tests using two oscilloscope coupling impedances (i.e., 1 MΩ and 50 Ω), and compared the use of commercial 50 Ω coaxial terminating resistors and 50 Ω carbon-film load resistors. I plot the recorded pulses in the lower panel of Figure 5.10. As I expect the 1 MΩ oscilloscope impedance gives a larger amplitude signal than the 50 Ω impedance. From Figure 5.10 I see that the 50 Ω terminator yields less ringing because the resistance value is more accurate than the 50 Ω 1/4 watt carbon film resistor.

I then determined the range of this signal for a linear response of this photodiode using the bias circuit shown in Figure 5.9. The measurement amplitudes with different input impedance are plotted in Figure 5.11. I measured the photodiode response with or without N_D attenuators. Each curve corresponds to 50 Ω, 499 Ω, 3.9K Ω, 4.7K Ω, 4.4K Ω, 6.9K Ω, and 9.1K Ω. The currents are 0.94 mA, 0.58 mA, 1.9 mA, and 2.8 mA corresponding to the attenuator of 0.3dB, 0.5dB, 1.0dB, and 2.0dB, respectively. Apparently for lower light incident intensity, the photodiode shows a linear response. The curve measured without attenuator shows saturation effect in photodiode. If the responded amplitude is greater than 10 volts, which will saturate the photodiode, the response shows a nonlinear change. For implementation, the manufacturer recommended value for external load resistor is 50 Ω [Thorlabs, 2007].

Reproduced with permission of the copyright owner. Further reproduction prohibited without permission.

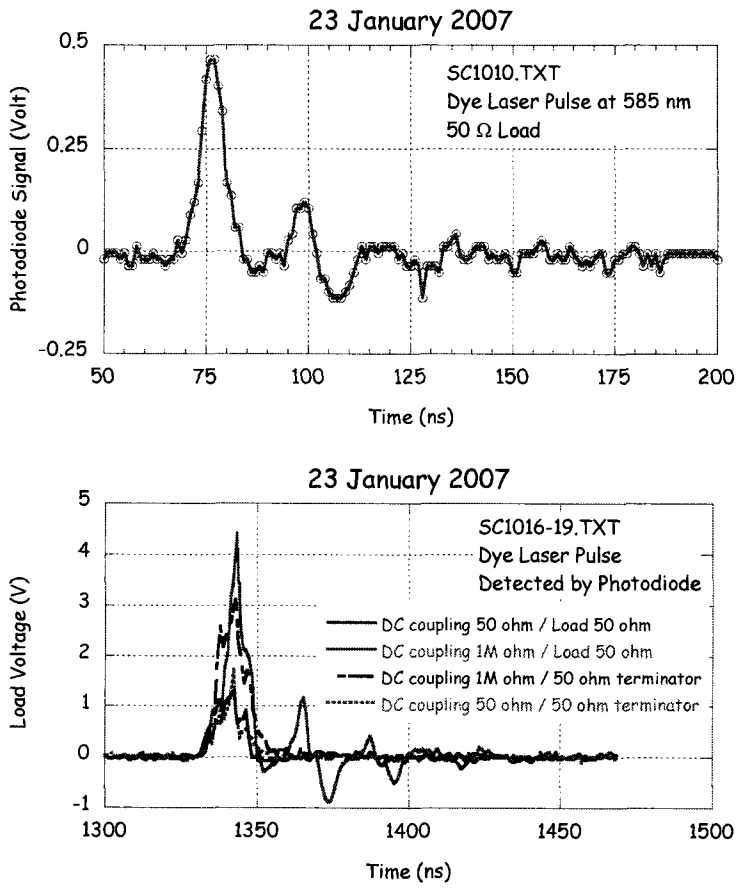

Figure 5.10 Dye laser pulse detected by DET10A photodiode.

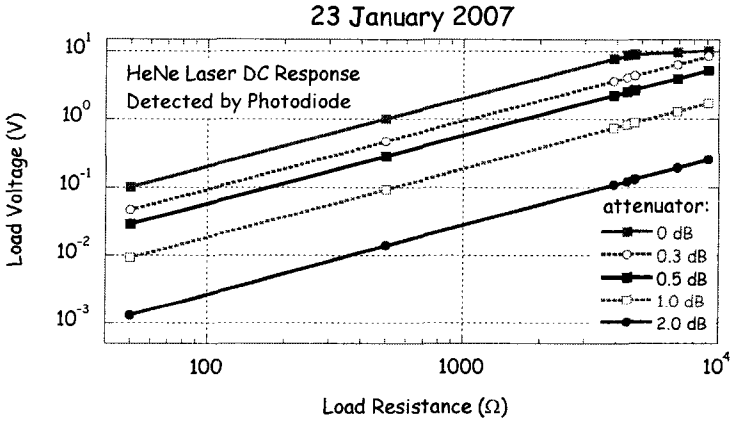

Figure 5.11 Calibrate DET10A photodiode.

Reproduced with permission of the copyright owner. Further reproduction prohibited without permission.

5.4.6 Peak Detector

I can use two approaches to detect and record the amplitude of such a narrow laser pulse. In the first approach I can directly sample the pulse, and determine the pulse shape by using very high speed analog/digital conversion circuits. However, this requires that I design a very high-speed set of mixed analog and digital circuits. To obtain 10 samples of the ~20 ns pulse would require a 500 MHz sample-and-hold circuit. Once sampled, I could analyze the digitized pulse. This is in effect what the high-speed oscilloscope does. The second approach is based on the fact that I only need to detect the amplitude of the pulse, and not the complete pulse shape. In this approach I can design and implement a peak detection circuit that yields a slowly varying voltage of the peak value, rather than a high-speed sample-and-hold circuit. This second approach provides us with a less costly and complicated way to capture and record the amplitude of these narrow pulses [Horowitz and Hill, 1993].

In principle, I can build a basic peak detector from a diode and a capacitor (Figure 5.12). However, the operation of such a simple device is limited by the input voltage and accuracy. In this basic configuration, the diode requires a significant input voltage to provide an accurate peak voltage signal across the capacitor. This input voltage must be much greater than the diode turn-on voltage. For germanium diodes the turn-on voltage is about 0.2 V; for silicon diodes the turn-on voltage is about 0.7 V. Thus, I require input voltages in excess of 1 V. Furthermore, the input must be greater than 10 times the turn-on voltage to yield an output voltage within 10% of the peak. Furthermore, since the voltage drop across the diode depends on temperature and current, the inaccuracies vary with temperature and rate of change of output voltage.

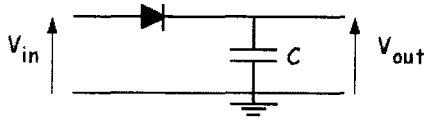

Figure 5.12 Simple peak detector.

Reproduced with permission of the copyright owner. Further reproduction prohibited without permission.

I can compensate for the diode turn-on voltage by using high-speed operational amplifiers (op-amp) [Ahrens, 1998]. I designed a circuit using these techniques (Figure 5.13). This design is based on an application design from Analog Devices [Analog Devices, 1995]. The full schematics, layout, and PCB artwork are attached in the Appendix. All files are generated by using ExpressPCB. I designed the peak detection circuit to support both pulsed and continuous-wave (CW) measurements. I can switch (SW1) the circuit between pulsed and CW detection modes. To detect the peak of a pulse, I put SW1 is in the up position and I use the active circuit. To detect the amplitude of a CW laser (e.g., precision He-Ne laser) I put SW1 in the down position and use the potentiometer (R5). The potentiometer allows us change the amplitude of the CW output signal.

The pulsed detector circuitry has three stages: the first two stages act as the peak detection circuit, and the third stage is a voltage follower or buffer amplifier. The first stage consists of an AD847 op-amp. The AD847 is a high speed, low power monolithic op-amp, that has been designed for use at VHF and UHF in video instrumentation, imaging equipment, cable driver, and DAC and flash ADC buffers. The op-amp has a bandwidth of 50 MHz suitable for the short duration photodiode pulse signal (20 ns). It has a slew rate of 300 V/μs which is faster than the high speed signal input (0.5 V in 5 ns = 100 V/ μs). The AD847 is specifically designed to drive capacitive loads without loss of gain. The slew rate, bandwidth, speed, and capacitive driver capability are all required in building stable feedback peak detectors [Analog Devices, 1992]. The 0.01 μF and 1 μF shunt capacitors work together as a filter to eliminate the noise from the power supply. The resistors, R1 and R6, at the input of the first stage provide a load for the photodiode as well as impedance matching. The MBD301 is a Schottky barrier diode with a very short low minority carrier lifetime (15 ps), a medium turn-on voltage (0.4 V), and very low capacitance (1.5 pF). While the 1N4148 is widely used in high speed circuits, the diode's higher turn-on voltage (0.6 V) and larger capacitance (4 pF) prevent it from use in this peak detection circuit. The second stage consists of an AD843 op-amp. AD843 is a CBFET fast setting op-amp with a bandwidth of 34 MHz, a slew rate is 250 V/μs, and temperature stabilization [Analog Devices, 1995]. The AD843 has been designed for high speed sample-and-hold amplifiers, high bandwidth active filters, high speed integrators, or high frequency

Reproduced with permission of the copyright owner. Further reproduction prohibited without permission.

signal conditioning. As a FET input amplifier it has a fairly low (0.6 nA) input bias currents and very high (10^{10} Ω) input resistance. Again, the 0.01 μF shunt capacitors connected to the power supply work as noise filters. The third stage consists of a TL052 op-amp, operating as a voltage follower. The resistor R7 limits the current delivered into the data acquisition card. During the development of this circuit I tested several other op-amps (e.g., AD8002, AD8066, AD8045, OPA657). However, these op-amps suffered from the following limitations; limited capacitance driving capability, low slew rate, output cannot follow the input signal, the output cannot sustain a long time delay, the output has a large droop rate.

While the input voltage is positive, the righthand diode from the output of the AD847 and the non-inverting input of the AD843 operate as a single voltage follower. The output signal from the second stage is fed back to the first stage. The first stage charges the capacitor, C5, as it follows the input voltage as it increases. The resistor, R3, in series with the capacitor, C5, keeps the capacitor from causing a phase shift that would destabilize the pair of op-amps in a feedback loop. Reducing the value of C5 increases the speed of response at the expense of increasing both overshoot and droop. Since the AD847 is specifically designed to drive capacitive loads, increasing the C5 value decreases the droop rate.

When the input pulse signal is negative, the lefthand diode conducts, and keeps the first op-amp from saturating its output against the negative rail. This ensures the peak detector recovers quickly when the input pulse signal goes positive again. During this time, the righthand diode isolates the AD847 from the voltage that has been stored across the capacitor. The resistor, R2, provides a current path from the AD843 output back to the AD847. This current relieves the need to disconnect the feedback path between two successive pulse peaks. The output DC signal from the AD843 is sent to the voltage follower and sampled by the data acquisition card at W1. A prototyping board is shown in Figure 5.14.

Reproduced with permission of the copyright owner. Further reproduction prohibited without permission.

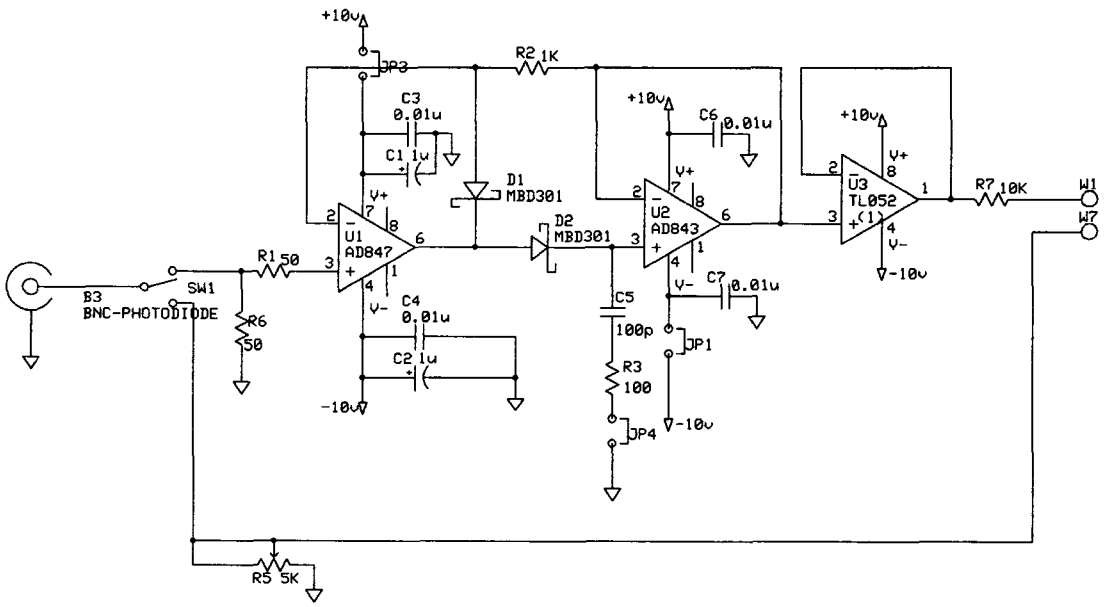

Figure 5.13 Schematics of the peak detector of the op-amp based peak detector.

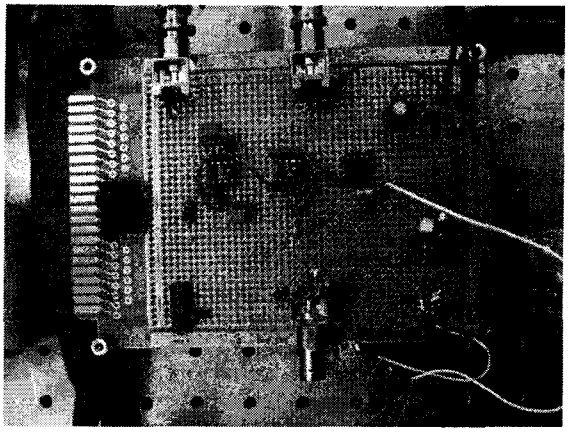

Figure 5.14 Peak detector board.

On 18 February 2007, I tested the pulse detector circuit using an electrical function generator. I wished to test two aspects of the circuit:

a. The fidelity of the peak detector as a function of the amplitude of the input

Reproduced with permission of the copyright owner. Further reproduction prohibited without permission.

voltage pulse;

b. The fidelity of the peak detector as a function of the frequency of the input voltage pulse.

I input pulses with amplitudes of 50 mV, 100 mV, 200 mV, 500 mV, 1 V, 2 V, and 5 V and at frequencies of 10 kHz, 100 kHz, 1 MHz, and 2 MHz with duty cycles of 10%, 10 %, 14% and 36% respectively. I recorded the input and output pulses with a high-speed 200 MHz oscilloscope. I illustrate the behavior with plots of the input and output pulses in Figure 5.15, 5.16, and 5.17. The pulse detector works better (i.e., the amplitude of the output DC level better matches the amplitude of the input pulse) as the amplitude of the input pulse and the width of the input pulse increases. From these tests I conclude that the signal from the photodiode detector exceeds 2 V. I tested the noise in the circuit by grounding the input and measuring the output signal. The output signal was less than 2 mV. I plot the relative error associate with input voltage in Figure 5.18.

Reproduced with permission of the copyright owner. Further reproduction prohibited without permission.

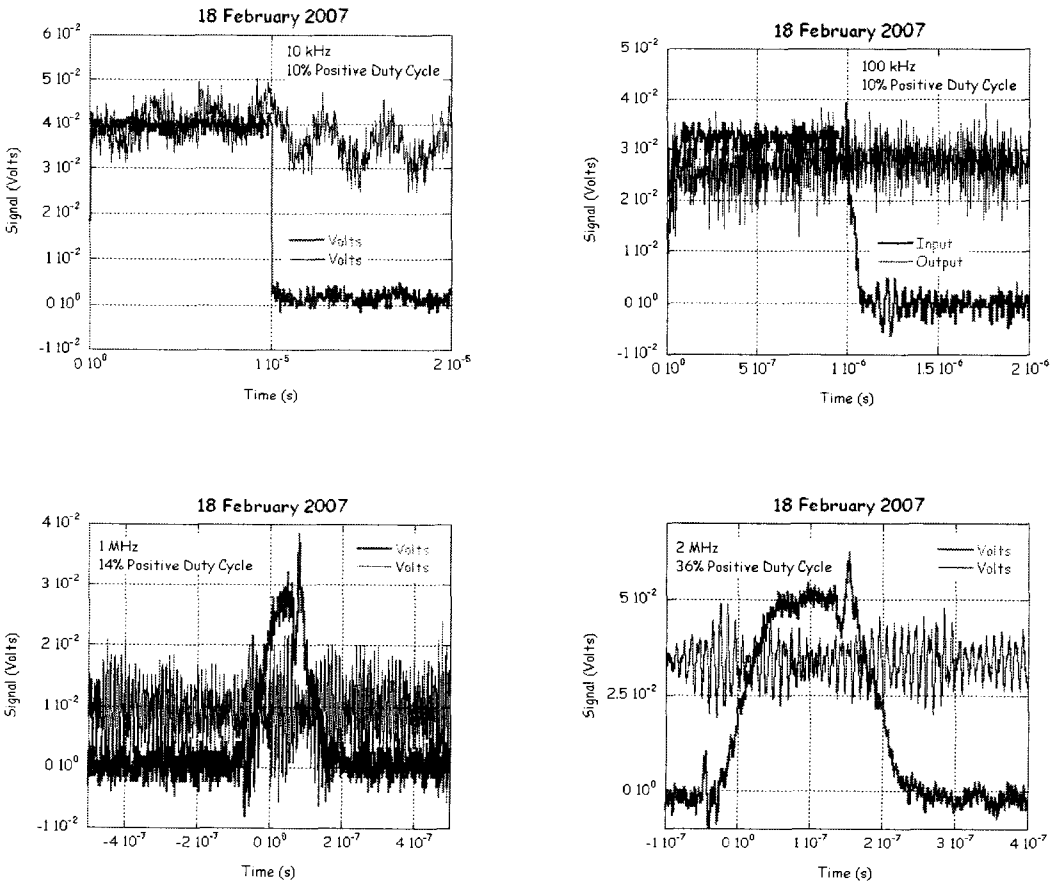

Figure 5.15 Performance of peak detector circuit for low amplitude (~40 mV) signals. The input and output signals are plotted as a function of time for four frequencies; (upper left) 10 KHz, (upper right) 100 kHz, (lower left) 1 MHz, (lower right) 2 MHz.

Reproduced with permission of the copyright owner. Further reproduction prohibited without permission.

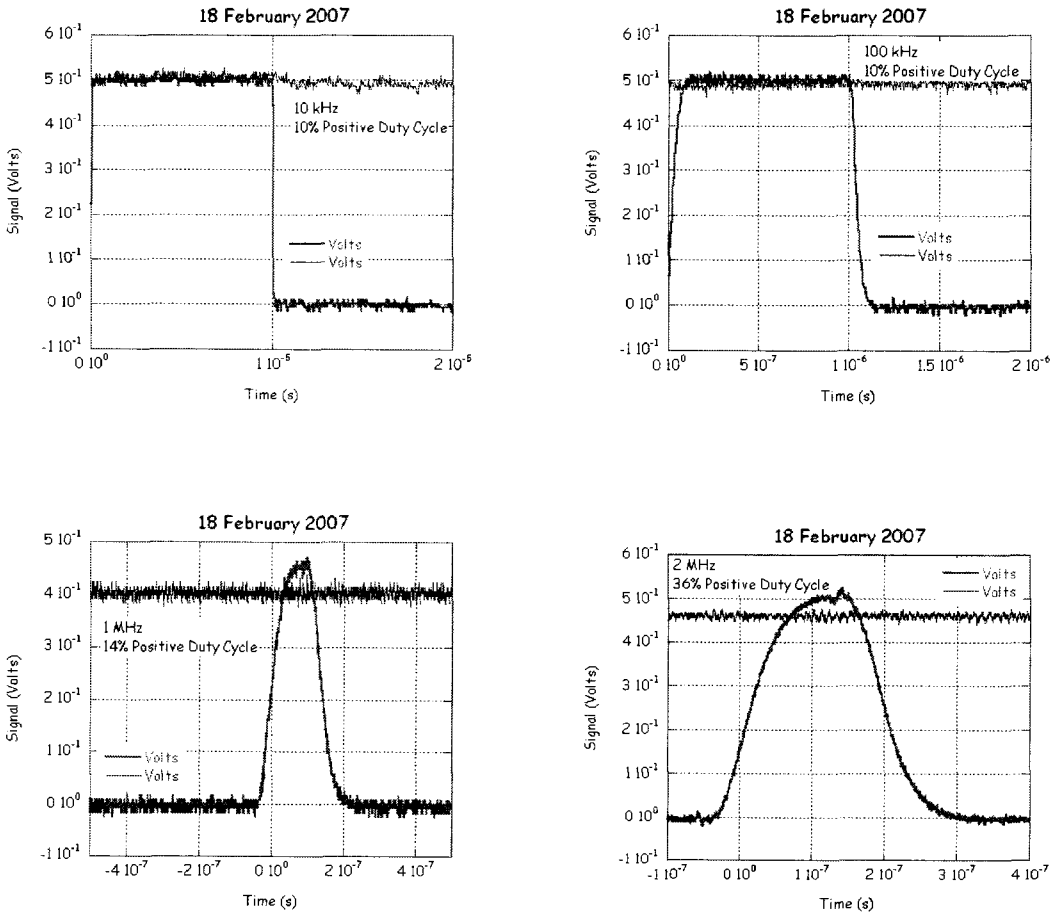

Figure 5.16 Performance of peak detector circuit for medium amplitude (~0.5 V) signals. The Input and output signals are plotted as a function of time for four frequencies; (upper left) 10 KHz, (upper right) 100 kHz, (lower left) 1 MHz, (lower right) 2 MHz.

Reproduced with permission of the copyright owner. Further reproduction prohibited without permission.

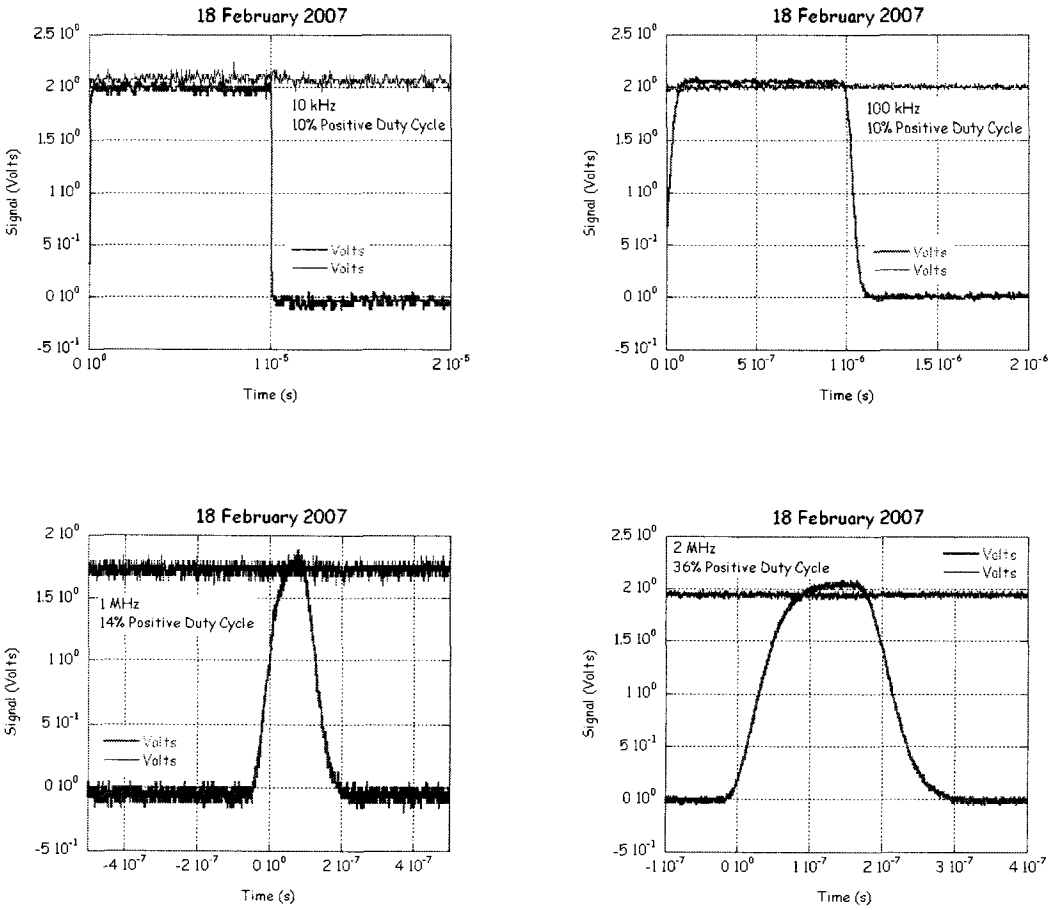

Figure 5.17 Performance of peak detector circuit for medium amplitude (~2 V) signals. The Input and output signals are plotted as a function of time for four frequencies; (upper left) 10 KHz, (upper right) 100 kHz, (lower left) 1 MHz, (lower right) 2 MHz.

Reproduced with permission of the copyright owner. Further reproduction prohibited without permission.

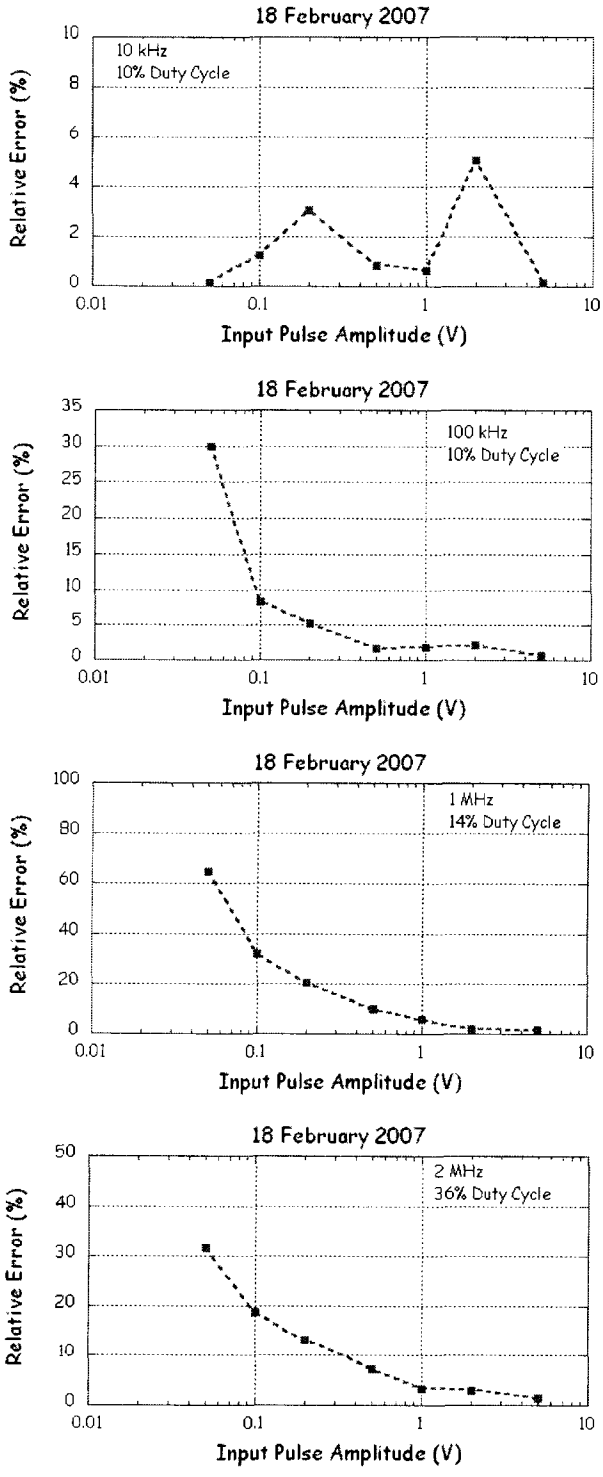

Figure 5.18 Relative error between amplitude of input and output signals of peak detector circuit.

Reproduced with permission of the copyright owner. Further reproduction prohibited without permission.

5.5 Experimental Tests of FPI System

5.5.1 Visible Wavelength Experiments

I conducted several experiments at visible wavelengths to determine the performance of the FPI system. I used the dye laser to investigate the performance of the system at the sodium D_1 line (corresponding to the vacuum wavelength of 589.637 nm) and D_2 lines (corresponding to the vacuum wavelength of 589.036 nm). I used the hollow cathode lamp as a reference for the sodium D_1 and D_2 lines. I also used a stabilized CW He-Ne laser (corresponding to the vacuum wavelength of 632.992 nm) to characterize the FPI.

I first measured the transmission of the FPI system as a function of pressure at the three wavelengths. For the sodium lines, I set the laser pulse detection board in pulse mode. I first set tuned the dye laser to the sodium D_1 line at 589.637 nm line. I set the dye laser repetition rate at 10 pps. I scanned from 16 to 85 psi in 0.1 psi steps. At each pressure step, I averaged the amplitude of 20 pulses detected by the photodiode and recorded the result. I plot the pressure scan at the D_1 line in the upper panel of Figure 5.19. The maximum signal has been normalized to one. I next tuned the laser to the sodium D_2 line at 589.036 nm and repeated the procedure. I plot the pressure scan at the D_2 line in the lower panel of Figure 5.19. Finally I conducted a pressure scan using the stabilized CW He-Ne laser at 632.992 nm (Figure 5.20). I set the laser pulse detection board in CW mode, and conducted the pressure scan in the same way as for the D_1 and D_2 lines. I see that all three pressure scans show two peaks associated with the transmission through the FPI of two successive orders. From these pressure scans I record the pressure at the peak and determine the centroid pressure of each peak as well as record the corresponding temperature. The centroid pressure is a more robust estimate of the actual peak pressure than the local maximum. I tabulate these results in Table 5.12.

I show the fringe patterns for a sodium lamp FPI in Figure 5.20. I show the fringe pattern at a pressure of 22 psi corresponding to the peak (or fringe) at the sodium D1 line in the left panel. I show the fringe pattern at a pressure of 31.5 psi corresponding to the peak (or fringe) at the sodium D_2 line in the right panel. I show the fringe

Reproduced with permission of the copyright owner. Further reproduction prohibited without permission.

pattern at a pressure of 26 psi corresponding to an intermediate wavelength in the middle panel. The sodium lamp transmits both the D_1 and the D_2 lines simultaneously. The pair of lines is evident in Figure 5.20 as the concentric circles (or fringes) appear in pairs. The bright spot in the center of the fringe pattern at 22 and 31.5 psi indicates the transmission of the light at normal incidence through the FPI, and hence the peak in the pressure scan.

Reproduced with permission of the copyright owner. Further reproduction prohibited without permission.

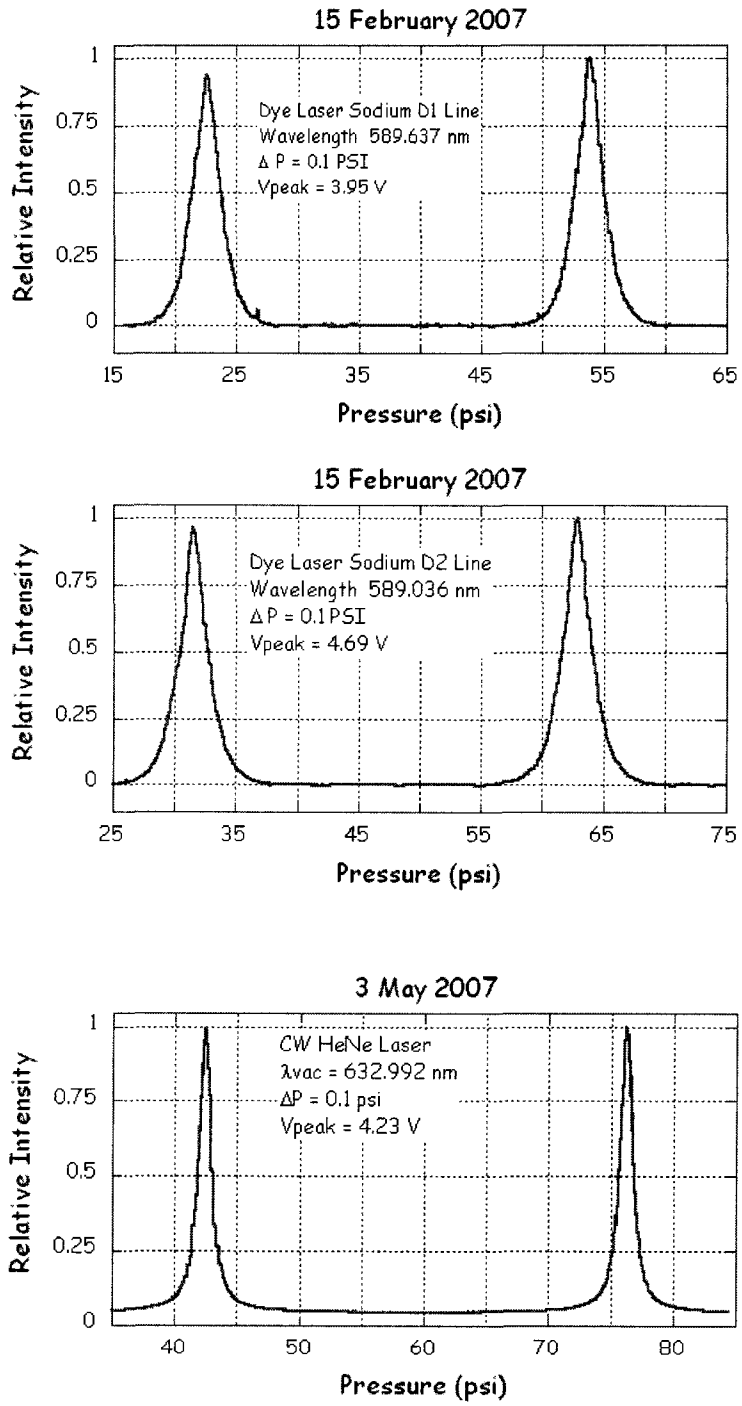

Figure 5.19 FPI pressure scans with laser light source at sodium D_1 (upper), sodium D_2 (middle) and He-Ne (lower) wavelengths.

Reproduced with permission of the copyright owner. Further reproduction prohibited without permission.

Table 5.12 Pressure peaks and centroids with 0.1 psi resolution

Sodium D_1	Peak (psi)	22.55	53.94
	Centroid (psi)	22.51	53.83
	Temperature (°C)	21.65	21.77
Sodium D_2	Peak (psi)	31.44	62.99
	Centroid (psi)	31.53	62.84
	Temperature (°C)	21.79	22.00
He-Ne	Peak (psi)	42.39	76.24
	Centroid (psi)	42.38	76.25
	Temperature (°C)	23.27	23.41

Reproduced with permission of the copyright owner. Further reproduction prohibited without permission.

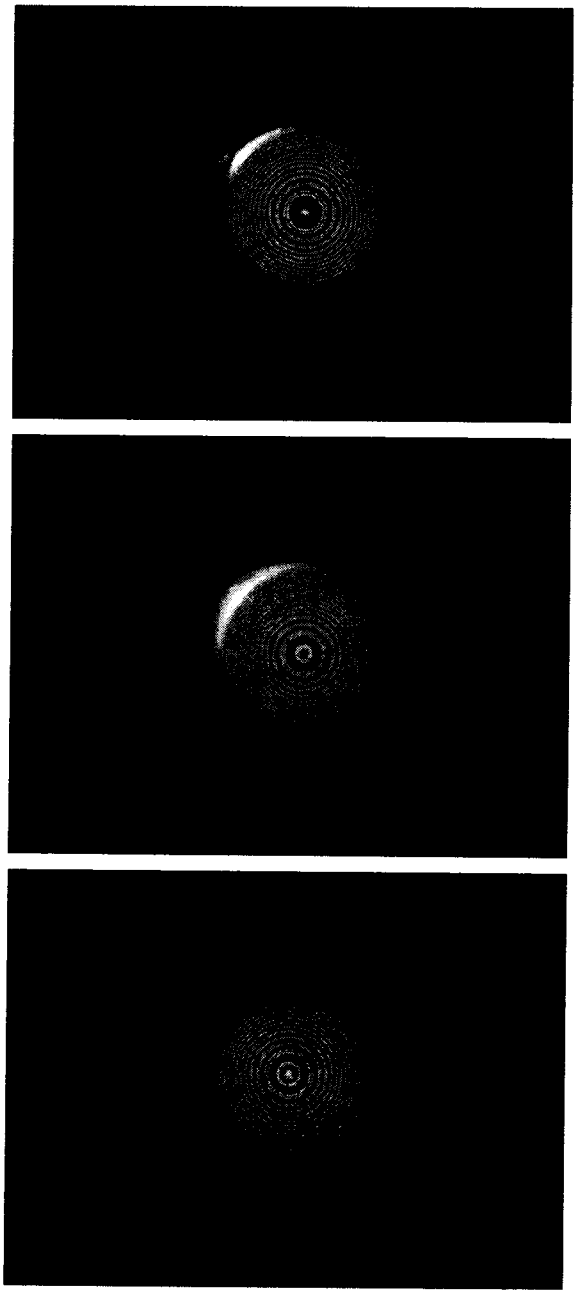

Figure 5.20 Fringe patterns for sodium lamp pattern at pressures of (left) 22 psi, (middle) 26 psi and right) 31.5 psi.

Reproduced with permission of the copyright owner. Further reproduction prohibited without permission.

From the earlier discussion of the FPI, I know that a peak in the Airy function (i.e., fringe) corresponds to a phase lag, φ, that is an integer multiple of 2π. The integer m is the order of the peak and corresponds to,

$$m = \frac{2\mu d \cdot \cos\theta}{\lambda} \tag{5.19}$$

where μ is the refractive index of air in the interferometer cavity, d is the spacing of interferometer, θ is the angle of incidence, and λ is the vacuum wavelength. The refractive index of air is a function of pressure and temperature. I can express the product of spacing and cosθ in terms of the order, m, the refractive index at the peak pressure and temperature, μ, and the wavelength, λ, as,

$$d \cdot \cos\theta = \frac{m\lambda}{2\mu} \tag{5.20}$$

I see that if the wavelength and refractive index at a peak are known, then there is an infinite set of pairs of dcosθ and m that satisfy the equation, and I cannot unambiguously determine the characteristics of the FPI. However, if I measure the refractive indices, μ_1 and μ_2, at two adjacent peaks with order number m_1 and m_2 respectively, where $m_2 = m_1 + 1$ I obtain,

$$d \cdot \cos\theta = \frac{\lambda}{2(\mu_1 - \mu_2)} \tag{5.21}$$

From the results in Table 5.12 I calculate the value of dcosθ based on the pair of fringes at each wavelength. I tabulate the results in Table 5.12. From Table 5.12, the spacing values calculated from the sodium D_1 and D_2 lines equal 510,319 nm and 510,324 nm respectively. These two values have a difference of less than 5 parts in 500,000. The value calculated based on He-Ne laser experiment is slightly less than that determined from the sodium lines experiments. This difference is probably caused by the change in experimental setup. For the sodium line experiments, the only change in the system is the wavelength of the dye laser. For the He-Ne line experiment, the He-Ne laser replaces the fiber optic cable in the set up. The orientation of the He-Ne laser may not be exactly the same as that of the fiber. The lower value of the estimated value of dcosθ is consistent with an angle offset of 1.8°

Reproduced with permission of the copyright owner. Further reproduction prohibited without permission.

in the placement of the He-Ne laser.

Table 5.13 Estimated product of spacing and cosθ (nm)

Na D_1	Na D_2	He-Ne
510319	510324	510074

Having characterized the FPI in terms of pressure scans at fixed wavelengths, I then measured the transmission of the FPI system as a function of wavelength at a given pressure. I compared the wavelength response of the FPI with that of the hollow cathode lamp. I first set the pressure of the FPI chamber to 31.3 psi and the bias current in the hollow cathode lamp to 14.9 mA. I set the dye laser repetition rate at 10 pps. I scanned from 589.024 nm to 589.050 nm in 1 pm steps. At each wavelength step, I averaged the amplitude of 20 pulses detected by the photodiode and recorded the result and also averaged the amplitude of 20 hollow cathode lamp current pulses and recorded the result. I plot the wavelength scan of the hollow cathode lamp in the left panel of Figure 5.21. I plot the wavelength scan of the FPI in the right panel of Figure 5.21. I find that the peak of the hollow cathode lamp response is at a laser wavelength of 589.036 nm while that of the FPI is at a laser wavelength of 589.038 nm. I find that the FWHM of the hollow cathode lamp is 10 pm while that of the FPI is 15 pm.

Reproduced with permission of the copyright owner. Further reproduction prohibited without permission.

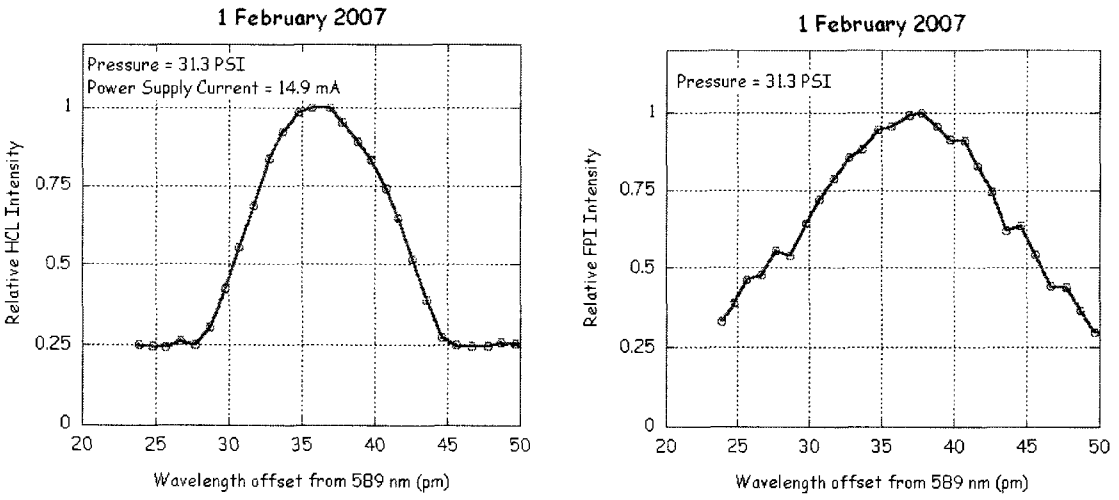

Figure 5.21 Simultaneously FPI and sodium hollow cathode lamp wavelength scans.

5.5.2 Ultraviolet Wavelength Experiments

I conducted several pressure scan experiments with the dye laser operating in the UV. I conducted these experiments in the same fashion as the visible wavelength experiments; scanning the pressure from 15 psi to 80 psi and recording the amplitude of 20 laser pulses at each pressure. I operated the laser at 10 pps. I first conducted an experiment at the laser wavelength of 372.015 nm. This wavelength corresponds to the iron resonance lidar wavelength that I conducted lidar measurements of the mesospheric iron layer on 30 April 2007. I then conducted six pressure scanning experiments at wavelengths in the neighborhood of 390 nm. I show the measurements at 390.015 nm, 390.134 nm, and 390.216 nm in Figure 5.22. I tabulate the results in Table 5.14. These measurements allow us to assess the sensitivity of the peak to wavelength changes. I plot the variation of peak pressure with laser wavelength in Figure 5.23.

Reproduced with permission of the copyright owner. Further reproduction prohibited without permission.

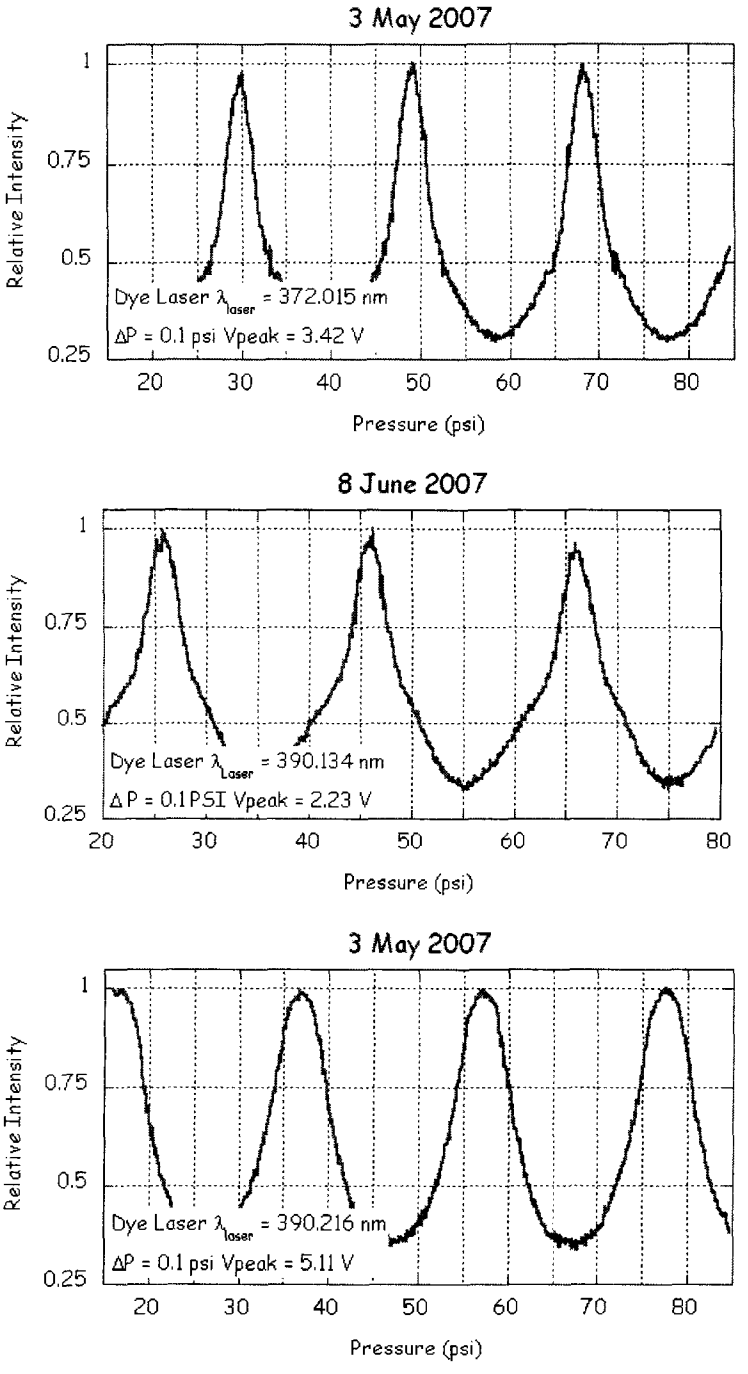

Figure 5.22 FPI pressure scans in UV.

Reproduced with permission of the copyright owner. Further reproduction prohibited without permission.

Table 5.14 Pressure at FPI peaks and centroids

Wavelength (nm)	Pressure at Peak (psi)	Centroid Pressure(psi)	Temperature (°C)
372.0993	30.01/49.21/68.23	29.79/48.93/68.34	22.68/22.59/22.51
390.1342	25.84/46.07/65.98	25.68/45.54/65.74	20.32/20.11/20.04
390.1592	28.81/49.16/69.50	28.55/48.72/69.42	20.06/19.81/20.15
390.1841	31.89/52.63/72.42	31.82/52.04/72.12	19.95/20.02/19.98
390.2091	35.41/55.15/75.81	35.07/55.16/75.81	19.87/19.84/19.95
390.2161	36.74/57.07/77.61	36.61/57.10/77.60	22.88/23.01/22.72
390. 2341	39.03/58.78/79.03	38.31/58.58/78.57	19.76/19.72/20.04

Measurements carried out at 0.1 psi resolution.

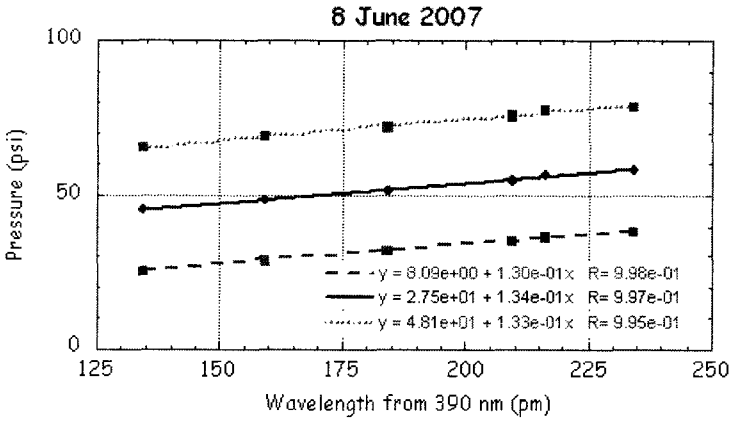

Figure 5.23 Variation of pressure at FPI peaks with laser wavelength in the UV region.

The data show that the FPI peak pressure increases with wavelength as expected. At a given peak, the order remains constant as the wavelength increases, and so the refractive index must increase. Thus the pressure for that peak at that order must increase. I applied linear fits to the data in Figure 5.22. The fits have high correlation coefficients (>0.99) and indicate that the peak pressure increases by 0.13 pm for every 1 pm change in wavelength in the UV range.

Having characterized the FPI in terms of pressure scans at fixed wavelengths in the

Reproduced with permission of the copyright owner. Further reproduction prohibited without permission.

UV, I then measured the transmission of the FPI system as a function of wavelength at a fixed pressure of 35.1 psi. I plot this FPI wavelength scan in Figure 5.24. There are three complete peaks with wavelengths at 390.048 nm, 390.200 nm, and 390.351 nm with a separation of 151 pm between the peaks. The FWHM of is between 34 and 36 pm, which is broader than the 15 pm FWHM measured at 589 nm. This increase in the width of the peaks could be due to a decrease in the reflectivity of the FPI plate coatings at UV wavelengths relative to visible wavelengths. To check the full width variation with a different threshold, only photodiode amplitudes above the threshold are considered; the full widths are listed in Table 5.15.

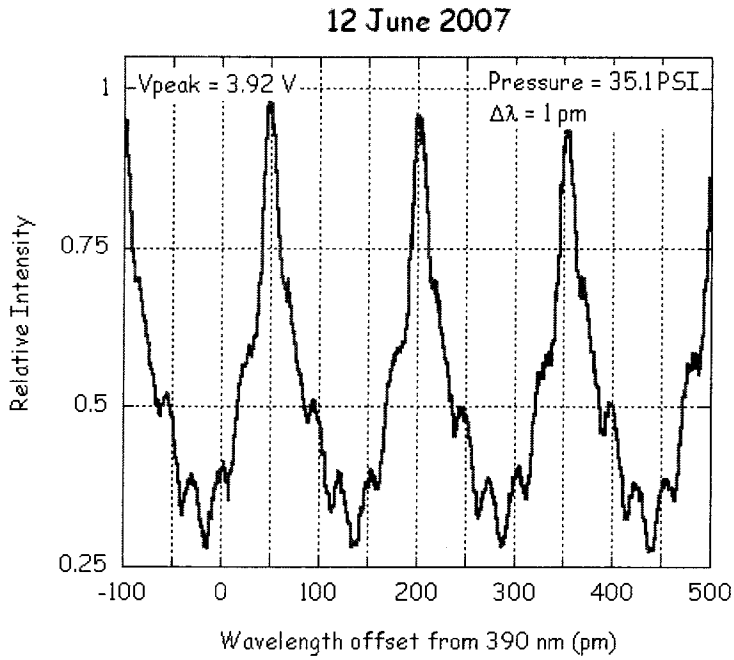

Figure 5.24 FPI wavelength scan at 390 nm.

Reproduced with permission of the copyright owner. Further reproduction prohibited without permission.

Table 5.15 Full width of UV wavelength scan

Threshold	Width (pm)		
	390.048	390.200	390.351
50 % of Peak	36	35	34
75 % of Peak	15	15	16
87.5 % of Peak	10	9	10

5.6 Summary

I have developed and tested an integrated computer-controlled FPI-based tuning control system for the pulsed dye laser. The FPI system has similar spectral sensitivity in the visible as the hollow cathode lamp used for sodium resonance lidar measurements. The sensitivity of the FPI transmission to changes in wavelength and pressure are consistent with a FWHM of 35 pm in wavelength corresponding to a 4.6 psi in pressure in the UV. Changes of 1 pm correspond to changes in pressure of 0.13 psi which is larger than the resolution of the FPI pressure controller.

Reproduced with permission of the copyright owner. Further reproduction prohibited without permission.

6 Field Tests of a N_2^+ Resonance Lidar System

In this chapter I present the results of field experiments at PFRR that I conducted during the spring 2007. I explain the experimental approach and then present the resonance lidar data. Finally I analyze the signal as well as receiver optics to examine the system performance.

6.1 Experimental Approach

In Chapter 2 I examined the performance of the resonance lidar system in making sodium and iron measurements. From these measurements, I confirmed the operation of the lidar system at both visible (589 nm) and ultraviolet (372 nm) wavelengths.

Based on the success of the iron and sodium measurements I expect that the receiver would support measurements of molecular nitrogen ions. The resonance wavelength for nitrogen measurements at 390 nm lies between the wavelength for iron measurements at 372 nm and sodium measurements at 589 nm (Figure 6.1). I anticipated that by changing the interference filter of the resonance channel from 372 nm to 390 nm and tuning the laser from 372 nm to 390 nm, that lidar will support measurements at the molecular nitrogen resonance wavelength. The dye, QUI, used to make measurements of iron at 372 nm also fluoresces at 390 nm. Since the lidar works at 372 nm, I expect that the lidar should also work at 390 nm by tuning the laser and changing the receiver bandpass filter. The goal of this experiment is not to detect N_2^+ scatter directively but to characterize the operation of lidar transmitter and receiver at 390 nm. I use the Rayleigh scatter signal from the stratosphere to determine the quality of the lidar measurements.

Reproduced with permission of the copyright owner. Further reproduction prohibited without permission.

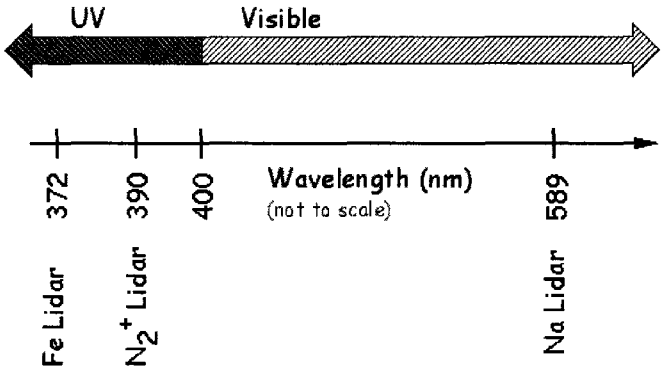

Figure 6.1 Lidar systems associated with different spectrum.

I made sodium and iron measurements with the dual channel lidar receiver illustrated in Figure 6.2. A photograph of the receiver system is shown in Figure 6.3. I have designed the lidar receiver to allow simultaneous operation at two wavelengths. I use two independent lasers to make simultaneous Rayleigh (532 nm) and resonance lidar (589 nm or 372 nm) measurements. I collect both the Rayleigh and resonance lidar echo from the sky with a 60-cm Newtonian telescope. I use Rayleigh lidar signal to assess system performance. The light from both echoes passes through the collimating lens and is separated by the dichroic beamsplitter. The light at 532 nm is transmitted by the beamsplitter through a narrow band interference filter to a photomultiplier tube (PMT) detector. The light at 589 nm and 372 nm is reflected by the beamsplitter through a narrow band interference filter to a PMT. I use different dichroic beamsplitters for the sodium and iron measurements. For simultaneous Rayleigh lidar and resonance iron lidar measurements at 532 nm and 372 nm respectively, I used a longpass beamsplitter (425DCLP, Omega Optical Brattleboro, VT). For simultaneous Rayleigh lidar and resonance sodium lidar measurements at 532 nm and 589 nm respectively, I used a shortpass beamsplitter (560DCSP, Omega Optical Brattleboro, VT).

Reproduced with permission of the copyright owner. Further reproduction prohibited without permission.

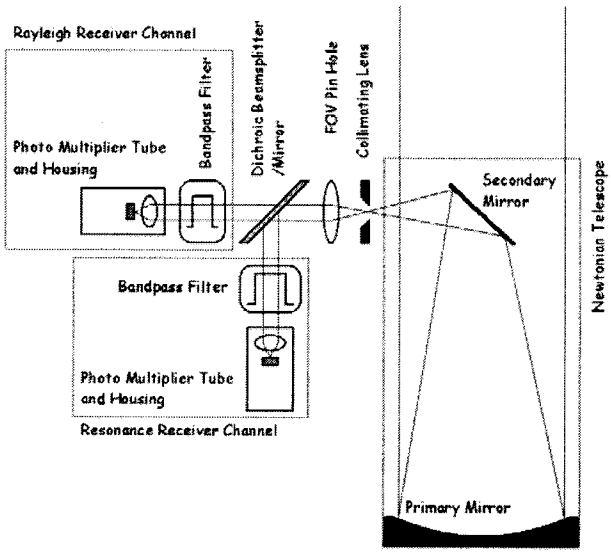

Figure 6.2 Schematic diagram of the dual-channel lidar receiver at PFRR.

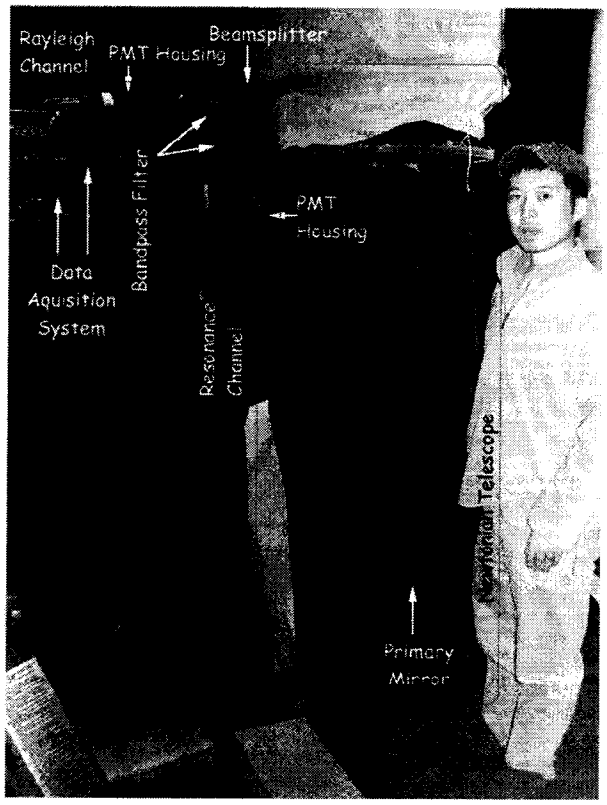

Figure 6.3 Photograph of the dual-channel lidar receiver at PFRR. Several key components are indicated.

Reproduced with permission of the copyright owner. Further reproduction prohibited without permission.

6.2 Field Experiments

6.2.1 First Experiment on 17 April 2007

During this experiment I operated both the Rayleigh and resonance lidar systems. I ran the Rayleigh system that I could monitor the transmission of the atmosphere during the resonance lidar measurements. I initially make measurements with the iron resonance lidar system. The iron resonance lidar measurements allow me to confirm the operation of the resonance lidar system in the ultraviolet. I have plotted the lidar signal profile in Chapter 2 (see Figure 2.14). I make two conclusions from that iron resonance lidar data, firstly the lidar transmitter and receiver are operating successfully at the ultraviolet wavelength, and secondly, the transmitted laser beam is well aligned with the receiver telescope field-of-view yielding echoes up to the iron layer at 100 km.

I measured the laser pulse energy as a function of wavelength (Figure 6.4). I see that while the laser pulse energy varies with the wavelength between 3.5 mJ/pulse and 8.5 mJ/pulse. The laser pulse energy at 372 nm and 390 nm is similar (~8 mJ/pulse). I then changed the bandpass filter of the receiver to a filter centered at 390 nm with the bandwidth of 1 nm. I tuned the laser to 390.994 nm. I chose this wavelength because the iron resonance corresponded to 372.015 nm, 22 pm away from the iron resonance wavelength of 371.993 nm in air. The wavelength of 390.994 nm is 22 pm greater than the molecular nitrogen ion resonance wavelength for J equal to 0 at 390.972 nm. I plot the lidar signal profile in Figure 6.5. This profile represents the integration of 12000 laser pulses at 390.994 nm. From 15 km to 35 km I see the lidar signal due to the Rayleigh scatter. Below 15 km I have suppressed the lidar signal. As I expected the iron layer is no longer visible.

Reproduced with permission of the copyright owner. Further reproduction prohibited without permission.

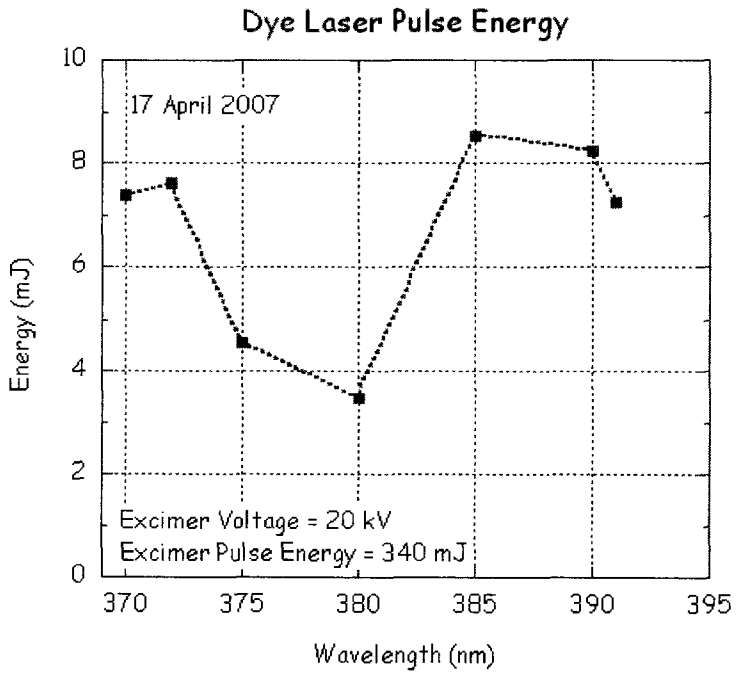

Figure 6.4 Energy of dye laser pulses as a function of wavelength measured on 17 April 2007.

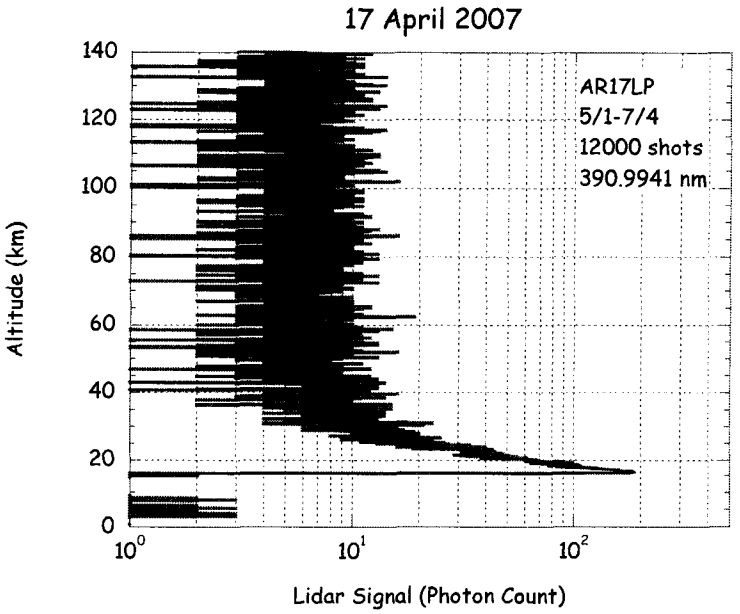

Figure 6.5 Raw lidar signal profile at 391 nm measured on 17 April 2007.

Reproduced with permission of the copyright owner. Further reproduction prohibited without permission.

From Figure 6.5 it is clear that the lidar signal at 390 nm is significantly less than at 372 nm (Figure 2.14). I quantify the lidar performance by comparing the integrated lidar signal from 20 to 25 km at both wavelengths. For the 32,000 laser pulses at 372 nm I detected a signal of 6.188×10^5 photon counts, equivalent to 19.3 photon counts per laser pulse. For the 12,000 laser pulses at 390 nm I detected a signal of 2.146×10^3 photon counts, equivalent to 0.179 photon counts per laser pulse. From these data the lidar system performance appears to decrease by a factor of 100. I find no significant change in the magnitude of the Rayleigh lidar signal during this period. Thus, this change of signal is not due to the change of atmospheric conditions. From the laser pulse energy measurements this change in signal is not due to a change of laser pulse energy.

6.2.2 Second Experiment on 30 April 2007

During this experiment I again operated the Rayleigh lidar in conjunction with the resonance lidar. I conducted two sets of resonance lidar experiments. I first made seven lidar measurements at wavelengths between 370 nm and 374 nm with a bandpass filter that had a center wavelength of 372 nm and 3 nm bandwidth. I then made seven lidar measurements between 385 nm and 391 nm with a bandpass filter that had a center wavelength of 404 nm and 40 nm bandwidth. During these measurements, the Rayleigh lidar signal remains relatively constant indicating that the sky conditions (therefore the atmospheric transmission) did not vary during this experiment.

I then measured the laser pulse energy as a function of wavelength (Figure 6.6), finding that while the laser pulse energy varies with the wavelength between 0.4 mJ/pulse and 3.5 mJ/pulse. The energies at 372 nm and 390 nm are similar (~2.5 mJ/pulse).

Reproduced with permission of the copyright owner. Further reproduction prohibited without permission.

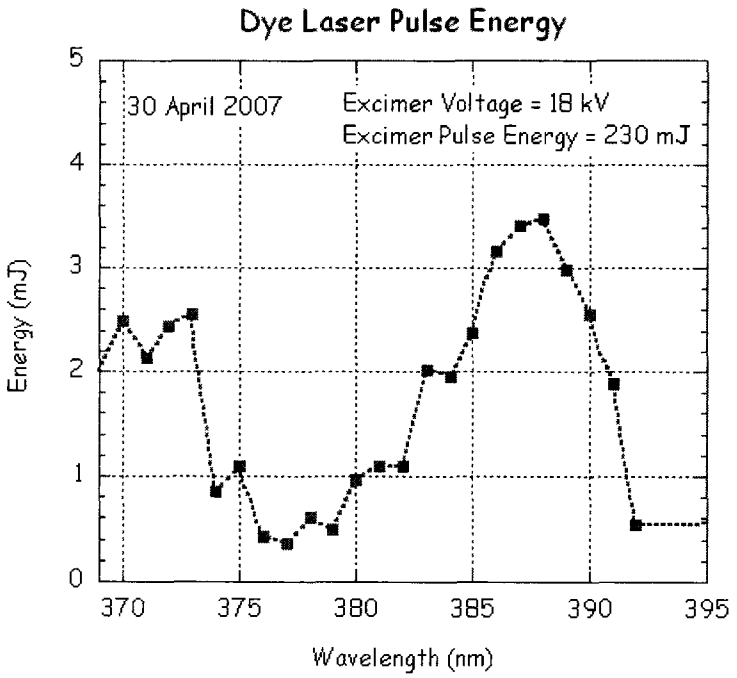

Figure 6.6 Energy of dye laser pulses as a function of wavelength measured on 30 April 2007.

I calculated the integrated lidar signal from 20 to 25 km per laser pulse for each measurement (Figure 6.7). From Figure 6.7 I see that for the first seven measurements the lidar signal follows the transmission curve of the bandpass filter. I obtained the maximum value in the third measurement of 10.6 photon counts per laser pulse at the wavelength of 372 nm. The value of the lidar signal at 372 nm is less than the measurements on the night of 17 April 2007, when I measured 19.3 photon counts per laser pulse. This decrease is consistent with the reduction of the laser energy due to aging of the dye solution and gases in the lasers over the two-week period between the two experiments. The sixth and seventh measurements have values close to 10 photon counts per laser pulse as I tuned the laser to the iron resonance line at 372 nm. In measurements of six and seven I detected echoes from the iron layer which confirms that the lidar transmitter and receiver are well aligned. In Figure 6.7 I see that in the next seven measurements the lidar signal decreases as I tuned the laser to

Reproduced with permission of the copyright owner. Further reproduction prohibited without permission.

391 nm. Between 385 nm and 389 nm the signal changes by a factor of 3.4 while the laser pulse energy changes by a factor of 1.1. I cannot explain the very low signal of 0.28 photon counts per laser pulse at 390.5 nm in terms of laser pulse energy. The lidar signal decreases by a factor of 20 between 387 nm and 390.5 nm while the laser pulse energy decreases by less than a factor of two.

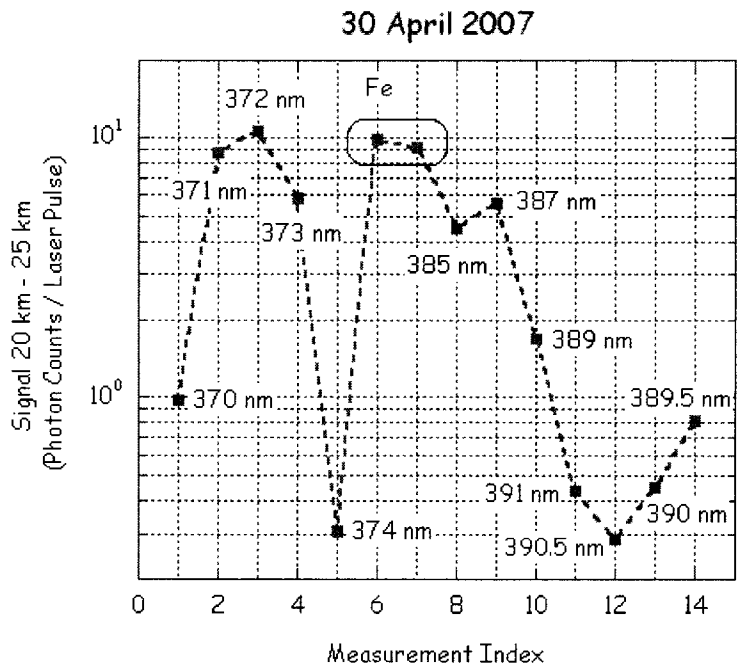

Figure 6.7 Rayleigh lidar signal taken on 30 April 2007.

I cannot explain these lidar measurements in terms of the wavelength dependence of the transmission of the bandpass filter. The lidar measurements appear to be opposite to the measurements of the bandpass filter. While the filter transmission increases by a factor of 1.6 between 385 nm and 390 nm, the lidar signal decreases by a factor of 3.7. The change in lidar system performance over the 0.5 nm interval between 390 and 390.5 nm is unexpected. The transmission of the bandpass filter increases from 52% to 55%, a relative increase of less 6% over this interval. The lidar

Reproduced with permission of the copyright owner. Further reproduction prohibited without permission.

signal decreases from 0.45 photon counts per laser pulse at 390 nm to 0.28 photon counts per laser pulse at 390.5 nm, a relative decrease of 38% over the same interval.

6.2.3 Third Experiment on 27 August 2007

During this experiment I again operated the Rayleigh lidar in conjunction with the resonance lidar. I conducted five sets of resonance lidar experiments. I first made five iron resonance lidar measurements with the bandpass filter that had a center wavelength of 372 nm and 3 nm bandwidth and the dichroic beamsplitter. I then made one iron resonance lidar measurement with the bandpass filter that had a center wavelength of 372 nm and 3 nm bandwidth and a UV reflective mirror (Melles Griot 02MPQ011/028). I then made one measurement at 385 nm with the bandpass filter that had a center wavelength of 404 nm and 40 nm bandwidth and the UV reflective mirror. I then made two measurements at 390 nm with the bandpass filter that had a center wavelength of 404 nm and 40 nm bandwidth and the UV reflective mirror. Finally I made one measurement at 390 nm with a bandpass filter that had a center wavelength of 404 nm and 40 nm bandwidth and the dichroic beam splitter.

I measured the laser pulse energy as a function of wavelength (Figure 6.8). I see that while the laser pulse energy varies with the wavelength between 0.1 mJ/pulse and 5.6 mJ/pulse. The energy at 372 nm and 390 nm is comparable (~5 mJ/pulse). During these measurements, the sky conditions changed considerably as clouds moved across overhead. The Rayleigh lidar signal varied between near clear sky values (0.8 photon counts/laser pulse at 60-65 km) to values 26 times less. I use these Rayleigh lidar measurements to correct the resonance lidar measurements for changes of the atmospheric transmission. I can only make simultaneous Rayleigh and resonance lidar measurements when the dichroic beam splitter is in the receiver. When I put the mirror in the receiver, the Rayleigh channel is blocked. Thus I can only determine the atmospheric transmission during the first five and the tenth resonance lidar measurement.

Reproduced with permission of the copyright owner. Further reproduction prohibited without permission.

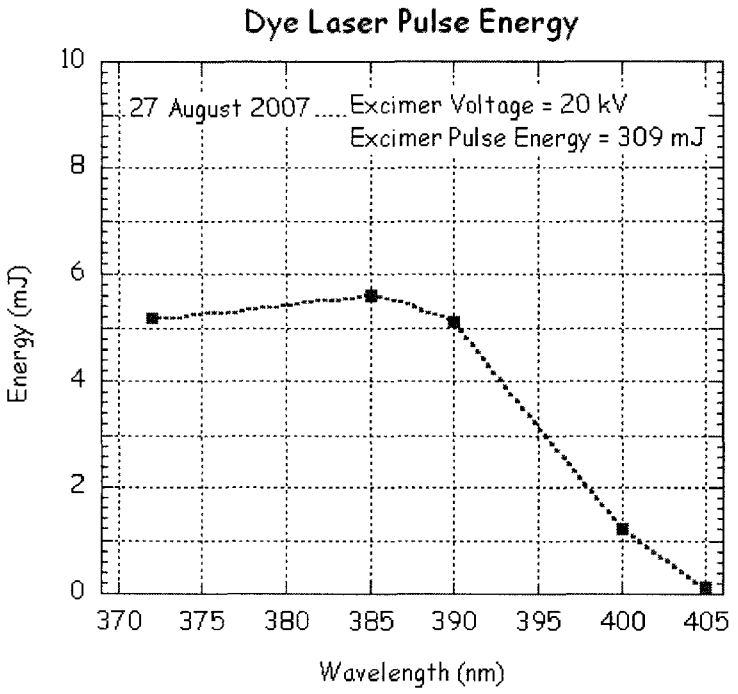

Figure 6.8 Energy of dye laser pulses as a function of wavelength measured on 27 August 2007.

I calculated the integrated lidar signal from 20 to 25 km per laser pulse for each measurement (Figure 6.9). From Figure 6.9 I see that for the first five measurements the iron resonance lidar signal varies by a factor of 5.5 between 28.4 (photon counts/laser pulse) and 5.2 (photon counts/laser pulse). During this period the Rayleigh lidar signal varies by a factor of 4.6. The difference in the two systems reflects the difference in absorption between light at 372 nm and 532 nm. The maximum value of the iron resonance lidar signal of 28.4 (photon counts/laser pulse) is larger than that measured in April and may reflect the absence of ice particles in the atmosphere in August. The fifth and sixth measurements yield signal values of 15.7 and 22.1 (photon counts/laser pulse). This confirms that the dichroic beamsplitter is behaving like a reflecting mirror in the receiver at 372 nm.

Reproduced with permission of the copyright owner. Further reproduction prohibited without permission.

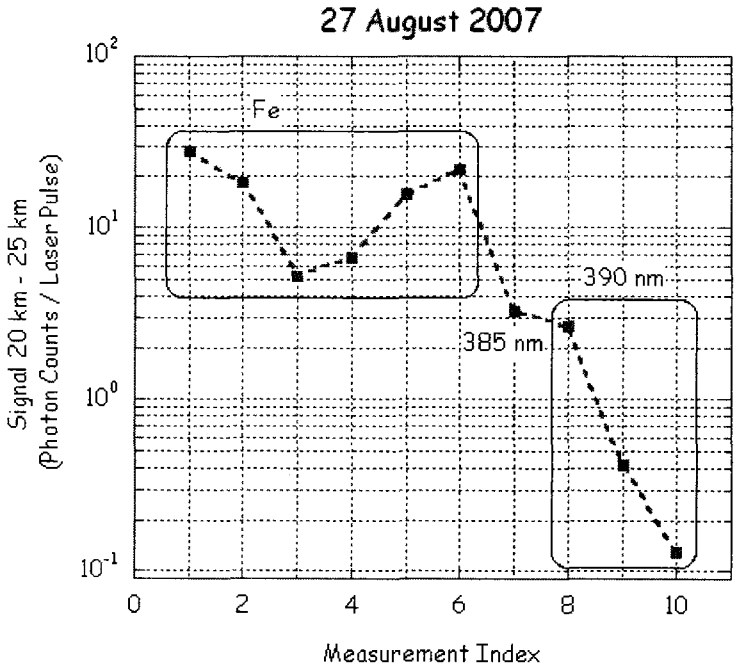

Figure 6.9 Rayleigh lidar signal taken on 27 August 2007.

The signals change by a factor of 1.2 between the seventh measurement at 385 nm and the eight measurements at 390 nm. This compares with a factor of 3.7 over the same wavelength range on 30 April 2007. However, I cannot say if the sky conditions changed during this time as I could not make simultaneous Rayleigh lidar measurements while the UV mirror was in place. The resonance lidar signals continue to decrease during simultaneous Rayleigh lidar measurements during the tenth measurement. The value of the resonance signal for the tenth measurement is 0.128 photon counts per laser pulse a factor of 222 less than the first measurement. However, the Rayleigh lidar signal decreases by a factor of 21 between the first and tenth resonance lidar measurement. Thus I conclude that the decrease in the performance of the resonance lidar is a factor of 10 (=222/21) between the measurement at 372 nm and 390 nm. This is a factor of two better than I measured on 30 April 2007.

I note that the environmental conditions at PFRR vary considerably between August

Reproduced with permission of the copyright owner. Further reproduction prohibited without permission.

and April. The telescope and filters are much warmer (~25 °C) during clear nights in August than in April. The transmission of the atmosphere in April is also lower due to the presence of ice crystals in the atmosphere.

6.3 Examination of Lidar Receiver Optics

To investigate the source of the difference in the first lidar experimental signals I consider the spectral response of the dichroic beamsplitter and the bandpass filter. I used a Horiba Yvon iHR550 spectrometer with a mercury lamp to record the spectral response of these optical components. I first recorded the spectrum of the mercury lamp. I then placed the 390 nm bandpass filter between the lamp and the spectrometer and recorded the transmission spectrum of the filter. I then placed the dichroic beamsplitter between the lamp and spectrometer at 45 degrees and measured the transmission spectrum of the beamsplitter. Finally, I positioned the lamp and the beamsplitter so that the reflected light entered the spectrometer and I measured the reflection spectrum of the beamsplitter. I recorded the spectra at 0.1 nm resolution. I present the spectrometer measurements of the bandpass filter in Figure 6.10. In the top panel I plot the measured spectrum of the mercury lamp and the transmission spectrum of the bandpass filter. In the lower panel I plot the spectral transmission which I have defined as the ratio of the transmission spectrum to the lamp spectrum. From Figure 6.10, I conclude that the transmission characteristics of the bandpass filter are as expected. The bandpass filter transmits light with a peak transmission of ~30% in a ~2 nm (FWHM) bandwidth at 390 nm. I present the spectrometer measurements of the dichroic beamsplitter in Figure 6.11. In the top panel I plot the measured spectrum of the mercury lamp and the transmission and reflection spectra of the dichroic filter. In the lower panel I plot the spectral transmission of the dichroic beamsplitter in transmission (T) and reflection (R). From Figure 6.11, I conclude that the transmission characteristics of the dichroic beamsplitter are as expected. The dichroic beamsplitter has a transmission of ~50% at 425 nm, transmits at longer wavelengths and reflects at shorter wavelengths. In comparison the bandpass filters used for iron lidar measurements have a peak transmission of 50-60% (Barr Associates, Westford, MA).

Reproduced with permission of the copyright owner. Further reproduction prohibited without permission.

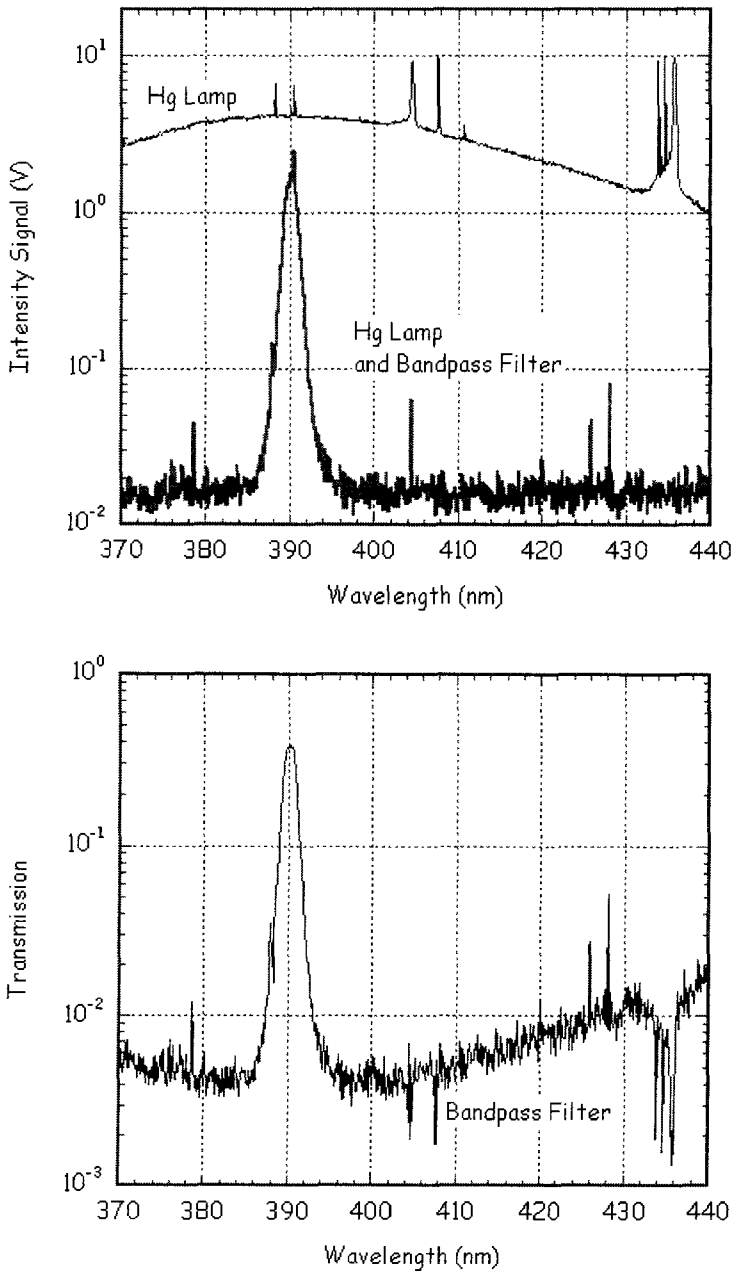

Figure 6.10 Characterization of bandpass filter (390nm, 1 nm bandwidth) by spectrometer. (upper) measured signal as a function of wavelength for Hg lamp with and without bandpass filter. (lower) transmission calculated as a ratio of signals in upper panel. Measurements were made with 0.1 nm resolution.

Reproduced with permission of the copyright owner. Further reproduction prohibited without permission.

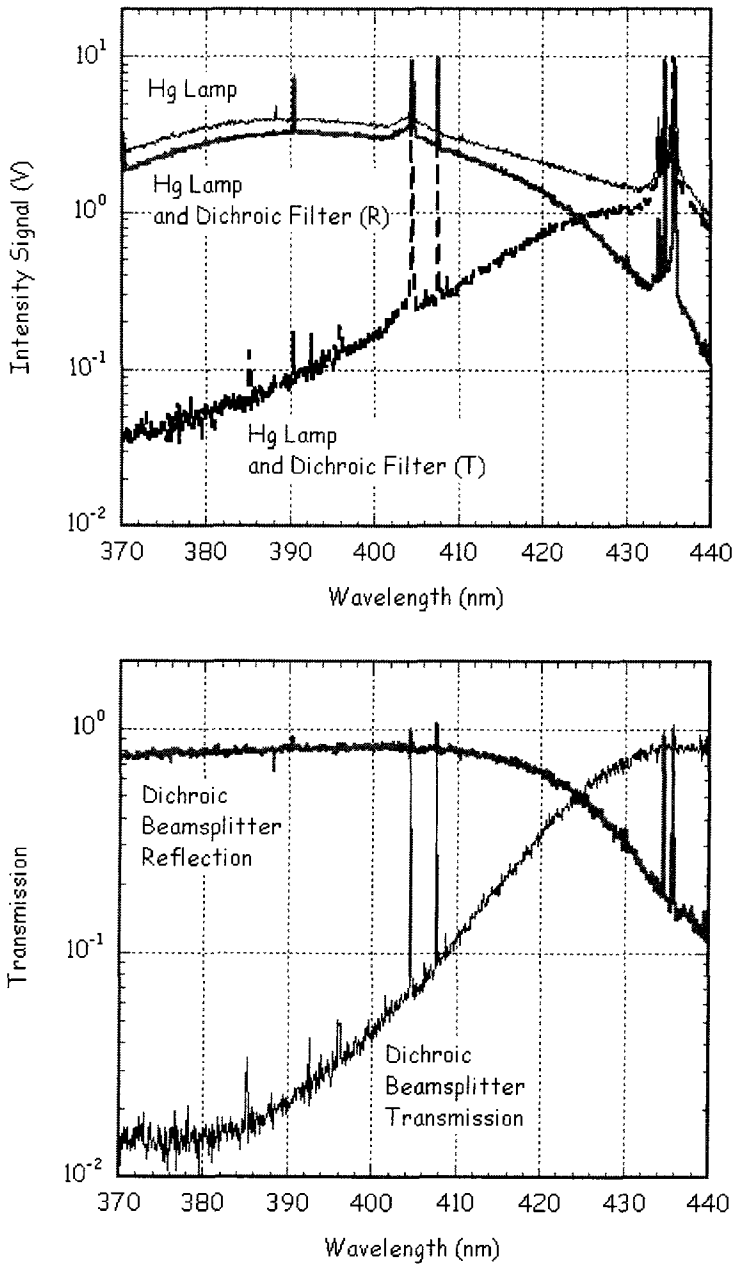

Figure 6.11 Characterization of Dichroic beam splitter (425DCLP) by spectrometer. (upper) measured signal as a function of wavelength for Hg lamp alone, with beamsplitter in transmission and with beamsplitter in reflection. (lower) transmission and reflection calculated as a ratio of signals in upper panel. Measurements were made with 0.1 nm resolution.

Reproduced with permission of the copyright owner. Further reproduction prohibited without permission.

The only difference between the first lidar experiment and the spectrometer measurements is the environmental conditions. During the lidar measurements the telescope is open to the night sky. The receiver room where the telescope and optics are housed is colder than the laboratory where the spectrometer is housed. Under these conditions the center wavelength of bandpass filter may change, thus reducing the optical transmission of the resonance optical channel. To test this possibility I acquired a bandpass filter with a wider bandwidth (40 nm) and conducted a second set of lidar measurements at PFRR.

In the second experiment, to investigate the source of the difference in the signals I again measured the spectral response of the bandpass filter using the Horiba Yvon iHR550 spectrometer with a mercury lamp. I first recorded the spectrum of the mercury lamp. I then placed the 404 nm bandpass filter between the lamp and the spectrometer and recorded the transmission spectrum of the filter. I present the spectrometer measurements of the bandpass filter in Figure 6.12. In the top panel I plot the measured spectrum of the mercury lamp and the transmission spectrum of the bandpass filter. In the lower panel I plot the spectral transmission of the bandpass filter. From Figure 6.12 I conclude that the transmission characteristics of the bandpass filter are as I expect. The bandpass filter transmits light with a transmission of 6 % at 380 nm, 34 % at 385 nm, and 55 % at 390 nm.

Reproduced with permission of the copyright owner. Further reproduction prohibited without permission.

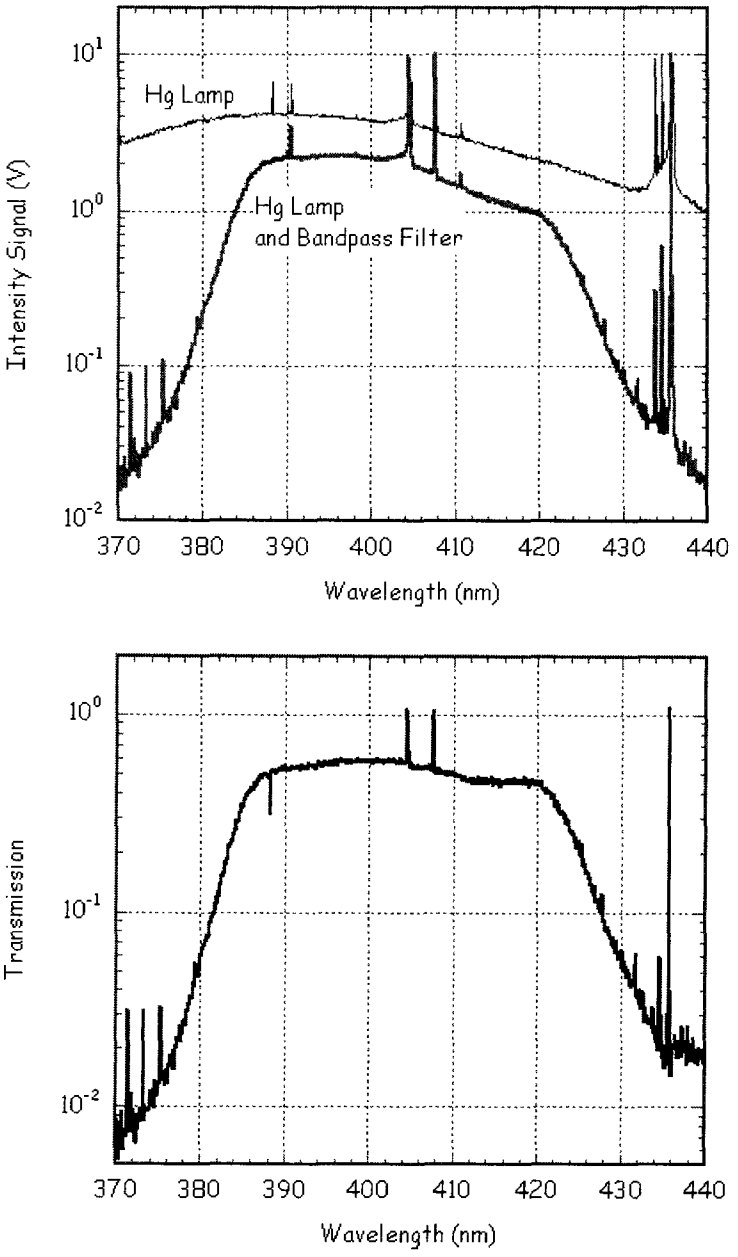

Figure 6.12 Characterization of bandpass filter (404 nm, 40 nm bandwidth) by spectrometer. (upper) measured signal as a function of wavelength for Hg lamp with and without bandpass filter. (lower) transmission calculated as a ratio of signals in upper panel. Measurements were made with 0.1 nm resolution.

Reproduced with permission of the copyright owner. Further reproduction prohibited without permission.

6.4 Examination of Laser Tuning Grating and Polarization

The Scanmate® dye laser employs a Littrow mount grating to tune the wavelength [Peshave, 2004]. The order of the grating is determined by the pitch angle of the grating relative to the optical axis of the laser oscillator. In Figure 6.13 I show the grating position at four different wavelengths. At 589 nm, the grating order is 5 and the decoder value is 945,291. At 372 nm, the grating order is 8 and the decoder value is 988,441. At 390 nm, the grating order is also 8 and the decoder value is 1,188,881. At 400 nm, the grating order changes to 7 and the decoder value is 743,460. I first note that the decoder setting at 589 nm and 372 nm (where I have successfully made sodium and iron measurements) have similar values even though the orders are different. The grating order changes from 7 to 8 at 397 nm. Thus 390 nm is in the wavelength region where grating order changes. The dye laser pulse energy could be lower in this transition region than in regions further from the order transition.

Reproduced with permission of the copyright owner. Further reproduction prohibited without permission.

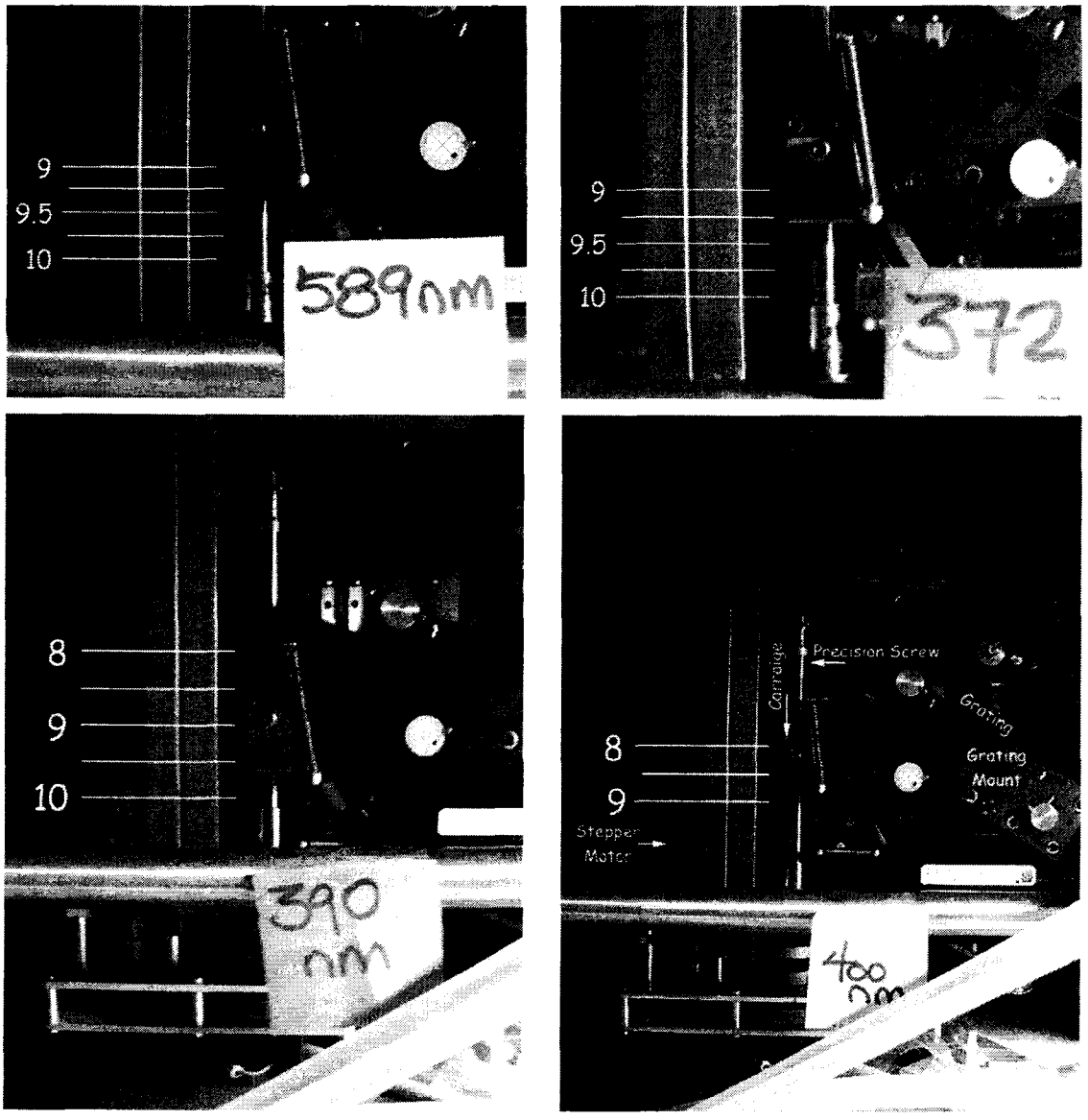

Figure 6.13 Dye laser grating position at four different wavelengths. A carpenter square is placed beside the grating as a reference. (Upper left) Grating at 589 nm with carriage just below 9.25 inch mark. (Upper right) Grating at 372 nm with carriage just below 9.25 inch mark. (Lower left) Grating at 390 nm with carriage just below 9.5 inch mark. (Lower right) Grating at 400 nm with carriage just above 9 inch mark.

Reproduced with permission of the copyright owner. Further reproduction prohibited without permission.

I also examine the polarization of the dye laser. In this experiment, the laser light was passed through a polarizer before the pulse signal was detected by the DET10A photodiode detector. The photodiode signal was recorded by an oscilloscope. I recorded the pulses when the polarizer was at 0 deg and rotated to 90 deg. I plot the laser pulse signals at 372 nm and 390 nm in Figure 6.14. From Figure 6.14, I clearly see that the lasing light is highly polarized at both wavelengths. This result provides evidence that even if the components in the lidar receiver system are sensitive to polarization, they are not so sensitive as to completely attenuate the iron resonance lidar signal. Thus I conclude that the loss of signal at 390 nm is not due to a change in the polarization of the laser light at that specific wavelength.

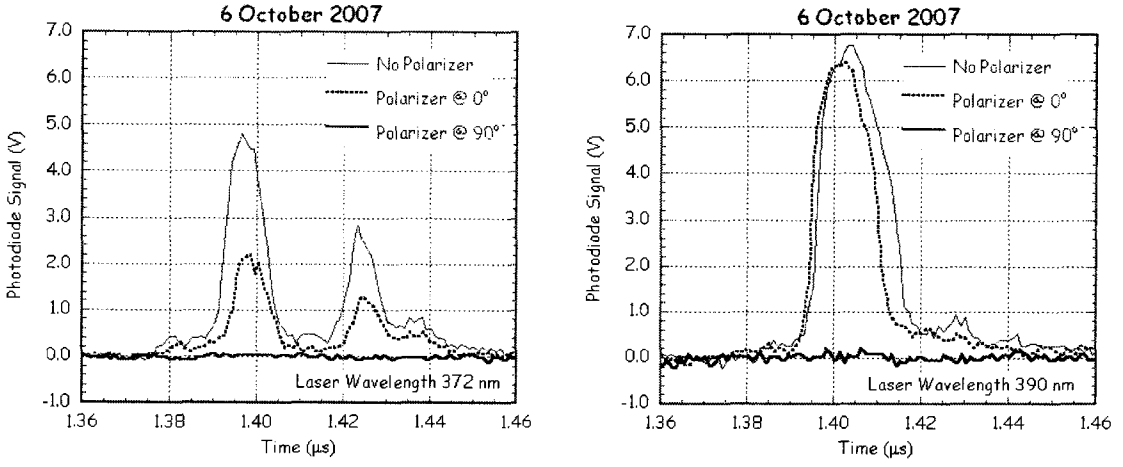

Figure 6.14 Dye lasing polarization at 372 nm and 390 nm.

6.5 Summary and Conclusions

I have conducted several experiments to determine the performance of the resonance lidar system at 390 nm. I have used sodium resonance lidar measurements at 589 nm to confirm and optimize the operation of the resonance lidar. I have then used iron resonance measurements at 372 nm to calibrate the measurements at 390 nm. In three field experiments I find that the lidar performs less efficiently at 390 nm than 372 nm by a factor of 100 in the first experiment, by a factor of 20 in the second

Reproduced with permission of the copyright owner. Further reproduction prohibited without permission.

experiment, and a factor of 10 in the third experiment. Our analysis suggests that the first experiment was compromised due to drift in the narrowband 390 nm filter. However, the results of the second and third experiment show that there is still a significant loss of efficiency (i.e., a factor of 10) in the resonance lidar system at 390 nm. At last, I scaled the N_2^+ resonance lidar simulation signal by a factor of 10 and calculated the confidence level. The results are tabulated in Table 6.1. Given the best SNR case, the confidence level reduces to 72%. Given the worst SNR case, the confidence level reduces to 54%.

Table 6.1 Expected N_2^+ X-B resonance lidar performance

LST (hour)	1905	1955	0055
Altitude(km)	126	162	114
N_{TOT} (Photon Count)	2622	453	8901
N_S (Photon Count)	29	2	36
N_B (Photon Count)	2593	451	8895
SNR	0.57	0.094	0.38
Confidence Level (%)	71.6	53.7	64.8

Resolution of lidar measurement is 6 km and 300 s
Probabilities taken from tables in Abramowitz and Stegun [1972]

Reproduced with permission of the copyright owner. Further reproduction prohibited without permission.

7 Conclusions and Further Work

7.1 Wind-Temperature Lidar Measurements of Heat Fluxes

I have conducted the first complete statistical analysis of the instrumental biases in sodium Doppler wind-temperature lidar measurements of vertical heat fluxes. My Monte Carlo analysis allows me to characterize the full nonlinear propagation of errors in the measurement. I have shown explicitly that the bias arises for two reasons. The first reason is that the measurements of wind and temperature in the three-frequency lidar technique are inherently correlated. Thee individual measurements are combined as sums and differences to yield a pair of temperature and wind estimates. The second reason is due to the curvature in the mapping that inverts the temperature and wind from the ratios of the lidar signals. The biases that I estimate are over an order of magnitude larger than those reported by earlier researchers [Gardner and Yang, 1998].

My analysis shows that there are certain geophysical conditions where the sodium Doppler wind-temperature lidar measurements yields inherent biases that are larger than the expected geophysical measurements. Specifically, I find that for midday summer measurements at mid-latitudes, (when sodium concentrations are seasonally low, and background signals are high) the instrumental bias is 4-30 times greater than the geophysical heat flux. I expect that the challenges are even greater at polar latitudes where the summertime abundance of sodium is lower than at mid-latitudes.
I can reduce the biases by changing the measurement approach. Using four rather than three frequencies would further decouple the wind and temperature measurements. The measurement frequencies could also be chosen to reduce the propagation of error. Temperature measurements at the peak and cross-over frequencies are most sensitive to temperature fluctuations and insensitive to wind fluctuations. Experiments with a scanning approach [Lautenbach and Höffner 2004] will allow researchers to minimize these biases and optimize these flux measurements.

7.2 Development and Implementation of N_2^+ Resonance Lidar

I have simulated the performance of the N_2^+ resonance lidar based on a single

Reproduced with permission of the copyright owner. Further reproduction prohibited without permission.

night of auroral observations using a meridian scanning photometer. The simulation model could be made more accurate if it was extended to include range-resolved information from the new Poker Flat Incoherent Scatter Radar (PFISR). The PFISR measurements would provide measurements of electric fields, ion and electron temperatures that would give a more accurate representation of the auroral thermosphere. This modeling effort would also lay a foundation for the final assimilation of radar, lidar and photometric measurements to better understand the auroral production of nitric oxide.

The photodiode detector and op-amp peak detector are working as designed. The integrated data acquisition and control system is working as designed. I have characterized the FPI in the tuning control system based on the differences between successive fringes. The estimate of the FPI plate spacing is accurate to less than 1 part in 100,000. However, the FPI calibration measurements did not yield an absolute calibration of the FPI. The operation of the FPI during lidar measurements will require that the FPI be calibrated with the dye laser tuned to a N_2^+ resonance signal from the thermosphere.

The field experiments have yielded signals that are an order of magnitude less than I expected. I have carefully tested the receiver optics and find that the key optical elements are behaving as designed and do not seem to be the source of the signal loss. The high degree of polarization of the laser light at both 372 nm and 390 nm indicates that there is a Brewster angle effect in the custom multi-prism optics in the dye laser tuning block. While the grating order changes from 8 to 7 in the vicinity of 390 nm, there does not appear to be a significant difference in the polarization of the laser light at 372 nm and 390 nm.

There may be a difference in the ratio of stimulated to amplified spontaneous emission at 390 nm relative to 372 nm. The QUI dye in the laser has maximum gain at 390 nm and thus could support significant amplification of spontaneous emission at this wavelength. A careful realignment of the laser would result in more efficient laser operation and yield higher laser pulse energy. An increase in laser energy would allow more careful investigation of the lidar performance. I recommend that the dye laser be completely realigned before continuing with further field trials.

Reproduced with permission of the copyright owner. Further reproduction prohibited without permission.

It is important to note that while I conducted my simulation at a resolution of 6 km and 300 s, the resolution of actual observations could be adapted to the particular geophysical conditions. Measurements during more active aurora could be made at higher resolution. The spatial and temporal resolution could be traded-off to yield the appropriate signal to noise ratio and confidence level while maintaining sufficient resolution in altitude or time to investigate specific characteristics of an auroral substorm. These adaptive modes of observation will be developed with experience at PFRR.

Reproduced with permission of the copyright owner. Further reproduction prohibited without permission.

Appendix: Schematics, layout and artwork of high speed peak detector

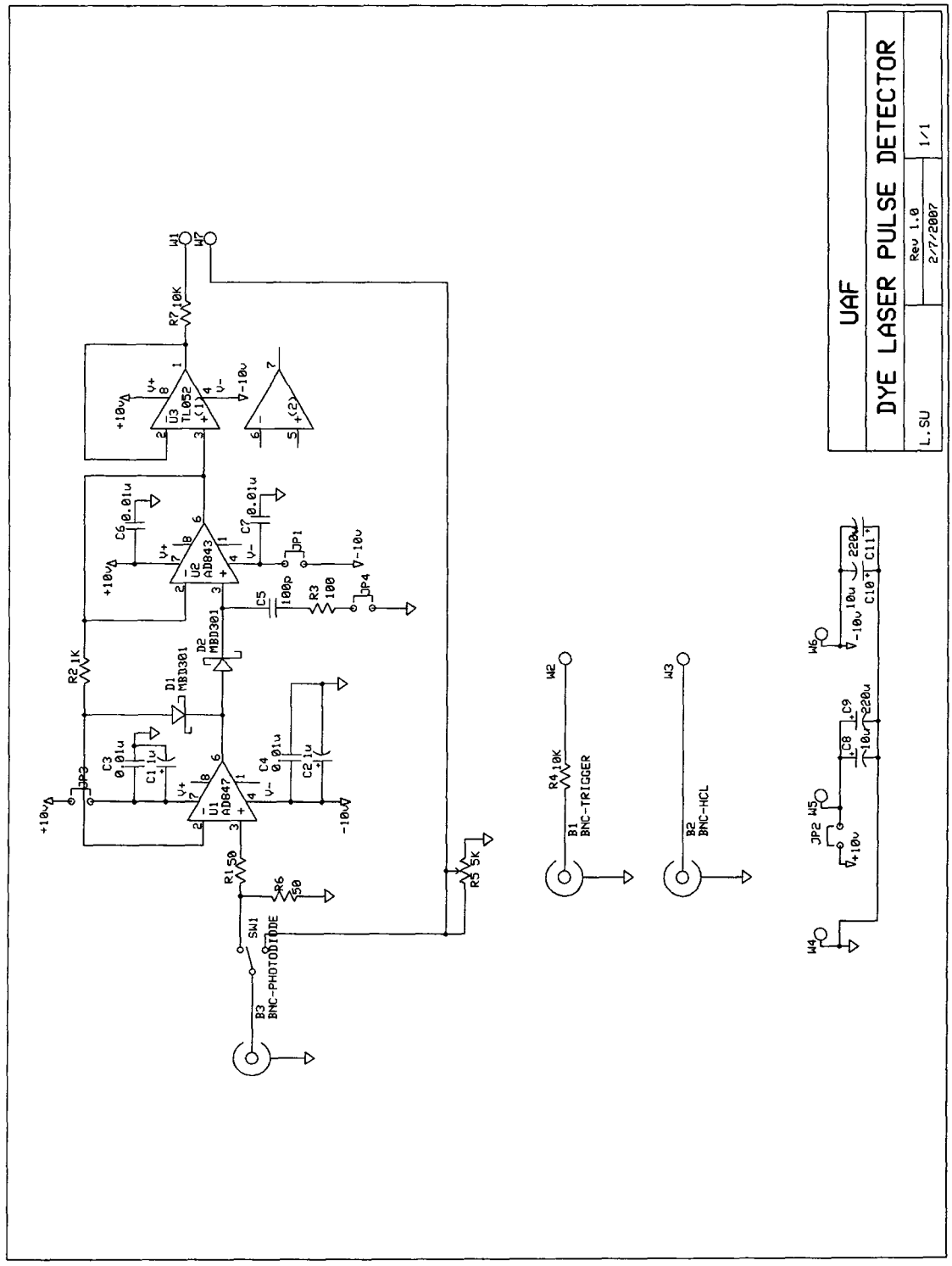

Reproduced with permission of the copyright owner. Further reproduction prohibited without permission.

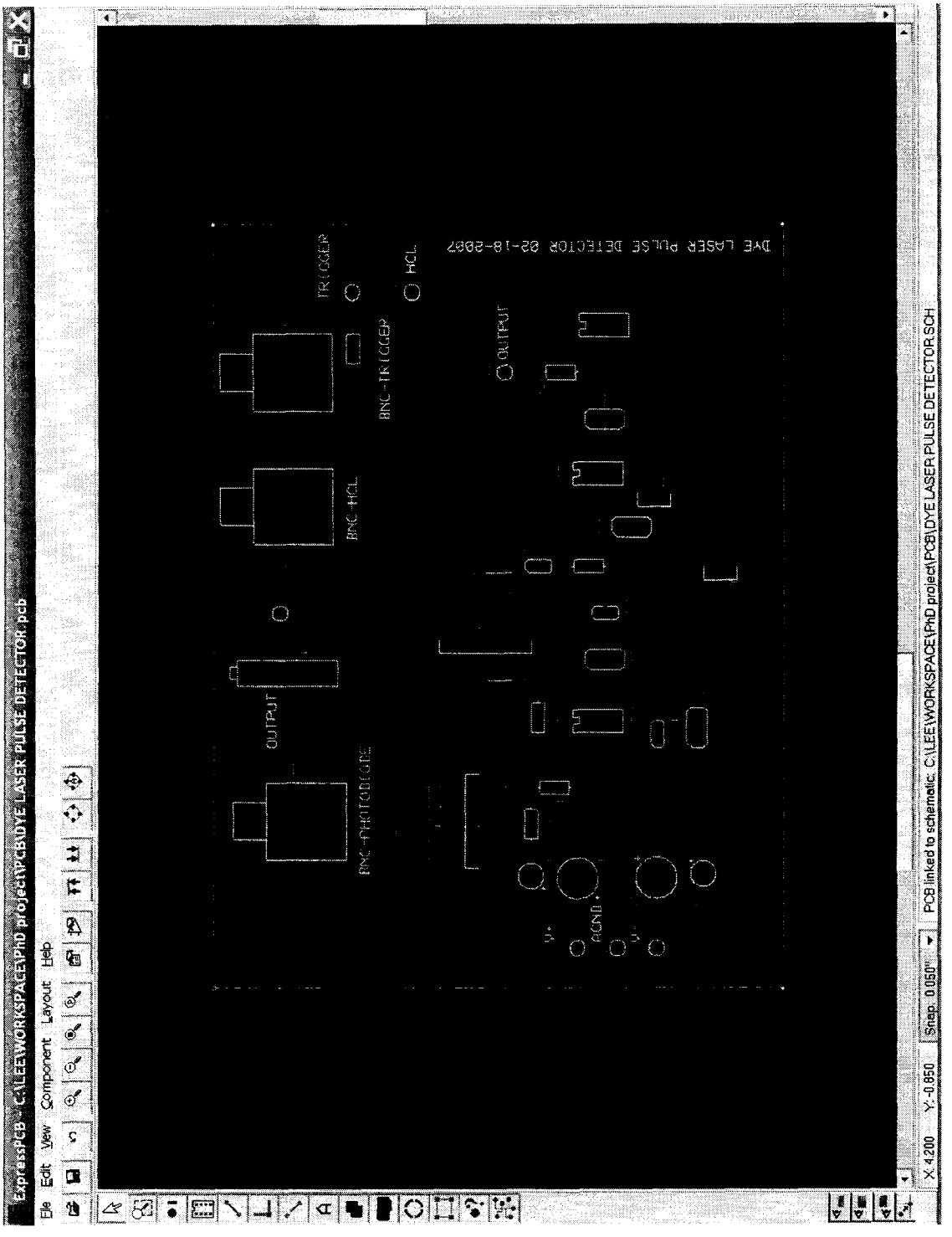

Reproduced with permission of the copyright owner. Further reproduction prohibited without permission.

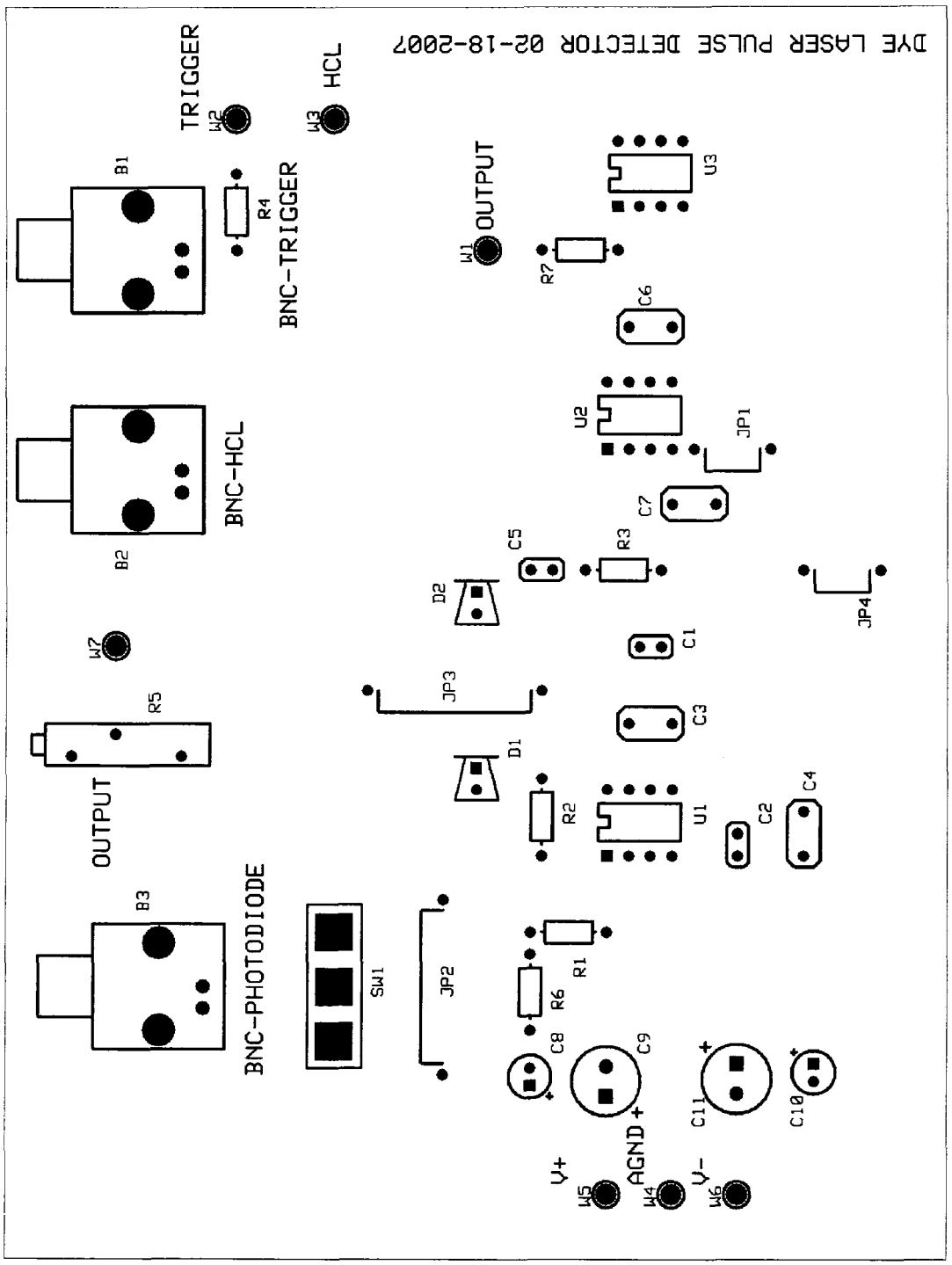

Reproduced with permission of the copyright owner. Further reproduction prohibited without permission.

References

Abramowitz, M, and I. A. Stegun, 1972: Handbook of Mathematical Functions with Formulas Graphs, and Mathematical Tables, Dover, New York.

Ahrens, T. I., 1998: An improved peak detector, Intersil Corporation.

Analog Devices, 1995: AD843 data sheet, Analog Devices.

_____, 1992: AD847 data sheet, Analog Devices.

Andrews, D. G., J. R. Holton, and C. B. Leovy, 1987: Middle Atmosphere Dynamics, Academic Press.

Arnold, K. S., and C. Y. She, 2003: Metal fluorescence lidar (light detection and ranging) and the middle atmosphere, Contemporary Physics, 44, pp. 35-49.

Atkins, P. W., Quanta: A Handbook of Concepts, Oxford, 1991.

Becker, E., 2004: Direct heating rates associated with gravity wave saturation, Journal of Atmospheric and Solar-Terrestrial Physics, 66, pp. 633-696.

Bills, R. E., C. S. Gardner and S. F. Franke, 1991: Na Wind-temperature lidar: Initial mesopause region observations and comparison with the Urbana MF radar, Journal of Geophysical Research, 96, pp. 22701-22707.

Born, M. and E. Wolf, 1993: Principles of Optics, Pergamon Press, Oxford.

Bowman, M. R., A. J. Gibson, and M. C. W. Standford, 1969: Atmospheric Sodium measured by a tuned laser radar, Nature, 221, pp. 457-459.

Boyd, R. W., 1992: Nonlinear Optics, Academic Press, Boston.

Reproduced with permission of the copyright owner. Further reproduction prohibited without permission.

Breese, J., 2001: Development of Fe Boltzmann Temperature Lidar, M.S. Thesis, University of Alaska Fairbanks.

Brown J. M., 1998: Molecular Spectroscopy, Oxford University Press.

Cariou, J., and P. Luc, 1980: Atlas du Spectre D'absorption de la Molecule de Tellure, Laboratoire Aim'Cotton, CNRS II, Orsay.

Chamberlain, J. W., 1995: Physics of the Aurora and Airglow, American Geophysical Union.

Chu, X., and G. C. Papen, 2005: Resonance fluorescence lidar for measurements in the middle and upper atmosphere, in Laser Remote Sensing, T. Fujii and T. Fukuchi, eds., CRC Press.

_____, G. C. Papen, W. Pan, and C.S. Gardner, J. Gelbwachs, 2002: Fe Boltzmann temperature lidar: design, error analysis and first results from North and South Poles, Applied Optics, 41, pp. 4400-4410.

Collins, R. L., 2004: A lidar tutorial: speak at the Colorado State University, Fort Collins, Colorado.

_____, D. Lummerzheim, and R. W. Smith, 1997: Analysis of lidar systems for profiling aurorally excited molecular species, Applied Optics, 36, 24.

_____, and H. Stenbaek-Nielsen, 1995: Barium ion lidar: analysis of a lidar system for measuring temperatures in the middle thermosphere (200-500 km), Optical remote sensing of the atmosphere, 2, Salt Lake City, Utah.

_____, M. C. Kelley, M. J. Nicolls, C. Ramos, T. Hou, T. E. Stern, K. Mizutani and T. Itabe, 2003: Simultaneous Lidar Observations of a Noctilucent Cloud and an Internal Wave in the Polar Mesosphere, Journal of Geophysical Research, vol. 108, no. D8, 8435.

Reproduced with permission of the copyright owner. Further reproduction prohibited without permission.

_____, and R. W. Smith, 2004: Evidence of damping and overturning of gravity waves in the Arctic mesosphere: Na lidar and OH temperature observations, Journal of Atmospheric and Solar-Terrestrial Physics, 66, pp. 867-879.

_____, T. Hou, M. A Peshave, M. G. Conde, B. W. Reinisch, 2003: Observations of Sporadic Sodium-, Iron- and E-Layers at a High-Latitude Site, Fall AGU Meeting, San Francisco, CA.

_____, T. J. Hallinan, R. W. Smith and G. Hernandez, 1996: Lidar observations of a large high-altitude sporadic Na layer during active aurora, Geophysical Research Letters, vol. 23, no. 24, pp. 3655-3658.

CRC, 2007: Handbook of Chemistry and Physics, 88th Edition, David R. Lide et al. eds., CRC Press.

Cutler, L. J., R. L. Collins, K. Mizutani, and T. Itabe, 2001: Rayleigh lidar observations of mesospheric inversion layers at Poker Flat, Alaska 65° N, 147° W, Geophysical Research Letters, 28, 8, pp. 1467-1470.

Demtroder W., 1996: Laser Spectroscopy: Basic Concepts and Instrumentation Second Enlarged Edition, Springer.

Engstrom, R. W., 1980: Photomultiplier Handbook, RCA.

Felix, F., W. Keenliside, G. Kent, and M. C. W. Sandford, 1973: Laser radar observations of atmospheric potassium, Nature, 246, pp. 345-346.

Fricke, K. H. and U. von Zahn, 1985: Mesopause temperatures derived from probing the hyperfine structure of the D2 resonance line of sodium by lidar, Journal of Atmospheric and Terrestrial Physics, 47, pp. 499-512.

Reproduced with permission of the copyright owner. Further reproduction prohibited without permission.

Fritts, D. C., and M. J. Alexander, 2003: Gravity wave dynamics and effects in the middle atmosphere, Reviews of Geophysics, 41, pp. 1003, doi:10.1029/2001RG000106.

Fukuchi, T., A. Y. Wong, and R. F. Wuerker, 1990: Ionospheric RF lidar, Radio Science, 25, pp. 1299-1309.

Fuhr, J. R., G. A. Martin, W. L. Wiese, 1988: Atomic Transition Probabilities Iron Through Nickel, Journal of Physical and Chemical Reference Data, 17 (Supplement 4), pp. 1-504.

Gardner, C. S., 1989: Sodium resonance fluorescence lidar applications in atmospheric science and astronomy, Proceedings of the IEEE, 77, pp. 408 -418.

_____, 2004: Performance capabilities of middle-atmosphere temperature lidars: comparison of Na, Fe, K, Ca, Ca+, and Rayleigh systems, Applied Optics, 43, pp. 4941-4956.

_____, D. C. Senft, and K. H. Kwon, 1988: Lidar observations of substantial sodium depletion in the summertime arctic mesosphere, Nature, 332, pp. 142-144.

_____, D. G. Voelz, C. F. Sechrist and A. C. Segal, 1986: Lidar studies of the nighttime sodium layer over Urbana, Illinois 1. Seasonal and nocturnal variations, Journal of Geophysical Research, 91, pp. 13659-13673.

_____, G. C. Paper, X. Chu, and W. Pan, 2001: First lidar observations of middle atmosphere temperatures, Fe densities, and polar mesospheric clouds over the north and south pole, Geophysical Research Letters, 28, 7, pp. 1199-1202.

_____, J. M. C. Plane, W. Pan, T. Vondrak, B. J. Murray, X. Chu, 2005: Seasonal variations of the Na and Fe layers at the south pole and their implications for the chemistry and general circulation of the polar mesosphere, Journal of Geophysical Research, 110, D10302, doi:10.1029/2004JD005670.

Reproduced with permission of the copyright owner. Further reproduction prohibited without permission.

_____, and W. Yang, 1998: Measurements of the dynamical cooling rate associated with the vertical transport of heat by dissipating gravity waves in the mesopause region at the Starfire Optical Range, New Mexico, Journal of Geophysical Research, 103, 16, pp. 16,909-16,926.

_____, Y. Zhao, and A. Z. Liu, 2002: Atmospheric stability and gravity wave dissipation in the mesopause region, Journal of Atmospheric and Solar-Terrestrial Physics, 64, pp. 923-929.

Garner, R. C. and P. Dao, 1995: Molecular nitrogen fluorescence lidar for remote sensing of the auroral ionosphere, Journal of Geophysical Research, 100, 74, pp. 14,131-14,140.

Gelbwachs, J. A., 1994: Iron Bolzmann factor LIDAR: proposed new remote-sensing technique for mesospheric temperature, Applied Optics, 33, pp. 7151-7156.

Gelinas, L. J., K. A. Lynch, M. C. Kelley, R. L. Collins, M. Widholm, E. MacDonald, J. Ulwick, and P. Mace, 2005: Mesospheric charged dust layer: Implications for neutral chemistry, Journal of Geophysical Research., 110, A01310, doi:10.1029/2004JA010503.

Gerrard, A. J., T. J. Kane, D. D. Meisel, J. P. Thayer, R. B. Kerr, 1997: Investigation of a resonant lidar for measurement of ionospheric metastable helium, Journal of Atmospheric and Solar-Terrestrial Physics 59, 16, pp. 2023-2035.

Gerstenkorn, S., 1978 : Atlas du spectre d'absorption de la molecule d'iode, 14800-20000 cm-1, Centre National de la Recherche Scientifique.

Gibson, A. J., L. Thomas, and S. K. Bhattachacharyya, 1979: Laser observations of the ground-state hyperfine structure of sodium and of temperatures in the upper atmosphere, Nature, 281, pp. 131-132.

Reproduced with permission of the copyright owner. Further reproduction prohibited without permission.

Gilmore, F. R., R. R. Laher, Patrick J. Espy, 1992: Franck-Condon factors, r-centroids, electronic transition moments, and Einstein coefficients for many nitrogen and oxygen band systems, Journal of Physical and Chemical Reference Data, 21, 5, pp.1005-1107.

Goree, J. and J. S. Neff, 1989: Lidar technique for measuring ionospheric barium release ion density, Journal of Geophysical Research, 94, pp. 1533-1536.

Grant, W. B., E. V. Browell, R. T. Menzies, K. Sassen, and C. Y. She, eds., 1997: Laser Applications in Remote Sensing, MS 141, SPIE Milestones Series, SPIE.

Hamamatsu, 2007: Photodiode Technical Guide, Hamamatsu USA.

Hauptmann, P., 1993: Sensors: Principles & Applications, Prentice Hall International (UK) Ltd.

Hecht, E. and A. Zajac, 1974: Optics, Addison Wesley.

Hernandez, G., 1988: Fabry-Perot Interferometers, Cambridge University Press, Cambridge.

Herzberg, G., 1950: Molecular spectra and molecular structure I. Spectra of diatomic molecules, Second Edition, D. Van Nostrand Company, Toranto-New York-London.

Hollas J. M., 2005: Modern Spectroscopy 4th Edition, John Wiley & Sons.

Horowitz, P, and W. Hill, 1993: The art of electronics, Second edition, Cambridge University Press.

Hou, T., 2002: Development of High Spectral Resolution Iron Boltzmann Lidar, M.S. Thesis, University of Alaska Fairbanks.

Reproduced with permission of the copyright owner. Further reproduction prohibited without permission.

Houghton, J. T., 1978: The stratosphere and mesosphere, Quarterly Journal of the Royal Meteorological Society, 104, pp. 1-29.

_____, 1986: The Physics of Atmospheres, Second Edition, Cambridge University Press.

Huang, T. Y. W., and A. K. Smith, 1991: The mesospheric diabatic circulation and the parameterized thermal effect of gravity wave breaking on the circulation, Journal of Atmospheric Sciences, 48, pp. 1093-1111.

Johnson, R. M., T. L. Killeen, (Eds.), 1995: The upper mesosphere and lower thermosphere; A review of experiment and theory, Geophysical Monograph, 87, American Geophysical Union, Washington.

Jones, A. V., 1974: Aurora, D. Reidel Publishing Company, Dordrecht, Holland.

Kelly, J. D., 2006: Heinselman, C. J., Valentic, T., A new instrument for ionospheric research - AMISR, Eos Transactions AGU, 87(52).

Kerr, R. B., J. Noto, R. S. Lancaster, M. Franco, R. J. Rudy, 1996: Fabry-Perot observations of helium 10830Å emission at Millstone Hill, Geophysical Research Letters, 23, 22, pp. 3239-3242.

Koechner, W., 1996: Solid-State Laser Engineering 4th Edition, Springer.

Kudeki E., and S. J. Franke, 1998: Statistics of momentum flux estimation, Journal of Atmospheric and Solar-Terrestrial Physics, 60, pp. 1549-1553.

Lambda Physik, 1997: Dye Laser Scanmate Instruction Manual, Lambda Physik Laser Technik.

Reproduced with permission of the copyright owner. Further reproduction prohibited without permission.

Lautenbach, J., and J. Höffner, 2004: Scanning iron temperature lidar for mesopause temperature observation, Applied Optics, 23, pp. 4559-4563.

Liu, A. Z., and C. S. Gardner, 2005: Vertical heat and constituent transport in the mesopause region by dissipating gravity waves at Maui Hawaii (20.7°N) and Starfire Optical Range, New Mexico (35°N), Journal of Geophysical Research, 110, D09S13, doi:10.1029/2004JD004965.

Lofthus A. and P. H. Krupenie, 1977: The Spectrum of Molecular Nitrogen, Journal of Physical and Chemical Reference Data, 6, 1, pp. 113-307.

Lummerzheim, D., 1987: Electron Transport and Optical Emissions in the Aurora, Ph.D. Thesis, University of Alaska, Fairbanks.

_____, and J. Lilensten, 1994: Electron transport and energy degradation in the Ionosphere: evaluation of the numerical solution, comparison with laboratory experiments and auroral observations, Annales Geophysicae, 12, 1039.

_____, M. H. Rees, and H. R. Anderson, 1989: Angular dependent transport of auroral electrons in the upper atmosphere, Planetary and Space Science, 37, 109.

Lynch K. A., L. J. Gelinas, M. C. Kelley, R. L. Collins, M. Widholm, D. Rau, E. MacDonald, Y. Liu, J. Ulwick, and P. Mace, 2005: Multiple sounding rocket observations of charged dust in the polar winter mesosphere, Journal of Geophysical Research, 110, A03302, doi:10.1029/2004JA010502.

Marsaglia, G., 1965: Ratios of normal random variables and ratios of sums of uniform variables, Journal of The American Statistical Association, 60, pp. 193-204.

Measures, R. M., 1992: Laser Remote Sensing, Krieger, Malabar, Florida.

Reproduced with permission of the copyright owner. Further reproduction prohibited without permission.

Megie, G., F. Bos, J. E. Blamont, and M. L. Chanin, 1978: Simultaneous nighttime measurements of atmospheric sodium and potassium, Planetary and Space Science, 26, pp. 23-35.

Mizutani, K., T. Itabe, M. Yasui, T. Aoki, Y. Murayama, R. L. Collins, 2000: Rayleigh and Rayleigh Doppler Lidars for the Observations of the Arctic Middle Atmosphere, IEICE Transactions on Communications, vol. E83-B, no. 9, pp. 2004-2009.

Morrill, J. S. and W. M. Benesch, 1996: Auroral N_2 emissions and the effect of collisional processes on N_2 triplet state vibrational populations, Journal of Geophysical Research, 101, pp. 261-274.

Morse, T. H. and G. J. Romick, 1982: The fluctuation and fading of auroral arcs preceding auroral substorm onsets, Geophysical Research Letters, 9, pp. 1065-1068.

NIST, 2007: Atomic Spectra Database version 3.1.2,http://physics.nist.gov/PhysRef Data/ASD/index.html, first accessed on 26 April 2007.

Oliver, B. M., 1965: Thermal and Quantum Noise, Proceedings of the IEEE, pp. 436-454.

Papalias, T. A. and M. Wong, 2007: Feedback gives peak detector more precision, Intersil Corporation.

Papoulis, A., and S. U. Pillai, 2002: Probability, Random Variables, and Stochastic Processes, McGraw Hill.

Pearson, E. S., and N. L. Johnson, 1968: Tables of the incomplete Beta function, Cambridge University Press.

Peshave, M., 2004: Design and Implementation of a Microcontroller-Based Closed-Loop Tuning-Controller for a Tunable Dye Laser, M.S. Thesis, University of Alaska Fairbanks.

Reproduced with permission of the copyright owner. Further reproduction prohibited without permission.

Phelps, F. M. III, 1982: MIT Wavelength Tables, 2: Wavelengths by Element, MIT Press, Cambridge, MA.

Plane, J. M. C., 1991: The chemistry of meteoric metals in the earth's upper atmosphere, International Reviews in Physical Chemistry, 10, pp. 55-106.

Press, W. H., S. A. Teukolsky, W. T. Vetterling, B. P. Flannery, 1992: Numerical Recipes, in FORTRAN: The Art of Scientific Computing, Second edition, Cambridge University Press.

Rao, A. M., 1995: Daytime Lidar Data Acquisition Using the Fabry-Perot Interferometer, University of Alaska Fairbanks, Fairbanks, AK.

RCA Staff, 1974: Electro-Optics Handbook, RCA, Lancaster, PA.

Research Systems, 1999: RANDOMN, IDL Reference Guide N-Z, Research Systems, Boulder, CO.

Schoeberl, M. R., D. F. Strobel, and J. P. Apruzese, 1983: A numerical model of gravity wave breaking and stress in the mesosphere, Journal of Geophysical Research, 88, pp. 5249-5259.

Seinfeld, J. H. and S. N. Pandis, 1997: Atmospheric chemistry and physics: from air pollution to climate change, Wiley-Interscience.

She, C. Y., H. Latifi, J. R. Yu, R. J. Alvarez II, R. E. Bills, C.S. Gardner, 1990: Two-frequency lidar technique for mesospheric na temperature measurements, Geophysical Research Letters, 17, pp. 929-932.

_____, and J. R. Yu, 1995: Doppler-free saturation fluorescence spectroscopy of na atoms for atmospheric applications, Applied Optics, 34, pp. 1063-1075.

Reproduced with permission of the copyright owner. Further reproduction prohibited without permission.

_____, J. R. Yu, H. Latifi, and R. E. Bills, 1992: High-spectral-resolution fluorescence lidar for mesospheric sodium temperature measurements, Applied Optics 31, pp. 2095-2106.

Sherman, J. P., 2002: Mesopause Region Thermal and Dynamical Studies Based on Simultaneous Temperature, Zonal and Meridional Wind Measurements with an Upgraded Sodium Fluorescence Lidar, Ph.D. dissertation, Colorado State University.

Shriever, B. A., 1960: Handbook of Geophysics, Macmillan, New York.

Siskind, D. E., S. D. Eckermann, and M. E. Summers, (Eds.), 2000: Science across the stratopause, Geophysical Monograph 123, American Geophysical Union, Washington.

Solomon, S. and G. Brasseur, 2005: Aeronomy of the Middle Atmosphere: Chemistry and Physics of the Stratosphere and Mesosphere, Springer.

SRI International, 2007: AMISR - Advanced Modular Incoherent Scatter Radar, http://isr.sri.com/iono/amisr, first accessed on 26 April 2007.

Stull, R. B., 1989: An Introduction to Boundary Layer Meteorology, Kluwer.

Su, L., R. Collins, D. Krueger, and C. Y. She, 2007: Statistical analysis of sodium Doppler wind-temperature lidar measurements of vertical heat flux, Journal of Atmospheric and Oceanic Technology (in press).

Thorlabs, 2007: FDS010 Si high speed photodiode datasheet, Thorlabs.

Thorsen, D., S. J. Franke and E. Kudeki, 2000: Statistics of momentum flux estimation using the dual coplanar beam technique, Geophysical Research Letters, 19, pp. 3193-3196.

Reproduced with permission of the copyright owner. Further reproduction prohibited without permission.

Vaughan J. M., 1989: The Fabry Perot interferometer: History, Theory, Practice and Applications, IPO Publishing Ltd.

Vincent, R. A., and I. M. Reid, 1982: HF Doppler measurements of mesospheric gravity wave momentum fluxes, Journal of Atmospheric Sciences, 39, pp. 1321-1333.

Walterscheid, R. L., 1981: Inertio-gravity wave induced accelerations of mean flow having an imposed periodic component: Implications for tidal observations in the meteor region, Journal of Geophysical Research, 86, pp. 9698-9706.

Wang, D.-Y., and D. C. Fritts, 1990: Mesospheric momentum fluxes observed by the MST radar at Poker Flat Alaska, 47, Journal of Atmospheric Sciences, pp. 1512-1521.

Wayne, R. P., 1985: Chemistry of Atmospheres, Oxford University Press.

White, M. A., 1999: A Frequency-agile Na Lidar for the Measurement of Temperature and Velocity in the Mesopause Region, Ph.D. dissertation, Colorado State University.

Wright, J., 1992: Peak detectors gain in speed and performance, Linear technology.

Wiese, W. L., M. W. Smith, and B. M. Miles, 1969: Atomic Transition Probabilities (Na through Ca - A Critical Data Compilation), National Standard Reference Data Series, National Bureau of Standards (United States), NSRDS-NBS 22, II.

Wuerker, R. F., L. Schmitz, T. Fukuchi, and P. Straus, 1988: Lifetime measurements of the excited states of N_2 and N_2^+ by laser-induced fluorescence, Chemical Physics Letters, 150, 6, pp.443-446.

Reproduced with permission of the copyright owner. Further reproduction prohibited without permission.